Development of Vanadium Alloys for Advanced Energy Systems

By

UTTAM JAIN

ENROLLMENT NUMBER: ENGG01201304035

Bhabha Atomic Research Centre, Mumbai

A dissertation submitted to the
Board of studies in Engineering Sciences

In partial fulfillment of requirements

For the Degree of

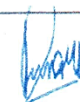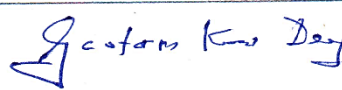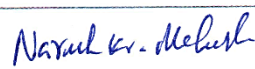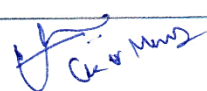## DOCTOR OF PHILOSOPHY

of

HOMI BHABHA NATIONAL INSTITUTE

October, 2020

Homi Bhabha National Institute[1]

Recommendations of the Viva Voce Committee

As members of the Viva Voce Committee, we certify that we have read the dissertation prepared by **Uttam Jain** entitled "**Development of vanadium alloys for advanced energy systems**" and recommend that it may be accepted as fulfilling the thesis requirement for the award of Degree of Doctor of Philosophy.
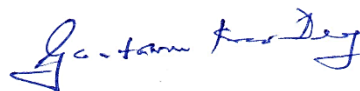
Chairman -	Dr. S. Banerjee	*Srikumar Banerjee*	Date:10/10/2020
Guide / Convener-	Dr. R. Tewari		Date: 10/10/20
Co-guide and Member	Dr. G.K. Dey	*Goutam Kr Dey*	Date: 10/10/2020
Examiner -	Dr. N.K. Mukhopadhyay	*N. K. Mukhopadhyay*	Date: 10.10.2020
Member -	Dr. N.K. Maheshwari	*Naresh Kr. Mahesh*	Date: 10/10/2020
Member -	Dr. G. Sugilal	*Sugilal*	Date: 10/10/20
Technology Advisor - Dr. K.V. Manikrishna			Date: 10/10/2020

Final approval and acceptance of this thesis is contingent upon the candidate's submission of the final copies of the thesis to HBNI.

I/We hereby certify that I/we have read this thesis prepared under my/our direction and recommend that it may be accepted as fulfilling the thesis requirement.

Date: 10/10/20

Place: TROMBAY BARC

Goutam Kr Dey
Signature
Co-guide

Signature
Guide

---

[1] This page is to be included only for final submission after successful completion of viva voce.

I

STATEMENT BY AUTHOR

This dissertation has been submitted in partial fulfilment of requirements for an advanced degree at Homi Bhabha National Institute (HBNI) and is deposited in the Library to be made available to borrowers under rules of the HBNI.

Brief quotations from this dissertation are allowable without special permission, provided that accurate acknowledgement of source is made. Requests for permission for extended quotation from or reproduction of this manuscript in whole or in part may be granted by the Competent Authority of HBNI when in his or her judgment the proposed use of the material is in the interests of scholarship. In all other instances, however, permission must be obtained from the author.

UTTAM JAIN

DECLARATION

I, hereby declare that the investigation presented in the thesis has been carried out by me. The

work is original and has not been submitted earlier as a whole or in part for a degree / diploma

at this or any other Institution / University.

UTTAM JAIN

List of Publications arising from the thesis

Publications in Refereed Journal

   a. <u>Published</u>

1. Thermodynamic properties of Ti in V-Ti-Ta alloys: Effect of Ta addition, U. Jain, A. Mukherjee, G. K. Dey; Journal of Alloys and Compounds, **2016**, *(686),* 946-950,

2. Wear behaviour of Vanadium and V-Ti-Ta alloys under reciprocating sliding conditions, U. Jain, K. Sairam, K. Singh, R. Tewari; Journal of Materials Engineering and Performance, ASM international, **2019,** *28,* 3372–3380,

3. High temperature oxidation behaviour of V-Ti-Ta alloys, U. Jain, J. Sonber, R. Tewari, Fusion Engineering and Design, **2019**, *144*, 125-132,

   b. <u>Under review:</u>

1. Recrystallization and structure-property correlation in V-Ti-Ta Alloys, U. Jain, N. Keskar, B. Vishwanadh, K.V. Mani Krishna, C. Gupta, R. Tewari, D. Banerjee, under review in Materials Science and Engineering A

Other Publications

   a. <u>Conference/Symposium</u>

1. Role of Tantalum addition on high temperature stability of V-Ti-Ta alloys, U. Jain, R. Tewari, ISMAS- November 2019, TSH, Mumbai

2. Development of vanadium based alloys for advanced energy systems, U. Jain, R. Tewari, NMD-ATM 2019, Trivandrum

UTTAM JAIN

Date: 26/04/2020

DEDICATIONS

Dedicated to my family, friends and teachers

Acknowledgements

Contents

Abstract

This work discusses the development of V-Ti-Ta alloys as structural material for fusion reactors with the purpose of widening the working temperature window of the material. Thermodynamic phase stability, evolution of microstructure during recrystallization, mechanical properties evaluation, oxidation and wear resistance have been investigated for a series of V-4Ti-xTa alloys. In doing so, the relevant temperature domains over which these alloys are expected to operate, have been considered.

Presence of Ta in V-Ti-Ta alloys decreases partial free energies of V and Ti, which indicates higher phase stability of vanadium matrix at high temperatures. Microstructural and phase investigations have revealed higher stability of precipitates where the role of Ta in enhancing the stability of the precipitates was rationalized by thermodynamic estimations and correlated with the experimentally observed high temperature stability of the precipitates. High yield strength (370 MPa) was achieved due to substitutional solid strengthening effect of Ta. Hence, the synergistic effect of Ta addition on strengthening of V-Ti-Ta alloy and as well as on enhancing high temperature precipitate phase stability, would increase the working temperature window of fusion reactor. Presence of Ta also influences the oxidation characteristics of V-Ti-Ta alloys. V-4Ti-7Ta alloy exhibited superior oxidation resistance (50 % lower specific weight gain in comparison to unalloyed V), which was attributed to the reduced thermodynamic activity of V. Based on the oxidation mechanism, higher activation energy for the onset of oxidation and lower diffusivity of oxygen ions (70 % lower compared to V) were the two major governing factors for improved oxidation performance of V-Ti-Ta alloys. Presence of Ta was also found to increase wear resistance of the developed alloys. Based on the wear mechanism, superior wear performance of V-Ti-Ta alloys were attributed to the formation of mixed tribo-layer encompassing elements like Ti, Ta, Fe in solid solution with vanadium oxides.

List of Figures

List of Tables

List of Abbreviations

Gen	Generation
DPA	Displacement per atom
CHTR	Compact high temperature reactor
MSBR	Molten salt breeder reactors
RAFMS	Reduced activation ferritic martensitic steel
ODS	Oxide dispersive steels
DBTT	Ductile-brittle transition temperature
KEMS	Knudsen effusion mass spectrometer
QMS	Quadruple mass spectrometer
XRD	X-ray diffraction
ICP OES	Inductively coupled plasma optical emission spectroscopy
XRF	X-ray fluorescence
TG-DTA	Thermogravimetric differential thermal analyser
DSC	Differential scanning calorimeter
EDS	Energy dispersive spectrometer
SEM	Scanning electron microscope
TEM	Transmission electron microscope
EBSD	Electron back scattered diffraction
TEM	Transmission electron microscope
PED	Precession electron diffraction
SAED	Selected area electron diffraction
GOS	Grain orientation spread
STEM	Scanning transmission electron microscope
ADXED	Angle-dispersive X-ray diffraction
OIM	Orientation imaging microscope
OR	Orientation relationship
IPF	Inverse pole figure
FIB	Focused ion beam
VHN	Vickers hardness number

RD   Rolling direction

ND   Normal direction

TD   Transverse direction

COF   Coefficient of friction

ID   Inner diameter

OD   Outer diameter

<div align="right">

CHAPTER 1

</div>

Introduction

1.1   Preamble

Advanced reactors, like nuclear fusion and fast breeder reactors, have the potential to provide a CO_2 emission-free, sustainable, safe and clean energy option for the future. In order to make these reactors technological feasible and commercially viable, selection of appropriate structural materials and understanding of their behaviour under specifically stringent and hostile loading conditions is critical for a safe and economic operation of the reactor. A broad requirements of the properties of structural materials for their use in nuclear reactors are summarized in Table 1.1 [1].

Table 1.1: Desirable properties of nuclear structural materials.

Nuclear	No harmful transmutation of atoms, low half-life daughter products, resistance to irradiation creep, growth and swelling, resistance to irradiation hardening and embrittlement, low void swelling
Physical	High melting point, low density, high dimensional stability, high thermal conductivity and low thermal expansion coefficient.
Mechanical	Adequate high temperature tensile strength, good creep resistance, low ductile- brittle transition temperature, fatigue strength and ductility, impact strength, at reactor operating temperature, resistance to thermal shock and thermal fatigue.
Chemical	Low hydrogen pick, chemically inert and good corrosion resistance against liquid metal under reactor environment
Metallurgical	Microstructure stability under radiation environment, no irradiation induced phase transformation, no grain growth and no preferential growth

1.2 Brief description of expected operating conditions in nuclear fusion reactor

First generation (Gen-I) nuclear reactors mostly deployed zirconium alloy based cladding materials due to their low neutron absorption cross section for thermal neutrons along with good mechanical strength at operating temperature of ~ 350 °C [2]. With the advancements in nuclear reactors, which were described in terms of different generations (Gen-I to Gen-IV) of reactors, the choices of materials have also been altered significantly [3]. For example, Gen-IV reactors (like fast breeder reactors) mostly use steels as the structural material with an operating temperature limit increased to 550 °C [3]. Thirst to develop advanced fast breeder reactors, which can operate even at higher temperature, like 700-750 °C, gets hampered due to non-availability of suitable structural materials [4]. Simultaneously, fusion reactors were also proposed which have even more stringent conditions as compared to Gen IV reactors. Fig. 1.1 [5] and Table 1.2 [6, 7] compare the proposed operating temperatures and lifetime displacement damage suffered by structural materials in the Generation IV concepts. Detailed description about fusion reactor is given in appendix-1. Significant increased operating temperatures, energy of neutrons and displacement per atom (dpa) in the case of fusion energy systems- as compared to any other rector systems- may be noticed from the figure and table [5-7]. Such stringent operational conditions demanded by fusion technology reduce the choice of a suitable structural material. For instance, higher energy neutrons of 14.1 MeV generated by fusion reactions induce far higher radiation damage (both displacements and transmutations) of lattice atoms as compared to the damage caused by any other reactor system. These high energy neutrons also react with structural materials to cause (n, α) and the (n, p) reactions with almost all the elements constituting the structural materials. Further complications arises by ((n,α) and (n,p)) reactions, as these reactions eventually lead to the high production rate of helium and hydrogen in the material respectively [8]. The rate of production of He in the

2

material by 14.1 MeV neutrons in a tokamak is very high (1500-10000 appm) [9]. The generated He being insoluble in the matrix diffuse towards grain boundaries at elevated temperatures causing high temperature embrittlement and void swelling in the material [7, 8]. Apart from neutron irradiation damage, molten metal coolants, such as Pb-Li, also impose high temperature phase stability, corrosion and compatibility concerns with structural materials [7, 10]. Molten metal coolant selectively dissolves certain elements from the structural material at high temperatures which induces thermodynamic instability of phases at high temperatures. It is also observed that dissolved oxygen transferred from the molten metal coolant to structural material and in addition pick up of oxygen from environment during accidental situation pose further risk of oxidation of structural material at high temperature during reactor operation [11]. This abrupt oxidation results in deterioration of the structural integrity of the reactor vessel. In addition, structural materials in a fusion reactor are also susceptible to undergo wear, during their service conditions, as the flowing high density molten metal coolant such as Pb-Li is expected to enhance the wear rate of structural materials due to flow induced vibrations.
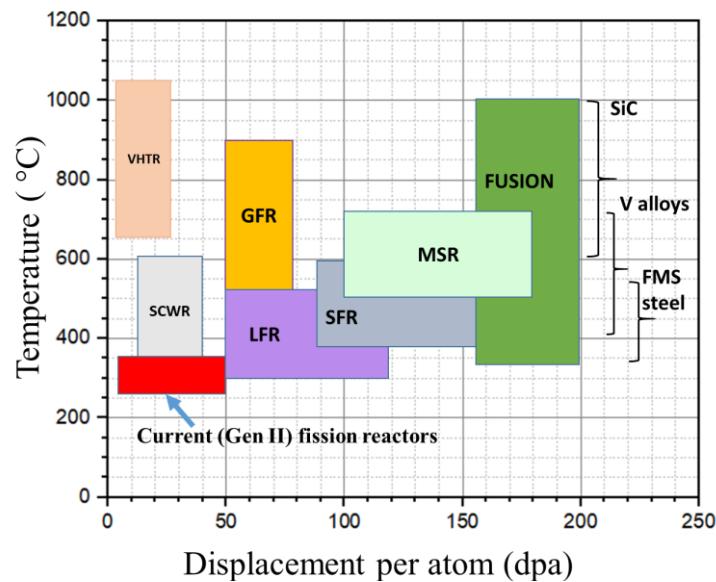
Figure 1.1: Overview of operating temperatures and displacement damage for various structural materials in fission and fusion energy systems. [Very High Temperature Reactor (VHTR), Molten Salt Reactor (MSR), Lead cooled Fast Reactor (LFR), Gas cooled Fast Reactor (GFR), Sodium cooled Fast Reactor (SFR), and Super Critical Water Reactor (SCWR) are Gen IV reactors) [5].

Table 1.2: Comparison of fission and fusion structural materials requirements [6, 7, 12].

	Fission (Gen. I)	Fission (Gen. IV)	Fission liquid metal breeder	Fusion (Demo)
Structural alloy maximum temperature	< 300 °C	600-850 °C (~1000 °C for GFRs)	500-600 °C	550-1000 °C Depending on structural material
Average neutron energy	0.025 ev	0.025 ev- 2 MeV	1-2 MeV	14.1 MeV
Max dose for core internal structures	~1 dpa	~30-100 dpa	150 dpa	~150 dpa
Max transmutation helium concentration	~0.1 appm	~3-10 appm	30 appm (F/M steel), 75appm (austenitic steel)	~1500 appm (~10000 appm for SiC)
Coolant	H_2O	He gas/ super critical H_2O	Na	Pb-Li

Structural materials for fusion reactor, therefore, require development of newly engineered structural materials having exceptional properties of low activation (upon irradiation) [13-18], high thermal conductivity, excellent mechanical properties at high temperature [19-22], strong resistance to irradiation swelling, He embrittlement [23-25] and high corrosion resistance in pure liquid alkali metals [11, 26-33]. Existing structural materials which has been used in various nuclear reactors are summarized in Fig. 1.2 [10].
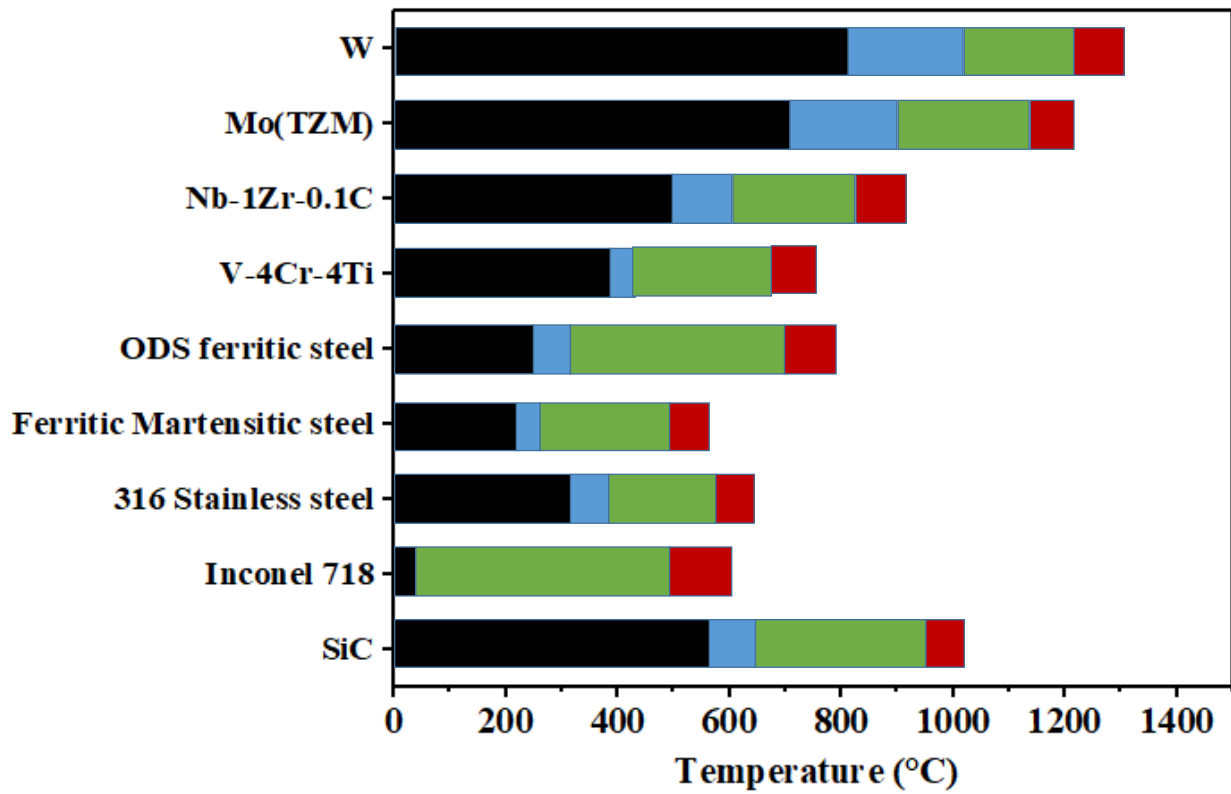
Figure 1.2: Operating temperature window of various nuclear structural materials. Green colour band represents the operating temperature range, while red and blue colour bands represent the uncertainties in the minimum and maximum temperature limits. Temperature beyond red colour band are limited by thermal creep, whereas, temperature lower than blue band are limited by irradiation embrittlement issues [10].

It may be noticed from the figure that each material has rather limited operating temperature regime where it can be utilized in a neutron irradiation environment [5, 8, 10]. Lower temperature limit of most of the materials is due to the reduced ductility associated with low temperature irradiation hardening, which reduces the fracture toughness of the materials. The upper limit of operation temperature of the materials is due to their thermal creep strength or high temperature helium embrittlement considerations. It can also be observed that mostly high temperature refractory metal based alloys, such as Mo bases alloys, Nb based alloys and Ni based alloys, which offer optimal properties at elevated temperatures, are routinely used as structural materials in fission based advanced reactors like Compact High Temperature Reactor (CHTR) and Molten Salt Breeder Reactors (MSBR) etc. Apart from optimal high temperature

properties; fusion reactors structural materials necessitate additional criteria of low activation of neutron activated radioactivity [13-18]. The idea behind this low activation criterion is to minimise the amount of harmful radioactive waste produced by neutron irradiation in order to be considered as a truly green energy source. Neutron-activated structural materials are the main contributors to radioactive inventory in fusion reactors. This low activation criterion severely limits the choice of alloys and alloying elements, that will not remain radioactive for extended periods of time after exposure to fusion neutrons (~14 MeV neutrons). Commonly used nuclear structural material, like Mo, Zr, Nb and Ni based alloys, do not satisfy the low activation criterion, hence would be unacceptable from a waste-management perspective in the fusion reactors. Only few handful of elements, like V, Fe, Si, Ti, Cr, Ta and W, satisfy the low activation criterion [34]. Hence, with a proper selection of materials, the radioactive inventory in fusion reactors can be effectively controlled. Based on these mandates of reduced activation and high performance, currently three major choices are under active consideration for the structural applications (first wall of ITER) in fusion reactors (i) Reduced activation ferritic martensitic steel (RAFMS), (ii) SiC and (iii) Vanadium based alloys [8, 12, 33, 35-37]. While each of these materials have specific advantages and limitations, choice has to be made on the basis of holistic comparison of the materials in different aspects. Table 1.3 compares the properties of each material. Some aspects of these materials are presented in the following section:

1. **Steels**

(a) **Low activation austenitic steels [SS 316 L (N)]**

Initially, low activation austenitic stainless steel (SS 316 (LN), due to its high temperature strength was selected for its use as the first wall structural material for fusion test reactor [9]. However austenitic steel generated very high amount of He (600 appm/yr) in the material upon neutron irradiation. The generated He being insoluble in metallic matrix, creates a strong

driving force for migration to sinks, such as grain boundaries resulting in bubble formation at elevated temperatures [8]. Thus resulting helium embrittlement became a major concern for this material. Furthermore, He gas also stabilises vacancy clusters (formed by displacement damage), thus causes excessive void swelling related issues in this steel.

(b) Reduced activation ferritic-martensitic steels (RAFAMS)

Based on the earlier experience of fast neutron reactors, RAFMS steels were designed by modifying ferritic steels (Fe-(8-12 %) Cr, Mo, Nb, V) as structural material. For achieving low activation criteria for fusion reactor application, alloying elements, such as Mo, Nb, were replaced with W and Ta to decrease the probability of producing undesirable radioactive nuclides. These materials are preferred because of relatively low cost, well established technology for the production and ease of fabrication. However, these steels show very high creep at elevated temperatures with their upper operational temperature limit is restricted to 550 °C [37]. As increasing the first wall temperatures would improve the efficiency of a fusion reactor, there were considerable research efforts dedicated to develop alternative materials that can be employed at higher temperatures without property degradation.

(c) Nanostructured ferritic/martensitic oxide dispersive steels (ODS)

ODS steel were developed to overcome the high temperature strength limitation of RAFMS steels. In ODS steel, nanoscale oxide particles of yttria and titania are dispersed in the ferritic steel matrix. These particles are stable at high temperatures and act as strong obstacles to dislocation motion by dispersion strengthening mechanism, thereby increasing high temperature strength and upper limit of temperature upto 750 °C. Being nano-meter in size, these particles have very large interfaces between the particles and the matrix which act as sinks for the irradiation-induced defects, thereby increasing the radiation resistance of ODS. ODS steel is, however, expensive, difficult to produce in large volumes and tends

to have high residual strains [8, 37]. The long-term stability of the nano-precipitates under irradiation is not fully established.

2. Silicon carbide composites

SiC based composites exhibit superior high temperature strength hence offer operational temperatures in range of 1000-1100 °C [2]. However, these ceramic based composites have poor fracture toughness, brittleness and susceptibility to He embrittlement. Immature fabrication and joining technology, high cost of production limits their application in the near future.

3. Vanadium based alloys

Vanadium alloys have following properties which make them superior choice for the fusion blanket as compared to other options:

i. *Low activation*: Vanadium alloys form lowest long term activation products under irradiation of 14.1 MeV neutrons [13-18]. Hence can be recycled with minimal waste generation. The comparison of recycling time is shown in Table 1.3, which shows that only vanadium alloys allow hands on recycling after 100 years of cooling, whereas in the case of steels and SiC only remote recycling is feasible [33, 38, 39].

ii. *Neutronic transmutation properties:* Vanadium alloys results in lower amount of He and hydrogen generation as a result of transmutation (Table 1.3). This results in longer life of the structural materials.

iii. *High temperature strength*: Vanadium being a refractory metal has melting point about 1900 °C. This allows to maintain good strength at the high temperatures expected in fusion reactors as compare to other potential alloys. For example, vanadium alloys allow higher operating temperature limit of ~700 °C as compared to RAFMS which offer a temperature ~550 °C.

iv. ***Swelling resistance***: Vanadium being a bcc metal has an open crystal structure, which provides relatively high swelling resistance as compared to fcc metals, and thus allows extended lifetime of the structural materials [40].

v. ***Non-magnetic and ductile***: Unique combination of ductility (especially in comparison to SiC) coupled with nonmagnetic nature (ensuring negligible interference with the magnetic fields of the plasma). Other two choices (RAFMS or SiC) are either magnetic or brittle respectively.

vi. ***Good thermo-physical properties***: Vanadium alloys show better thermo-physical properties compared to RAFMS such as higher melting point, lower density, higher thermal conductivity, lower thermal expansion coefficient (Table 1.3) [41]. These properties provide vanadium alloys to bear higher heat load capabilities.

These unique combination of properties provide an edge to vanadium based alloys over other competing materials for fusion applications. If the impact of the ferromagnetism of the RAFMS on plasma operation should be unavoidable and the brittleness of SiC/SiC is unaccepted by design studies, vanadium alloys could be the only potential candidate of low activation structural materials for fusion reactors.

Table 1.3: Comparison of physical and nuclear related properties of fusion reactor structural materials [7, 9, 10, 12, 41].

Material / Property	Austenitic stainless steel 316	Ferritic steel (RAFMS)	V-alloy (V-4Cr-4Ti)	SiC composite SiC_f - SiC
Melting temperature (°C)	1400	1420	1880	2600
Operation temperature range (°C)	300-600	200-550	400-700	600-1000
Density (gm/cm^3)	8	7.8	6.1	3
Poisson's ratio	0.27	0.27	0.36	
Modules of elasticity (GPa)	168	180	120	
Linear thermal expansion (10^{-6}/K) @ 500 °C	18	12.3	10.3	4
Thermal conductivity W/m-K	21	27.3	34.5	12
Fracture toughness	200-300	150-200	200-300	3-5
Specific heat (J/ kg-K)	575	680	560	600
Helium transmutation rate (appm) @11dpa	174	130	57	1500
Helium transmutation rate (appm) @170 dpa	2400	1800	855	19500
Hydrogen transmutation rate (appm) @11dpa	602	505	240	560
Hydrogen transmutation rate (appm) @170 dpa	8550	7350	4050	13350
Contact dose after 100 years of cooling (Sv/hr)	1	10^{-3}	10^{-5}	10^{-2}
Possibility of recycling	Not feasible	Remote recycling	Hands on recycling	Remote recycling
Cost per Kg	-	< 5.5 $ (Plate form)	200 $ (CVI processing)	2000 $ (Plate form)
Limiting factor	Poor radiation resistance/high He production	Poor high temperature strength	Immature technology	Immature technology and high He production

1.3 Objectives of the present study

Vanadium alloys have potential to replace existing steel for the structural application in fusion reactor. In spite of huge potential, research on the development of vanadium alloys was limited in early years due to processing challenges for preparation of high purity vanadium with respect to interstitial impurities. Interstitial impurities are detrimental, as they result in low temperature embrittlement of the alloys [31, 33]. With the development of advanced processing techniques, it became possible to prepare high purity vanadium at cheaper cost. This opens-up the scope of research towards development of vanadium based alloys as structural materials for fusion reactor applications.

In this connection, V-Ti alloys were developed, as addition of titanium (Ti) to vanadium was found to be the most effective in scavenging the interstitial impurities by forming precipitates, which, not only improve fabricability and resistance to radiation swelling to the alloy but also provide additional strength by precipitation hardening [18, 33, 42-44]. In order to further increase the high temperature strength of V-Ti alloys, Cr and W were added as alloying elements. W addition in V-Ti could not provide significant gain in the strength of the alloy, whereas, addition of Cr has shown promising results [22, 45-47]. Based on several studies, development of vanadium alloys have converged to V-4Cr-4Ti alloys largely because this optimizes the radiation-induced ductile-brittle transition temperature (DBTT) shift and high temperature strength compared with alloys containing amount of Cr and Ti. V-4Cr-4Ti was identified as optimized alloy composition which can be used in the temperature window of 400-700 °C [21, 31, 33, 43, 48]. However, it is the need of the hour that newer vanadium alloys must be developed to increase safe temperature window of operation for the advanced reactor applications. There are few scientific and technological challenges that need to be addressed before using these as the structural materials for future fusion reactors. These are:

1. Though the vanadium alloys showed superior performance in comparison to RAFMS steel upto 700 °C operating temperature, V-based alloys lose their strength drastically at temperature beyond 700 °C [21, 31, 33, 48]. In addition, V-based alloys are susceptible to helium embrittlement related issues at elevated temperatures (exceeding 700 °C). With the rapid pace of development of advanced reactors, present situation demands in the improvement of the mechanical properties at high temperatures, in order to extend the upper limit of the operating temperature.

2. Secondly, the low temperature operation window of the vanadium alloys is majorly limited to 400 °C which is highly sensitive to the interstitial concentration leading to the irradiation embrittlement [21, 31, 33, 48]. Vanadium alloys are reported to exhibit precipitates which tend to dissolve under neutron irradiation. This Irradiation induced dissolution of precipitates (Ti(CON)) led to increase of interstitial contents in matrix, which by locking the dislocation superstructures increases the DBTT [18, 21, 48-50].

3. In addition to the development of newer vanadium alloy with wider operating temperature window, the oxidation performance of the material is also extremely important during accidental condition, as a catastrophic leak in the vacuum may expose the structural materials to abrupt oxidation [51, 52]. Hence the oxidation performance of the developed vanadium alloys should be investigated under extreme conditions and a fair comparison of oxidation behaviour with existing vanadium alloys is required.

4. Structural materials in a fusion reactor are susceptible to undergo wear, during their service conditions, as the flowing molten metal coolant is expected to induce the wear due to flow induced vibrations. Hence the developed alloys should also be investigated for its wear performance under the reciprocating sliding conditions. It is also necessary to know the effect of alloying addition on the wear performance of the vanadium based alloys.

From above mentioned points, it could be stated that one of the major limitations of existing vanadium based alloys is their limited temperature window of operation. The reduction in the strength, He embrittlement and rise in DBTT together limit the high and low operation temperatures of the alloy. This emphasizes for a need of designing new V-alloys exhibiting superior high temperature strength without compromising the low neutron activation criteria and at the same time, special attention should be paid towards enhancing the stability of precipitates phase formed in the V-alloy. Such a V-alloy possessing high temperature strength and enhanced stability of the precipitate phase would widen the working temperature window of a fusion reactor.

One of the principal objectives of the present research work is to add refractory metals to V–Ti alloy system. The essential idea behind selecting refractory metals is that they can provide superior high temperature properties, as these metals are effective solid solution strengthener and are also known for forming stable interstitial compounds. Among refractory metals, only W and Ta satisfy low neutron activation criteria. Recent studies have shown that the addition of W in V could not impart any significant gain in the strength of the alloy [45-47]. Detailed literature survey showed that no such systematic study is available on the addition of Ta as an alloying element in V. Present study is, therefore, aimed to explore effect of addition of Ta in V-Ti alloys. For this purpose, a series of V-4Ti-xTa alloys with varying proportion of Ta are synthesized and characterized in the present study. The proposed V-alloys having combination of both Ti and Ta are envisaged to exhibit superior solid solution strengthening and phase stabilities. Some of the pertinent aspects that are addressed in this study on the role of Ta could be summarized as:

1. Investigation of high temperature thermodynamic stability of phases in V-4Ti-xTa alloys and elucidation of the role of Ta in the stability of phases in these alloys.

2. Study on the evolution of microstructure during deformation, recrystallization and precipitation of second phase. In this investigation, textural evolutions with special emphasis on precipitate characterization would also be explored.

3. As these alloys are being developed for fusion reactor application, detailed structure property correlations encompassing high temperature oxidation behaviour and wear resistance of the V-Ti-Ta alloys would be probed.

1.4   Structure of the thesis

This thesis is divided into eight chapters. A brief introduction about properties of materials demanded by fusion reactor structural materials, comparison of properties of potential candidate materials and objectives of the present study are given in the Chapter 1. In Chapter 2, detailed literature review on the development of V- alloys and evolution of precipitates in V-Ti alloy system, development of textures during deformation and annealing in various bcc materials are compiled. Details of the research work on the oxidation behaviour and wear aspects of V alloys are summarized in the chapter. Details of the alloy preparation, fabrication and the experimental methods employed in the present study are given in Chapter 3. Chapters 4, 5, 6 and 7 present the experimental results obtained in the present study. Chapter 4 probes the role of Ta addition on the alloy stability of V-Ti-Ta system using Knudsen Effusion Mass Spectrometric (KEMS) measurements. Chapter 5 describes detailed microstructural characterization of as-solidified, deformed and annealed samples. It includes identification of the precipitates, their stabilities and understanding the role of Ta in stabilizing the precipitates. Chapter 6 investigates high temperature oxidation behaviour of the V-Ti-Ta alloys and the underlying mechanism of oxidation has been identified. Chapter 7 reports wear performance of V-Ti-Ta alloys under reciprocating sliding condition. Finally, the main conclusions drawn in the present study are summarized in chapter 8.

Literature Review

Vanadium-based alloys, as structural material for fusion reactors, offer significant advantages over other candidate alloys. In spite of the availability of limited data base in comparison to other candidate structural materials, viz, austenitic, ferritic steels, ferritic/ martensitic steels, vanadium-based alloys exhibit properties that make them attractive for the fusion reactor applications. This chapter presents a review of the materials data base for selected vanadium-base alloys and compares the projected performance characteristics of V-based alloys as compared to other candidate alloys.

2.1 Historical prospective of the development of vanadium based alloys

Yamamoto et al. were the first who as early as 1950s initiated the development of the phase equilibria and alloying behaviour of the V based alloy systems [53]. V-Ti alloys were one of the first alloys which were developed in competition to the Ti-6Al-4V alloy where vanadium based alloys showed three times superior creep strength as compare to Ti based alloys [53]. Subsequently Rajala and Thyne have studied effect of refractory metal addition (Nb, W, Ta, Mo) in vanadium alloys with the objective of improving elevated-temperature properties [54]. Refractory metals were chosen as alloying elements because binary phase diagrams of these metals with V show extensive solid solubility which could be utilized in enhancing the elevated-temperature strength. Along with refractory metals, Ti was also added with two fold objectives. (1) Mechanical properties of vanadium alloys, particularly, DBTT, have shown high sensitivity for the concentration of interstitial impurities (1400 ppm), purpose of addition of Ti is, therefore, to scavenge interstitial impurities by forming carbides and (2) Ti can also act as a solid solution strengthener [54]. Rajala and Thyne have used tensile tests to

study the alloying behaviour in these alloys and have shown that among refractory metals, Nb, on a density-corrected basis, acts as most potent strengthener [54]. It was also found that upto 10 % Ti was beneficial for high temperature strength as well as in improving ductility but when the concentration of titanium exceeds 20 % it was found to be detrimental for high temperature (1000 °C) strength.

After having detailed initial studies on the alloying behaviour in V alloys, in 1965, first report on potential applications of these alloys for structural applications under sodium environment in fast breeder reactors for alternate fuel cladding apart from stainless steel in a sodium-cooled reactor was published [55]. Incompatibility between stainless steel and a uranium-plutonium-fizzium fuel alloy spurred development of vanadium alloys as an alternate to steel, which resulted in the development of V-20Ti alloy [55]. Despite good compatibility of V-20Ti with U-Pu-Fz alloy, efforts were made toward the development of other vanadium-based alloys having improved high temperature strength and corrosion resistance under sodium environment. Later, by 1964, V-15Ti-7.5Cr alloy emerged as a "second-generation" alloy having significantly improved creep properties and moderately improved sodium-corrosion resistance in comparison to the V-20Ti alloy [56]. In 1966, Argonne National lab published a comprehensive report on the fabrication, mechanical properties evaluation and welding aspects of the V-15Ti-7.5Cr alloy [56]. In 1969, Westinghouse also published a report on the development of VANSTAR series of vanadium based alloys (V-Fe-Cr-Zr, V-Fe-Nb-Zr, V-Fe-Ta-Zr) for cladding application in fast breeder reactor [57] (Table 2.1). These alloys were investigated for microstructural characterization, heat treatment, creep in vacuum, welding, thermal stability of welds and chemical compatibility with Na coolant and U-Pu-Fz alloy fuel. The irradiation performance of these alloys were also tested in EBR II reactor upto 1 to 2 x 10^{22} neutron/cm^2 neutron fluence to test the effect of fast flux irradiation on the mechanical and structural properties of the alloys. With detailed studies carried out on the VANSTAR-9

alloy, it has been reported that the alloy has shown promising results on mechanical and creep properties required for structural application in a fast breeder reactor [57, 58]. In 1969, Edison in his review article compared these vanadium alloys with stainless steel (SS 316) for its application as clad material from economical point of view [58].

Table 2.1: Chronology of vanadium alloys development along with mechanical properties [58]. (Stainless steel (SS 316) is included in the Table for comparison).

Alloy	0.2 % yield strength at 700 °C (MPa)	Minimum creep rate for stress of 200 MPa (% / h)	Reference
Stainless steel (SS-316)	130	0.154	Simmons [59]
V-20Ti	310	0.009	Argonne National lab [55]
V-15Ti-7.5Cr	372	0.0027	Argonne National lab[56]
V-5Ti-20Nb	470	-	Rajala and Thyne [54]
V-9Cr-3Fe-1.3Zr-0.05C (VANSTAR-7)	193	0.0031	WESTING house [57]
V-8Cr-10Ta-1.3Zr-0.05C (VANSTAR-8)	220	0.0020	WESTING house [57]
V-6Fe-5Nb-1.3Zr-0.05C (VANSTAR-9)	317	0.0008	WESTING house [57]

By virtue of their favourable neutronics properties, high temperature strength and good corrosion resistance, vanadium alloys got further attention (1970's) for potential applications

as structural material in fusion reactor [60]. Though, the VANSTAR series V-alloys demonstrated their suitability for fast reactor application, higher neutron absorption cross section and production of long half-life daughter products (mainly due to alloying elements such as, Nb, Zr and Mo) under 14 MeV neutrons, restricted their usage as structural materials for fusion reactor. Therefore, by avoiding those elements that have adverse effects due to the formation of long half-life daughter products, a new series of V-15Cr-(5-15)Ti alloys were widely investigated [61]; where Cr and Ti would be acting as solid solution strengthening agent and scavenger for interstitial impurities, respectively [42].

Binary V-Cr alloys, though met the requirement of desired mechanical properties, these alloys exhibited poor void swelling resistance. Upon the introduction of Ti as ternary element (V-Cr-Ti), the swelling resistance of the alloy was greatly improved which was attributed to: (a) the atomic size effect as described in dislocation bias theory[62] and/or (b) the formation of Ti(CON) precipitates in V-Cr-Ti ternary alloys. The former effect is due to the oversize effect of Ti, which counterbalances the undersize contribution of Cr and the later effect is due to the formation of precipitates offering additional sites (interfaces) for recombination of defects generated by high energy neutrons [62]. These precipitates are also reported to have beneficial effects in restraining the irradiation induced hardening by restricting growth rate of dislocation loops. However, alloys having high amounts of Cr and Ti (i.e. Cr + Ti > 10 wt.%), showed excessive irradiation hardening and poor impact properties, which synergistically raise DBTT above room temperature [21, 63, 64]. Eventually, V-4Cr-4Ti was identified as an optimal alloy composition for fusion reactor structural application, which can be used within the temperature window of 400-700 °C [21, 31, 33, 43, 48].

2.2   Basic properties and crystallography of vanadium metal

One of the most important property of vanadium is its high melting point (1910 °C) which qualifies vanadium as a refractory metal. High melting point imparts the high temperature strength to vanadium. Apart from high temperature strength, vanadium has low cross section to neutrons, produces shorter half-life daughter products, low activation properties and good resistance against neutron irradiation, non-magnetic, high void swelling resistance, liquid metal compatibility, and low density (6.1 gm/cc, 28 % lighter than Fe) etc. These excellent properties warranted vanadium as a promising candidate materials for structural components of advanced nuclear reactors.

Vanadium belongs to group V of the periodic table along with Nb, Ta, all of which exhibit BCC crystal structure from room temperature to melting points. Reported lattice parameter for purest vanadium (99.97 % pure) is 0.30240 nm. Vanadium dissolves significant quantities of interstitial impurities like C, N and O in its lattice. The lattice parameter of V changes with increasing concentration of interstitials in its lattice. Lattice parameter of vanadium increases from 0.302 nm to 0.304 nm as the concentration of interstitials (O, N) increases from 0.1 to 0.35 wt.% [65]. Apart from interstitials, vanadium also dissolves other refractory metals in significant quantities. Lattice parameters of some of pure metals are shown in Table 2.2. It may be noticed from the Table 2.2, that Cr is undersize and other metals (Ta, Nb, W, Ti) are oversize as compared to V. These refractory metals (Cr, Ti, Ta, Nb, W) forms substitutional solid solution with V, and also reported to significantly affect the lattice parameters of V due to difference in the atomic size of elements.

Table. 2.2: Crystal structure and lattice parameter of some of the alloying elements of V.

Element	Crystal structure	Lattice parameter; nm
V	BCC	0.3024
Ti	HCP (RT to 880 °C)	$a_0 = 0.2951$ $c_0 = 0.4684$
	BCC (above 880 °C)	0.3276
Cr	BCC	0.2879
Ta	BCC	0.3302
Nb	BCC	0.3301
W	BCC	0.3165

2.3   Effect of alloying addition on phase stability of vanadium based alloys

The phase equilibria of vanadium with other refractory metals (W, Ta, Mo, Nb), Ti and Cr have been extensively studied. Binary phase diagrams of V based alloys can be broadly divided into three categories; one which show complete solubility, second which show limited solubility and third which show formation of intermetallic phases. For example, binary V-Cr, V-Nb, V-Mo, V-W phase diagrams show complete solubility (Fig. 2.1-2.4) forming bcc crystal structure throughout the composition [66-68]. In the case of Ta, there is general agreement that Ta and V alloy form a continuous bcc solid solution at elevated temperatures and a laves phase (V_2Ta) having tetragonal structure at lower temperatures for Ta content exceeding 28 % (Fig. 2.5) [69]. In the case of Ti, it can be seen that up to 40 wt.% Ti is soluble in V even at room temperature, but it precipitates out in the bcc V matrix as hcp even at concentration of V above 40 wt.% (Fig. 2.6). Binary Ti-Cr phase diagram (Fig. 2.7) shows intermetallic compound $TiCr_2$ formation which precipitates as a Laves phase. This $TiCr_2$ phase has three different allotropes

(α, β and γ). Similarly, in Ti-Ta phase diagram (Fig. 2.8), it could be seen that (β-Ti) and (Ta) phases shows complete mutual solubility above the α to β allotropic transformation temperature of Ti (~ 880 °C). The (β) and (β + (α-Ti)) phase boundary forms a single curve beyond 80 at.% Ta at low temperatures [66].

For the ternary phase diagram, most widely studied V-Ti-Cr system has been reported in the literature. The isotherms of the V-Ti-Cr system are shown in Fig. 2.9 at selected temperatures [70]. It may be noted that for Cr concentrations reaching to 10-15 wt.%, the intermetallic α-TiCr$_2$ phase is formed within the bcc matrix at lower temperature 700 °C. However, at temperatures above 900 °C, β-TiCr$_2$ phase also appears in the phase diagram. Increasing temperature reduces the stability of the TiCr$_2$ Laves phases in the bcc matrix. The solidus and liquids of V-Ti-Cr system is shown in Fig. 2.10. It may be noted that the increase in Ti content leads to decrease in melting point of V-Ti-Cr alloys (Fig. 2.10) [66]. It could be also be seen that the most commonly studied V-4Ti-4Cr alloy retains the bcc structure up to the melting point. For V-Ti-Ta system limited data are available in the literature. As the liquidus data are not available for Ti-Ta system, limited assessed phase diagram is available in literature which is shown in Fig. 2.11 (a-d) [71]. Fig. 2.11 (a-c) are isothermal sections of the phase diagram at selected temperatures. Fig. 2.11 (d). The phase boundary of (V) and (β + V$_2$Ta) can be notice in the vanadium rich corner, which shrinks on increasing the temperature [71]. The assessed solidus temperature of V-Ti-Ta system is shown Fig 2.11 (d), however, liquidus temperature are not available in the literature. Experimental thermodynamic data on V-Ti-Ta system are also not available in the literature.
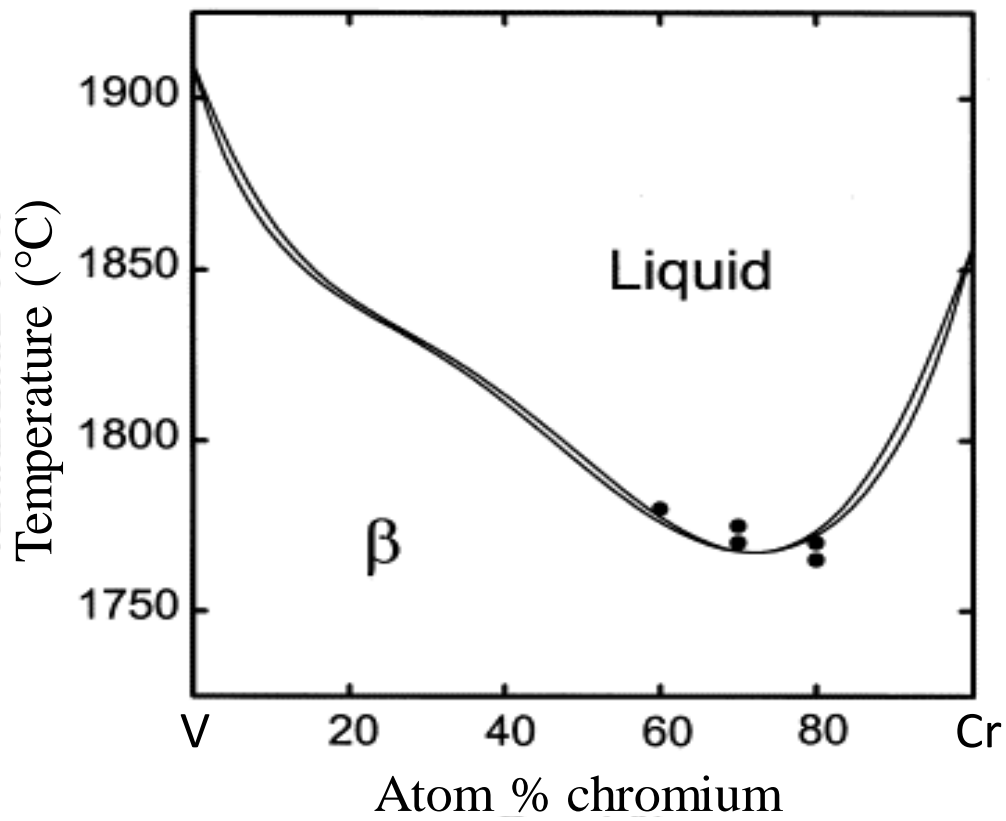
Figure 2.1: Binary phase diagram of V-Cr system [66].
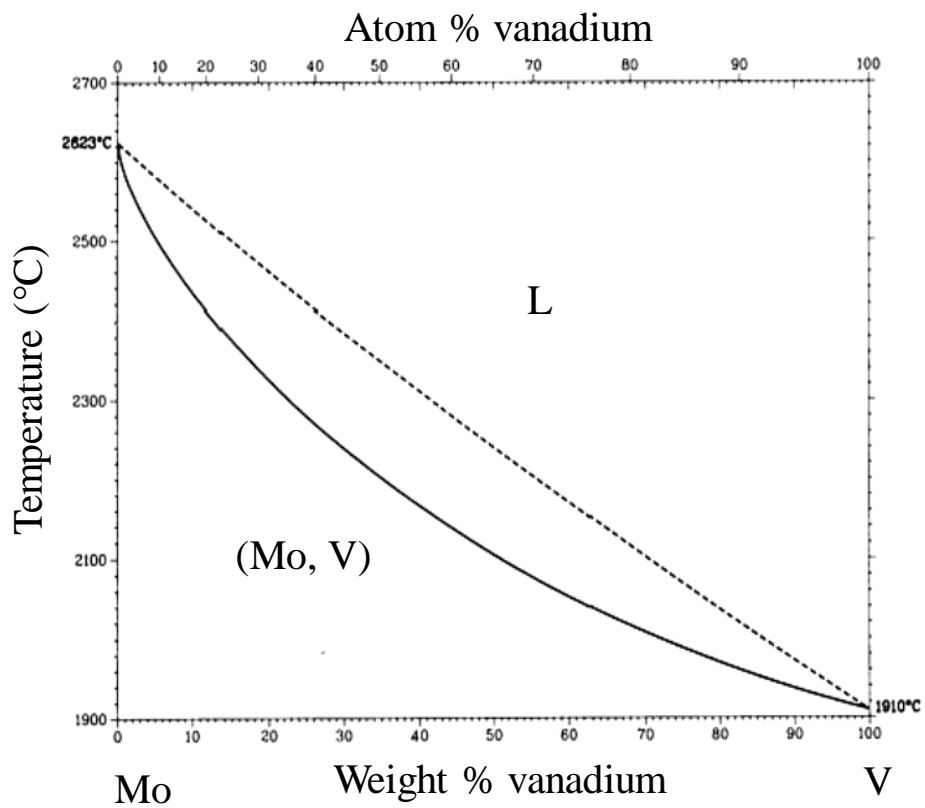
Figure 2.2: Binary phase diagram of V-Mo system [67].

Atom % niobium
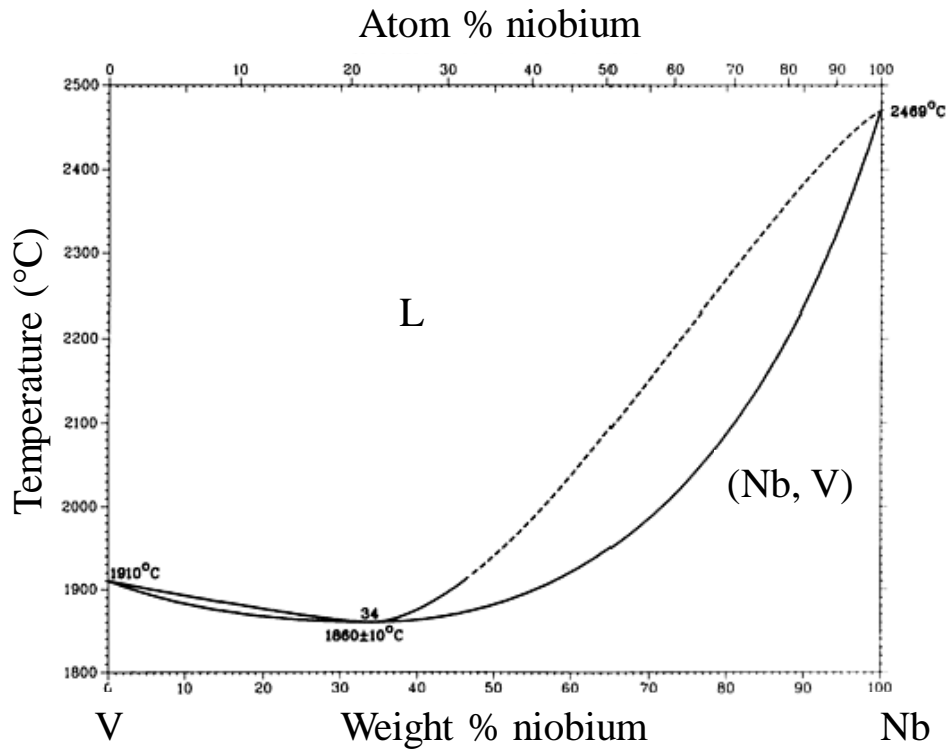
Figure 2.3: Binary phase diagram of V-Nb system [68].

Weight % tungsten
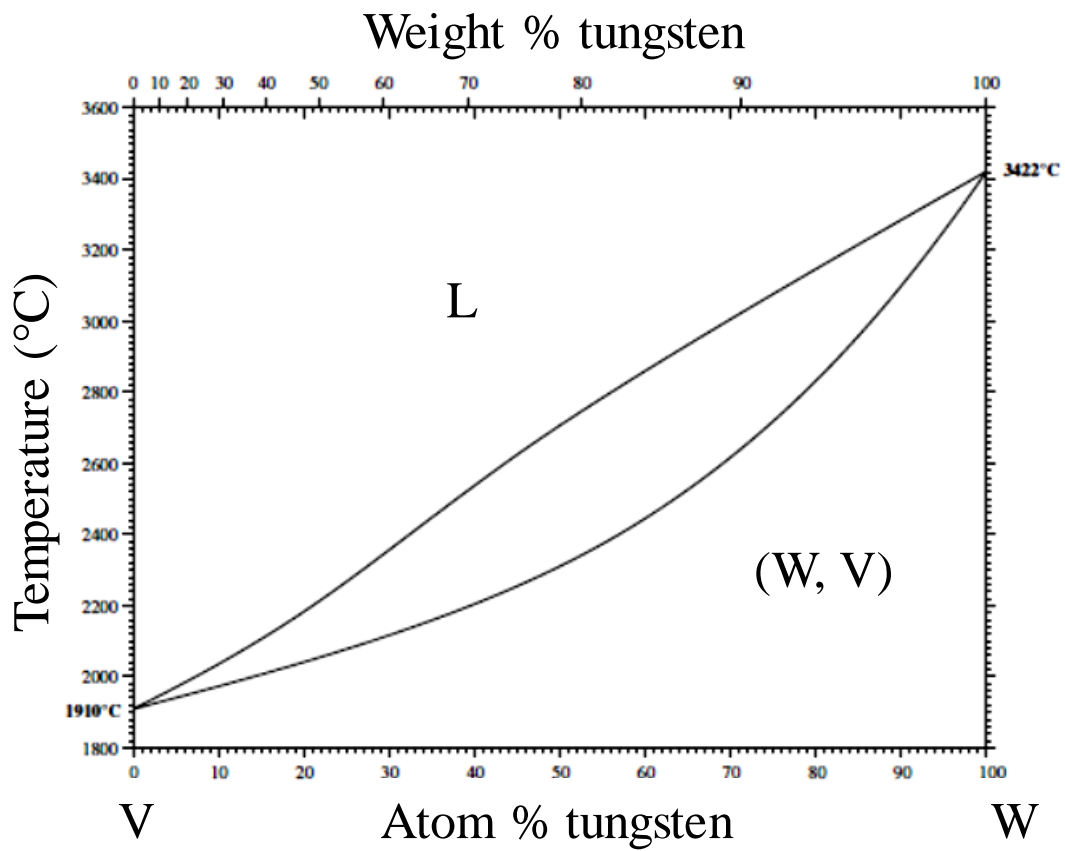
Figure 2.4: Binary phase diagram of V- W system [68].
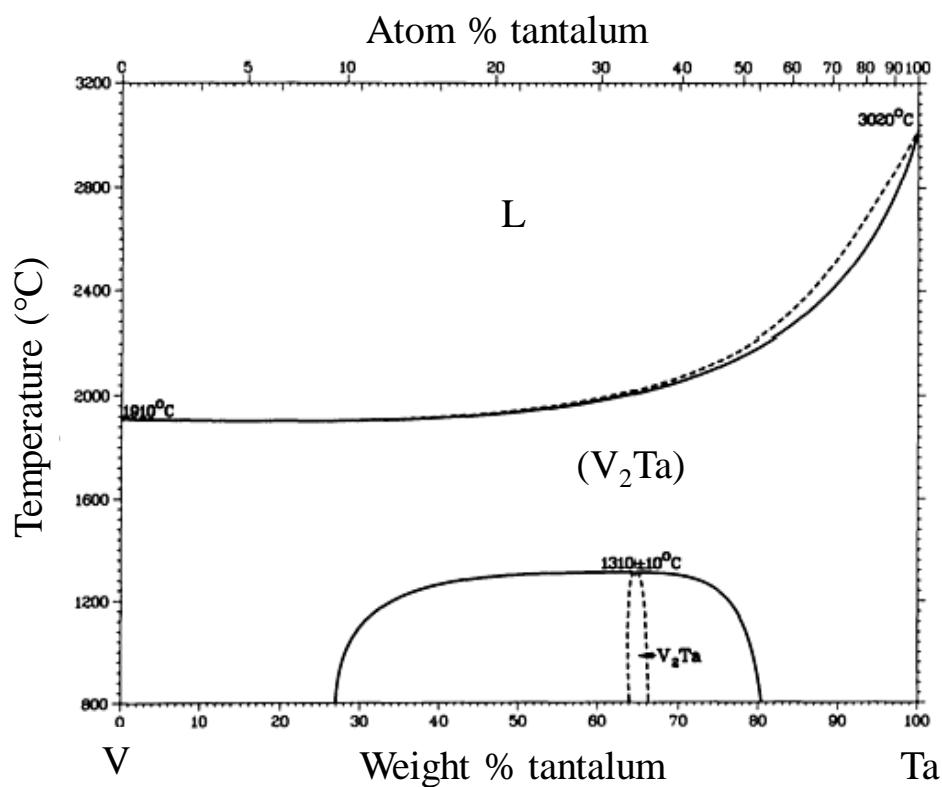
Figure 2.5: Binary phase diagram of V-Ta system [69].
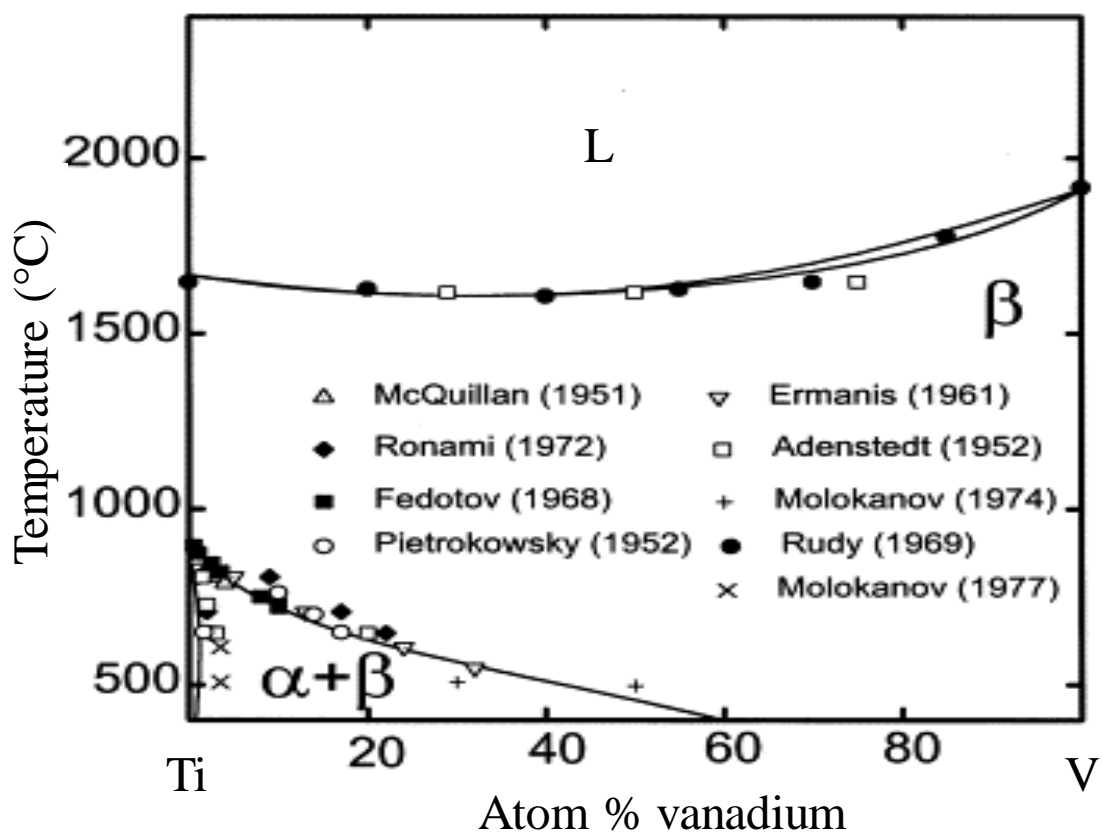
Figure 2.6: Binary phase diagram of V- Ti [66].
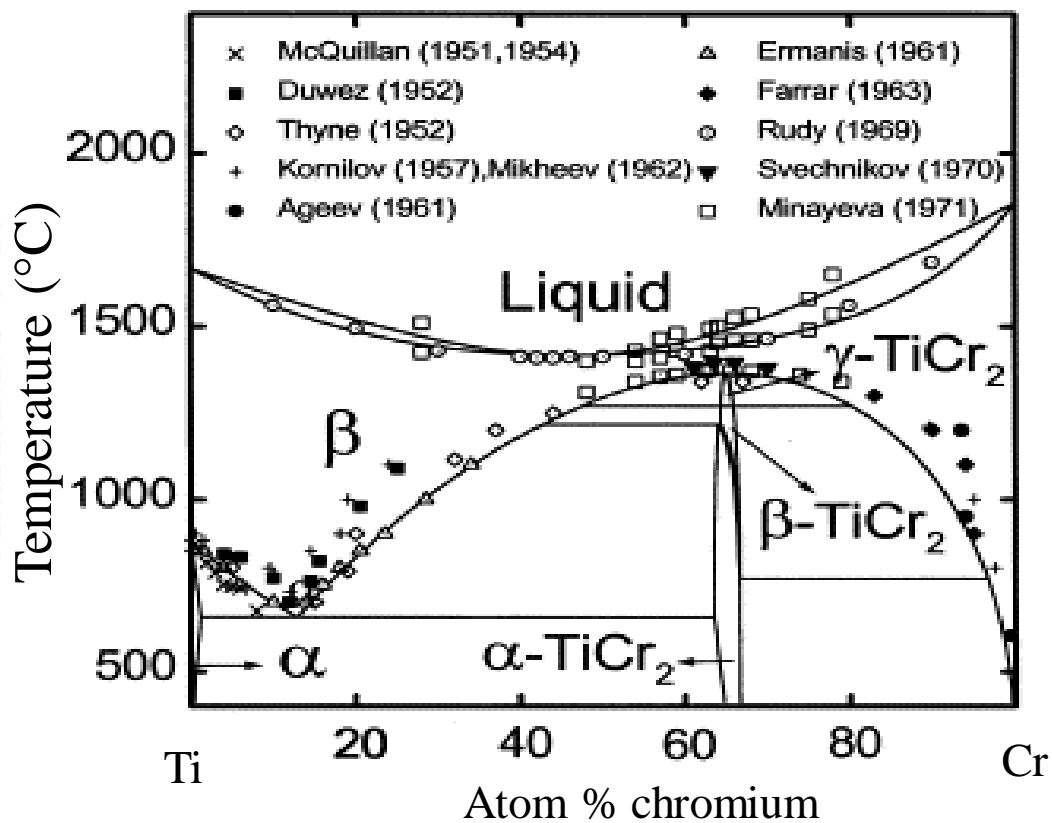
Figure 2.7: Binary phase diagram of Ti-Cr system [66].
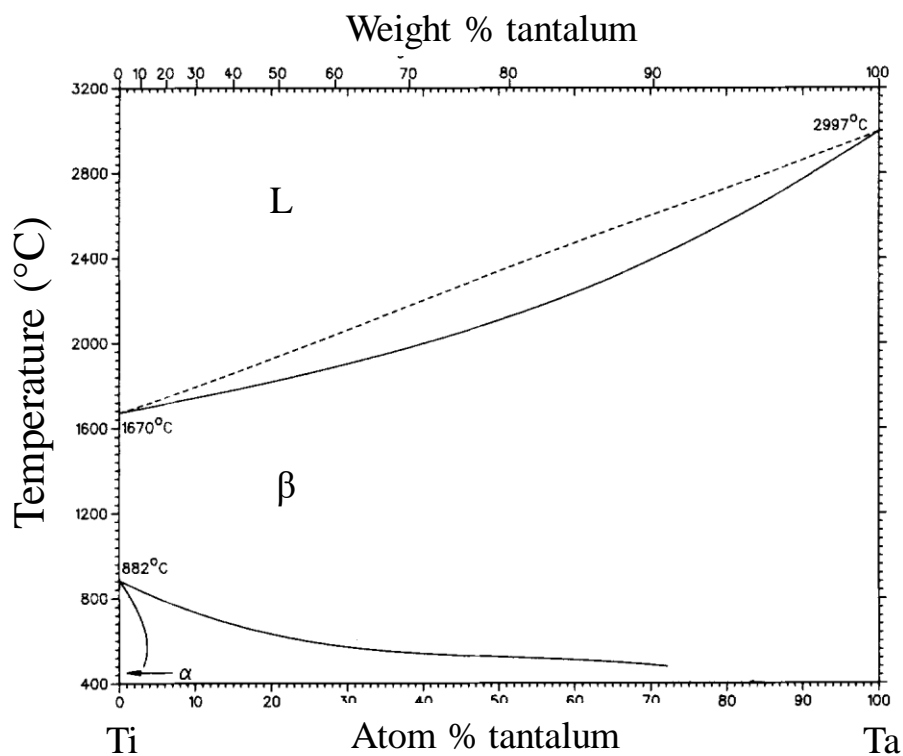
Figure 2.8: Binary phase diagram of Ti-Ta system [72].

25
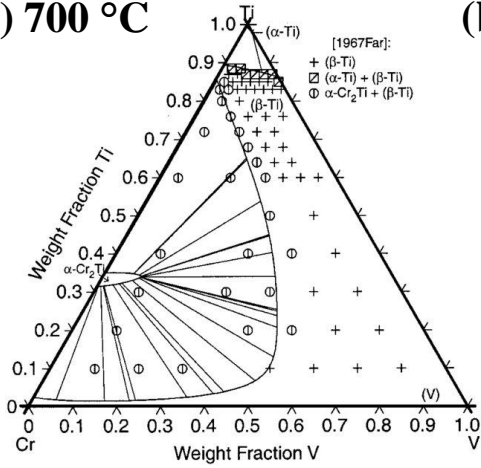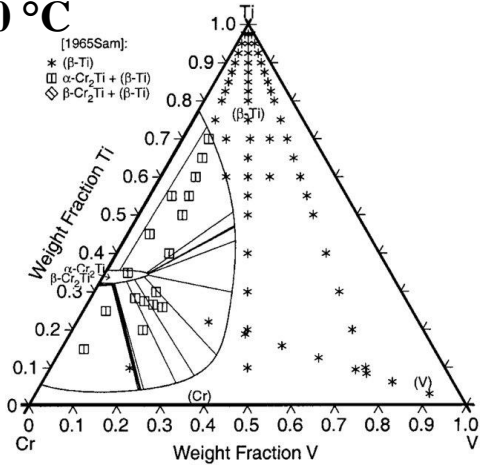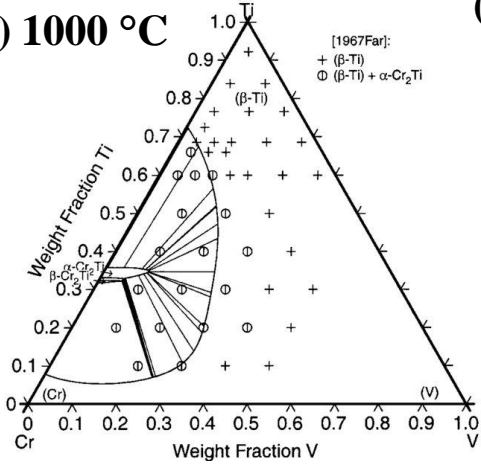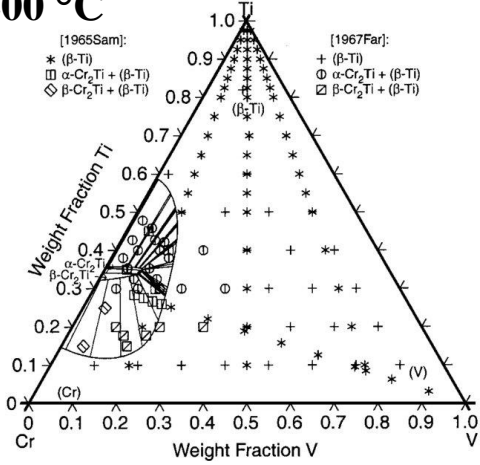
Figure 2.9: Ternary phase diagram of V–Ti-Cr system at selected temperatures. β and α-TiCr2 1are bcc and hcp phases [70].
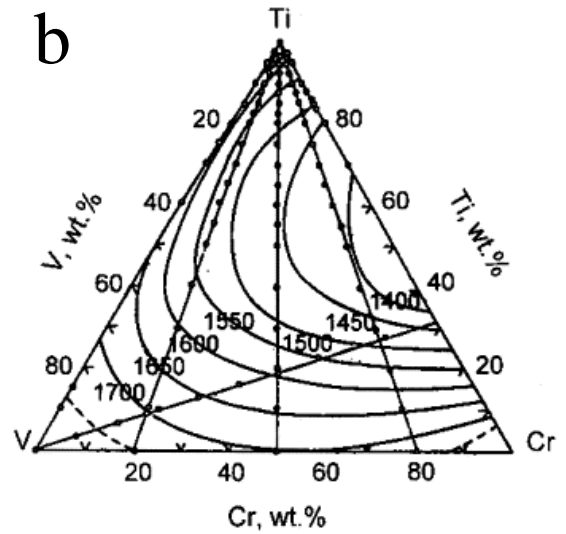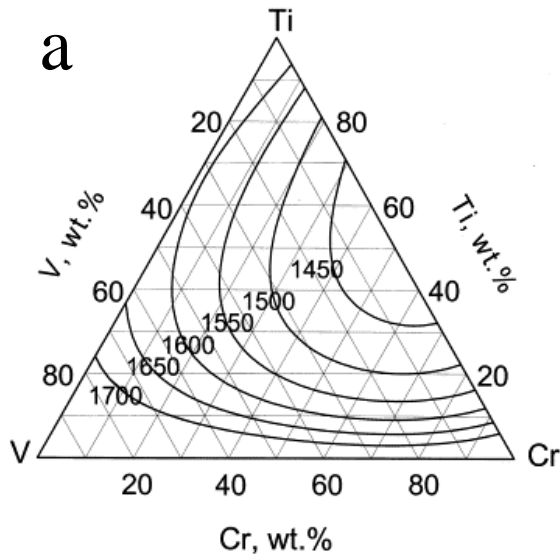
Figure 2.10: (a) Calculated solidus, β/(β+liquid), contour (in °C) in the ternary Ti–Cr–V system, and (b) experimental solidus contour [66].
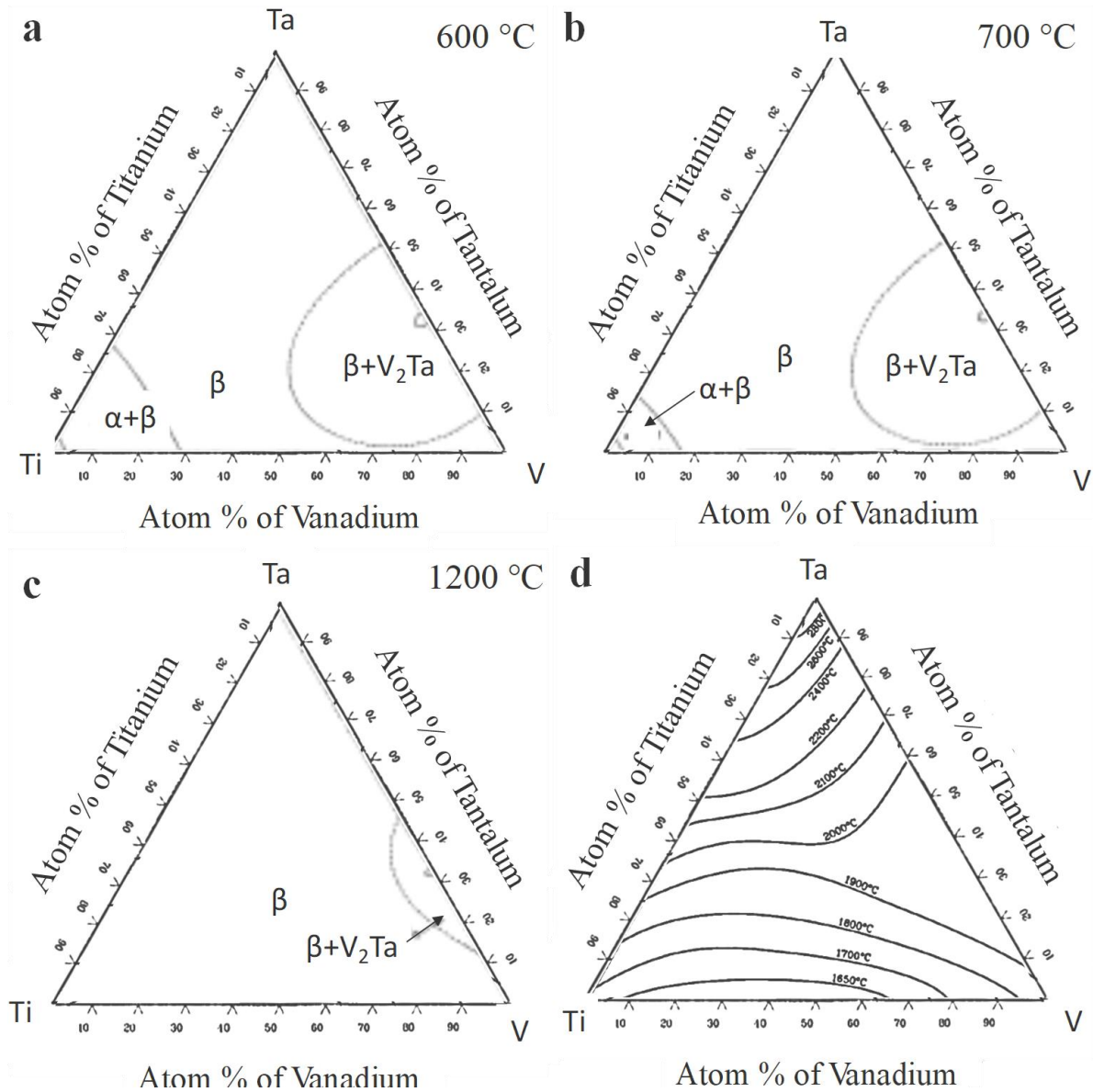
Figure 2.11 (a-c): Assessed Ta-Ti-V isothermal sections at (a) 600 °C (b) 700 °C (c) 1200 °C (d) Assessed Ta-Ta-V solidus contours (liquidus data are not available) [71].

2.4 Effect of alloying additions on the formability of vanadium based alloys

Real term application of any metal and alloy requires good formability so that it can easily be formed into various components without experience tearing or fracture. Pure vanadium (iodide refined) is quite ductile, which can be deformed easily at room temperature [40]. However, interstitial impurities cause deterioration in ductility of vanadium metal.   Vanadium, like the other refractory BCC metals, is known to have high affinity towards interstitial elemental

impurities like carbon, nitrogen and oxygen. Very high solubility of these elements in vanadium allows considerable amount of these interstitial elements to go in solid-solution with vanadium. There are several sources which contribute in the ingress of interstitial impurities in vanadium alloys. Few of these sources are raw metals and processing steps like melting, fabrication, heat treatments, etc. In addition, high affinity of these interstitial elements with V make it difficult to remove during refining processes. These interstitial impurities though provide strength to vanadium, their detrimental effects during fabrication offset all their beneficial alloying effects. These interstitial impurities induce embrittlement in vanadium and its alloys, which make formability of the alloy very difficult. The effect of interstitials on ductility of vanadium can be understood in terms of rise in DBTT temperature. The DBTT of iodide-refined pure vanadium is - 196°C; whereas even 10 ppm hydrogen is shift up the DBTT to -100 °C [73]. It has been reported that O is more detrimental as compared to other interstitial elements for low temperature ductility of vanadium [40].

Reduction of interstitial solute concentrations in vanadium matrix is desirable, hence mainly two approaches have been adopted to overcome these issues. (i) Reduction of interstitial impurities content in vanadium by choosing pure starting metals with better reduction/refining techniques and controlled atmosphere during thermomechanical processing and (2) by adding scavengers of interstitial impurities (like Ti, Zr, Hf) which form stable precipitates and thereby remove these impurities from the matrix phase. The former approach of reduction of interstitial impurities has its own limitation due to high processing cost. The later approach became more popular, in which impurity getter elements are incorporated in the vanadium alloys resulting in the formation of stable M(CON) [M= Ti, Zr, Hf] precipitates. Scavenging of interstitials results in improved fabricability, on one hand, and, on other hand, provides additional strength by forming precipitates. Such precipitates amicably compensate for the reduction in strength due to loss in interstitial solid solution hardening.

Apart from scavenging elements, like Ti, Zr, other substitutional elements, such as Cr, are commonly added in vanadium to optimize the critical properties of vanadium. These substitutional elements also affect the ductility and hence DBTT temperature of the vanadium alloys. DBTT of un-irradiated V-Ti-Cr alloys is below -200 °C for lower (Cr + Ti) concertation but increases sharply when (Cr + Ti) concentration exceed 10 %. Sakai et al. reported that DBTT of V-4Cr-4Ti alloys was around -190 °C, while for the alloys containing 10 % Cr the DBTT raised to -30 °C [63]. Further increase in chromium content shifts the DBTT above room temperature [21, 63, 64].

Large scale facilities for melting and thermomechanical processing is necessary for any alloy development. One of the major limitations associated with vanadium alloys development is the lack of a large industrial infrastructure facility. In one of the pioneering efforts, US has produced two large heats of V-4Cr-4Ti alloy in 500 Kg and 1200 kg (1998) scale and fabricated in various shapes [74]. Subsequently NIFS, Japan melted ingot of 30-150 kg (2005) [38, 39], CEA, France melted 30 kg ingot (2011) [75] and recently Russia melted 110 kg ingot (2013) of V-4Cr-4Ti alloy [76]. All of these ingots have shown consistently similar mechanical and physical properties [33]. Interstitial impurities pickup in these large heats was comparable to that in previous small laboratory heats of vanadium alloys and the mechanical properties were also in agreement with data obtained on small heats. The primary step in breaking the cast structure of vanadium alloys is generally hot working by extrusion or forging at temperatures of 1000 to 1200 °C. For this purpose, the billet is sealed under vacuum in stainless steel tube, followed by welding to avoid any interstitial element pickup from the atmosphere during primary forming. Secondary forming operations, including rolling, swaging, tube drawing, etc., are usually performed at nearly 500 °C or below and intermediate vacuum annealing treatments are generally carried out at 800 to 1000 °C, though temperatures as high as 1200 °C may be used for some alloys. The fabrication of a wide variety of product forms including tubing,

sheets and rods, from a number of alloys, V-Ti, V-Cr, V-Cr-Ti and Vanstar series has been successfully demonstrated.

2.5 Effect of alloying addition on the precipitation behaviour of vanadium based alloys

As mentioned in the previous section, impurity getter elements like Ti are incorporated in the vanadium alloys resulting in the formation of Ti(CON) precipitates. These precipitates are desirable in vanadium based alloys due to many fold advantage offered by them. Some of them are listed below:

1. Improvement in the formability by scavenging the interstitial impurities (C, O and N) [42].

2. Mitigating the high temperature, He embrittlement and void swelling related issues by providing additional potential sites (precipitate/matrix interface), which acts as a sink for radiation-induced lattice defects, such as vacancies, dislocation loops and He atoms generated by high energy neutrons [77, 78].

3. Reduces the low temperature embrittlement related issues (by lowering the DBTT) by scavenging the interstitials as the presence of 'free interstitials' in the V matrix causes the detrimental shift of the DBTT from −200 °C to values well above room temperature [18, 42, 79].

4. These precipitates are also reported to have beneficial effects in restraining the irradiation induced hardening by restricting growth rate of dislocation loops.

As mentioned above, precipitates have vital role in improving the mechanical properties of vanadium alloys which decides the operating temperature window of the alloys. Hence understanding of the evolution of precipitates in vanadium based alloy is important. Evolution of precipitates in V-4Cr-4Ti alloy has been studied extensively [18, 44, 48, 80-83]. Sizes,

morphologies and compositions of the precipitates depend on the thermomechanical processing of the alloy. The as-cast structure depending on the cooling rates is reported to exhibit either absence of these precipitates or scanty presences of few [82, 84]. Needle or plate shapes Ti(CON) precipitates are reported to form during early stage of fabrication and upon annealing above 700 °C [11, 21, 50, 82, 84, 85]. Muroga et al. have also reported the formation of VC precipitates which form at grain boundaries at 1100 °C, as a result of the redistribution of C from the dissolution of the thin Ti(O, C,N) precipitates [39]. Zhu et al. have systematically studied evolution of these precipitates in V-4Cr-4Ti alloy system [84]. They have reported presence of needle shape Ti rich precipitates in local zones in the as-cast structure with typical length of these precipitates in the range of 0.2 to 2 µm and width 5 nm [84]. The structure of these precipitates was found to be FCC with {200} planes of the matrix as the habit plane. Using electron diffraction and the fast Fourier transformation of the high resolution image, the orientation relationship between the precipitates and the matrix was determined as:

$$(02\bar{2})_P \text{ // } (200)_M \text{ and } [0\bar{1}1]_P \text{ // } [001]_M \text{ and } [\bar{1}00]_P \text{ // } [010]_M \ldots\ldots\ldots (2.1)$$

where the subscript P denotes the precipitates, and the subscript M denotes the matrix [84]. The lattice parameter of the Ti-rich Ti(CON) precipitates was found to be 0.423 ± 0.006 nm with NaCl type prototype structure. This specific orientation relationship between the precipitate and the matrix phases led to the formation of coherent interfaces which explains needle morphology and preferential distribution of the precipitates within grains. While the intra-granular precipitates can maintain coherence with the matrix phase, the precipitates at the growth boundaries can only form coherent interfaces only with one of the grains at the grain boundaries. Thus, the grain boundaries do not become favoured sites for the nucleation of precipitates [84]. Apart from preferential intergranular precipitation, considerable inhomogeneity in the spatial distribution of the precipitates was also observed in most of the V-Ti-Cr alloys [39, 75, 79, 80, 82, 83]. Non-uniform distribution of precipitates in the matrix

phase was explained by Peng et al. and they proposed the formation mechanism of the precipitates [82]. As pointed out by Tyumentsev et al. that most of the precipitates form during the thermomechanical processing of the alloy [86], they proposed formation of metastable VC phase during thermo-mechanical processing which subsequently transformed to thermodynamically stable Ti(CON) phases with a high titanium content. The proposed mode of formation is shown in the following equations

V(solid solution) + C , N, O (solid solution) $\rightarrow$ V(C,N,O) precipitates …..(2.2)

Ti(solid solution) + V(C,N,O) precipitates $\rightarrow$ V(solid solution) + Ti(C,N,O) precipitates …………………………………………………………..(2.3)
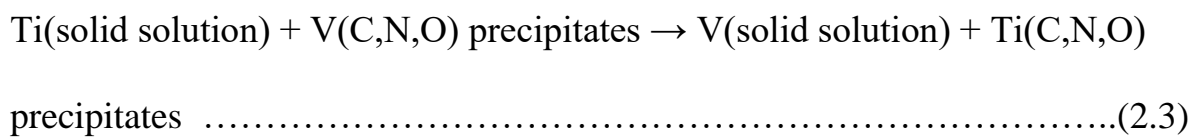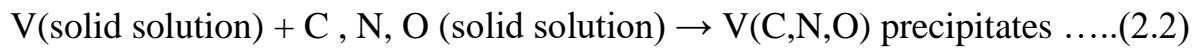
The rate determining factor in the above reactions is the concentration of interstitial content (300-500 ppm) in equation 2.2, as the solid solution Ti involved in reaction (2.3) is sufficiently available in the matrix phase (3.5 to 4.6 wt.%). Therefore, the amount of Ti(C,N,O) precipitates in local are mainly determined by the impurity content [86].

It is a known fact that thermo-mechanical processing of bcc materials produces non-uniform local deformation zones resulting in the non-homogeneous distribution of defects, such as dislocations. Regions of high dislocation density act as preferential sites for nucleation, as they not only provide necessary driving force but also allow faster diffusion of impurity atoms to preferentially form Ti(CON) precipitates, because of which these precipitates form clusters in these regions. This results in inhomogeneous distribution of the precipitates in V-Ti-Cr alloys [82]. These inhomogeneous distribution of precipitates were reported to have consequences on mechanical properties and especially induce anisotropic fracture. Homogenization of the precipitate distribution may be effective to avoid such anisotropy of fracture mode. Nagasaka et al. found that increasing degree of deformation to be around 99 %

by cold working process was an effective solution for the homogenization of the precipitate distribution [79].

Mechanism suggested by Zhu et al. also requires critical concentration of C, N, O near Ti atoms, but mode of transformation slightly differ from the earlier proposed theory [84]. Zhu et al. have proposed a two steps sequence mechanism for the formation of Ti-rich precipitates in the V–4Cr–4Ti alloy [84]. First step consists of transformation from the BCC structure to the twined FCC structure and in the second step, the twined FCC structure changes into the twin-free FCC structure [84]. This proposed mechanism is also able to describe that why only Ti rich precipitates form and not vanadium rich or chromium rich precipitates, although all the three elements are equally strong carbide formers. The binding capacity of the titanium element in the V–4Cr–4Ti alloy with carbon and nitrogen is stronger than that of vanadium and chromium. Thus, as long as Ti is in solid solution in vanadium, due to its size effect, strain field around its attracts interstitial atom which results in relatively higher concentration of interstitials like carbon, oxygen and nitrogen around titanium atoms. When titanium atoms gather in some locations of the matrix originating from composition fluctuation, carbon and nitrogen atoms will follow immediately and gather in the same locations due to the attraction from titanium atoms and their obviously larger diffusion coefficient. Once the critical condition of the nucleation is attained, the precipitates will nucleate by a shear mode, which results in the formation of a high density of twins. But twins are rarely seen in equilibrium microstructure. The absence of twins in the precipitate phase was explained on the basis of rearrangements of atoms. In the initial stage, the precipitates in the V–4Cr–4Ti alloy might contain a large number of vanadium atoms; just like the copper precipitates in the iron based alloys containing iron atoms at the nucleation stage [87]. Therefore, diffusion of titanium atoms from the matrix into the precipitates and the counter diffusion of vanadium atoms are needed to enrich titanium

atoms in the precipitates. Due to diffusion of atoms in the precipitates, the structure has the opportunity to rearrange itself by eliminating twin structures in this process.

In addition to the origin of precipitates, their orientation relationship (OR) with matrix, formation mechanism and their distribution in the matrix, attention has also been paid towards the stability of the precipitates [21, 48-50]. As vanadium alloys will be used as structural material in nuclear reactor at high temperature and under radiation environment, stability of precipitates both at high temperatures and under irradiation environment are important. Dissolution of precipitates in V-4Cr-4Ti alloy has been widely studied by several researchers using combination of microscopy and mechanical property correlations [48, 50, 80, 82, 83]. Muroga et al. have shown the sequence of precipitate formation and dissolution using the microstructural development and changes in the yield strength, which are shown in Fig. 2.12 [81]. Samples were first subjected to solution annealing treatment at 1100 °C for 1 hr to dissolve all the precipitates, followed by quenching. Subsequently, samples were re-heated for 1 hr at various temperatures (600-1100 °C). The yield strength of the samples increased with the formation of high density of fine precipitates with the peak in yield strength appearing upon annealing at 700 °C. Increasing the annealing temperature from 700 to 900 °C led to decrease in yield strength with a corresponding decrease in density of precipitates due to coarsening. Further increase in annealing temperature from 1000 °C to 1100 °C led to again increase in yield strength which was attributed to solution hardening effect of interstitials due to the dissolution of Ti(CON) precipitates.
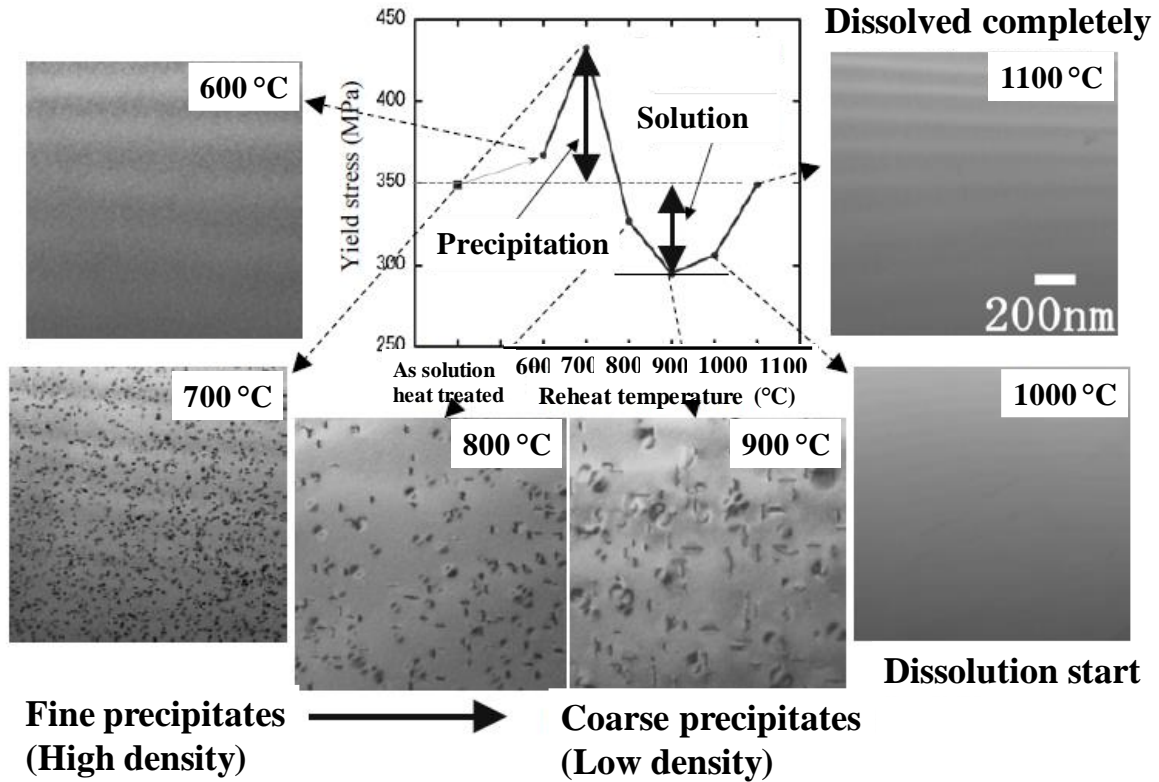
Figure 2.12: Microstructure and yield stress of V-4Cr-4Ti after solution annealing treatments at 1100 °C for 1 hr and the following re-heating for 1 hr at various temperatures [81]. The correlation between the increase in yield strength and appearance of precipitates in the matrix phase may be noted.

Heo et al. have reported that annealing treatments above 1100 °C for V-4Cr-4Ti alloy led to the dissolution of Ti(CON) precipitate phase and thereby result in enhanced levels of interstitial contents in the alloy matrix [80]. In addition to the temperature effects, irradiation was also reported to induce precipitate dissolution. Jiang et al. have reported that at the irradiation dose of 3.4 dpa, Ti(CON) phase was getting destabilized due to the introduction of vacancies into the precipitate phase and thereby altering the local atomic arrangements [48]. The introduction of structural vacancies enhanced atomic mobility which resulted in effective dissolution of precipitates by the rejection of interstitials into the matrix phase. As a result of both temperature and radiation assisted precipitate dissolutions, the enriched concentration of interstitials in the vanadium matrix is reported to lock the dislocation superstructures and thereby causes embrittlement of the matrix phase and subsequent upward shift in DBTT

temperature. Muroga et al. have shown nearly 20 % increase in hardness of V-Ti-Cr alloy upon irradiation which was attributed to radiation induced precipitate dissolution [50]. The irradiated samples exhibited increase in the dislocation density, which effectively got pinned down by the presence of higher interstitial in the matrix causing increased hardening and embrittlement. Upon irradiation up to 0.5 dpa, almost 3 times higher yield strength was observed in V-4Cr-4Ti samples which were tested in the temperatures range up to 400 °C [21]. Zinkle et al. have also reported higher yield strength upon irradiation which they attributed to the increased interstitial content which eventually contributed towards large increase in the DBTT temperature shift [21].

Apart from V-4Cr-4Ti alloys, precipitation behaviour of the other vanadium alloys is not so well studied. Very few studies have been carried out to understand the effect of the substitutional alloying elements on the precipitation behaviour. Sakai et al. has reported the effect of Cr content and annealing temperature on the size and density of precipitate in V-xCr-4Ti alloys [63]. It was found that the size of the precipitate was almost unaffected by variation in Cr content from 4 to 15 % in vanadium alloys, whereas annealing temperature was found to have direct correlation with the size of the precipitates and it was increasing with the temperature above 900 °C. Apart from Cr, effect of W addition on the precipitation behaviour of the vanadium alloys has also been studied [46]. It is reported that the V–6W–4Ti alloy has shown almost similar number density of precipitates as was observed in the case of the V–4Cr–4Ti alloy, which elucidated that the growth of the precipitate is essentially controlled by the diffusion of the C, N and O interstitial solutes and not by Cr or W, as later being substitutional solute atoms show slow diffusivity [46]. TEM-EDS investigation of V-6W-4Ti revealed the composition of precipitates to be Ti(CON) with no tungsten in the precipitates [46]. Apart from these, effect of other refractory metals such as Ta, Mo and Nb on the precipitation behaviour of vanadium alloys have not been reported. In view of the beneficial role of the precipitates in

vanadium alloys, role of alloying addition on precipitation behaviour needs further investigations.

2.6 Effect of alloying addition on recovery and recrystallization temperature of vanadium based alloys
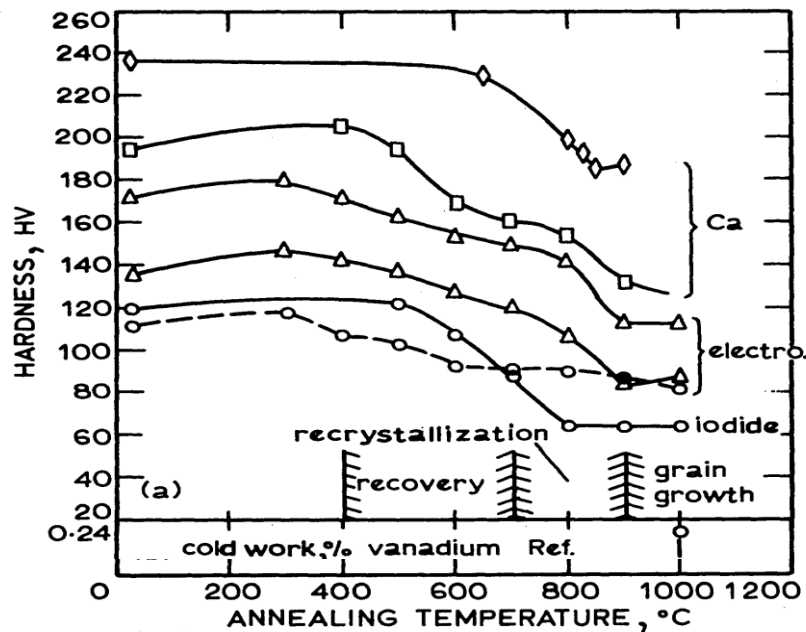
Figure 2.13: Recovery, recrystallization, and grain-growth behaviour in calciothermic, eletrorefined and iodide refined vanadium showing the effect of interstitial elements on recovery and recrystallization [40].

Vanadium exhibits significant recovery (softening) before the start of recrystallization, which is a typical behaviour of Group V refractory metals (V, Nb and Ta) as could be noticed form Fig. 2.13. However, depending upon the route of production of V, for example, calciothermic, eletro-refining or iodide reduction, the recovery behaviour of vanadium changes significantly. This difference in the recovery process is primarily influenced by the presence of interstitial impurities like C, N and O. Reduction in interstitial impurities shifted down the recovery temperature by approximately 200 °C. These interstitial impurities migrate to the dislocations during the heat treatment in the temperature range of 200-400 °C and reduce the mobility of dislocations. This interaction between dislocations and interstitials make the alloy

37

harder where the hardness of the alloy peaks around 300 °C, as shown in Fig. 2.13 [40]. The effect of interstitials was demonstrated using electro-refined vanadium (highly pure vanadium) which has shown the start of the recovery process at temperatures as low as 400 °C. The role interstitial become much better evident in the case of iodide refined vanadium where substantial reduction in hardness was noticed even before the start of recovery process. In addition, a wide temperature ranges of 650 to 1000 °C for the starting recrystallization process in vanadium is reported in literature, which is shown in Table 2.3.

Table 2.3: Recrystallization temperature of vanadium metal reported in literature.

Recrystallization start temperature (°C)	Recrystallization completion temperature (°C)	Reference
650	800	Rostoker et al. [88]
650-700	<800	Nash et al. [89]
750	850-900	Lecy et al. [90]
750-850	950-1000	Abrahamson et al. [91]
600-700	1000	Loria et al. [92]

Table 2.4: Effect of alloying elements on recrystallization temperature and mechanical properties of vanadium alloys [54, 57, 58, 93].

Alloy	Recrystallization temperature (°C)	Yield strength at room temperature (MPa)	Yield strength at 800 °C (MPa)
V	700-800	170	70
V-5Al	900	200	80
V-5Ti	1050	300	190
V-6Nb	1100	300	195
V-8Ta	1300	400	240
V-5Cr	1050	250	130
V-5Mo	1100	290	100
V-6W-1Ti	900	250	-
V-4Ti-4Cr	1000	290-310	180
V-15Ti-7.5Cr	1000	630	280
V-8Cr-10Ta-1.3Zr-0.05C (VANSTAR-8)	1050	365	206
V-6Fe-5Nb-1.3Zr-0.05C (VANSTAR-9)	1100	490	300
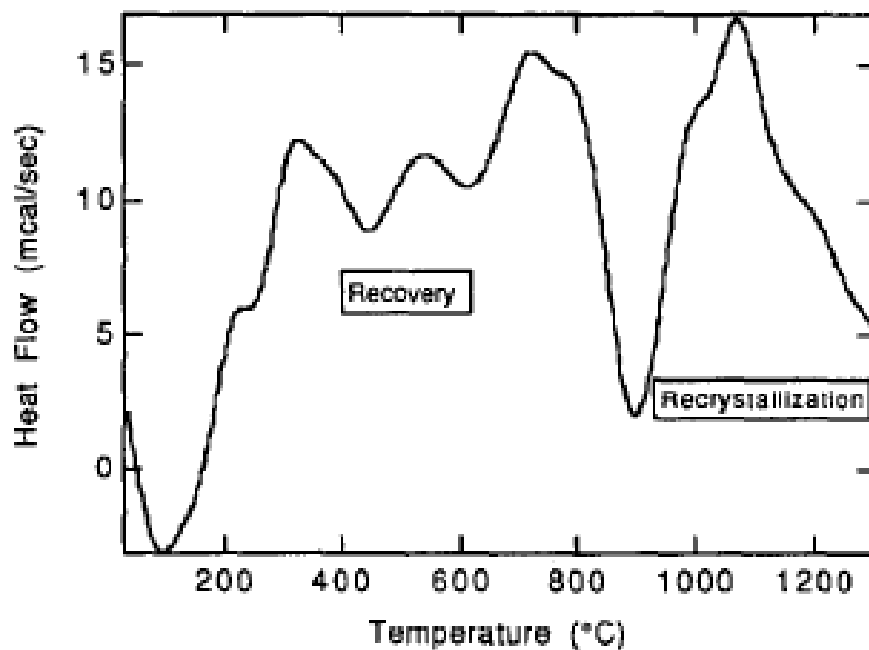
Figure 2.14: DSC plot of deformed V-4Cr-4Ti alloy obtained at a heating rate of 20 °C/min showing the recovery and recrystallization behaviour of the alloy [94].

In addition to the role of interstitial elements, effect of alloying addition to V has been studied by various researchers [54, 57, 58, 93], which is summarized in Table 2.4. The effect of the alloying additions of Ti, Zr, Mo, Nb, W, Ta, Cr to V on the recrystallization temperature of the alloy has been studied. For example, Ti and Cr do not increase the recrystallization temperature significantly, but simultaneous presence of both the element raises the recrystallization temperature above 1000 °C. Refractory metals, such as Nb and Ta, on the other hand, were found to be more effective in increasing the recrystallization temperature of vanadium alloys which increases in the range of 1100-1200 °C.

Among all the vanadium alloys the recrystallization process of the V-4Cr-4Ti alloy has been extensively studied. Using DSC thermal analysis, recrystallization behaviour of V-4Cr-4Ti was studied by Gubbi et al. [94]. Fig. 2.14 gives a typical thermogram of V-4Cr-4Ti alloy which is exhibiting a broad region of peaks showing prolonged recovery from 200 to 800 °C. The broad exothermic recovery region between 200 and 800 °C (Fig. 2.14) is a consequence

of contributions from several recovery processes, including segregation of interstitial elements to dislocations, annihilation of vacancies, the climb and annihilation of dislocations, to name a few. A well-defined sharper exothermic peak at 900 °C is the signature of recrystallization start temperature and it has been reported that for full recrystallization, a typical temperature of 1000 °C is required. Gubbi et al., by combining optical and TEM investigations, have correlated changes in the hardness of the alloy with the annealing temperature [94]. Optical and TEM examinations showed that rapid drop in hardness was due to the recovery of the cold worked dislocation structure into a system of cells. Evolution of the deformed microstructure of V-4Cr-4Ti during annealing in the temperature range from room temperature to 1100 °C has been reported in the literature [80, 94]. Microstructural investigations revealed that recovery of V-4Cr-4Ti occurs below 800 °C and full recrystallization occurs in 1 h at around 1000 °C [80, 94]. At and above 1100 °C significant grain growth can also be observed. This abnormal grain growth was reported due to the reduced Zener pinning because of the dissolution of Ti(CON) precipitates which were acting as pinning centres for grain boundaries and dislocations [82]. In order to retard the grain growth in vanadium based alloys, yttrium was added which being strong oxide former led to the formation of finer yttrium oxide precipitates [82]. These insoluble oxide precipitates effectively inhibited the abnormal grain growth with the help of Zener pinning effect to some extent and compensated the reduction in the volume fraction of Ti(CON) precipitates to some extent. Duquesnes et al. have also studied the progress of recrystallization of V-4Ti-4Cr alloy as a function of annealing temperature in the range of 600-1200 °C [75]. Using hardness and microstructural characterization to monitor the recrystallization, they have reported that recrystallization starts at 600-700 °C and completes at 1000 °C [75]. It was also reported that recrystallization temperature also depends on the degree of cold work, as evident from Fig. 2.15, which compares the study of Heo et al. [80] in which 90 % deformed alloy samples were used whereas Duquesnes et al. [75] used 54 % and

87 % deformed samples for recrystallization studies. Full recrystallization (minima in hardness) of 54 % deformed samples occurs at 1000 °C while 850–900 °C for Heo et al. samples which were 90 % deformed [75, 80]. In addition to various phenomena observed below 1000 °C, the increase in hardness with annealing temperature exceeding 1000 °C was clearly highlighted. This increase in hardness has been interpreted in terms of dissolution of small Ti(CON) precipitates, releasing interstitial impurities in the matrix and then resulting in solid solution reinforcement [75, 80].
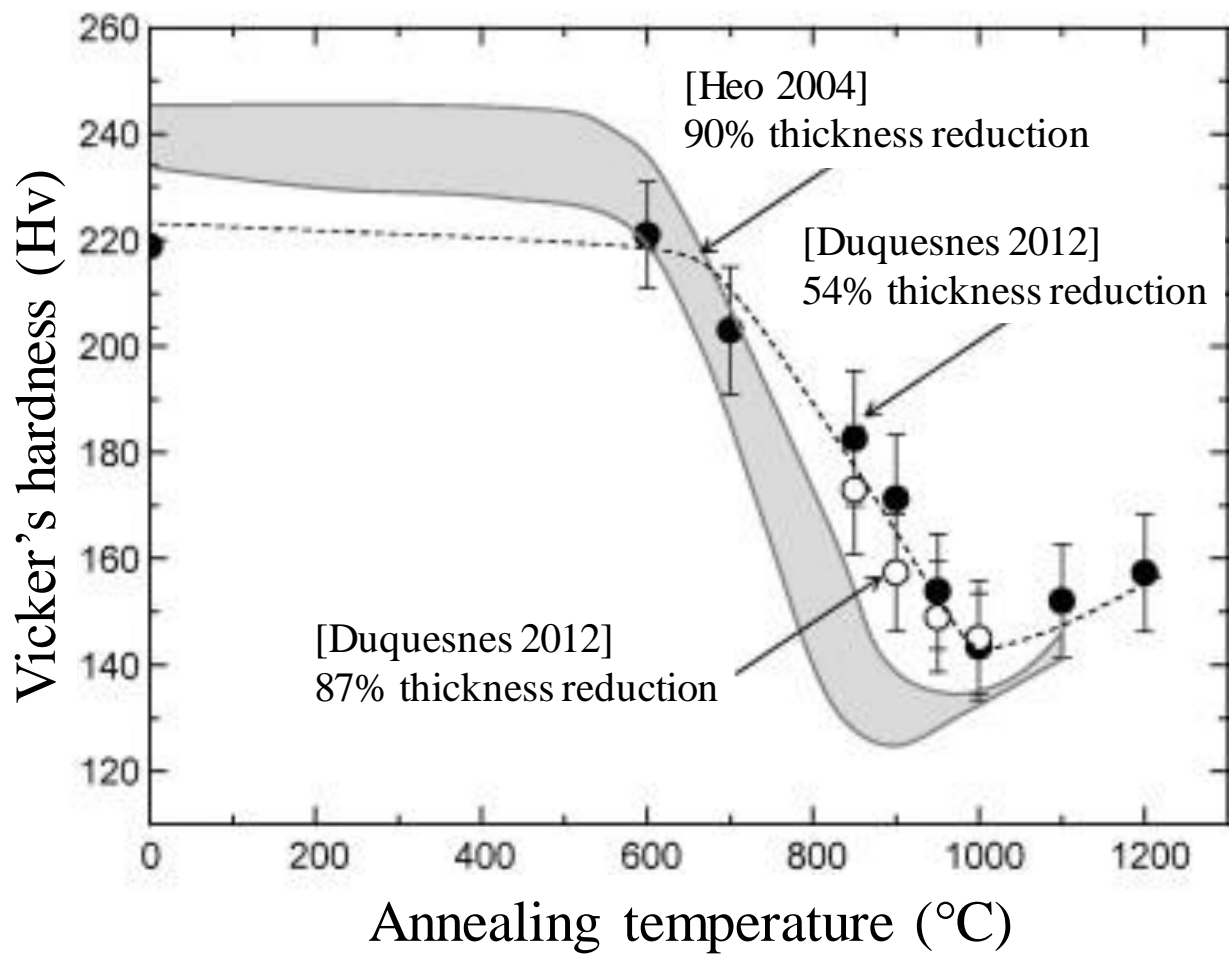
Figure 2.15: Change in hardness versus annealing temperature showing the effect of degree of deformation on the recrystallization temperature. 54 % and 87 % rolled material by Duquesnes et al. is compared with 90 % rolled sample by Heo et al. [75, 80].

Peng et al. have recently studied the recrystallization behaviour of V-4Cr-4Ti alloy using EBSD technique and have reported complete recrystallization at 900 °C [82]. They have also reported that recrystallization of V-4Ti-4Cr alloy led to heterogeneous grain structures, while heating to higher temperatures (1150 °C) lead to abnormal gain growth and heterogeneous gain structures were still prevailing. It has been widely recognized that grain structure in V-4Ti-4Cr alloy is influenced by the presence of Ti(CON) precipitates. These precipitates were considered to render significant influence on the processes of recrystallization and their non-uniformity result in a substantially non-uniform grain structure of the alloys [12]. One of reason for these precipitates to be responsible for non-uniform grain structure is their alignment along the rolling direction with a band distribution during rolling [3,6,11,13]. Such distribution of the precipitates led to much finer grain size near the band structure as compared to the regions away from the precipitates bands [13]. These heterogeneous grain structures were reported to have consequences on mechanical properties of the alloy and especially induce anisotropic fracture mode [11]. It was, therefore, proposed that homogenization of the distribution of precipitates would be effective to avoid such anisotropy of fracture mode. Addition of yttrium in the alloy has helped in getting homogenous recrystallized microstructure. As the role of precipitates is important in V based alloys in developing inhomogeneity in the microstructure and influencing mechanical properties, the next section has been devoted on the evolution of precipitates.

2.7 Development of texture during deformation and annealing of vanadium based alloys

Crystallographic texture in a material plays an important role in improving the formability and mechanical properties of a material. The crystallographic texture is mainly depending on the crystal structure, microstructural constituents like grain size, type of precipitates, phases and their sizes and most importantly on prior deformation texture of the material. Therefore, it is

necessary to study texture developments during deformation and annealing of a material. Texture in BCC metals can be broadly categorized into two groups: The first group comprises pure bcc refractory metals like Ta, Nb, Mo and W and dilute alloys like low carbon steels. The second group like high alloyed bcc transition metals (steels with 10 -17 % Cr). It has been shown that the cold rolling texture of all bcc materials have two common features: the formation of a strong but incomplete α-fiber between {001} <110> and {111} <110> and the increase in the γ -fibre texture with deformation. For first group like low carbon steels, for deformation <70 %, {001} <110> and {112} <110> are the dominant components in the α-fiber and a weak preference for {111} <112> component in the γ -fiber. In the case of second group materials, it is observed that strong texture gradient develops from surface to the centre. At the centre, in the α-fiber increase in {001} <110> and {112} <110> and in the γ-fiber strong {111} <110> component is observed. At the surface, strong {001} <110> and {111} <112> components in α and γ -fibers are observed, respectively. The reason for the formation of texture gradient in the second group materials is the presence of inhomogeneous microstructure and preference of texture in the pre-deformed materials. However, specifically for vanadium and its alloys, the reported crystallographic textures data are very rare. Pure vanadium sheet with 95 % deformation was reported to show a typical bcc rolling texture of <110> ∥ RD and <111> ∥ ND fibre and had a recrystallization texture of {111} <112> + {001} <740> after annealing at 870 °C [7]. It has been seen that he additions of alloying elements can change the texture of pure material considerably [9]. Texture development in V-4Cr-4Ti alloy has been studied recently by Peng et al [42]. The rolled V-4Cr-4Ti sheet exhibited a macro rolling texture of α- fibre {001} <110> + {112} <110>and γ-fibre. After annealing at 1100 °C for 10 minutes, decrease of the α-fibre texture and an invariability of the γ-fibre texture has been reported. It has also been found that apart from initial rolling texture, evolution of precipitates during annealing in V-4Ti-4Cr alloys also affects the texture.

2.8 Effect of alloying addition on the mechanical properties of vanadium based alloys

The mechanical properties of commercially pure vanadium were studied extensively throughout the 1950s and 1960s. Among various studies, Harrod et al. have published a classical review paper on mechanical properties of vanadium and its alloys [40]. The stress-strain behaviour of vanadium is similar to that of other bcc metals, which is characterized by a strong temperature dependence of strength, yield point phenomenon and strain -aging at room temperature, dynamic strain aging in the intermediate temperatures (300-500 °C), ductile-brittle transition and low temperature twinning.

The effects of alloying additions and impurity elements on the mechanical properties of vanadium alloys are important considerations in alloy selection, particularly with respect to the optimization of high-temperature properties. Most of the reports published on the effects of alloying additions are summarized by Harrod et al. [40]. Effect of most of the transition metals like Ti, Zr, Hf, Fe, Ni, Cr, Mo, W, Nb, Ta, etc., were studied and it was found that in binary V alloys, Ta acts as most effective solid solution strengthener among all studied elements (Fig. 2.16). Votinov et al. [30, 95] have also reported that V-Ta alloys exhibit relatively higher strength at 600 and 800 °C as compared to other binary vanadium based alloys. Direck et al. have also summarized the effect of various alloying elements in vanadium based alloys [42]. Although all studied binary alloys, except V-Ti and V-Zr alloys, were showing high strength but with brittle failure [40]. V-Zr alloys showed hot-shortness during fabrication in alloys where concentration of Zr content exceeded 3 %. This led to the development of only V-Ti alloys and it was accepted that Ti is a necessary element to retain ductility during fabrication of vanadium based alloys.
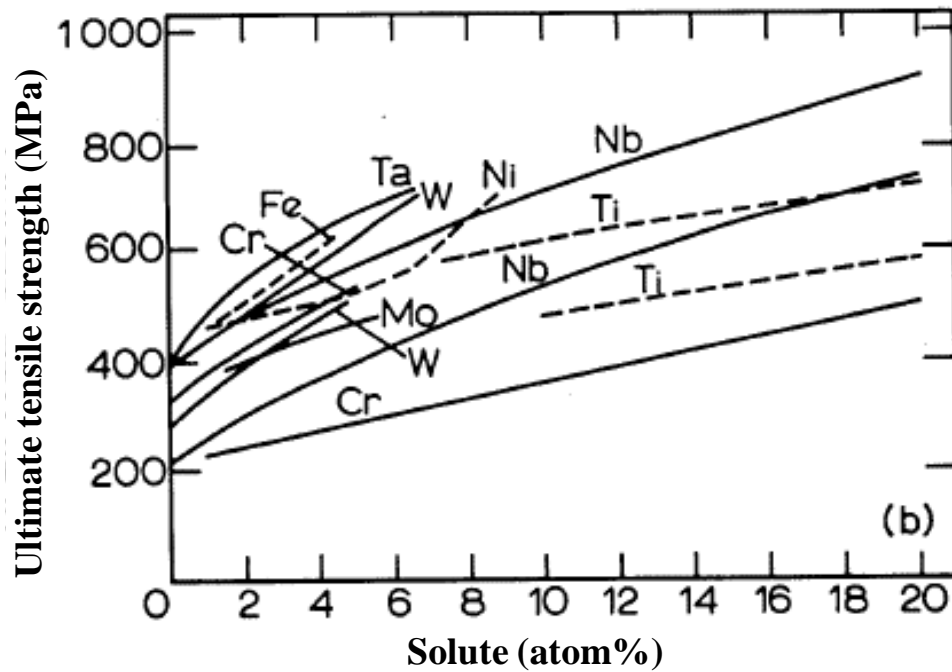
Figure 2.16: Comparison of relative strengthening effect of various solutes in vanadium [30].

To enhance the high temperature strength of binary V-Ti alloys, series of ternary V-Ti-X (X= Mo, Nb, W, Ta) alloys were synthesized by Rajala et al. [54]. In preliminary investigation, it was found that Ta is most effective in increasing high temperature strength of V-Ti alloys. It was also reported that 5-10 % Ti is optimum to increase the tensile strength at elevated temperatures with an improved room-temperature ductility [54]. Higher content of Ti was found to be detrimental for high temperature strength. Later on, as fusion reactor become more popular, and thirst emerged to develop alloys which have shorter half-life daughter products to have low long term activation materials. The elements, like, Nb and Mo, do not qualify from the view point of low activation daughter products. Hence later on, the development of V-Ti alloys was mainly confined to V-Ti-Cr and V-Ti-W [46, 47, 96]. Chen et al. have studied V-Ti-W alloys in detail and compared their properties with the V-Ti-Cr alloys [46, 47, 96]. The V-Ti-W alloys were found to have difficulty in melting, fabrication with a limited gain in the high temperature strength. Due to these limitations of V-Ti-W alloys, V-Ti-Cr alloys gained more popularity and efforts were on to optimize the composition of Cr and Ti

in V-xCr-yTi alloys. The yield strength of V-Ti-Cr alloys appears to show strong dependence on (Cr + Ti) concentration, which is shown in Fig. 2.17 [97]. It could be observed that strength of V-Ti-Cr alloy increases linearly with (Cr + Ti) content in the alloy. Selection of higher (Cr + Ti) alloy although will have higher strength but limited by their impact properties, since DBTT should be kept below the operational temperatures of the reactor. Impact properties of vanadium alloys are strong function of (Cr + Ti) content. DBTT temperature of V-Ti-Cr alloys with (Cr + Ti) concentration is shown in Fig 2.18. It could be seen that DBTT of un-irradiated V-Ti-Cr alloys is below -200 °C for lower (Cr + Ti) concentration but increases sharply when the concentration of (Cr + Ti) exceeds 10 %. This behaviour was explained by stress-controlled cleavage (equivalent yield stress) models [98]. Irradiation is known to increase the DBTT of alloys [21]. Loomis et al. [64] have reported that when the concentration of Cr or Ti is increased beyond 6 %, DBTT of the alloy after neutron irradiation increases to room temperature (> 25 °C), which is dangerous for the safe operation of a fusion reactor. Based on these experimental facts and with systematic efforts, V–4Ti–4Cr has been identified as the optimum composition to be considered for structural applications in fusion reactors. Apart from (Cr + Ti) concentration, the impact properties of V-Ti-Cr alloys are also dependent upon the annealing temperature and the size of the precipitates. DBTT curve shows step function above 10 % concentration of (Cr + Ti) for 950 °C annealing. It could also be noted that DBTT curve shifts towards lower (Cr + Ti) content for higher annealing temperature. It could be seen from Fig. 2.18 that DBTT increases as the annealing temperature is increased above 1000 °C. The physical mechanism responsible for heat treatment sensitivity of the DBTT is related to not only the solid solution hardening but also the difference in precipitation behaviour of vanadium alloys. Precipitates in V-4Cr-4Ti alloys are reported to dissolve above 1000 °C, which results in the release of interstitial atoms to the matrix. These increased interstitials exert pinning effect

on the gliding of dislocations, which results in a significant rise of DBTT in vanadium alloys [21, 85, 99].
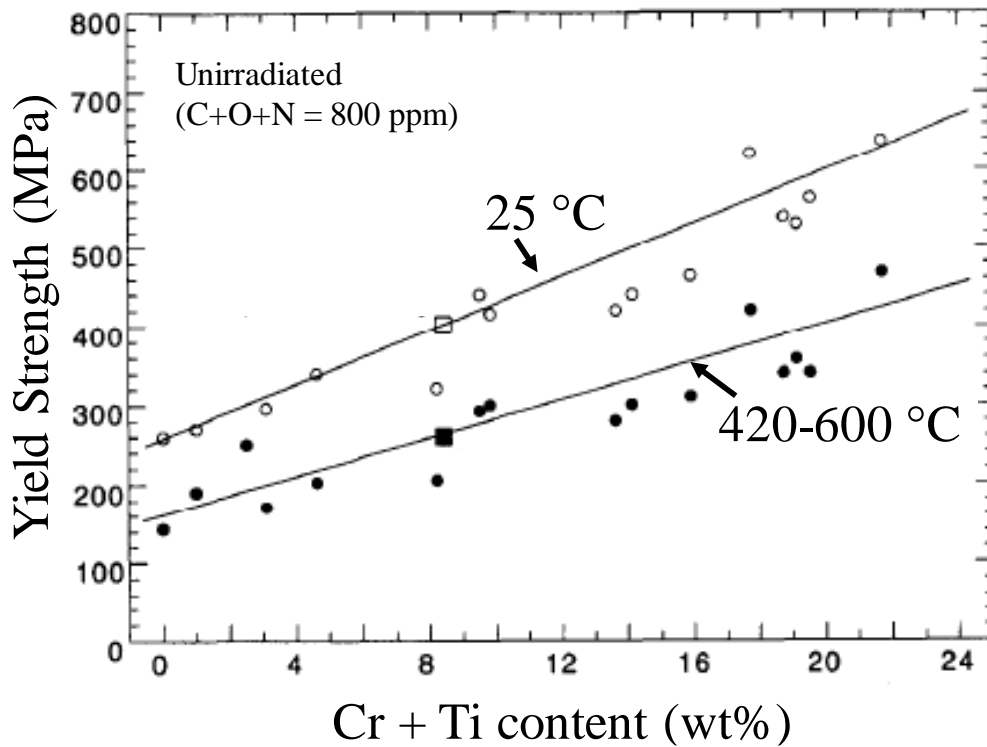
Figure 2.17: Yield strength of V-Ti-Cr alloys as a function of (Cr + Ti) content in the alloy [97].
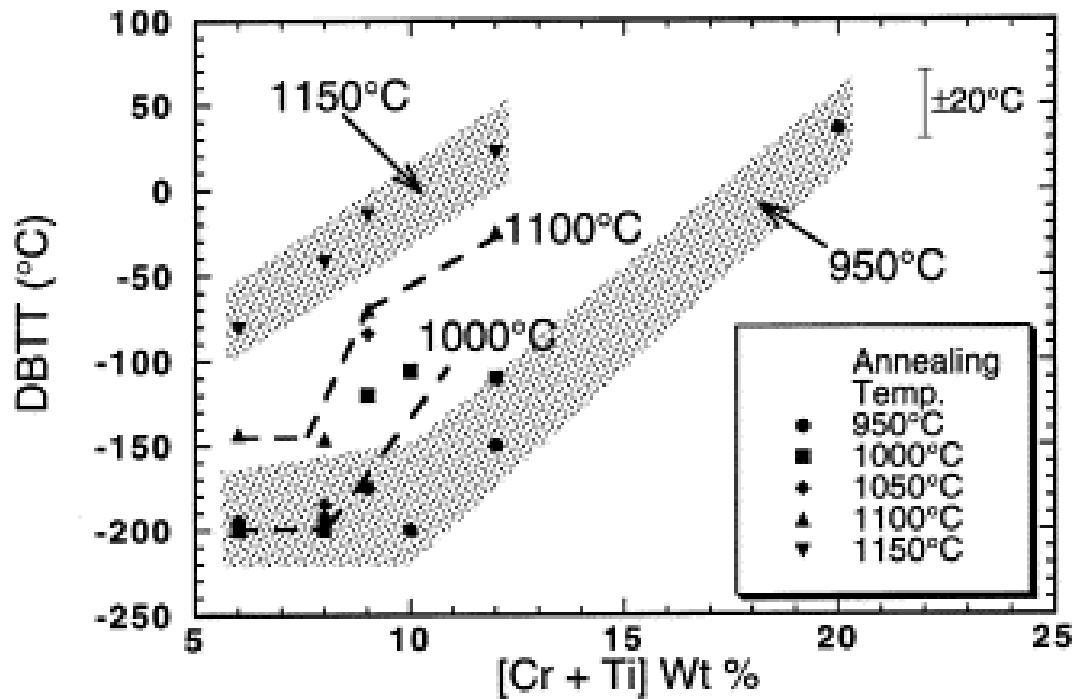
Figure 2.18: Effect of (Cr + Ti) concentration and annealing temperature on the DBTT of V–Ti-Cr alloys [21, 97].

Dependence of DBTT on concentration of Cr has a lot of significance during reactor operation. It has been reported that the composition of vanadium alloys was altered significantly due to transmutation during irradiation. In one such study, it has been found that 16 % of vanadium gets transmuted into chromium upto 17 dpa irradiation [100]. Such alterations in the chemistry of the alloy can significantly increase the DBTT of vanadium alloys to room temperature, which can adversely affect the reactor safety. So for the safe operation of the reactor and to avoid embrittlement, starting (Cr + Ti) total must be kept below 8 %.

Apart from strength and impact properties, thermal creep of vanadium alloys is also an important property from the view point of reactor operation. One of the issues limiting upper operating temperature of V alloy is thermal creep resistance. Thermal creep of pure vanadium and various V–Cr–Ti alloys have been widely studied [19, 33, 36, 101-103]. In pure vanadium, rate of creep is controlled by the vacancy diffusion mechanism [101]. Alloying elements are reported to increase the creep resistance of pure vanadium. Koyama et al. have reported that creep strength of vanadium alloys is related to the yield and ultimate tensile stresses of the alloy [102]. It was found that interstitial free high purity V-4Cr-4Ti alloy has shown poor creep strength in the temperature regime between 400 to 700 °C, which was attributed to the elimination of hardening caused by the effect of lesser interstitial content. It was also reported that substitutional solid solution strengthening also helps in improving creep properties of V alloys. It has been found that increased Cr addition helps in increasing the creep resistance of V-Ti-Cr alloys [36, 102]. Higher strength of V-5Ti-15Cr alloys have shown superior creep properties as compared to lesser Cr containing V-4Ti-4Cr alloy [36]. Hence it could be concluded that higher interstitial and higher Cr content increase the creep strength of vanadium alloys.

From the above discussion, it is clear that mechanical properties of V alloys, such as strength, impact properties and creep strength, are influenced by interstitial content (C, O and

N), substitutional alloying content (Cr and Ti) and by the stability of precipitates. Higher interstitial and (Cr + Ti) content are detrimental for impact properties but beneficial for creep properties of vanadium alloys. Hence, for fusion reactor structural applications the chemical composition of V–Cr–Ti alloys should be optimized by balancing the Cr and interstitial concentrations.

2.9   Effect of alloying addition on oxidation behaviour of vanadium alloys

The major limitation for the application of the vanadium alloys at high temperatures is their poor oxidation resistance. Oxygen is reported to degrade the properties of V-alloys during service through dissolution in the matrix as well as by the formation of low melting oxide which are deterrent for its high temperature applications. Hence, it is important to study oxidation behaviour of the V alloys at elevated temperatures.

2.9.1   Basic Mechanism of oxidation of metals

The chemical equation for an oxidation reaction between a metal (M) and oxygen (O_2) is shown below

$$M_{(s)} + \frac{1}{2}O_2 = MO_s \dots\dots\dots\dots\dots\dots\dots\dots\dots\dots.. (2.4)$$
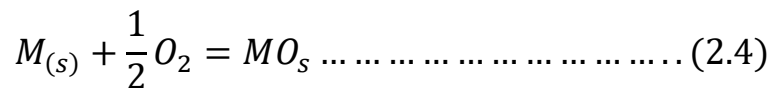
This equation looks very simple but oxidation of metal is a multistep process, which is broadly represented as:

$$\frac{1}{2}O_{2(g)} \rightarrow \frac{1}{2}O_{2(ad)} \rightarrow O_{(ad)} \rightarrow O^-_{Chem} \rightarrow O^{-2}_{Lattice} \dots\dots\dots\dots\dots\dots\dots\dots. (2.5)$$
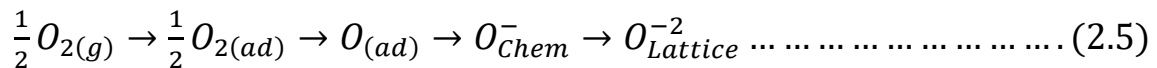
The first step in this metal oxygen reaction involves the adsorption of oxygen on a clean metal surface. In the second stage, the adsorbed oxygen may dissolve in the metal and then oxide is formed on the surface either as a oxide film or as separate oxide nuclei. it is obvious that the solid reaction product, MO, will separate the two reactants as shown below:

$$S_{m\text{-}mo} \qquad S_{mo\text{-}o}$$

$$M \quad \| \quad MO \quad \| \quad O_2 \text{ ……………... (2.6)}$$
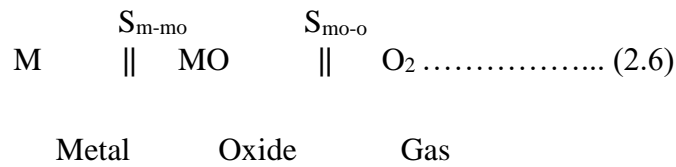
Metal   Oxide   Gas

The solid reaction products (metal oxide) separate the two reactants by creating two surfaces; metal and metal-oxide surface ($S_{m\text{-}mo}$) and metal-oxide and air surface ($S_{mo\text{-}o}$) (marked in the equation 2.6). For the oxidation reaction to proceed further, one or both reactants must penetrate into the reaction product, which is generally present in form of a scale on the top of the surface, through these interfaces. There are two possible scenarios; in one, ions of metal diffuse through the oxide to the oxide–gas interface ($S_{mo\text{-}o}$) and reaction takes place at $S_{mo\text{-}o}$, and in the second scenario, oxygen ions diffuse to the oxide–metal interface ($S_{m\text{-}mo}$) and the oxidation reaction occurs at $S_{m\text{-}mo}$. Therefore, phenomena by which the reactants penetrate the oxide layer become important parts of the mechanism by which high temperature oxidation occurs. Either one or both reactants (O_2 or Metal), could reach to the metal/oxide interface ($S_{m\text{-}mo}$) (reaction interface) by two ways diffusing through the oxide layer or penetrating through the pores or cracks. Fig. 2.19 shows all these possible reactions [104].

It has been shown that for thick compact scales, driving force for transport through the oxide is the chemical potential gradient across the scale and for thin films it may also be due to electric fields across the film.

In case, the oxide scale is porous or has cracks, the oxide scale will not act as a solid-state diffusion barrier between the reactants. In such cases the kinetics of the oxidation reaction are limited by processes occurring at phase boundaries. In addition, another complication may arise at high temperatures due to volatility or liquefaction of the oxides phase.

Metal **Oxide Layer** **Gas**

$$V^{+5} \quad V^{+5} \quad V^{+5}$$

$$V = V^{+5} + 5e^-$$

or

$$V + 2.5O^{-2} = 0.5V_2O_5 + 5e^-$$

$$O^{-2} \quad O^{-2} \quad O^{-2}$$

$$V^{+5} + 5e^- + 1.25O_2 = 0.5V_2O_5$$

$$1.25O_2 + 5e^- = 2.5O^{-2}$$

$$e^- \quad e^- \quad e^-$$

Activation energy for air oxidation (Q_{ox})   Activation energy for diffusion of oxygen (Q_D)
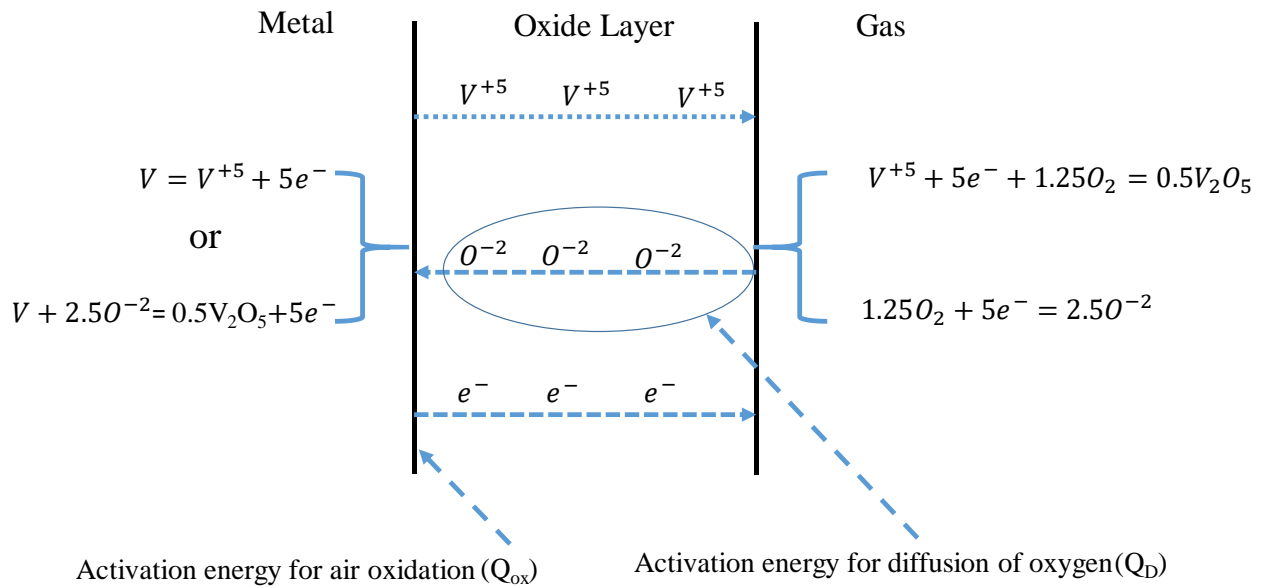
Figure 2.19: Simplified model for diffusion-controlled oxidation.

2.9.2 Measurements of reaction kinetics of oxidation

The extent of the oxidation reaction may be measured either by measuring the amount of metal consumed, or the amount of oxygen consumed or the amount of oxide produced. While representing the kinetics of oxidation, at a given temperature any of these variables can be measured as a function of time to assess the extent of oxidation reaction. Nowadays it is most general to measure the change in mass of a specimen exposed to oxidizing conditions. The experimentally determined change in the mass of the specimen can be expressed in terms of several rate laws which are majorly identified as (1) linear law, (2) parabolic law, and (3) logarithmic law.

(1) The linear law, for which the rate of reaction is independent of time, is found to refer predominantly to reactions where the oxidation rate is controlled by a surface-reaction step or by diffusion through the gas phase.

(2) The parabolic law, for which the rate is inversely proportional to the square root of time, is found to be obeyed when diffusion through the scale is the rate-determining process.

(3) The logarithmic law is only observed for the formation of very thin films of oxide, i.e., between 2 and 4 nm, and is generally associated with low temperatures.

It has already been seen that for an oxidation process to proceed under conditions where the two reactants are separated by the reaction product, it is necessary to postulate that ionic and electronic transport processes through the oxide are accompanied by ionizing phase-boundary reactions and the formation of new oxide at a site whose position depends upon whether cations or anions are transported through the oxide layer. Taking this very simple model and making still more simplifying assumptions, Wagner was able to develop a theory of the high-temperature oxidation of metals. In fact, the theory describes the oxidation behaviour only for the case where diffusion of ions is the rate determining step and under highly idealized conditions.

According to the Wagner's theory, lattice diffusion of reacting atoms or ions (cations, anions) or the transport of electrons through the oxide scale is the rate determining step in the kinetics of oxidation [104]. Following assumption were considered in Wagner's theory:

(1) The oxide layer is adherent and compact.

(2) Migration of electrons, cations and anions across the oxide scale is the rate-controlling process.

(3) Thermodynamic equilibrium is established at both the oxide–gas and metal–oxide interfaces.

(5) Thermodynamic equilibrium is achieved locally throughout the oxide layer.

(6) The oxide scale is thick compared to the distances over which electrical double layer forms.

(7) Solubility of oxygen in the metal may be neglected.

The Wagner theory permits an evaluation of the rate constant of high temperature parabolic oxidation provided the ion and electron mobilities or the diffusion coefficients are known.

2.9.3 Oxidation behaviour of vanadium and its alloys

Oxidation of vanadium has been extensively studied in literature under different environmental conditions such as in pressurized water [105], gaseous helium coolant containing water vapor [106], air [107], low pressure oxygen [108], atmospheric oxygen [108, 109], dry and moist oxygen-argon mixture over the years [110]. Table 2.5 summarizes some of the results at various temperatures for vanadium and its alloys. It has been shown that upto 670 °C, vanadium shows adequate oxidation resistance in air due to the formation of a protective oxide layer [111] where VO_2 is the predominant phase in the oxide scale in specimens exposed to low-pO_2 environments; the oxide scales are continuous and tenacious. V_2O_5 was the predominant phase in specimens oxidized in air or 100 % O_2 environments. The breakaway oxidation starts beyond 670 °C due to melting of the oxide layer [109, 110]. The breakaway oxidation is, in fact, the primary deterrent in the use of V based alloys beyond 670 °C. Therefore, to improve the oxidation properties of V several alloying additions have been tried.

It has been well documented that binding energies between interstitial and substitutional elements, along with their electronegativity difference affect the diffusivity of oxygen in transition metal elements. The main contribution to the interaction between substitutional - interstitial solute is believed to arise from the chemical effect through perturbations induced by these solute atoms on the electronic structure of the solvent atom. Roberto et al. have found that on the addition of Cr, Ni, Nb and Ta in vanadium increases the activation energy for oxygen diffusion which reflects the effect of these substitutional solutes on the activity coefficient of oxygen [112]. They have reported the activation energy for oxygen diffusion in

V, V-0.95Cr and V-3.6Ta alloys as 124, 129 and 152 kJ/mol respectively, which suggest that Ta can significantly affect the oxidation behaviour of vanadium alloys.

It could be seen from Table 2.5 that oxidation of V-Ti-Cr alloys largely depends upon the pressure of oxygen which influences the formation of VO_2 or V_2O_5. No oxides of Cr or Ti were detected on the surface, even though Ti is a stronger oxide former than V [109]. Uz et al. have attributed higher oxidation resistance of V-Ti-Cr alloys as compared to vanadium, to the higher activation energy of oxygen diffusion in V-Ti alloys [113]. For example, V-5Cr-5Ti alloys have shown higher activation energy of oxygen diffusion as compared to V-4Cr-4Ti alloys (Table 2.5). Chen et al. have studied the effect of W addition in vanadium alloys where oxidation of the V–W–Ti alloys in air was found to obey parabolic kinetics with small effects of the alloying elements [47].

Table 2.5: Rate constants , diffusion coefficients and activation energies of diffusion of oxygen for oxidation of vanadium based alloys under indicated conditions [47, 113].

Alloy	Temperature (°C)	P_{O2} Torr	Oxidation behaviour	Oxide formed	Rate constant $mg^2mm^{-4}h^{-1}$	D m^2/h	Q_D KJ/mol
V	500	7.6	parabolic	VO_2	3.67×10^{-7}	5.69×10^{-14}	193.6
V	600	7.6	parabolic	VO_2	7.40×10^{-6}	1.15×10^{-12}	197.8
V	500	760	parabolic	V_2O_5	2.74×10^{-6}	6.30×10^{-13}	164.7
V-4Cr-4Ti	500	160	parabolic	V_2O_5	9.82×10^{-7}	2.25×10^{-13}	178
V-5Cr-5Ti	500	160	parabolic	V_2O_5	7.02×10^{-7}	1.61×10^{-13}	181.7
V-4Cr-4Ti	575	160	parabolic	V_2O_5	1.07×10^{-5}	2.46×10^{-12}	179
V-5Cr-5Ti	575	160	parabolic	V_2O_5	2.90×10^{-6}	6.73×10^{-13}	194
V-6W-1Ti	650	160	parabolic	V_2O_5	9.0×10^{-5}	-	-

2.10 Effect of alloying addition on wear behaviour of vanadium based alloys

Structural materials in a fusion reactor are susceptible to undergo wear, during their service conditions, as the flowing molten metal coolant is expected to induce the wear due to flow induced vibrations. In fast neutron reactor also, the structural materials such as fuel rod and control rod cladding assemblies are reported to undergo "wear" during its service conditions majorly due to the relative motion of the sub-assemblies as well as caused by flow induced vibrations in reactor pool [114, 115]. Thus, tribological properties of the material to be used as structural component are important for its application.

2.10.1 Basic mechanism and modes of wear

Wear is a process that result in progressive removal, deformation and damage of materials due to relative motion between that surface and a contacting substance. Wear of structural materials deteriorates its properties which results in loss of reliability for real time application. Wear is quantified by the term 'wear rate' which is defined as the mass or volume loss of material removed per unit time or sliding distance. Wear rate of materials changes drastically depending on operating conditions and material selections. Hence wear can be controlled by suitably designing the operating conditions and by the selection of proper materials with the wear maps data, which predict the wear mode and wear rate of material under relevant operating conditions. In order to design conditions and select materials based on the wear map, an understanding of wear rate, varieties of wear modes, and wear mechanisms is essential. In general, wear is evaluated by the amount of volume lost and the state of the wear surface. The degree of wear is described by wear rate or specific wear rate. Wear rate is defined as wear volume per unit distance. Specific wear rate is defined as wear volume per unit distance and unit load. There are generally three different representative types of wear volume curves

observed in materials which are shown schematically in Fig. 2.20 [116, 117]. In type 1 curve, wear rate remains constant throughout the process. In type 2, initially high wear rate is observed which attain steady state after some time. This type of wear behaviour is most commonly observed in metals. Type 3 wear is characterized with catastrophic transition from initial wear of low wear rate to wear of a high rate. This type of wear is commonly observed in ceramics.
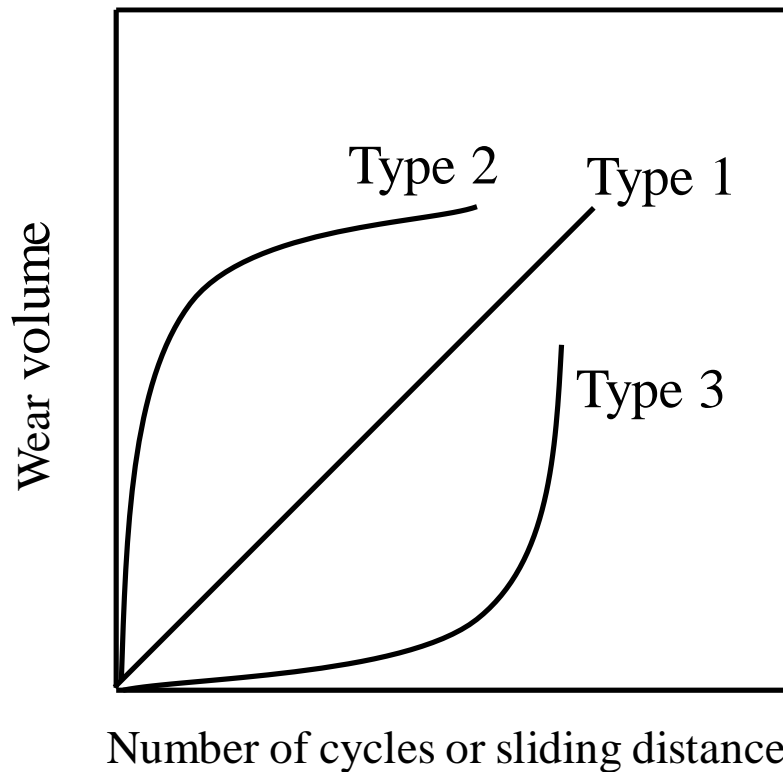
Figure 2.20: Three different types of wear curve observed for materials in repetitive contact.

Wear is normally investigated for different type of contact configurations of solid surfaces. Unidirectional sliding, reciprocative sliding, unidirectional rolling, reciprocal rolling, normal compression are few contact configurations used regularly based on motion. Different geometry configuration like ball on disk, pin on disk are used in practice to test the wear behaviour of materials. Investigations of wear behaviour of different materials reveal four different fundamental wear modes, which are as follows: (i) Adhesive wear, (ii) Abrasive wear, (iii) Fatigue wear, and (iv) Corrosive wear

i. *Adhesive wear*: This mode of wear occurs because of the adhesive bond at the contact points of two alloys having similar chemical composition. Normally, adhesion occurs only when contact surfaces are free from oxide layer, which is usually in vacuum or an inert atmosphere. This mode of wear is due to the transfer of material from one surface to another surface by shearing of solid welded junctions of asperities. It leaves pits, cavities or valley on the surface.

ii. *Abrasive wear*: This type of wear occurs due to plastic contact between hard material and relatively soft material, the harder material penetrates to the softer one. It results in ploughing, wedging and cutting phenomena. In ploughing (also called ridge formation) process, material is displaced at both the sides and forms a groove with or without removal of the material.

iii. *Fatigue wear*: Wear caused by fracture arising from cyclic loading is called Fatigue wear. It results in a series of pits or voids. It usually occurs in rolling or sliding contact bodies such as bearings, roads, etc.

iv. *Corrosion wear*: Corrosive wear occurs when sliding takes place in corrosive or oxidative environment. Corrosive medium led to the formation of tribo-chemical layer and the resultant wear is called corrosive wear. In air, oxygen acts as corrosive medium which led to the formation of mixed oxide tribo-chemical layer. This mode of wear of metals in air is generally called oxidative wear.

2.10.2 Wear behaviour of vanadium alloys

Despite of its attractive combination of strength and density, vanadium and its alloys have been given least importance on the tribological front. One possible reason for the negligence of tribological studies on V based alloys could be the dominance of Ti and Al based systems in wear resist applications. Significant amount of databases on the wear aspects of some of the nonferrous metal/alloys systems, like Al-Si, Ti and Nb [118-124] are available in

open literatures. It has been reported that Al and Ti alloys show wear rate of the order of 10^{-4} mm^3/Nm, when steel ball is used as counter body material [120, 123]. The wear resistance of these alloys has also been well investigated with respect to microstructures [119, 125], morphology of second phase [121], alloying additions [122] and surface treatments. Further, it has been reported that the wear characteristics of the alloys can be tailored by having a suitable combination of these conditions. The work of Garcia et al. [126] is one of the few reports in literature that probed the modifications in wear properties of V-alloys (V-5%Ti alloy) by surface treatment procedures. However, the reported study lacks information on the wear mechanisms that are active in the vanadium and its alloys.

Experimental methodology

3.1   Preamble

In this chapter, experimental details for the preparation of V-4Ti-xTa (x = 0,1,3,7) alloys, their characterization are presented in addition to the equipments, machines and processes used in the synthesis or characterization of the alloys. Four different aspects of synthesized vanadium alloys studied in the present study are shown in Fig 3.1.
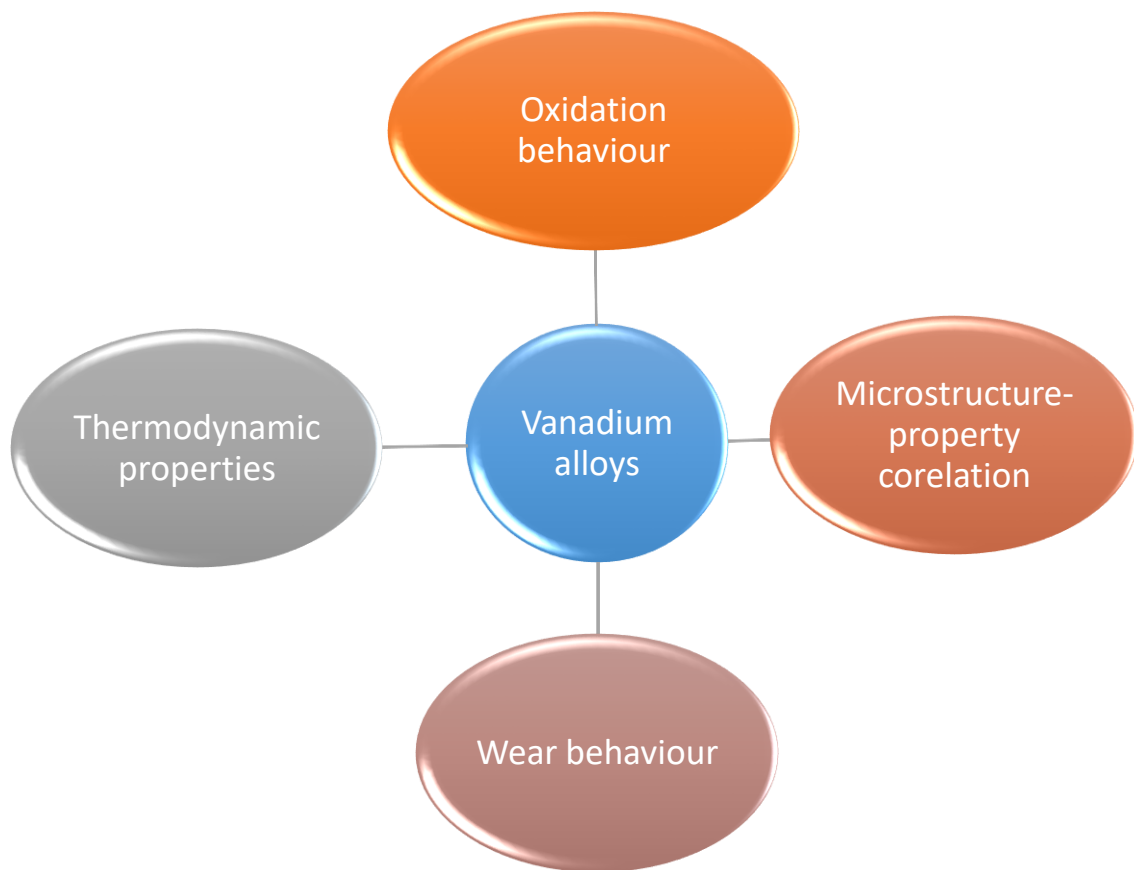
Figure 3.1: Showing schematic representation of the various aspects of the V alloys studied in the present study.

This chapter also describes the experimental methodology adopted to study the thermodynamic properties determination, microstructure-property correlation, oxidation and wear behaviour of the developed V-Ti-Ta alloys. The alloy preparation, fabrication, processing equipment and characterization tools used in above studies has also been described in detail.

3.2   Alloy preparation and characterization

3.2.1   Vacuum arc melting

V, Ta are refractory metals having 1905 °C and 3020 °C as their melting points. Both the metals have high affinity for oxygen and nitrogen. Therefore, in the present study ample precautions were taken to minimize the contamination. For this, firstly, high purity (> 99.8 %), vanadium, titanium (sheet) and tantalum (sheet) were used to prepare V-Ti-Ta alloys. These metals were thoroughly degreased before charging for arc melting. Alloy buttons of V-4Ti-xTa (x = 1, 3, 7 wt.%) alloys were prepared by melting pure metals in a non-consumable vacuum arc furnace. Secondly, prior to melting, the chamber of the furnace was flushed with ultra-pure Ar gas to remove any trace of residual gases in the chamber. In addition, pure Ti was used as getter which was melted several times to ensure removal of residual gases from the chamber. Each specimen was melted several times to achieve desirable chemical homogeneity. The homogeneity of the alloys was confirmed by chemical analysis and typical composition of the alloys are shown in Table 3.1.

3.2.2   Composition and phase analysis

Inductively coupled plasma atomic emission spectroscopy (for substitutional elements) and Inert gas fusion techniques (for interstitial elements) were used to determine the compositional analysis of samples. For the identification of phases XRD technique was used. The details are as follows:

(a) Inductively coupled plasma atomic emission spectroscopy

ICP-AES, an emission spectroscopy, which uses the inductively coupled plasma to produce excited atoms and ions emitting electromagnetic radiation at wavelengths characteristic of a particular element, has been used in the present study. Alloy chemistry and impurity contents were analyzed by inductively coupled plasma (ICP OES JY2000) optical emission spectroscopy. For this purpose, samples of ~0.02 gm were dissolved in 1ml HCl and 1ml HNO_3 mixture and made up by distilled water to 100ml. These solutions were subsequently passed to plasma and the emission spectra were quantified by comparing them with the standards. All the samples were analyzed at least four times for better accuracy.

(b) Inert gas fusion analysis

For the analysis of carbon, oxygen and nitrogen content in the samples inert gas fusion method was used and the analysis was carried out in LECO TC-300 analyzer. In this analyzer, the charge was melted in a graphite crucible and oxygen present in the sample combined with carbon to form CO which subsequently was converted to form CO_2. Oxygen was detected as CO_2 by IR detector and nitrogen by thermal conductivity detector. As refractory metals have high melting points, Tin was used as a flux for lowering the melting temperature during the analysis. The analyzer was consistently calibrated using standard samples after every 4-5 samples. All the samples were analyzed at least four times. Average analysis has been reported in this work with standard deviation mentioned.

(c) X-ray fluorescence (XRF) spectroscopy

Once the standards were made for quantitative chemical analysis of samples XRF were used. The measurements were done using EDXRF (model Innov-X). This system has two beams: of 40 kV and 15 kV. All the samples were analysed five times for better accuracy and to assess homogeneity of the sample. XRF results of the samples were found to be consistent with the ICP data.

Table 3.1: Chemical composition of V-4Ti-xTa (x = 0, 1, 3, 7 wt.%) alloys prepared by vaccum arc melting.

Metal or Alloy	Elements (wt.%)			Impurities (wt. ppm)		
	V	Ti	Ta	C	N	O
V-4Ti	99.90 ± 0.05	3.90 ± 0.05	-	170 ± 6	100 ± 5	210 ± 12
V-4Ti-1Ta	95.20 ± 0.20	3.95 ± 0.05	0.80 ± 0.02	185 ± 5	90 ± 4	195 ± 8
V-4Ti-3Ta	93.25 ± 0.18	4.10 ± 0.20	2.60 ± 0.05	175 ± 5	85 ± 4	190 ± 9
V-4Ti-7Ta	89.40 ± 0.26	3.90 ± 0.10	6.60 ± 0.12	170 ± 4	95 ± 5	220 ± 13

(d)   ***X -Ray diffraction***

Phase identification was carried out by Inel-make x-ray diffraction unit (model MPD) using Cr-Kα (2.290Å) target at current level 25 mA and voltage level 35 kV. Chromium target was used in this study instead of conventional copper targets to eliminate the fluorescence of vanadium in copper radiation. The unit has a curved position sensitive-detector, whereby the diffraction data in complete 2θ range of interest could be recorded simultaneously thereby taking substantially lesser time as compared to the conventional XRD units. The XRD patterns were analyzed with the help of PCPDF data base software.

3.3   Thermodynamic activity determination experiments

Synthesized V-4Ti-xTa alloys were subjected to partial vapor pressure measurements of elements for thermodynamic investigations. The measurements were carried out with an indigenously made Knudsen effusion mass spectrometer system (KEMS). Detailed description of KEMS theory, principle of operation and technique is given in Appendix-2. The KEMS system consists of two chambers, one containing the Knudsen cell furnace assembly and the other compartment having the quadruple mass spectrometer (QMS). A vacuum-isolation metallic valve is provided in between the two chambers to connect or disconnect the ion source to the Knudsen cell chamber as and when required. This metallic valve is extremely important for the measurements of activities of various species. In practice, the valve does not lead to decrease of the sensitivity due to the slight increase of the distance between the ion source and the Knudsen cell. Its principal, advantage is that it permits a rapid change of the material in the Knudsen cell while keeping the ion source running under high vacuum. By this means, the day-to-day fluctuations of the pressure calibration constant were typically maintained below 5 %.

Design of the equipment used in the present study is based on the KEMS described by Darwin et al. [127]. The detailed description of the machine along with the figures can be found

in Appendix-2 and in the reference [127]. Temperatures were measured by sighting the infrared pyrometer onto a blackbody hole drilled at the bottom of the Knudsen cell assembly. Pyrometer was calibrated by melting high pure metals Cu, Ag, Ni, Ti etc. The QMS in the machine was Hiden Analytical (UK) make where ions were generated by electron impact with typical energy of 70 eV.

3.4   Recrystallization and structure-property correlation experiments

As-cast samples were deformed by cold rolling and subsequently subjected to various heat treatments (time and temperature) for the optimization of recrystallization parameters. Subsequently all the samples were subjected to microstructural characterization, phase analysis and bulk texture measurements. Mechanical properties of the alloys were characterized using hardness and yield strength measurements. The details of all the sample preparation processes and characterizations for these experiments are given below:

3.4.1   Deformation

As cast samples of the alloys having typical thickness of 10 mm were cold rolled upto 70 % at room temperature to break the as-cast structure. Rolling direction was strictly maintained along the single direction. The rolling operation was carried out in several passes to achieve a final sheet thickness of 3 mm. Mid-thickness sections of the deformed samples were taken for any further processing or characterization to avoid surface effects.

3.4.2   Recrystallization experiments

In order to determine optimum conditions (time & temperature) of recrystallization, cold rolled samples were subjected to various heat treatments starting from 1000 °C to 1300 °C for different soaking time periods varying from 1 hr to 3 hrs. The samples were wrapped in

tantalum foils and heat treated under high purity argon atmosphere to avoid oxidation during annealing. Temperature of the furnace was maintained within ± 1 °C.

3.4.3   Microstructural Characterization

Microstructures of deformed (cold rolled) and annealed samples were characterized using: (a) optical microscopy (b) scanning electron microscopy (SEM) (c) Electron back scattered diffraction (EBSD) (d) transmission electron microscopy (TEM) coupled with precession electron diffraction (PED) techniques.

(a)   *Optical microscopy*

For optical metallography, the specimens were mounted in bakelite and ground using successive grades of emery papers. They were mirror polished and microstructures were revealed using a solution containing KOH, $K_3Fe(CN)_6$, H_2O in the ratio of 1:1:8. Optical microstructural investigations were carried out on Leica microscope.

(b)   *Electron back scattered diffraction*

Samples were prepared by standard metallographic technique followed by electro polishing to remove the superficial deformed layer (to improve the quality of Kikuchi Pattern). Electro-polishing was done at 25 °C with an operating voltage of 25 V in an electrolyte of 90 % acetic acid and 10 % perchloric acid for about 30 seconds for each sample. The polishing was performed using a commercial electro-polisher LectroPol®. A SEM of Carl Zeiss Auriga microscope) attached with Oxford NORDLYSEBSD system and TSL- OIM systems was used for micro-texture study. Measurements were performed on transversal sections of the rolled and annealed specimens in the rolling direction-transverse direction (RD-TD) plane. A tilt of 70° was used for the sample with respect to electron beam axis to capture Kikuchi Patterns by a CCD camera. A working distance of 7 mm was employed for the recording of the EBSD data. For the analysis of the EBSD data, grain identification was done using a grain tolerance angle

of 5°. The plastic strains inside the deformed grains was indirectly correlated with grain orientation spread (GOS). GOS for each grain was estimated by finding out the misorientation between all of the neighbouring pixels of the grain. The mean GOS for the selected area of the EBSD map was then estimated by taking either area based average or number based average of individual grains' GOS values. For the purposes of analysis, all the raw measured data sets were subjected to a clean-up process based on the confidence index (CI). Only those data points which exceeded a CI cut-off value of 0.1 were included in the analysis.

(c) *Scanning electron microscopy*

Samples prepared for optical microscopy or EBSD were directly used for SEM examination using the secondary electron (SE) and In-lens modes of imaging. A field emission scanning electron microscope (FE-SEM-Zeiss) has been used for this purpose.

(d) *TEM-PED-EDS characterization*

In order to find the compositions and crystal structures of the precipitates, selected samples were examined under transmission electron microscopy (TEM). For TEM, 3 mm disk samples were jet thinned in an electrolyte consisting a solution of 10 % perchloric acid and 90 % acetic acid and thinning was carried out at 25V, 25 °C. TEM investigations were performed in JEOL 3010 transmission electron microscopes. Composition analyses of the precipitates and the matrix phases were carried out using Energy Dispersive Spectroscopy (EDS) 3010 in STEM (scanning transmission electron microscopy) mode. As the EDS results are more prone to errors for quantitative analysis of low Z elements, like C, O N, the relative concentrations of Ti were estimated without considering low Z elements from the EDS profiles. Nano-Megas Precision electron diffraction (PED) attached to JEOL 3010 TEM was used to determined orientation of the precipitates with respect to the matrix phase. The major advantage of PED over EBSD is that in PED it is possible to perform orientation mapping on those particles which are even smaller than 100 nm.

3.4.4 Phase identification using Synchrotron X -Ray diffraction

Synchrotron XRD measurements on selected samples were carried to determine the precipitate phase using angle-dispersive X-ray diffraction (ADXRD), beamline BL-12 at the Indian synchrotron source INDUS-2 (2.5 GeV). The synchrotron radiation of ~ 17.298 keV energy (λ = 0.7167 A°) was selected with the help of double-crystal monochromator setup to obtain XRD peak profiles in the angular range (2θ) of 18° to 50°. The energy (17.298 keV) was accurately calibrated using the XRD pattern of LaB6 NIST standard.

3.4.5 Bulk texture analysis using X -Ray diffraction

The development of macro-texture on the rolled and annealed specimens was investigated using X-ray Diffractometer in a Bruker^{TM} D8 Discover X-ray diffraction unit with Cu Kα radiation (50 kV, 1000 mA). Three pole figures, {011}, {020} and {121}, were determined. Subsequently, orientation distribution function (ODFs) and volume fraction of the specific texture in samples were calculated using the MTEX toolbox. It should be noted that sample symmetry was taken as orthorhombic and crystal symmetry as cubic for analysis of ODF plots.

3.4.6 Mechanical properties evaluation

Mechanical properties of deformed (cold rolled) and annealed samples were characterized using following techniques: (a) Macro-hardness testing and (b) Compression testing. The details of all characterizations for these experiments are given below:

(a) Macro hardness Test

Deformed and annealed samples were subjected to macro-hardness measurements using a diamond pyramidal indenter, with Vickers Hardness Tester Model HPO-250 at a load of 200 gm for 15 sec duration. Before measuring hardness, nearly ten hardness trails were carried out on standard samples to calibrate the hardness of the machine.

(b)   *Compression testing*

Cylindrical specimens were fabricated from 1300 °C recrystallized samples V-4Ti-xTa alloy for compression test. The compression tests were performed using cylindrical specimens of 2 mm diameter with L/D = 1.5 (L = length and D = diameter) at a nominal strain rate of 5 x 10^{-4} s^{-1}. The compression tests were performed in a Deben (UK) make portable screw driven miniature test frame of 5 kN capacity, with a versatile load resolution in the range 10 – 100 mN under nominal vacuum of ~10^{-2} mbar. For accommodating the miniature sample, a special compression test fixture made up of high modulus Ni-Cr alloy was fabricated. The upper and lower loading platen surfaces of the fixture were polished with 0.1 µm diamond grit to reduce friction during the compression test. The load and crosshead displacement were monitored and recorded during the test. Measured data were monitored and recorded electronically. The 0.2 % offset yield stress was derived from stress- strain plots. The flow stress was fitted with a new phenomenological equation based on Voce adaptation of Holloman equation or VaH (that provides a power law construct to the well-known Voce relation between flow stress and strain) to predict the saturation stress under compression and the nature of strain hardening [128].

3.5   Oxidation experiments

Oxidation studies of V metal and alloys were carried out in non-isothermal as well as in isothermal conditions. The phase analyses of oxidized samples were carried out using grazing incidence x-ray diffraction (GIXRD) technique. The morphology of the oxidized surfaces was characterized by scanning electron microscopy (SEM) coupled with energy-dispersive spectroscopy (EDS).

3.5.1   Non isothermal oxidation experiment (Thermal analysis)

To study initiation of oxidation and oxidation behaviour of pure V, Ti and Ta, simultaneous thermo-gravimetric differential thermal analysis (TG-DTA) was used. The pure

metal samples were non-isothermally heated under 100 standard cubic centimetre per minute (sccm) continuous air flow upto 1000 °C at 12.5°/min heating rate in LENSIS make thermal analyser in alumina cup and with alumina as the reference material. Thermo-analyser was calibrated using standard silver and aluminium samples.

3.5.2   Isothermal oxidation experiments (Box type furnace)

Isothermal oxidation experiments were carried out to study long-term oxidation behaviour of the samples. Isothermal oxidation experiments were carried out in a box type air furnace. The temperature accuracy of the furnace was maintained within ± 2 °C. For the isothermal oxidation experiments 10 mm ×10 mm × 3 mm samples were used. Prior to oxidation experiments, weight and surface area of each sample were measured. Samples were kept in the furnace only after attaining the desired temperature. The polished samples were subjected to oxidation at temperatures 250, 300, 500 and 750 °C, for the time periods of 1, 2, 4, 8, 16, 32 and 64 h. After oxidation, specimens were allowed to cool down to room temperature in the ambient air and the weight of the specimens was recorded after each experiment by an electronic weighing balance having an accuracy of 0.001 mg.

3.5.3   Microstructural and phase characterization

The morphologies and compositions of the oxide phase formed on the surfaces of samples were characterized by a scanning electron microscopy (SEM) in back scattered electron mode coupled with energy-dispersive X-ray spectroscopy (EDS) (Oxford, X–Max 80 model). The phase characterization of the surface oxide was carried out using a GIXRD unit with Mo Kα radiation (0.709 A°).

3.6   Wear experiments

Wear experiments were conducted on pure vanadium as well as on it alloys V-4Ti-xTa)

in dry unlubricated condition at room temperature with 60 % relative humidity, using a ball-on-flat reciprocating sliding wear and friction machine (Plint TE 70SLIM Micro-friction, DUCOM, India). The schematic of the wear testing configuration is shown in Fig. 3.2. Hardened Steel ball (AFBMA Grade-10, diameter: 10 mm) was used as a counter body material. Samples were subjected to normal loads of 5, 10 and 15 N with varying sliding frequencies (5 Hz to 15 Hz) keeping an amplitude of 1 mm for 100-minute duration.

3.6.1   Microstructural and phase characterization of wear surfaces

Wear debris were collected on an adhesive tape and analyzed for its phase(s) using X-ray diffraction technique (MoKα, XRD). Wear scars were characterized for surface topography, depth and volume using non-contact 3D optical profilometer (CCIMP3D, Taylor Hobson, UK). Microstructure of wear track regions was also investigated using SEM-EDS (SEM Zeiss EV040). In order to understand the micro-chemistry of wear track regions, electron spot pattern analysis was performed.
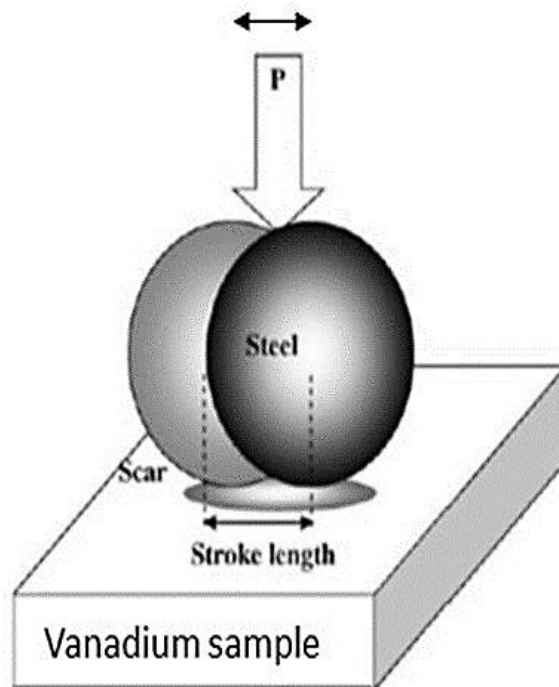
Figure 3.2: Schematic of experimental setup for wear experiments.

Effect of Ta addition on thermodynamic properties of V-Ti-Ta alloys

4.1 Preamble

Structural materials in the fusion reactor will be used at high temperatures under the flowing molten metal coolant. These severe condition impose high temperature phase instability in the materials. Present chapter provides details of the thermodynamic stability of the phases upon addition of Ta in V-4Ti alloy system estimated using Knudsen effusion mass spectrometer system (described in detail in Chapter 3 and Appendix-2). As thermodynamic interaction parameters for ternary V-Ti-Ta system are not available in open literature, it is necessary to experimentally determine the effect of Ta addition on the thermodynamic stabilities of phases in V-Ti-Ta alloys. In this chapter, therefore, in-situ study of vaporization behaviour of V-4Ti-xTa (x = 0,1,3,7 wt.%) alloys using the KEMS technique is presented. Partial vapor pressure and thermodynamic activities of Ti and V in V-4Ti-xTa alloys obtained using Knudsen effusion method are reported and the effect of Ta addition on the activities of Ti and V has been clearly elucidated. Partial free energy and its excess values have been derived. It was observed that the activities of Ti and V decreased with increasing Ta content in V-4Ti-xTa alloy system.

4.2 Experimental observations

4.2.1 Vaporization of pure Ti (s) and pure V (s)

(a) Enthalpy of vaporization

The vaporization of pure titanium (Ti) and vanadium (V) was studied separately to check the reliability of the mass spectrometer - Knudsen cell system and especially of the ion counting

system for the determination of vapor pressures in the temperature range of 1800-2100 K. The results of these investigations are shown in Fig. 4.1 and Fig. 4.2 respectively. Figs 4.1 and 4.2 are plots of natural log of product of the Ti^+ ions intensity and V^+ ions intensity respectively and the temperature T (ln(IT)), which are plotted against the reciprocal temperature in K^{-1} (1/T). The product (IT) is proportional to the respective vapor pressure (either Ti or V) [equations (4.1) - (4.3)].

In the course of the measurement, the temperature of the Knudsen cell was decreased step-by-step between 2100 K and 1800 K. Subsequently, the temperature was raised in the same way. The intensity was noted at each step. It was seen that a given temperature, the points in Fig. 4.1 and Fig. 4.2 coincided in the heating and cooling steps, which indicated that the solid titanium or vanadium were in equilibrium with its vapor during the course of the measurement. The enthalpy of evaporation (ΔH_v), according to the second law method as shown in equation (4.1), was computed from the slope of the graphs shown in Figs 4.1 & 4.2. The enthalpy change of vaporisation was determined using the Clausius–Clapeyron equation

$$\frac{d \ln p_i}{d\left(\frac{1}{T}\right)} = \frac{d \ln(IT)}{d\left(\frac{1}{T}\right)} = -\frac{(\Delta H_v^\circ)_i}{R} \dots\dots\dots\dots\dots\dots\dots(4.1)$$

Where p_i is the partial pressure of species i , T is the temperature in K, R is the universal gas constant and $(\Delta H_v^\circ)_i$ is the enthalpy of vaporisation of species i. (IT) indicates the multiplication of intensity of a ion and temperature.

A value of $(\Delta H^\circ_v)_{Ti}$ at 1860 K = (- 453.19 ± 3.47) kJ/mol and $(\Delta H^\circ_v)_V$ at 2010 K = (- 501.04 ± 1.04) kJ/mol was obtained for the heat of evaporation at the mean temperature of the measurements. The values determined in the present study are in excellent agreement with the values of 455 kJ/mol and 500 kJ/mol for V and Ti respectively as reported in the literature [129]. Further, $(\Delta H^\circ_v)_{Ti}$ and $(\Delta H^\circ_v)_V$ at 298 K were determined and found to be - 471 kJ/mol

74

and - 516 kJ/mol respectively which are again in excellent agreement with the literature values [129, 130].
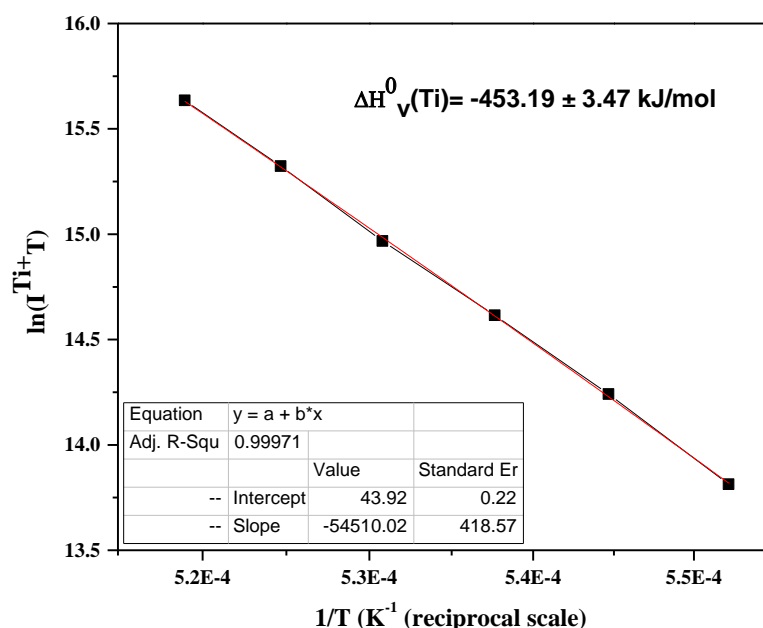
Figure 4.1: Logarithm plot between the product of Ti⁺ ion intensity and temperature and reciprocal of temperature determined by vaporizing titanium in KEMS. The slope of the plot on multiplying with gas constant results in the enthalpy of vaporisation of titanium.
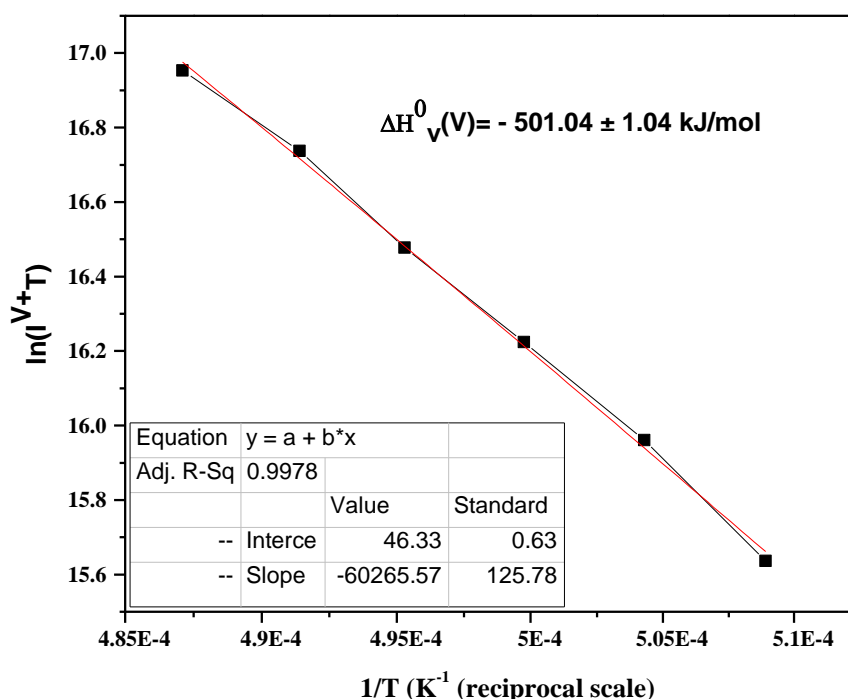
Figure 4.2: Logarithm of (V⁺ ion intensity × temperature) vs reciprocal of temperature determined upon vaporizing pure vanadium. The slope of the plot on multiplying with gas constant provides an estimate of the enthalpy of vaporisations of vanadium.

(b)   Pressure calibration with pure Ti(s) and pure V(s)

The measured ion intensities (Ti$^+$ and V$^+$) in QMS were converted into partial pressures by means of the standard mass spectrometric relation:

$$p_i = \frac{kI_iT}{\sigma_i A_b^i} \dots\dots\dots\dots\dots\dots\dots\dots\dots\dots\dots\dots\dots\dots\dots\dots\dots\dots(4.2)$$

where T is the temperature; k is the general pressure calibration constant; p_i, σ_i and A_b^i are the partial pressure, the ionization cross section and isotopic abundance of species i respectively; and I_i is the ion intensity of species i.

The pressure calibration constant for species i ($k_i = k/\sigma_i$) was determined by means of experiments on pure i; both before and after the experiments with the actual alloys. For the current study, titanium (99.9 % pure) was taken to be pure i. The calibration results with titanium are described in the next section of this chapter.

The mean value of k_i calculated from the two runs was used in calculating the partial pressures over the alloy samples. Because the calibration procedure was always performed with pure Ti, the vapor pressures over the alloy samples can be expressed as follows

$$p_{Ti} = k_{Ti} I_{Ti}^+ T \dots\dots\dots\dots\dots\dots\dots\dots\dots\dots\dots\dots\dots\dots\dots\dots(4.3)$$

$$p_V = k_V I_V^+ T \dots\dots\dots\dots\dots\dots\dots\dots\dots\dots\dots\dots\dots\dots\dots\dots(4.4)$$

P_{Ti} and P_V are the partial vapor pressure of Ti and V respectively. k_{Ti} and k_V denotes the pressure calibration constant for Ti and V respectively.

From equations 4.3- 4.4, and rearranging, the partial pressure of V in terms of Ti becomes

$$p_V = k_{Ti} \frac{\sigma Ti}{\sigma V} \frac{A_b^{Ti}}{A_b^V} I_V^+ T \dots\dots\dots\dots\dots\dots\dots\dots\dots\dots\dots\dots\dots\dots\dots\dots(4.5)$$

where $\sigma_{Ti} = 4.6{\times}10^{-16}\,\text{cm}^2$, $\sigma_V = 6.4{\times}10^{-16}$ [131] and isotopic abundance of Ti is $A_b^{Ti} = 0.73$ and isotopic abundance of V is $A_b^{V} = 0.99$.

In order to further check the reliability, pressure calibration constant for pure Ti was determined using equation 4.3 and the same pressure calibration constant was used to determine the vapor pressure of pure vanadium using equation 4.5. The vapor pressure values of pure vanadium so obtained are in excellent agreement with the values reported in the literature [129].

4.2.2 Vaporization of V-4Ti-xTa (x = 0, 1, 3, 7) alloys

V-4Ti-xTa (x = 0, 1, 3, 7) alloys were heated in the temperature range of 1960-2120 K. In the course of the measurement, the temperature of the Knudsen cell was decreased step-by-step between 2120 K and 1960 K. Subsequently, the temperature was raised in a similar manner. The intensity of Ti$^+$ ions were recorded at each step in the given temperature range. The measured ion intensities were converted into partial pressures by means of the standard mass spectrometric procedure using equation 4.2 and straight lines were fitted by the least squares method to plots of the natural logarithm of pressure versus the reciprocal of temperature. Fig. 4.3 and Fig. 4.4 indicate large dynamic range and high precision of the vapor pressure measurements of Ti and V in V-Ti-Ta alloys respectively by KEMS. The temperature dependence of vapor pressure is also listed in Table 4.1. It could be observed form Table 4.1 that the vapor pressure of Ti at 2040 K decreased from 6.93 x 10^{-7} atm to 2.06 x 10^{-7} atm as Ta content increases from 0 to 7 wt.% in V-4Ti alloys. Similarly vapor pressure of vanadium was also found to decrease from 4.60 x 10^{-6} to 1.51 x 10^{-6} atm under identical conditions. It can, therefore, be inferred that as Ta content in V-4Ti alloys increases, the partial vapor pressures of both Ti and V decrease substantially.
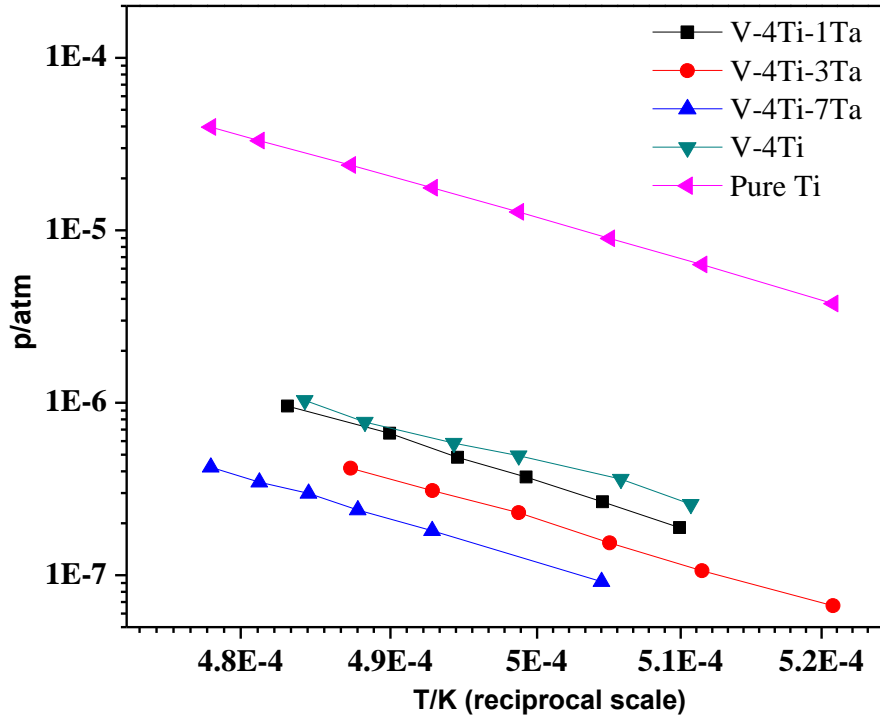
Figure 4.3: Equilibrium partial vapor pressures (p) of Ti over the V-4Ti-xTa alloys as well as over pure Ti as a function of temperature (T). (The pressure in logarithmic, the temperature in reciprocal scaling).
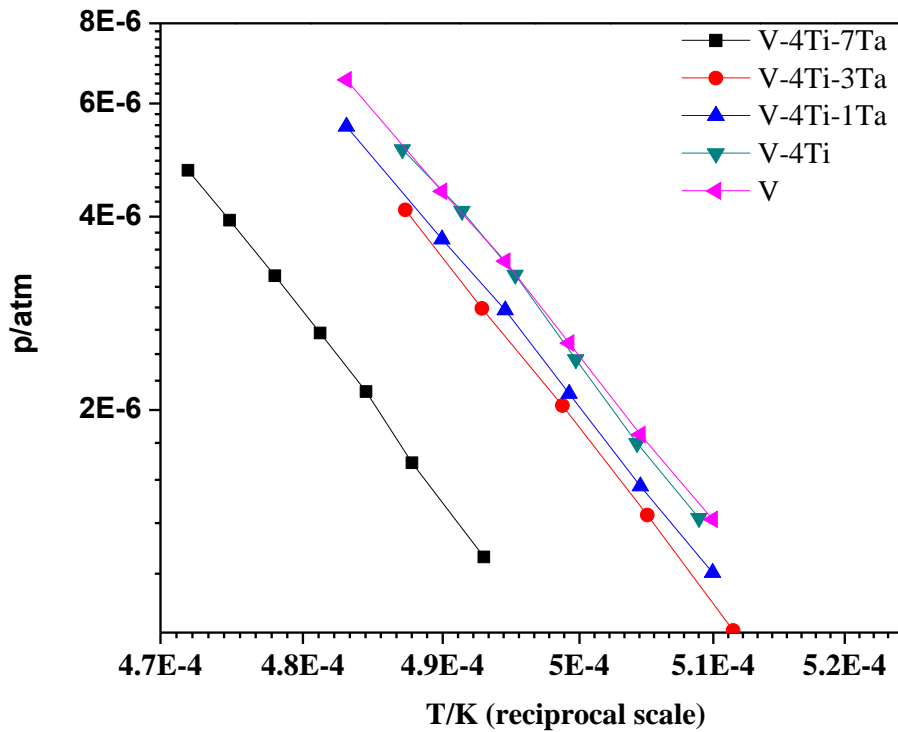
Figure 4.4: Equilibrium partial vapor pressures (p) of Vanadium over the V-4Ti-xTa alloys as well as over pure V as a function of temperature (T). (The pressure in logarithmic and temperature in reciprocal scaling).

From the vapor pressures, thermodynamic functions like chemical activities (a_i), partial molar free energies of mixing $\Delta \overline{G}_{Ti}$ and excess partial molar free energies $\Delta \overline{G}_{Ti}^{XS}$, enthalpy of mixing ΔH_i^{mix} were evaluated using the following equations:

$$a_i = \frac{p_i}{p_i^o} \quad\text{..(4.6)}$$

$$\Delta \overline{G}_i = RT \ln a_i \quad\text{...(4.7)}$$

$$\Delta \overline{G}_i^{XS} = \Delta \overline{G}_i - RT \ln x_i \quad\text{...............................(4.8)}$$

$$\ln a_i = \frac{\Delta H_i^{mix}}{RT} - \frac{\Delta S_i^{mix}}{R} \quad\text{.............................(4.9)}$$

where a_i denotes the activity of component i, and p_i and p_i^o denote the equilibrium vapor pressures of i over the alloy and the pure substance, respectively, x_i is the molar fraction of i in the alloy and R is the universal gas constant (8.314 J/mol K). $\Delta \overline{G}_i$ and $\Delta \overline{G}_i^{XS}$ shown in equation 4.7 and 4.8 are the partial and excess partial molar free energy of mixing component i. ΔH_i^{mix} and ΔS_i^{mix} shown in equation 4.9 are the enthalpy and entropy of mixing of component i respectively.

The chemical activities of Ti and V calculated using equation 4.6 are shown in Fig 4.5. The temperature dependence of activity in the form of lna=A/T+B is listed in Table 4.2. Activity and activity coefficient at mean temperature of measurement (2040 K) are also listed in Table 4.2. It can be clearly observed from Table 4.2 that activities of Ti and V decrease as Ta content increases from 0 to 7 wt.% in V-4Ti-xTa alloys.
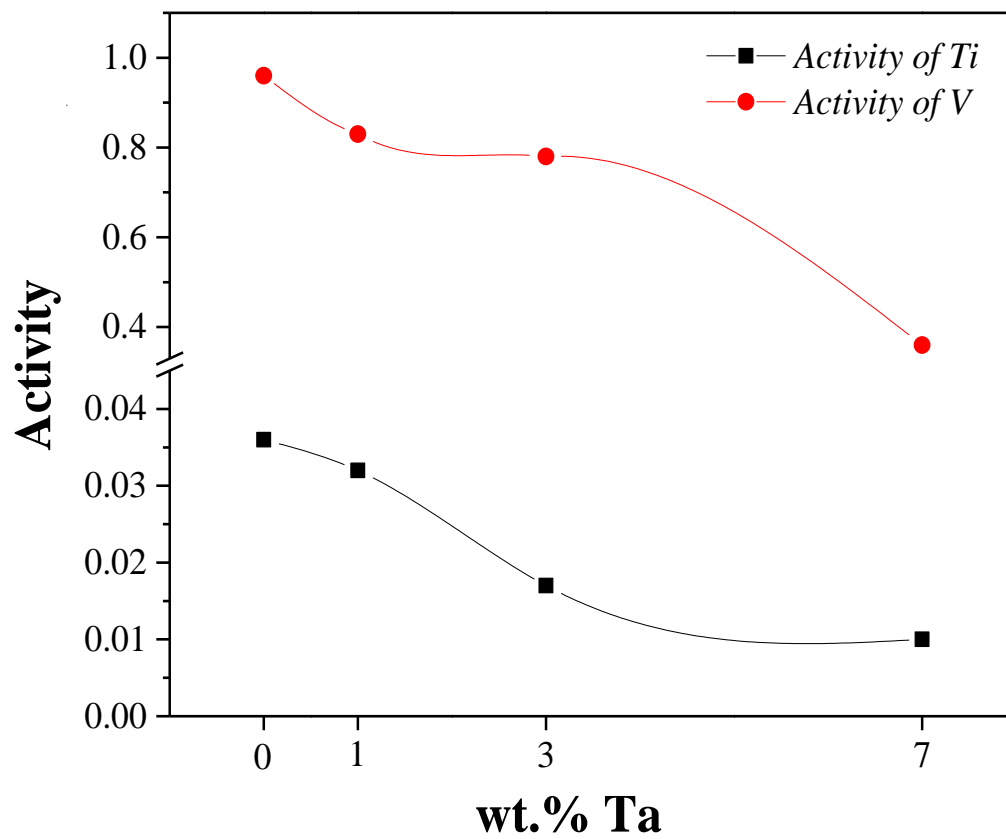
Figure 4.5: The mean activities of Ti and V, as a function of composition at 2040 K, showing decrease in activity as Ta content in V-4Ti-xTa alloy increases.

Table 4.1: Partial vapor pressure curve of Ti and V in V-4Ti-xTa alloys.

Alloy	Vapor pressure curve of Ti and V (P in atm, T in K)	Temperature range (K)	Vapor pressure of Ti at 2040 K (atm)	Vapor pressure of V at 2040 K (atm)
V-4Ti	$LogP_{Ti}$ = -(2.15 ± 0.095) 10^4/T+ (4.38 ± 0.46)	1958-2065	6.93×10^{-7}	4.60×10^{-6}
	$LogP_V$= -(2.68± 0.055) 10^4/T+ (7.80 ± 0.28)			
V-4Ti-1Ta	$LogP_{Ti}$ = -(2.64± 0.043) 10^4/T+ (6.754 ± 0.21)	1961-2070	6.50×10^{-7}	3.53×10^{-6}
	$LogP_V$= -(2.60± 0.03) 10^4/T+ (7.32 ± 0.12)			
V-4Ti-3Ta	$LogP_{Ti}$= -(2.41± 0.043) 10^4/T+ (5.38 ± 0.21)	1920-2052	3.68×10^{-7}	3.38×10^{-6}
	$LogP_V$= -(2.66± 0.02) 10^4/T+ (7.57 ± 0.09)			
V-4Ti-7Ta	$LogP_{Ti}$= -(3.00± 0.21) 10^4/T+ (8.02 ± 1.0)	2050-2120	2.06×10^{-7}	1.51×10^{-6}
	$LogP_V$ = -(2.74± 0.01) 10^4/T+ (7.61 ± 0.06)			

Table 4.2: Chemical activity and activity coefficient of Ti and V in V-4Ti-xTa alloys.

Alloy	Activity curve of Ti and V (T in K)	Temperature range (K)	Activity of Ti at 2040 K	Activity coefficient of Ti at 2040 K	Activity of V at 2040 K	Activity coefficient of V at 2040 K
V-4Ti	$Loga_{Ti}= +(0.40)\ 10^4/T-3.38$ $Loga_V = -(0.036)\ 10^4/T+0.16$	1958-2065	0.036	0.92	0.96	1
V-4Ti-1Ta	$Loga_{Ti} = -(0.24)\ 10^4/T-0.31$ $Loga_V = -(0.039)\ 10^4/T+0.11$	1961-2070	0.032	0.75	0.83	0.87
V-4Ti-3Ta	$Loga_{Ti} = -(0.25)\ 10^4/T-0.54$ $Loga_V = -(0.051)\ 10^4/T+0.15$	1920-2052	0.017	0.38	0.78	0.82
V-4Ti-7Ta	$Loga_{Ti} = -(0.40)\ 10^4/T-0.028$ $Loga_V = -(0.15)\ 10^4/T+0.29$	2050-2120	0.010	0.22	0.36	0.38

4.3 Discussion

As it can be derived from Figs. 4.3 and 4.4 and Table 4.2, vapor pressure of Ti was two order higher than the vapor pressure of pure vanadium in the investigated temperature range. Inspite of inherent higher vapor pressure, in V-4Ti alloy, Ti exhibits one order lower vapor pressure than vapor pressure of vanadium. This could be attributed to relatively smaller content of Ti (3.93 %) in V-4Ti alloy as compared to vanadium (96.07 %). This observation clearly indicates that the vapor pressures over the V-4Ti alloy depend on the pressures of the pure metal components as well as on their concentrations in the alloy.

The chemical activities shown in Table 4.2 elucidate the influence of the concentrations on the partial pressures of the components in the alloy. In V-4Ti alloy, activities of V and Ti were found to follow ideal solution behaviour and activities were equal to corresponding atomic fractions of the components of 0.96, 0.036. Effect of Ta addition on the activities of V and Ti could be seen from Fig. 4.5 and Table 4.2. It was found that the activity of Ti decreased from 0.036 to 0.010 as Ta content increased from 0 to 7 wt.% in V-4Ti-xTa alloys. Activity of vanadium was also found to decrease from 0.96 to 0.36 for similar variation of Ta content. So it is obvious that Ta addition decreases the activities of both V and Ti substantially and found to exhibit negative deviation from the ideal solid solution behaviour. For V-xTi alloy ($0.1 < x < 0.9$), Rolinski et al. [132] have reported that the activity of titanium could be expressed as $RTlna_{Ti} = RT\ lnN_{Ti} + N_V^2 (1.82 \pm 0.13)$ kcal per g-atom (a_x: activity of x, N_x: mole fraction of x). For $0.1 < Ti < 0.9$, the activity of Ti has shown a slight positive deviation from ideality. In our study, we observe that the activity of Ti in V-4Ti behaves ideally. The slight deviation from ideal behaviour apparently occurs for higher atom% of Ti in the alloy [132].

In binary V-Ta phase diagram (Fig 4.6), it can be seen that V-Ta alloy system form a continuous bcc solid solution at temperatures higher than 1583 K. A clustering tendency in V-Ta system could be seen at temperature lower than 1583 K till room temperature, however it may be

noticed from V-Ta binary phase diagram that clustering forms only at Ta > 26 wt.% (Ta > 9 atom%). At lower composition lesser than 26 wt.% Ta, V-Ta are completely soluble even at room temperature. Even assessed ternary phase diagram of V-Ti-Ta system by Enamoto et al. at also indicate the presence of two phase region (β-Ti, V, Ta) + (V_2Ta) at 873-1473 K temperature [71] (Fig. 4.7). It could be observed from phase diagram that two phase region contracts with the increase of the temperature from 873-1473 K. It could also be noticed that even at 873 K, V-4Ti-xTa system exhibit single phase region in the vanadium corner upto 10 atom% Ta [71].

In the present investigations, it was observed that activity of V exhibit negative deviation on addition of Ta in V-4Ti-xTa alloys and no phase separation tendency was observed. Microscopic and XRD investigation presented in chapter 5 also did not indicated any V_2Ta laves phase formation. It may be worth to note that in all the activity measurements in the present study were carried out in the temperature range of 1950 - 2120 K, which is a single phase region. In addition, the compositions of V-4Ti-xTa alloys of the present investigation have Ta content in the range of 0.25 atom% (1 wt.%) to 2 atom% (7 wt.%) maximum, which is also a continuous solid solution region at all the temperatures. Hence, the negative deviation observed for activity of V on account of Ta addition in the present investigation are in agreement with the theoretically assessed V–Ti-Ta phase diagram available in the literature [71].
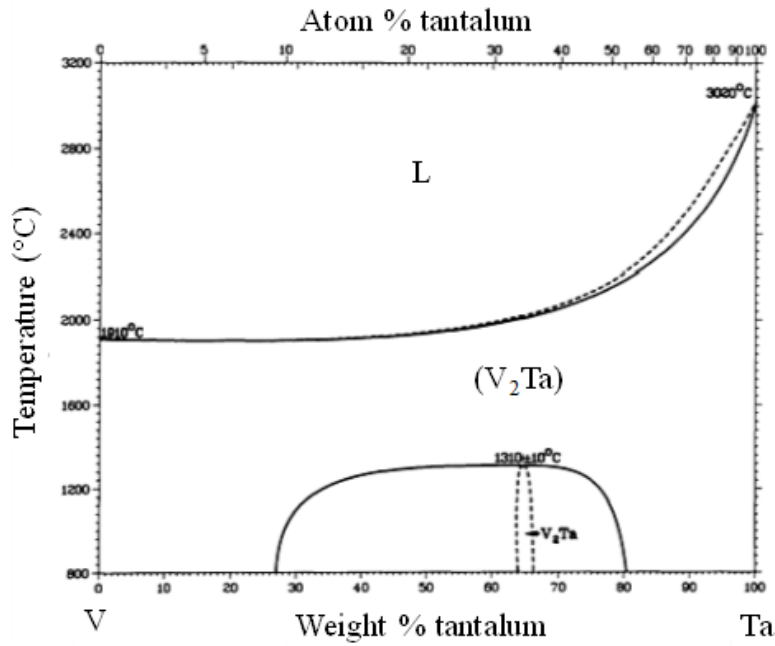
Figure 4.6: Binary phase diagram of V-Ta system showing the two phase region for > 10 atom% Ta [69].
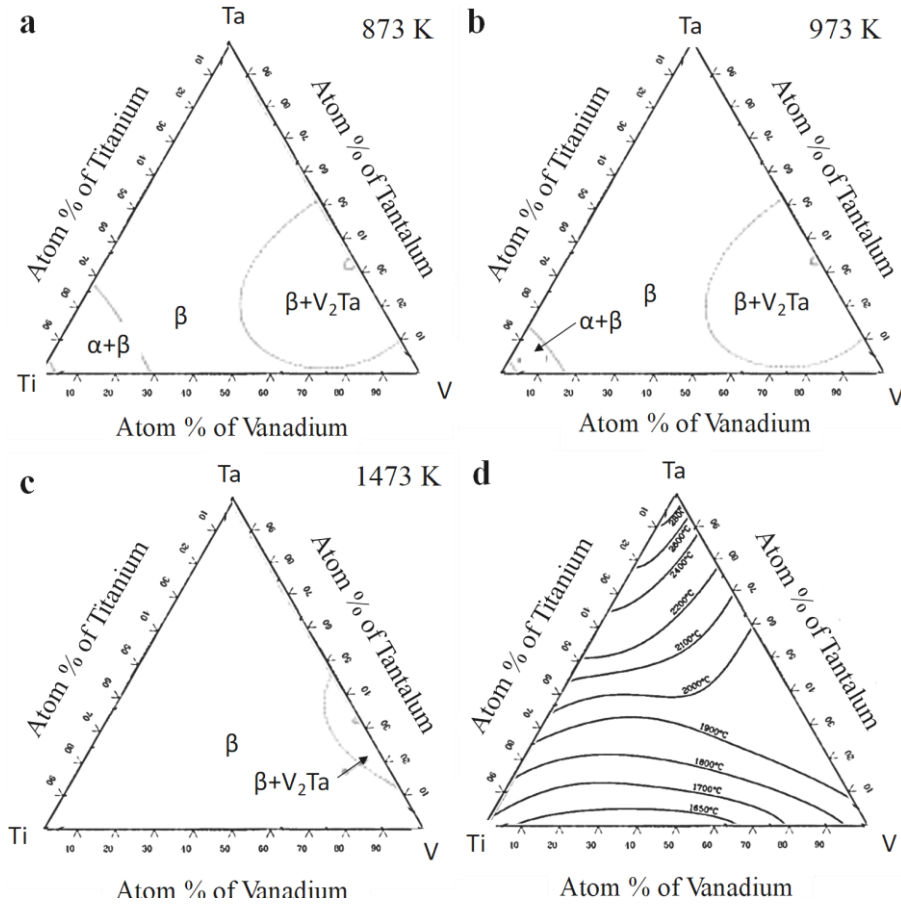
Figure 4.7 (a-c): Assessed Ta-Ti-V phase diagram isothermal sections at (a) 873 K, (b) 973 K, (c) 1473 K, and (d) assessed Ta-Ta-V solidus contours (liquidus data are not available) [71].

Table 4.3: Partial free energies of mixing of Ti and V in V-4Ti-xTa alloys.

Alloy	Partial free energy of mixing curve of Ti and V ($\Delta \overline{G}_{Ti}$ and $\Delta \overline{G}_{V}$ (J/mol))	Temperature range (K)	$\Delta \overline{G}_{Ti}$ at 2040 K (kJ/mol)	$\Delta \overline{G}_{V}$ at 2040 K (kJ/mol)
V-4Ti	$\Delta \overline{G}_{Ti} = 7.66 \times 10^4 - 64.71T$ $\Delta \overline{G}_{V} = -0.69 \times 10^4 + 3.06T$	1958-2065	-55.4	-0.56
V-4Ti-1Ta	$\Delta \overline{G}_{Ti} = -4.59 \times 10^4 - 5.93T$ $\Delta \overline{G}_{V} = -0.76 \times 10^4 + 2.10T$	1961-2070	-58	-3.31
V-4Ti-3Ta	$\Delta \overline{G}_{Ti} = -4.78 \times 10^4 - 10.33T$ $\Delta \overline{G}_{V} = -0.95 \times 10^4 + 2.87T$	1920-2052	-68.87	-3.64
V-4Ti-7Ta	$\Delta \overline{G}_{Ti} = -7.66 \times 10^4 - 0.53T$ $\Delta \overline{G}_{V} = -2.87 \times 10^4 + 5.55T$	2050-2120	-77.68	-17.37

Table 4.4: Excess partial free energy of Ti ($\Delta \overline{G}_{Ti}^{XS}$) and V ($\Delta \overline{G}_{V}^{XS}$) in V-4Ti-xTa alloys.

Alloy	Excess partial free energy of mixing curve of Ti and V ($\Delta \overline{G}_{Ti}$ and $\Delta \overline{G}_{V}$ (J/mol)	Temperature range (K)	$\Delta \overline{G}_{Ti}^{XS}$ at 2040 K (kJ/mol)	$\Delta \overline{G}_{V}^{XS}$ at 2040 K (kJ/mol)
V-4Ti	$\Delta \overline{G}_{Ti}^{XS} = 7.66 \times 10^4 - 56.96T$ $\Delta \overline{G}_{V}^{XS} = -0.69 \times 10^4 + 3.39T$	1958-2065	-39.6	-0.015
V-4Ti-1Ta	$\Delta \overline{G}_{Ti}^{XS} = -4.59 \times 10^4 + 1.24T$ $\Delta \overline{G}_{V}^{XS} = -0.76 \times 10^4 + 2.48T$	1961-2070	-43.37	-2.54
V-4Ti-3Ta	$\Delta \overline{G}_{Ti}^{XS} = -4.78 \times 10^4 - 3.56T$ $\Delta \overline{G}_{V}^{XS} = -0.95 \times 10^4 + 3.31T$	1920-2052	-55.06	-2.74
V-4Ti-7Ta	$\Delta \overline{G}_{Ti}^{XS} = -7.66 \times 10^4 + 6.39T$ $\Delta \overline{G}_{V}^{XS} = -2.87 \times 10^4 + 6.09T$	2050-2120	-63.56	-16.27

Partial enthalpy of mixing ΔH_i^{mix} was calculated using equation 4.9 and Table 4.2. It can be observed that in the case of binary V-4Ti alloy, the enthalpy of mixing is positive (75 kJ/ mol). However, with increasing Ta content in V-4Ti, the enthalpy of mixing became more and more negative. It was also observed that log (a) vs 1/T plots for V and Ti are nearly straight lines over the wide temperature ranges covered, which means that the partial and excess enthalpies of formation are independent of temperature within this range.

The concentration dependence of thermodynamic activities of V-Ti-Ta investigated in the present work shows that the energetic in the ternary alloys are influenced by the strong Ti-Ta and V-Ta bond energies leading to negative deviations from the ideal behaviour. The interactions between the Ta-Ti and Ta-V seem to be stronger as compared to those between V-Ti, which leads to large negative deviation from Raoultian behaviour.

Partial free energies and excess partial free energy of mixing of Ti and V were calculated using equations 4.7 and 4.8 respectively which are shown in Fig. 4.8 and derived partial and excess free energy functions are shown in Tables 4.3 and 4.4 respectively. It can be observed that partial free energy of mixing of Ti becomes increasingly more negative from -55 kJ/mol to -77 kJ/mol as Ta content increases from 0 to 7 wt.%. It was also observed that partial free energy of mixing for vanadium was negative but magnitude of the values was lesser compared to titanium values. Similarly, partial excess free energies (Table 4.4) values for Ti and V becomes increasingly more negative as Ta content in V-Ti-Ta alloys increases. The partial excess free energies describe the deviation of the alloy from a regular solution. It could be seen from the Table 4.4 that deviation for V is smaller than for titanium. As the partial free energy and its excess value becomes increasingly negative with addition of Ta, it is clear that V-4Ti becomes thermodynamically more stable with addition of Ta.
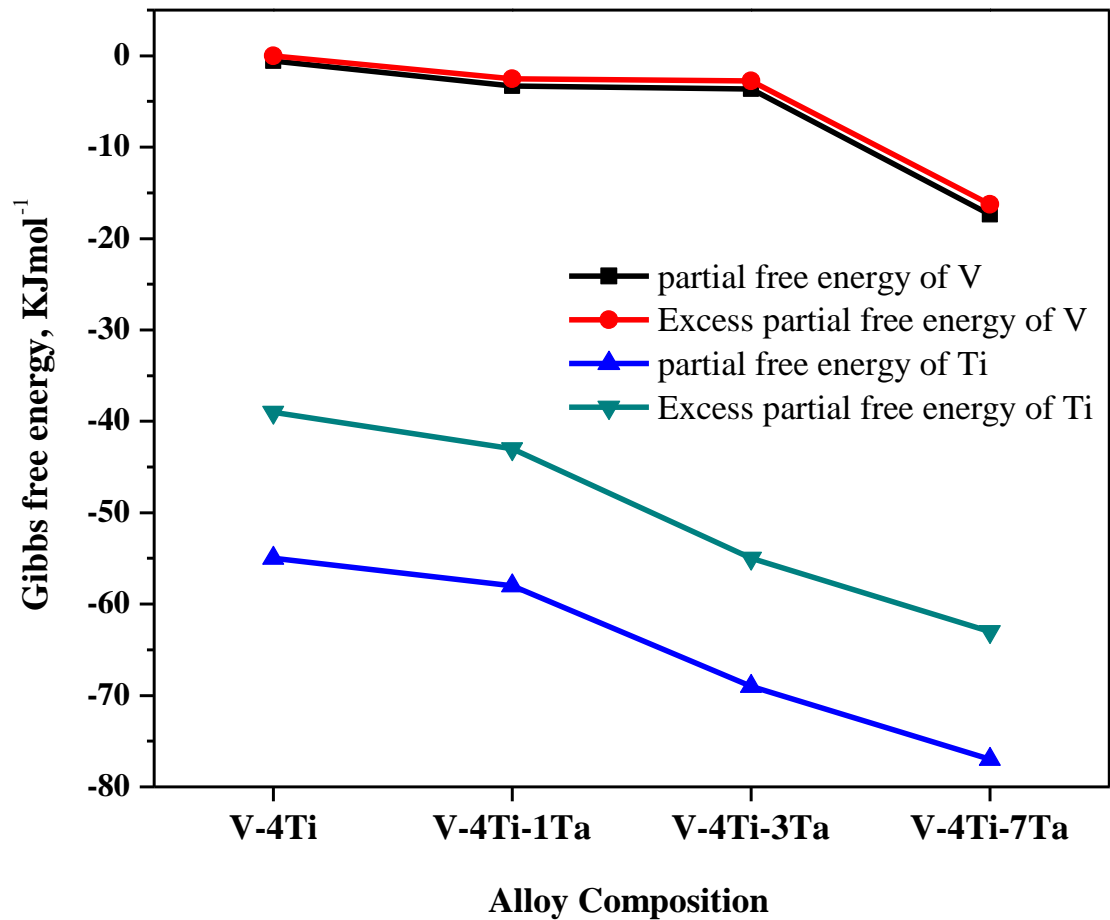
Figure 4.8: The partial and excess free energy of mixing of Ti and V in V-4Ti-xTa alloys as a function of composition at mean temperature 2040 K.

It was found that partial free energy and excess free energy of the alloy becomes increasingly negative on the addition of Ta in V-4Ti alloys, which indicates higher thermodynamic stability of V-4Ti-xTa alloys. These higher stable alloys would provide the high temperature phase stability during in-service operation under higher energy neutrons and flowing liquid metal alloy environment. In addition, thermodynamic activities of elements in an alloy have pronounced role in determining its high temperature oxidation properties during in-service conditions. It is known that alloying addition can change the oxidation behaviour of the alloys significantly by changing the activity and diffusivity of elements the constituting elements. Present study shows that alloying of Ta in vanadium based alloys decreases the activity of vanadium, which, in turn, improves the oxidation behaviour of the alloys during in-

service conditions, which is most important limiting issues in the application of vanadium based alloys. The effect of Ta addition on the oxidation behaviour of the developed V-Ti-Ta alloys have been discussed in chapter 6.

4.4   Summary

Vaporisation behaviour, chemical activities and Gibbs energies of formation for V-Ti-Ta ternary alloys have been determined for the first time as primary data with particularly high accuracy and precision. The measurements were performed in the temperature range 1900 – 2100 K using Knudsen Cell Mass Spectrometry. The study can be summarized under the following points:

1. It was observed that the activities of Ti and V decrease upon increasing Ta content from 0 to 7 wt.% in V-4Ti-xTa alloys.

2. It was observed that the partial free energies of Ti and V and their excess values become increasingly negative with addition of Ta, which is indicative of increasing thermodynamic stability of V-4Ti-xTa alloys.

3. The log (a) vs 1/T plots for V and Ti are substantially linear over the wide temperature ranges covered, which means that the partial and excess enthalpies of formation are independent of temperature within this range.

4. The concentration dependence of thermodynamic activities of V-Ti-Ta investigated shows that the energetics in the ternary alloys are influenced by the strong Ti-Ta and V-Ta bond energy leading to negative deviations from ideal behaviour.

Recrystallization and structure-property correlation in V-Ti-Ta alloys

5.1   Preamble

In the present chapter effect of addition of Ta in V-4Ti-xTa alloys on the recovery, recrystallization, precipitation behaviour and mechanical properties of the V-Ti-Ta alloys has been reported. As the presence of interstitial impurities adversely affect the low temperature properties of V based alloys, strong carbide, nitride or oxide forming tendencies of Ta are expected to be beneficial to V-Ti-Ta alloy system. In addition, Ta offers higher potential for solid solution strengthening and is expected to slow the kinetics of thermal and irradiation induced degradation phenomena. In order to exploit these potentials of Ta and retain the beneficial scavenging effect of Ti, in the current work synergistic effects of Ta and Ti in the V-Ti-Ta alloys are studied. Some of the pertinent aspects that are addressed in this study are the role of Ta on

(a) the deformation and recrystallization behaviour with associated microstructural and textural evolutions

(b) precipitation formation and dissolution behaviour

(c) structure property correlations.

5.2   Microstructure evolution during recrystallization treatments

For the purpose of determining the optimized combination of temperature and time for breaking the initial as solidified structure and achieving full recrystallization (with a desirable homogenous equi-axed microstructure), cast buttons of the alloys (with different Ta contents) were subjected to 70 % cold work (by uniaxial rolling) followed by heat treatments with

different combinations of temperature and time. Temperature range for heat treatments was kept as $0.55–0.75T_m$ of pure vanadium. This works out to be 1000–1300 °C. Time scales employed were chosen to correspond to typical industrial practices of few hrs (1 and 3 hrs). The deformed and heat treated samples were analysed in detail by EBSD mapping to bring out quantitative aspects of the progress of recrystallization as a function of Ta content, temperature and time. The results of microstructural studies using EBSD are summarized in the Fig. 5.1 (a-x). Multiple EBSD scans were recorded for each sample condition to increase the statistical confidence on the results and only representative scans are included in the Fig. 5.1.

Deformed microstructures, shown in Fig. 5.1(a-c), has all the characteristic features in terms of (i) presence of significant in-grain mis-orientation (revealed through colour gradients in the IPF maps), (ii) large fraction of sub grain boundaries and (iii) dislocation tangles (corresponding to poorly indexed regions, shown as black patches in the IPF maps). It may be noted that while typical grain sizes of the as-solidified buttons were of the order of few millimetres, the cold worked samples (with 70 % rolling) showed grain fragmentation (Fig. 5.1(a-c)). However, majority of the 'large grains' of the as-solidified structure were retained in terms of their sizes and showed very little fragmentation, i.e. did not form smaller grain fragments with high angle grain boundaries.
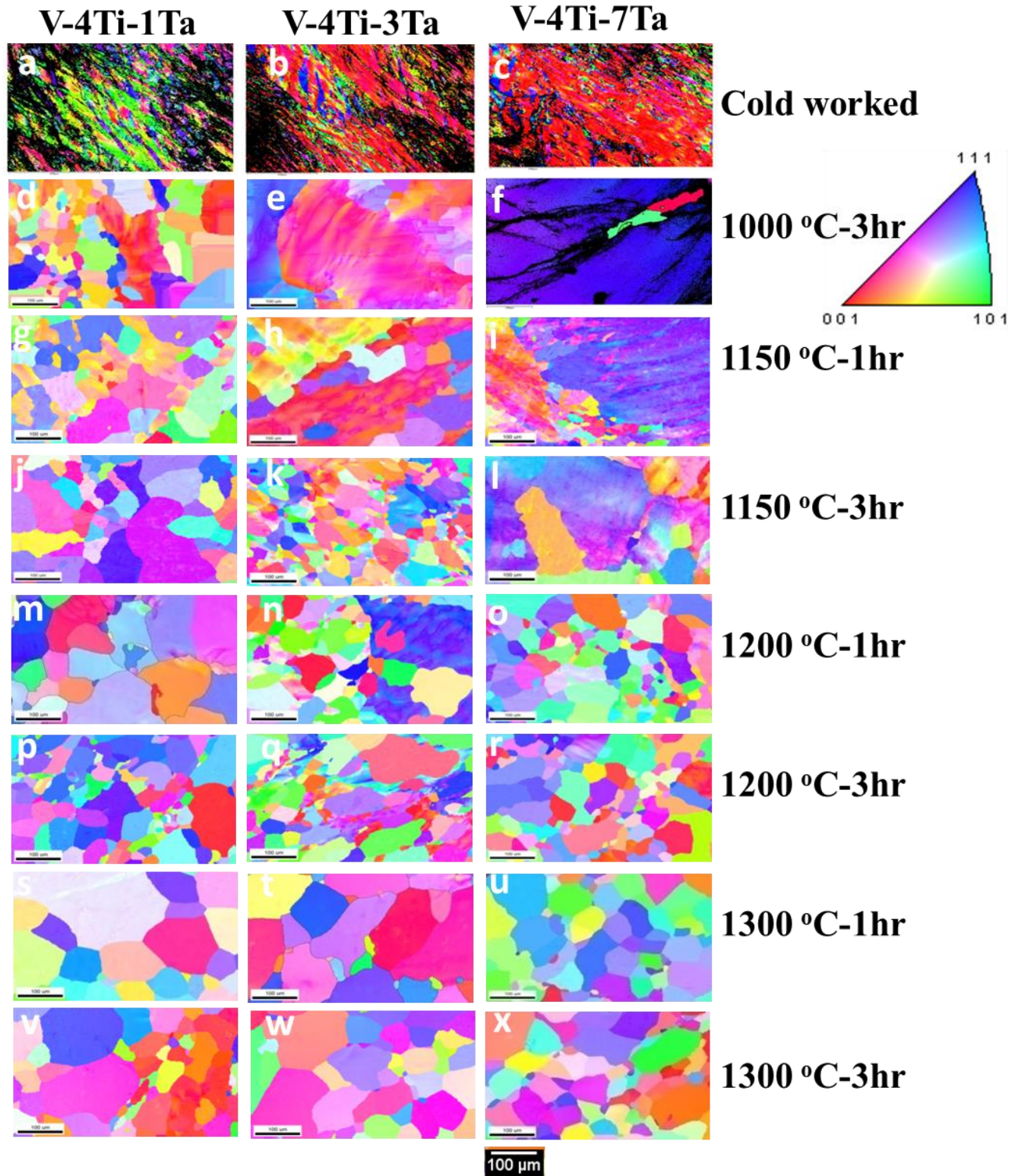
Figure 5.1 (a-x): Inverse pole figure color coded maps of deformed (i.e. initial structures for recrystallization studies) and heat treated samples as a function of annealing time and temperature, depicting evolution in microstructure during the recrystallization. Poorly indexed regions are shown in black, typically correspond to highly deformed or regions with high dislocation densities).

When heat treated upto 1000 °C, microstructures of the samples containing 3-7 % Ta did not show any appreciable extent of recrystallization. The alloy with low Ta (1 %), on the other hand, did show noticeable extent of recrystallization. A closer observation of the IPF map for this alloy indicated presence of orientation gradients in some of the larger grains. Thus even for the low Ta alloy, it is desirable to employ higher recrystallization temperature to achieve full recrystallization. One can notice significant increase in the quality of EBSD indexing of the samples treated at 1000 °C in comparison to the cold worked ones, for the 3-7 % Ta alloy samples. This signifies underlying recovery processes which helped in the unlocking of dislocation tangles and in the rearrangement of dislocations in a low energy configuration (dislocation patterning) leading to the formation of sub-grains and in-grain orientation gradients, see Fig. 5.1(e, f).

The role of Ta in determining the extent of recrystallization at any given temperature and time is evident from the Fig. 5.1. It can clearly be noticed that samples having higher Ta (in particular 7 % Ta) showed signatures of fully equi-axed grains only at 1300 °C. The lower Ta content alloy, on the other hand, had undergone practically full recrystallization at as low as 1150 °C. The behaviour of 3 % Ta, as expected, is in between these two extremes.

In order to quantify the percentage of recrystallization as a function of time and temperature, GOS (grain orientation spread) has been estimated from the EBSD data. A large value of GOS indicates that grains have remnant plastic strain (in the form of dislocations) and they are not fully recrystallized. A fully recrystallized grain will have low GOS ($< 1°$). Based on this criterion percentage of recrystallization has been estimated and presented in the Fig. 5.2. The figure clearly brings out the stark differences in the extent of recrystallization among the alloys with varying Ta contents. The lower temperature regime clearly demarcates the alloys in terms of their recrystallization extents. For the heat treatments above 1250 °C, however, such differences decrease and convergence in the percentage of recrystallization is

observed among alloys. Further, one can notice that the extent of recrystallization did not differ significantly between the 1 hr and 3 hrs treatments.
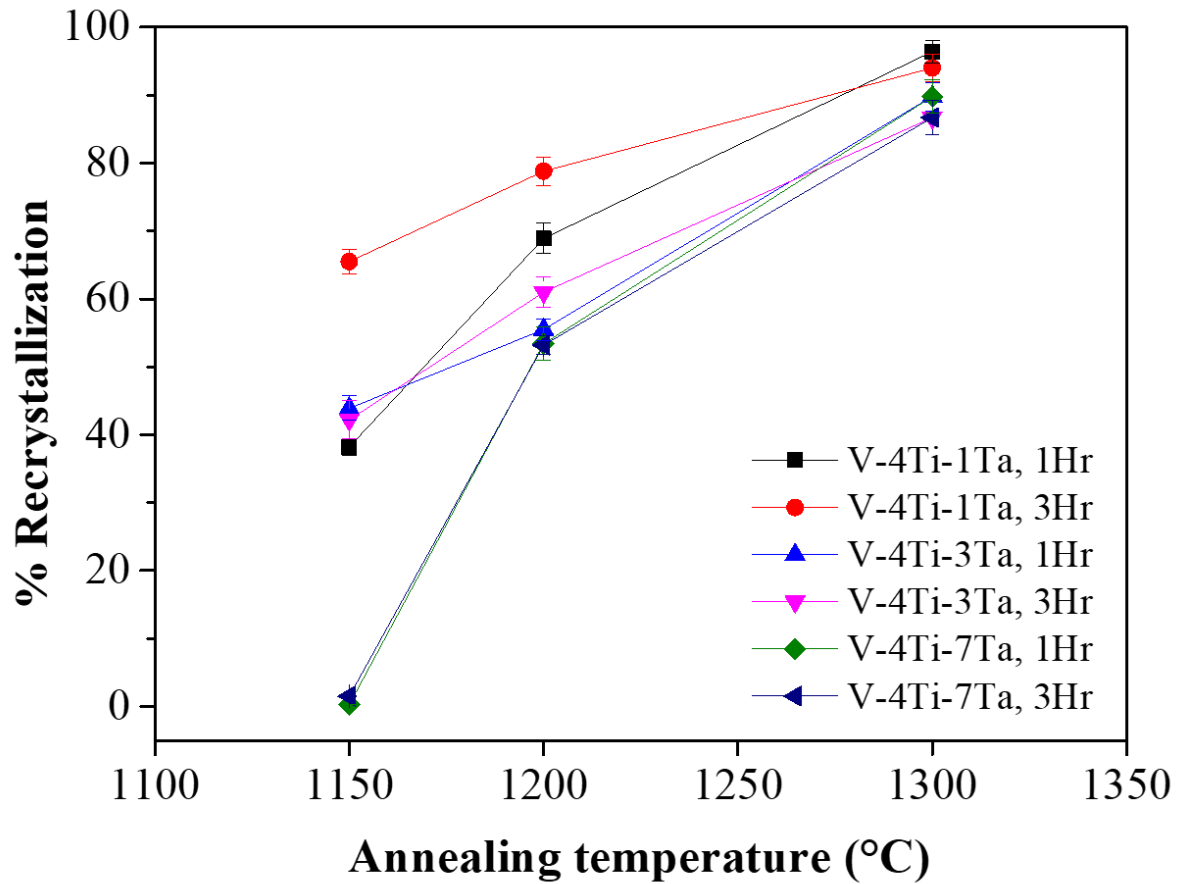
Figure 5.2: Variation of percentage of recrystallization as a function of annealing temperature for alloys with different Ta content and different holding times.

While the results presented so far have given a gross picture of microstructural evolution, in general, subtle changes in the microstructures associated with the heat treatments are depicted in the Fig. 5.3, taking examples from the alloy containing 7 % Ta. The figure illustrates the key features of the evolution of sub-structures as captured through the EBSD mapping for this alloy as a function of temperature. These can be summarised in the following points.

(i) The recovered structure where formation of sub-grain boundaries with low angle (less than 15° misorientation can be seen in Fig. 5.3 (a). Such low angle boundaries (reflected as white colour in Fig. 5.3 (a) are due to dislocation patterning in the recovery process.

(ii) Fig. 5.3 (b) shows an interesting phenomenon of adjacent regions with strikingly different features. It depicts a microstructure of combination of finer well recrystallized grains exist in conjunction with large recovered (not yet recrystallized) grains. This points towards discontinuous recrystallization being the primary operative mechanism [133]. Another possible reason for such microstructure development could be in-homogenous distribution of the underlying driving force for the recrystallization which can originate from the orientation sensitive deformation heterogeneities in the cold work stage. Further, the region with apparently recrystallized portion, did show morphological alignment of grains, indicating the recrystallization is incomplete and influence of underlying shear bands (from cold work) is not fully eliminated.

(iii) The microstructure corresponding to 1300 °C, however, is completely devoid of any noticeable in-grain misorientations, and morphological alignment of the newly formed grains (Fig 5.3 (c)). It is characterized by the presence of high angle boundaries most of which were with well-defined triple junctions having triple point angle close to 120°. The fact that this microstructure presented a combination of finer grains and coarser grains (bi modal distribution) indicates that growth regime has started for this alloy at the employed time of 3 hrs. The evolution in the density of the low angle grain boundaries is shown quantitatively in the Fig. 5.3 (d). The average measured grain size at 1300 °C samples was almost similar (40-50 μm) irrespective of Ta content in the alloy.
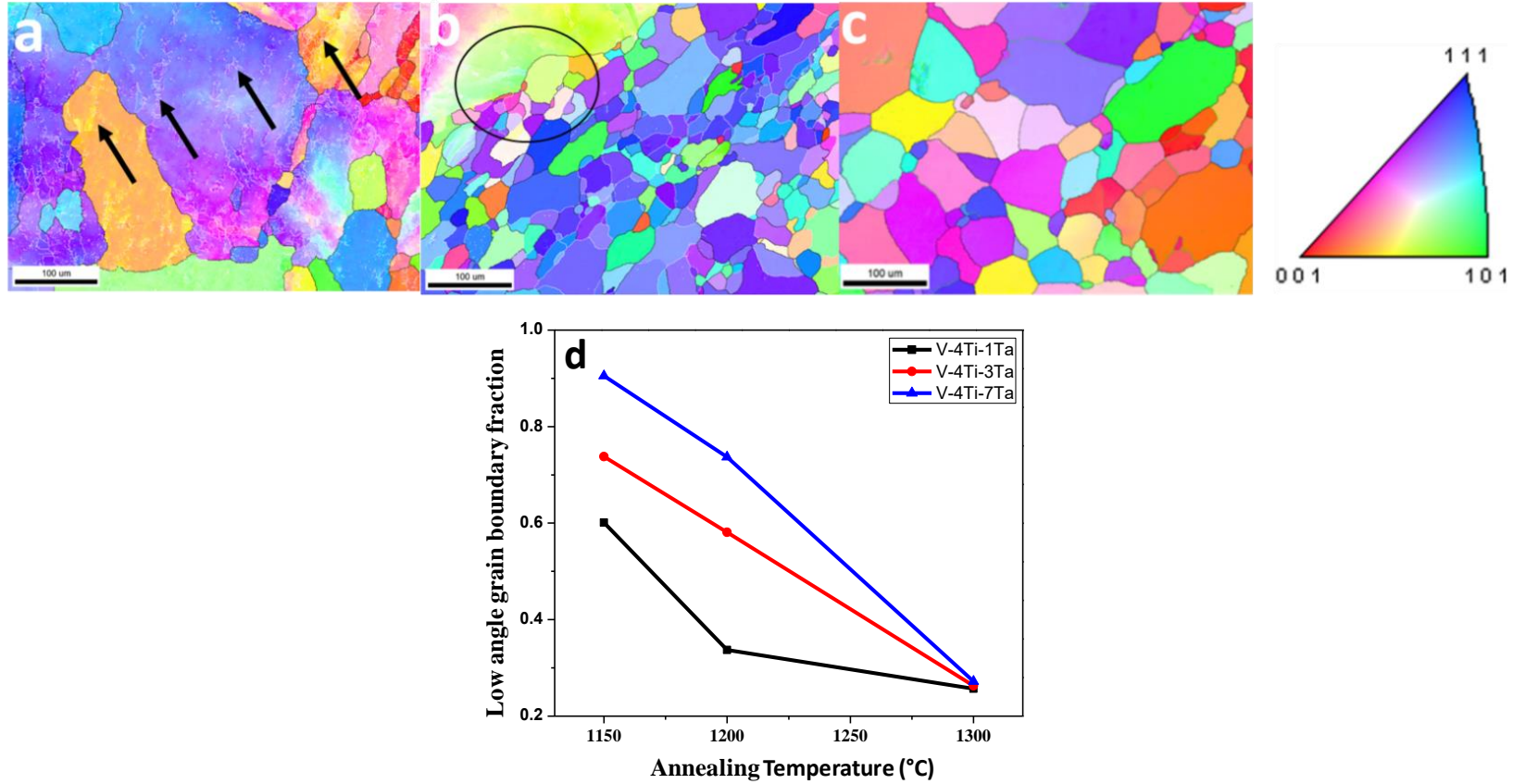
Figure 5.3 (a-d): EBSD images showing the low angle grain boundaries as a function of annealing temperature in V-4Ti-7Ta alloy samples

    (a) 1150 °C-3hrs, arrow shows dislocation patterning leading to formation of low angle grain boundaries

    (b) 1200 °C-3hrs, circle shows combination of finer well recrystallized grains exist in conjunction with large recovered (not yet recrystallized) grains

    (c) 1300 °C-3hrs, showing presence of high angle boundaries with well-defined triple junctions signifying the fully recrystallized microstructure

    (d) *Low angle grain boundaries fraction of V-4Ti-xTa alloy samples as a function of annealing temperature .*

5.3   Evolution of precipitates

Apart from the basic microstructural parameters and extent of recrystallization, the inventible presence of precipitate influence the structural properties of V-Ti-Ta system. The nature, size, composition and morphology of these precipitates have a role in determining the properties of the alloys. These aspects have been characterized in the current work and additional details in terms of crystal structure and orientation relationship (OR) with the matrix were also brought out as detailed below.

SEM micrographs of the samples showing the morphology and distribution of precipitates corresponding to various heat treatment conditions are presented in the Fig. 5.4 (a-j). Micrographs corresponding to alloy samples with lowest (1 %) and highest (7 %) Ta are the ones which are included in the figure as the behaviour of the alloy with the intermediate Ta (3 %) content was always in-between these two extreme cases. It may be noted that considerable inhomogeneity in the spatial distribution of the precipitates was observed in the current study. This is consistent with previous reported observations which emphasised the notable inhomogeneous distribution of precipitates in most of the V-Ti-Cr alloys [39, 75, 79, 80, 82, 83]. In view of this, large areas covering high field of views were examined for analysing the precipitates and only representative images are included in Fig. 5.4. Typical needle-like precipitates in the localized zones in the as cast microstructure can be seen in Fig. 5.4 (a-b). In general, all of the annealed samples also exhibited, needle shaped precipitates (Fig. 5.4 (c-j). The size of the precipitates was estimated to be in the range of 80-150 nm (width) and 500-5000 nm (length). It was noticed that width of the precipitates had shown systematic increase with annealing temperature.
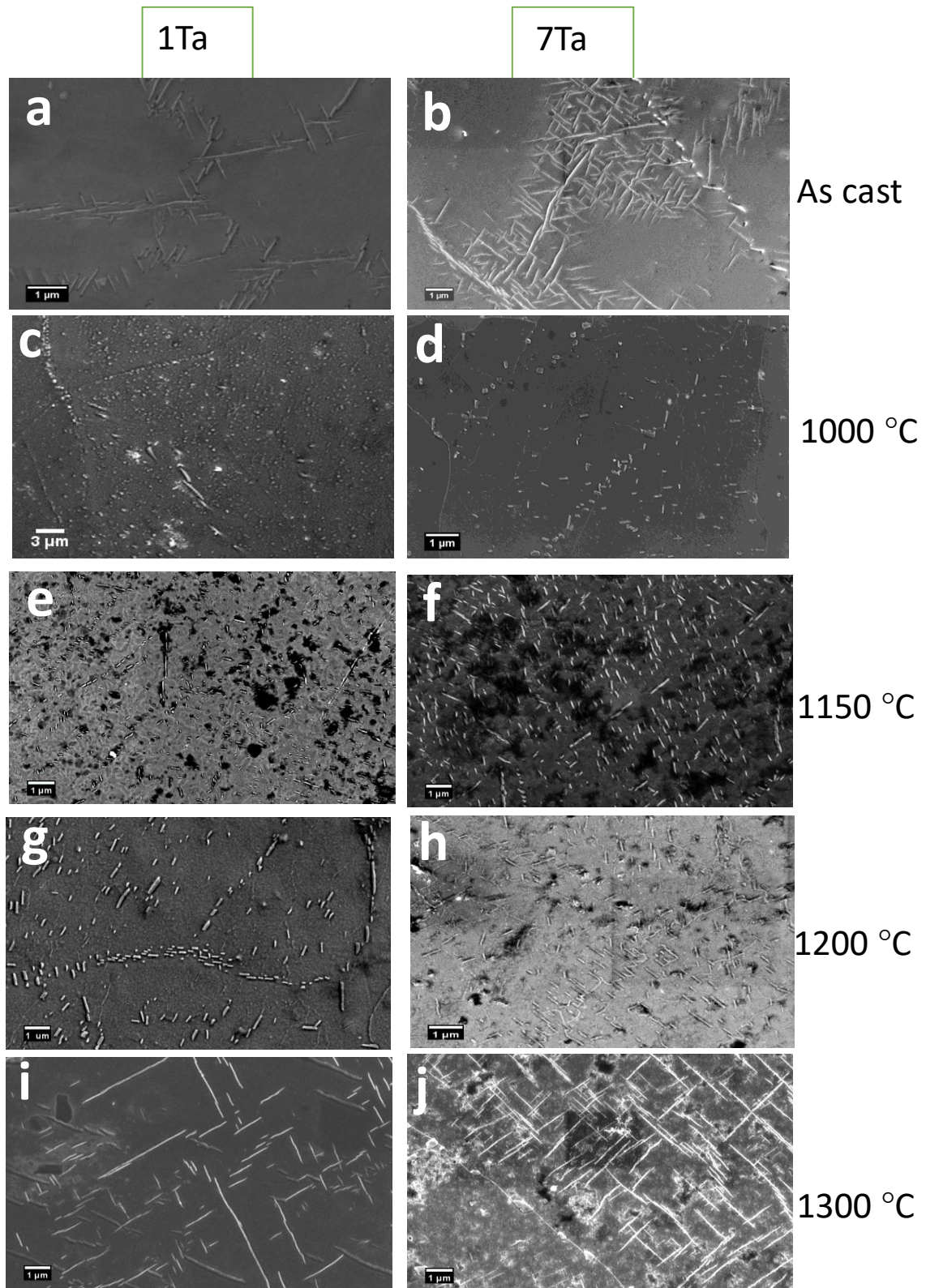
Figure 5.4 (a-j): SEM micrographs of V-4Ti-1Ta and V-4Ti-7Ta alloys as function of annealing temperature for 3 hr, showing the presence of needle shaped precipitates.

99

In order to find the effect of Ta content on the crystal structure of the precipitates, the annealed samples of different Ta content and different annealing temperature samples were subjected to conventional XRD characterization. However, second phase could not be detected as its volume fraction was below the detection limit of conventional XRD. Hence, synchrotron X-ray diffraction was employed for the further studies.

Fig. 5.5 depicts the diffraction spectra recorded from synchrotron beam line for the V-4Ti-xTa alloy samples. For the base line comparison, results from binary V-4Ti are also included in the figure. It may be noted that many of the peaks of the matrix phase (V) and the precipitate phase (TiC) are very close to each other due to high degree of lattice correspondence between the two phases (Refer Table 5.1). This makes the diffraction peaks corresponding to precipitates appear mostly as shoulder to the matrix phase peaks. In order to gain confidence that the observed shoulder peaks indeed correspond to the precipitates and not artifacts, each spectrum recording was preceded by measuring standard reference sample (LaB_6). It was positively ascertained that the reference sample did not show any un-explained shoulder like features in the diffraction peaks. Thus the minor shoulder features shown in the Fig. 5.5 can be attributed to Ti(CON) type of precipitates only. Note that the position of the shoulders did coincide with the $TiC_{0.7}N_{0.3}$ positions, see the Table 5.1. For simplicity these precipitates will be referred to as TiC precipitates, here after.

It could be seen that addition of Ta in V-4Ti shifts the V peaks towards lower 2θ angle (Fig. 5.5), which is due to substitution of bigger size Ta atom in place of smaller V and Ti atoms. The role of Ta in shifting the peak position of the TiC precipitates is brought out in Fig. 5.5 (b). It can be noticed that peak shift is towards lower 2θ angles and the extent of shift is proportional to the amount of Ta in the sample. This peak shift may be attributed to lattice expansion on the account of substitution of Ti by Ta in TiC lattice. Lattice parameter of TiC phase was measured to be 4.287A° and 4.296A° for V-4Ti and V-4Ti-7Ta alloy respectively.

This corresponds to 0.2 % change in lattice parameter and indicates the presence of Ta in the precipitate phase. The samples that were heat treated at different annealing temperatures did not exhibit any measurable changes in their lattice parameter as a function of annealing temperature. Thus it was inferred that annealing temperature has no significant effect on the lattice parameter and hence on the composition of the precipitates (Fig. 5.6).
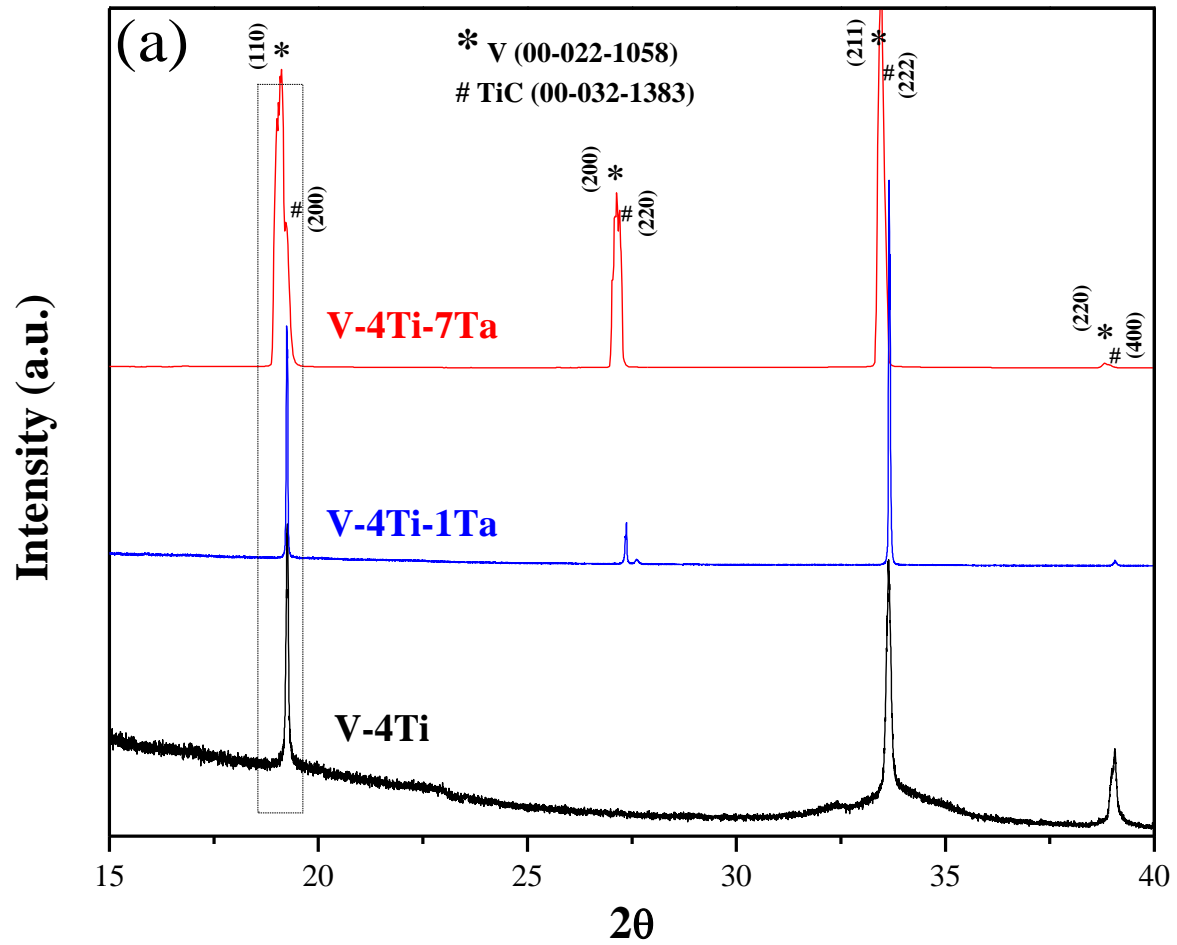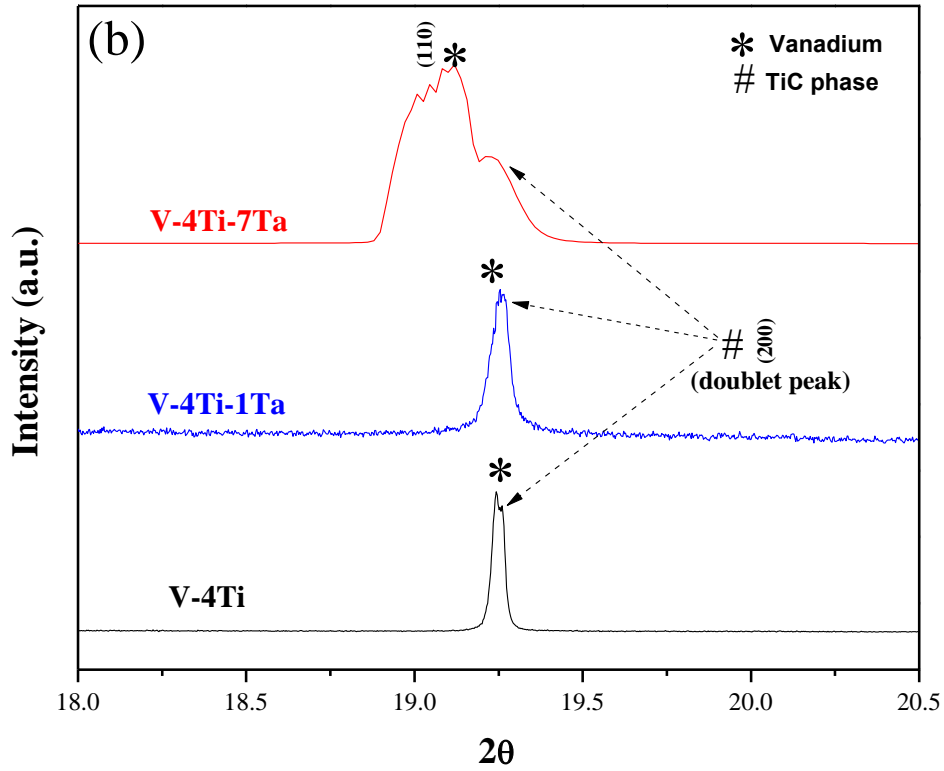
Figure 5.5 (a, b): Synchrotron XRD pattern of V-4Ti-xTa alloy samples, (a) showing the presence of V and TiC phases. (b) Enlarged region of dashed portion of Fig. 5(a) showing the peak shift in V and TiC phases on addition of Ta in V-4Ti-xTa alloys.
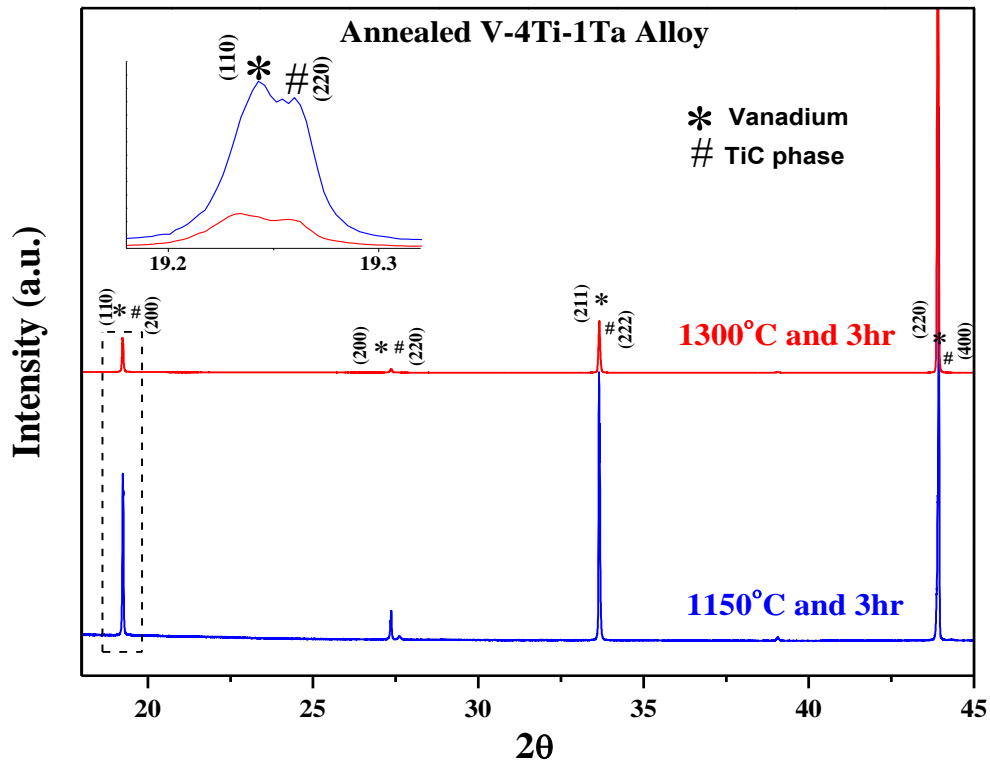
Figure 5.6: Synchrotron XRD pattern of V-4Ti-xTa alloy samples showing the effect of temperature of annealing on the peak position of V and TiC phases.

Table 5.1: X-ray diffraction peak positions of TiC, TiN and V phases showing the close proximity of peak positions.

Sl. No.	TiC JCPDS No. (00-032-1383)		TiN JCPDS No. (00-038-1420)		V JCPDS No. (00-022-1058)	
	2θ	hkl	2θ	hkl	2θ	hkl
1.	16.49	111	16.83	111	-	-
2.	19.07	200	19.46	200	19.27	110
3.	27.09	220	27.65	220	27.38	200
4.	31.89	311	32.55	311	-	-
5.	33.34	222	34.04	222	33.70	211
6.	38.69	400	39.50	400	39.12	220
7.	42.32	331	43.22	331	-	-
8.	43.47	420	44.40	420	43.96	310
9.	47.87	422	48.90	422	48.42	222
10.	50.98	511	52.08	511	52.20	321

The fact that majority of the precipitates were of needle shape and oriented along specific directions clearly indicate towards the presence of an orientation relationship (OR) between the matrix and precipitates. In order to confirm this OR, ESBD was performed on the samples, with appropriate conditions (smaller step size of 30 nm and longer exposure time) to index the precipitates along with the matrix. However, efforts to index the precipitates by EBSD were not successful as one of the dimensions (width) of the precipitates was of the order of ~80-100 nm. In order to resolve this issue, precession electron diffraction (PED) under TEM was performed to characterize the details of precipitates using precession angle of 1°. For this, a site specific TEM lamellae prepared using FIB technique was used. Before acquiring the orientation map of the recrystallized sample by PED, one of the precipitates was brought to [100] zone axis. Fig. 5.7 shows the orientation map of the V-4Ti-7Ta alloy fully recrystallized (by annealing at 1300 °C for 3 hrs). The successful indexing of the fine needle shaped precipitates is evident from electron diffraction pattern. It may be noted that a fine step size of 5 nm coupled with the fine spot size of TEM beam ensured effective indexing of such fine precipitates. The successful indexing of the precipitates confirmed the crystal structure to be FCC. A composite SAED pattern from matrix and precipitate containing reflections from both phases was indexed (Fig. 5.7(b)). The pattern exhibited a common diffraction vector, based on which unique orientation relationship (OR) between the precipitates and matrix was determined, as expressed below:

$$(020)_m||(200)_p,$$

$$[001]_m||[011]_p$$
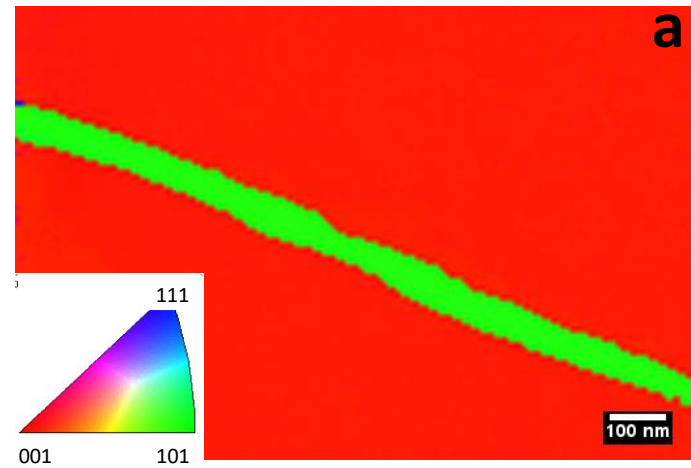
Figure 5.7(a): (a) Orientation image of V-7Ta-4Ti alloy after cold rolling, followed by heat treatment at 1300 °C for 3 h acquired by precession electron diffraction in TEM showing the presence of specifically oriented (<100>V//<110>TiC) needle morphology of (Ti,Ta)C carbides (Confirmed By EDS).
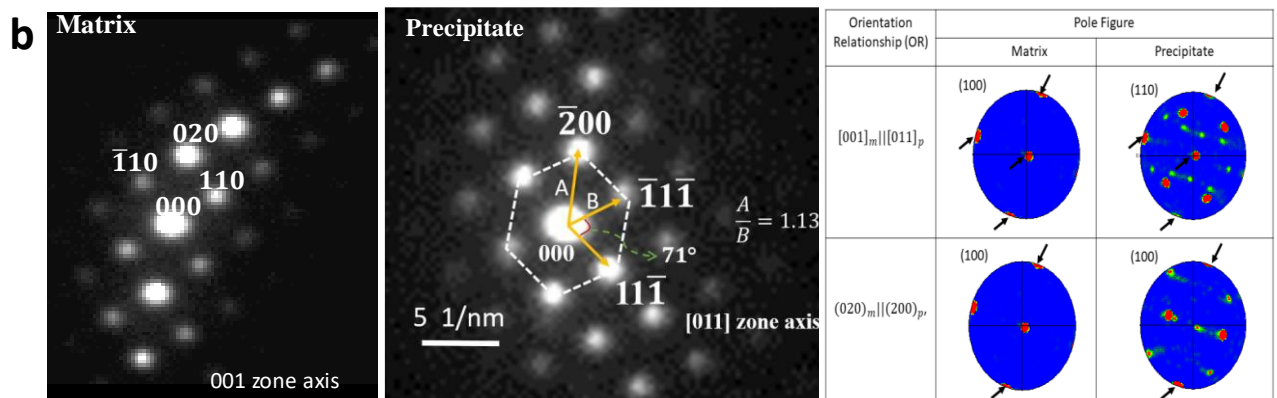
Figure 5.7(b): Composite SAED pattern and pole figure of the V matrix and needle morphology of TiC carbides showing the presence of B-N OR between them.

The above OR (Fig. 5.7(b)) is in agreement with the reported Baker Nutting OR in BCC-FCC systems [18]. In order to ascertain the chemical composition of the precipitates and hence to detect selective partitioning of the Ta, if any, EDS spot patterns taken from several precipitates. The average composition of precipitates was found to be: Ti (wt.%) - 3.9, Ta (wt.%) - 6.6. In addition, substantial presence of carbon, nitrogen and oxygen in the sample was also noticed. Based on the information obtained from SAED patterns and EDS analysis,

the precipitates were identified as (Ti,Ta)(CON) carboxy nitride phase. This corroborates the XRD results which have revealed the substantial presence of Ta in the precipitates (TiC lattice) by peak shift. This is in contrast to the other comparable alloy system (V-Ti-Cr), where presence of Cr in precipitates was not observed. In the present case, Ta was observed to be present both in the matrix as well as in the precipitate phases, showing no specific preference for either of the phases.

5.4   Mechanical property evaluation

5.4.1   Influence of different heat treatments on hardness of the alloy

The influence of annealing temperature and Ta content on the hardness of the alloys is plotted in Fig. 5.8. Also shown are the relevant microstructures corresponding to specific data points of the plot to emphasize the role of microstructure in determining the hardness. There are few points to be noted from this figure.

(i) Hardness of the sample increases with increasing Ta content highlighting the contribution of Ta in improving the strength of the alloy.

(ii) The hardness of all the samples annealed at 1000 °C for 3 hrs significantly decreased in comparison to deformed samples. This large drop in the hardness without significant change in matrix grain morphology, see the corresponding microstructures, suggests that samples have undergone the recovery process without any noticeable recrystallization. It can, therefore, be inferred that major changes in hardness represent a regime where recovery was the dominant operative mechanism.

(iii) Hardness values have exhibited a minimum at 1150 °C. Beyond this temperature, drop in hardness is negligible. In the case of alloy where Ta was lowest, the minimum in hardness was

observed at 1000 °C. This can be attributed to the delayed recovery in the case of higher Ta alloy.

Another interesting observation from the plot is the noticeable increase in the hardness beyond 1150 °C and upto 1200 °C, particularly in the case of low Ta alloy. This is in agreement with those reported in literature and has been attributed to the dissolution temperature of Ti(CON) precipitates in the range of 1100 to 1200 °C [48, 50, 80, 81, 85], which releases the interstitial impurities in the matrix and thus resulting in increased hardness due to solid solution reinforcement [75, 80]. However, for higher Ta containing alloys, the expected increase in hardness beyond the recovery was relatively lesser significant. This could be due to slower kinetics of dissolution of the precipitates.
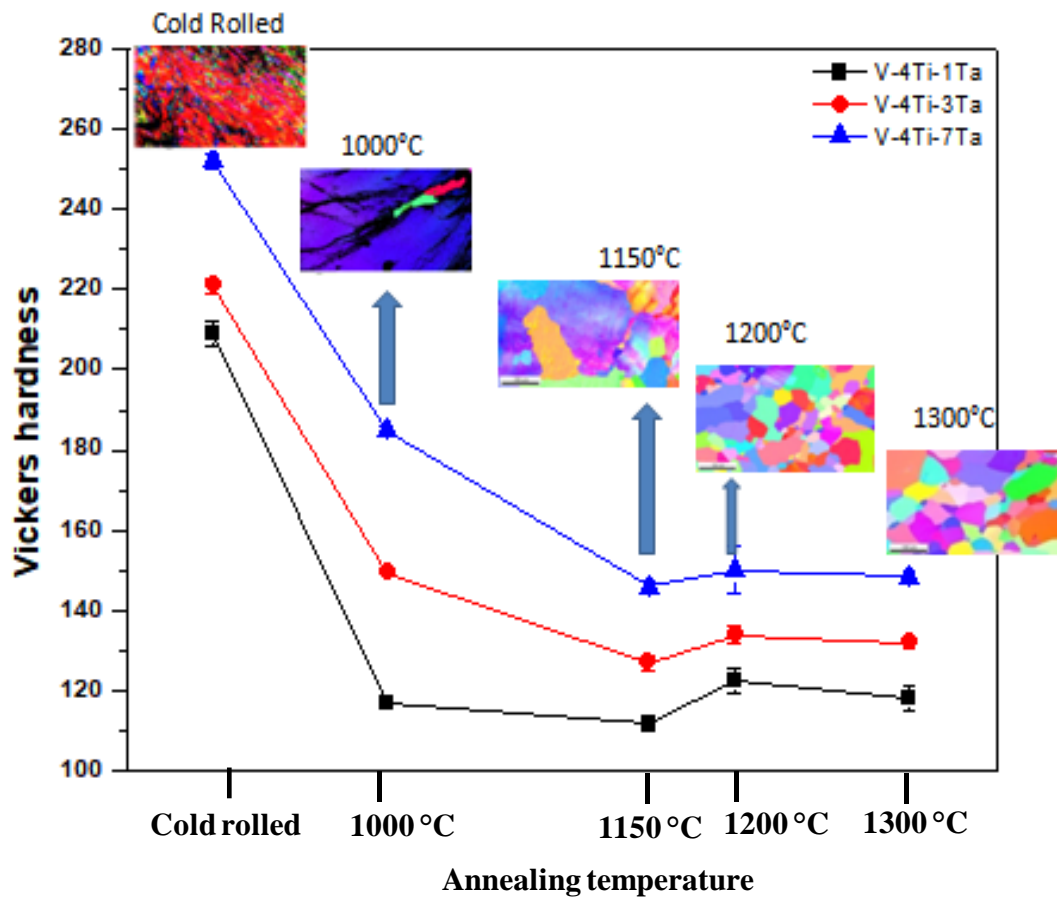
Figure 5.8: Vicker's hardness of V-4Ti-xTa alloy samples as a function of annealing temperature.

5.4.2 Flow behaviour

The behaviour of yield and flow stresses was determined for each of the fully recrystallized V-4Ti-xTa (x = 1, 3, 7 wt.%) alloys from room temperature compression tests at a nominal strain rate of ~ 5 x 10^{-4} s^{-1}. True stress -true strain curves obtained by compression testing are shown in Fig. 5.9. The flow curves indicate that V-4Ti-xTa (x = 0,1,3,7) alloy samples tend to reach a saturation stress within 10 % plastic strain. Thus the flow behaviour can be concluded to be largely controlled by the initial deformation behaviour. However, with the increasing additions of Ta, the level of flow stress is seen to systematically increase. Thus, as the Ta content increases, the V-4Ti-xTa alloy series displays increasing value of both 0.2 % yield and saturation stresses, which is evident in Fig. 5.10. V-4Ti alloy exhibited yield strength of 206 ± 4 MPa, whereas corresponding values for V-4Ti-1Ta, V-4Ti-3Ta and V-4Ti-7Ta were 248 ± 5, 276 ± 7, 369 ± 5 MPa respectively. The increase in the hardness also corroborates the observed increase in yield stress due to the addition of Ta. Upon comparing V-4Ti-4Cr, which is a reference material, it can be noticed that while tensile and compressive yield strengths of V-4Ti-4Cr were 300 ± 5 MPa [99] and 310 ± 5 MPa [134] respectively, V-4Ti-7Ta alloy , has superior strength even at effective lesser alloying content (~ 2 atom% of Ta). The flow behaviour is described by the new phenomenological fit, VAH [128] within the strain range, as shown in the Fig. 5.11 in the double logarithmic plot of true stress – true strain. The initial non-linear portion is not fitted as the equation is relevant for essentially the stage III of work hardening where a decreasing work hardening rate with strain results in a parabolic flow stress – strain behaviour. It is seen that the saturation stress is described by the parameter K_L provides reasonable prediction of the saturation stress within 10 %. Furthermore, the values of n_j denoting the propensity of scaling of the dislocation network as a result of work hardening is observed to be low in V-4Ti [128]. Furthermore, the addition of Ta in the V based ternary alloy does not appreciably change the value of n_j. It can thus be rationalised that the work

hardening during flow behaviour of V-4Ti-xTa (x = 0,1,3,7) only tenuously depends on the extent of downward scaling of the dislocation network. Thus the flow behaviour of the V-4Ti-xTa (x = 0,1,3,7) can be summarised as being largely influenced by the increases in strength as a result of solid solution hardening rather than work hardening assisted by rapid increase in dislocation density.
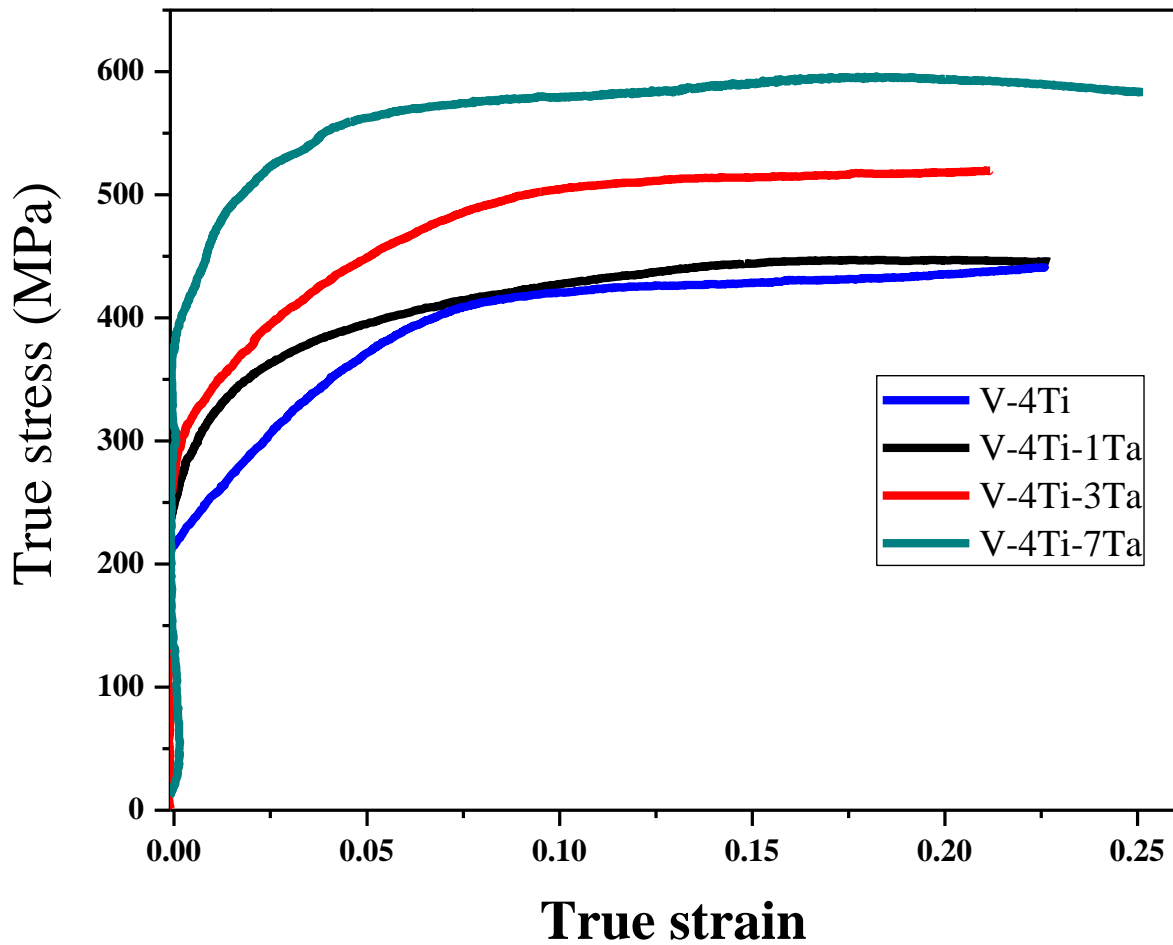
Figure 5.9: True stress- true strain curve of V-4Ti-xTa alloy showing the flow stress of the samples.
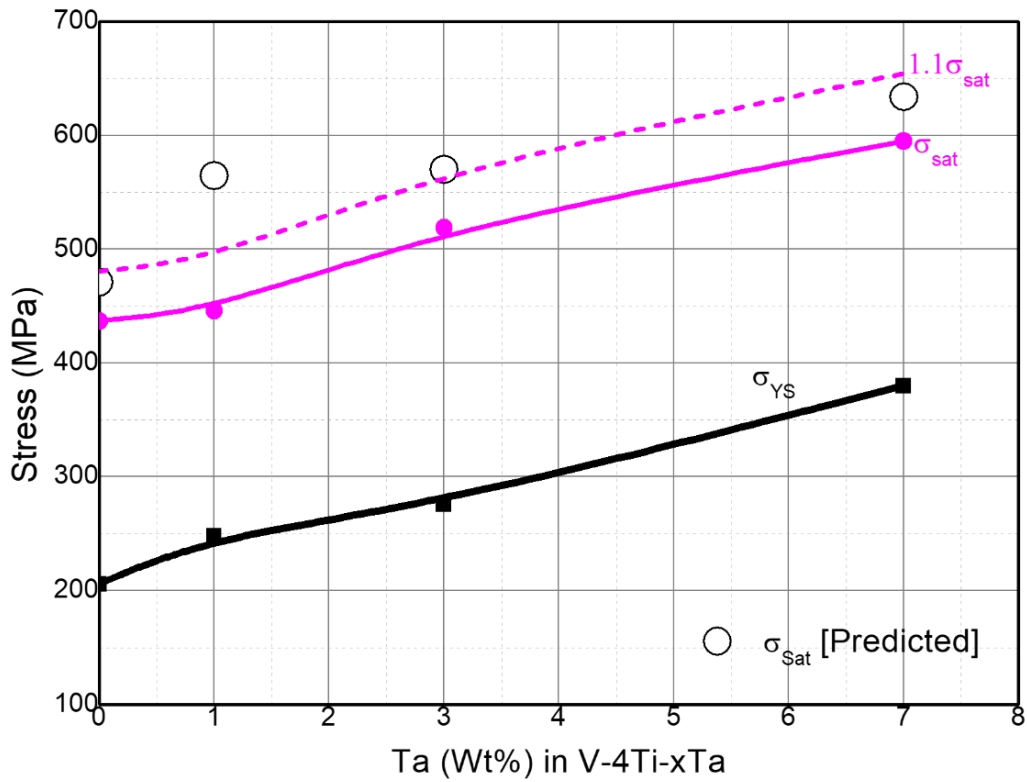
Figure 5.10: Yield strength of V-4Ti-xTa alloys as a function of Ta composition in the alloy.
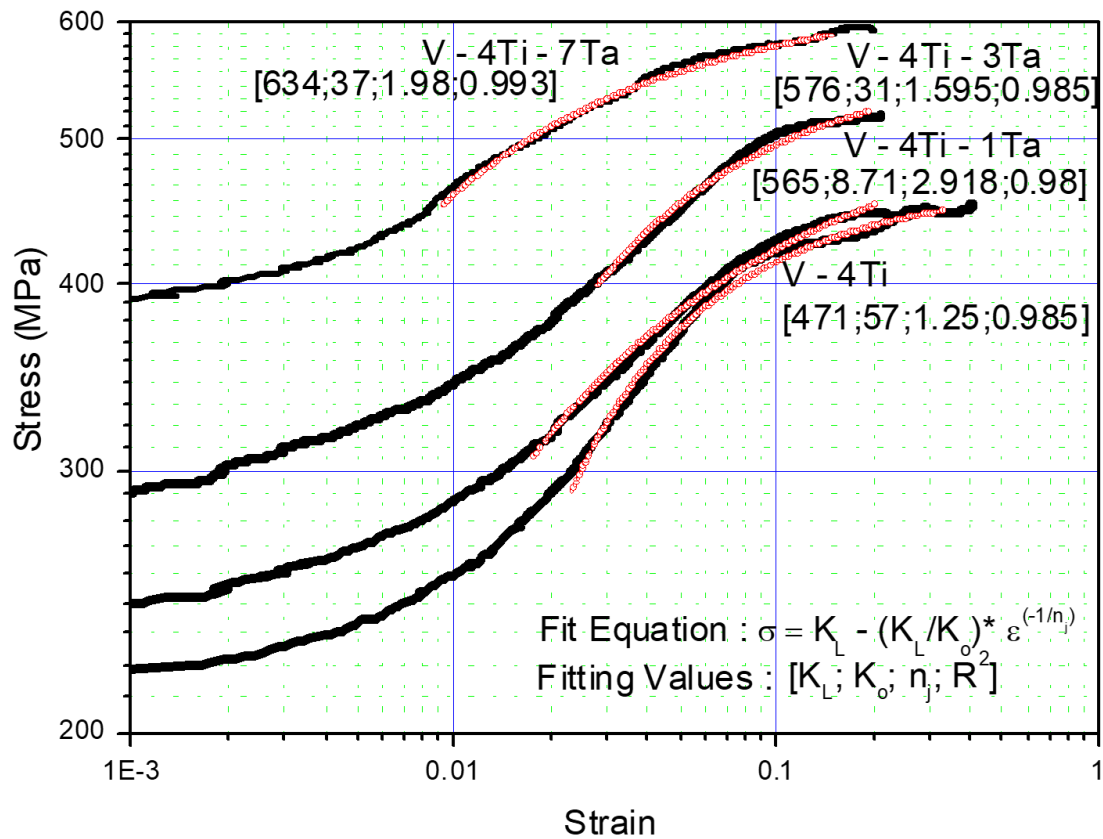
Figure 5.11: The flow behaviour of V-4Ti-xTa alloys described by the new phenomenological fit, VAH [128] in the double logarithmic plot of true stress – true strain.

5.5 Bulk texture analysis

Fig. 5.12 shows the $\phi_2 = 45°$ sections of ODFs of the deformed and annealed samples of V-4Ti-1Ta alloy. Even though texture was, in general, low in these samples (maximum ODF intensity was below 2.5), presence of specific orientation fibres in the ODF plots was noticed. For instance, deformed samples exhibited strong presence of θ - fibre (Fig. 5.12). Till date, no reported data exists on deformation textures of V-Ta alloy to compare our deformation texture results obtained in this study. Comparison with other BCC systems, however, reveals marked difference. Most of the BCC materials (α-Fe, Nb etc) [135, 136] , in general, are known to exhibit strong α-fibre due to the rolling deformation. However, specific BCC alloys, such as Fe-Si system, were reported to produce strong θ – fibre [137, 138] after rolling deformation. Thus the current V-Ti-Ta systems seems to be following deformation characteristics of Fe-Si alloys. It is worth noting that in both these cases, alloying elements exert substantial solid solution strengthening effect (due to Ta and Si) and hence their deformation behavior and deformation texture development is expected to be similar to each other.

Recrystallized samples, on the other hand, were characterized by a strong γ fibre (Fig. 5.12). The intensity of the γ-fibre was seen to be correlated with the annealing temperature and hence to the extent of recrystallization. Fig. 5.13 (a-b) shows the quantitative evolution of the principal texture components and fibres for different heat treatment conditions for the V-4Ti-1Ta alloy respectively. In the annealed samples, increase in strength and continuity of the γ-fibre was noticed as the annealing temperature was increased from 1000 °C to 1300 °C, with a corresponding decrease in the strength of the θ - fibre. These textural changes point towards the oriented nucleation being the dominating mechanism for the recrystallization texture. Under this mechanism, large number of suitably oriented nuclei exist in the deformed regions from which new strain free recrystallized grains form.
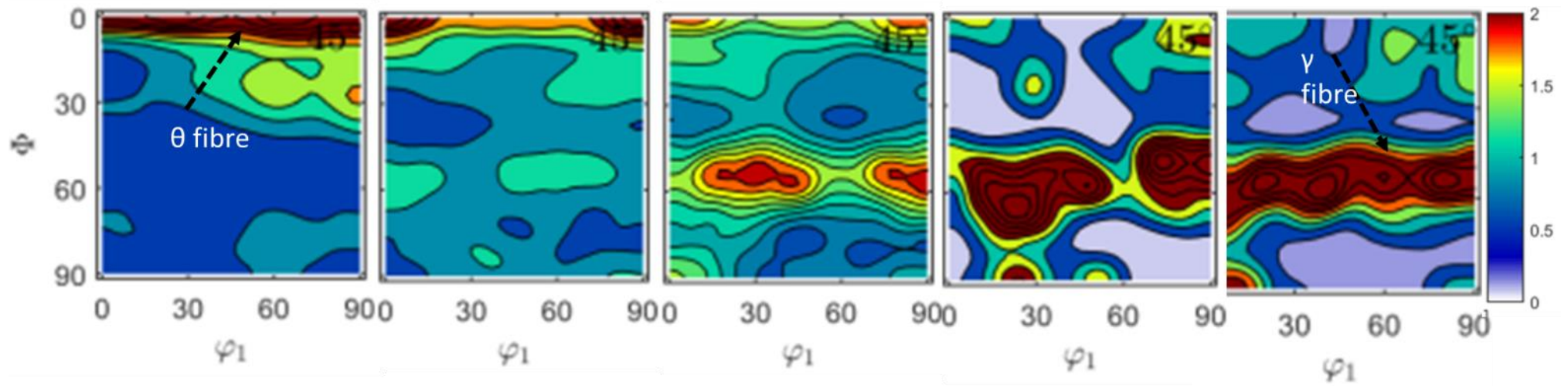
Figure 5.12: ODF φ2 = 45° sections of (a) Cold rolled (b) 1000 °C-3hr (c) 1150 °C-3hr (d)1200 °C-3hr (e) 1300 °C-3hr annealed samples showing the presence of θ and γ fibre texture.
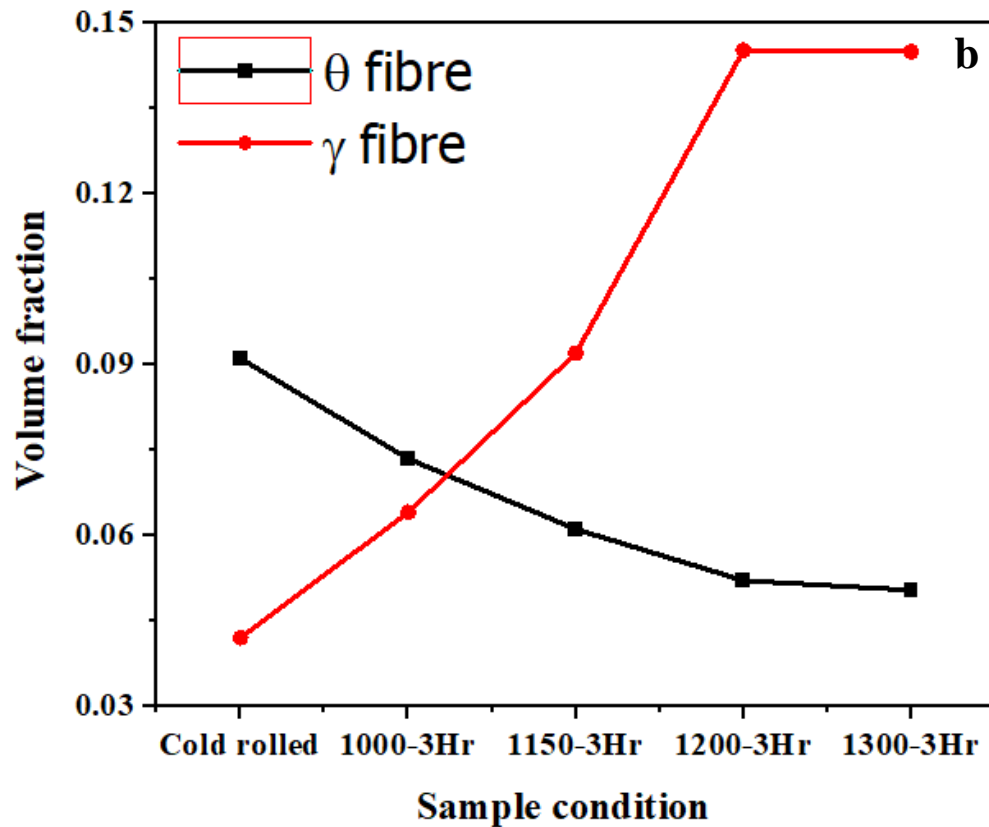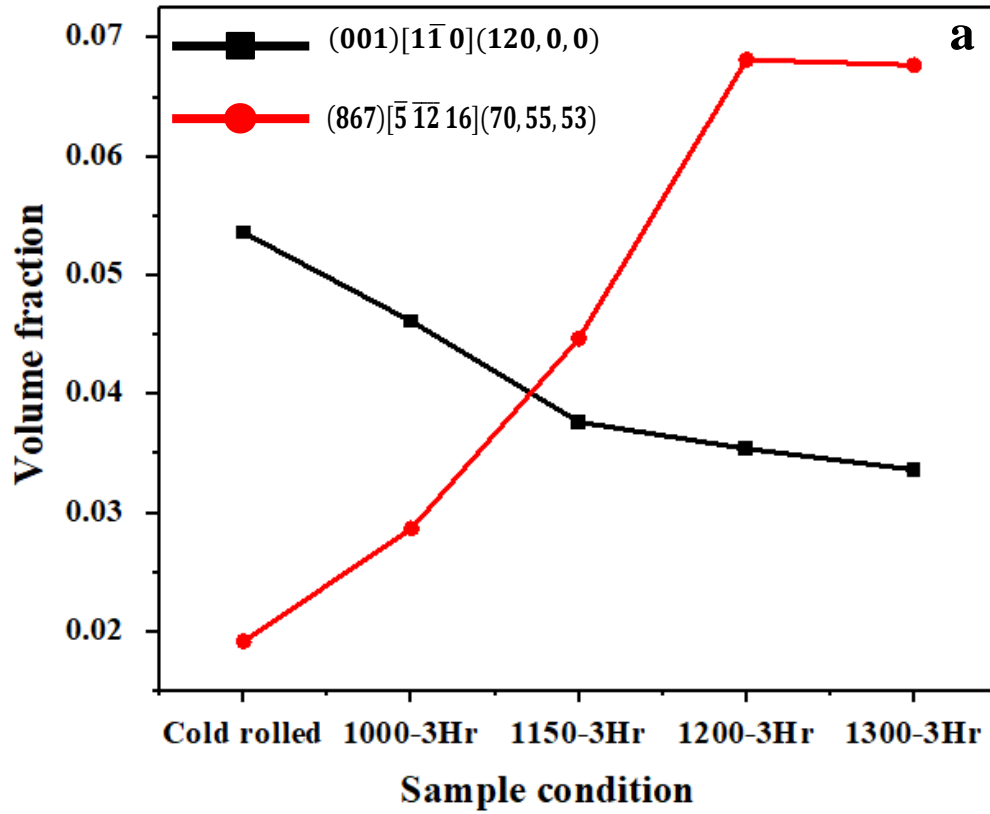
Figure 5.13(a-b): (a) Fraction of particular texture component in 70 % deformed and annealed V-4Ti-1Ta alloy samples (b) θ and γ-fibre fractions of 70 % deformed and annealed V-4Ti-1Ta alloy samples.

Due to high degree of misorientation of these nuclei with the deformed parent grains, they possess higher growth velocities and lead to the formation of significantly different recrystallized texture from that of the deformed state. Disappearance of θ-fibre and simultaneously strengthening of the γ-fibre does indicate this is the operative mechanism in the present case. However, particle stimulated nucleation is also expected to be operative in this system as majority of the precipitates did not dissolve during the recrystallization treatment. This makes over all texture relatively weaker.

5.6   Discussion

Current investigation explored the role of Ta in a potentially high temperature structural alloys of the V-Ti-Ta system. The focus was laid on bringing out various aspects of recrystallization behavior, and structure-property correlations in this novel alloy system. The strong potential of Ta for substitutional solid solution strengthening has been the motivating force behind the employment of Ta in this system. In line with the envisaged context, the developed V-Ti-Ta alloy system necessitates 200 °C higher recrystallization temperature as compared to V-Ti-Cr system. This can be attributed to high melting point of Ta, which results in relatively lower diffusion, rendering the kinetics of the thermally activated processes of recovery, nucleation and growth slower. The developed V-Ti-Ta alloy system exhibited increase in the strength and hardness proportional to its concentration of Ta in the alloy. Strengthening due to Ta addition needs a further analysis before it can be attributed to any specific factor. This is because contribution to strength can come from various factors, of which solid solution strengthening is one of the factors. Additional factors that influence strength are the role of precipitates. As already brought out, the current alloy system does show significant precipitation of TiC precipitates whose role cannot be ignored. In this context it is pertinent to discuss the observed trends in the strength and hardness (Fig. 5.8-5.10) properties as a function of Ta.

In an alloy system, (i) substitutional solid solution effect of Ta, (ii) interstitial solid solution effect of C, N, and O impurities, (iii) precipitation hardening due to TiC based precipitates, (iv) Hall-Petch effect (matrix grain size 40-50 µm) and (v) degree of cold work are the major factors which contribute to the strength in the alloy. In the case of current alloy system, increase in the yield strength, as shown in Fig. 5.10, aforementioned factors (i), (ii) and (iii) are relevant, as the microstructures employed for compression testing were fully recrystallized having similar grain sizes (40-50µm). Further, variation due to precipitate size and its volume fraction among the 1300 °C recrystallized alloys can also be ruled out (based on the microscopy evidence of 'nominally' similar volume fraction of precipitates[1] in all these alloy samples with different Ta contents). Note that the origin of the precipitation is due to the presence of C, N and O, which are present in nearly same concentration in all the samples of present study as given in experimental chapter. This rules out contribution from both the interstitial solid solution strengthening and precipitation strengthening for the observed systematic variation of strength with changing Ta content. Thus the observation of linear increase in strength with Ta (see Fig. 5.10) could be due to solid solution strengthening effect of Ta in this alloy system. In order to understand the role of Ta in substitutional solid solution strengthening, a simplified model based on the elastic interaction between local stress fields of solute atoms with dislocations was used. The magnitude of the interaction force (between solute atom and dislocation) or strengthening increases with an increase in both the atomic size misfit parameter (δa) and the modulus misfit parameter (δ_G) of the solute and solvent atoms as defined below [139].

$$\delta a = \frac{1}{a}\frac{da}{dc} \dots \dots \dots \dots \dots \dots \dots \dots \dots \dots \dots \dots (5.1)$$

---

[1] Due to inhomogeneous distribution of precipitates, volume fraction quantification based on image analysis was not attempted. Observance of large regions of samples, however, indicated no significant difference in the number and size of precipitates among different samples treated at 1300 °C. Hence, it was concluded that precipitate volume fraction is "nominally" similar among the different samples used in the compression testing.

$$\delta G = \frac{1}{G}\frac{dG}{dc} \ldots \ldots \ldots \ldots \ldots \ldots \ldots \ldots \ldots (5.2)$$

where a is the lattice parameter, G is shear modulus and c is concentration.

The resultant solute-induced solid solution strengthening ($\nabla\sigma$) arising from both of these factor can be estimated as

$$\nabla\sigma = AG\delta^{\frac{4}{3}}C^{\frac{2}{3}} \ldots \ldots \ldots \ldots \ldots \ldots \ldots \ldots (5.3)$$

Where the effective misfit parameter $\delta = \delta_G + \beta\delta_a$, A is a material-dependent dimensionless constant of the order of 0.1 and β is a constant dependent on the type of mobile dislocation, which is 3 for screw dislocations. C is the concentration of the solute [139].

Table 5.2 shows the relevant parameters used for computation in equations 5.1-5.3. Comparison of theoretically computed (from equation 5.3) and experimentally obtained values for the current alloy samples are shown in Table 5.3. It can be seen that that on the addition of Ta, the computed strength of the alloys increases which is very close to the experimentally obtained values in the alloy. This substantiates the hypothesis that solid solution strengthening effect of Ta is the chief governing factor in determination of strength in this system. The fact that the fitting parameter n_j (Fig. 5.11) remains low suggests weak influence of dislocation based hardening on the evolution of strength and corroborate the above conjecture.

Table 5.2: Atomic radius (r) and shear modulus (G) of metals.

Element /property	V	Ti	Ta
r (pm)	135	141.8	143
G (GPa)	46.6	44	69

Table 5.3: Computed yield strength (σ_{Th}) due to solid solution strengthening and experimentally determined yield strength (σ_{Exp}) of V-4Ti-xTa alloys.

Name of the alloy	Measured atom fraction of Ti in alloy (X_{Ti})	Measured atom fraction of Ta in alloy (X_{Ta})	Incremental strengthening contribution arising from Ti $\Delta\sigma_{Ti}$ (MPa)	Incremental strengthening contribution arising from Ta $\Delta\sigma_{Ta}$ (MPa)	Total incremental strengthening arising from both Ti and Ta $\Delta\sigma_{Total}$ (MPa)	Computed yield strength σ_{Th} (MPa)	Experimentally determined yield strength σ_{Exp} (MPa)
V-4Ti	0.0393	0	54	0	54		206
V-4Ti-1Ta	0.0422	0.0024	56	30	86	236	248
V-4Ti-3Ta	0.0432	0.0076	57	65	122	271	276
V-4Ti-7Ta	0.0435	0.0198	58	123	181	329	369

The presence of Ta increases the strength of V-Ti-Ta alloys by substitutional solid solution strengthening. In addition of that, role of Ta in increasing the high temperature stability of the precipitates is also equally important. In V-4Ti-4Cr alloy, TiC precipitates were reported to get dissolved at temperatures above 1100 °C, whereas, in the present study (V-Ti-Ta alloys), the precipitates remained stable at temperature as high as 1300 °C. In order to ascertain the presence of precipitate at high temperature (1300 °C), a series of high temperature quenching experiments were conducted. Alloys with different Ta contents were deformed to 70 % and heat treated at 1300 °C for 3 hrs (in vacuum capsules made of quartz) followed by rapid quenching in water to arrest the high temperature structure. The resulting microstructure was characterized by SEM and also EBSD (Fig. 5.14 (a-c)), clearly shows the presence of precipitates (shown by arrows) in the microstructure. In order to delineate the location of the precipitates (with respect to underlying matrix phase) grain boundaries, determined by EBSD analysis, was overlaid on the SEM map, from the corresponding region. It is clear that majority of the precipitates are present inside the recrystallized grains in the form of bands, while noticeable fraction was present along the grain boundaries of the recrystallized grains. It may be noted that bands of the precipitates correspond to the prior shear bands of the deformed samples (which were subjected to 1300 °C treatment). Thus one can infer that the intra-grain precipitates did not dissolve at as high temperature as 1300 °C indicating superior high temperature stability of the precipitates in this V-Ti-Ta alloys. The precipitates identified in the present study exhibited the presence of Ta in TiC phase. The peak shift observed in XRD results coupled with EDS spot pattern analysis indicated the presence of Ta in the precipitates, even in the samples annealed at 1300 °C. However, in case of V-4Ti-4Cr alloy, TiC precipitates were reported to be devoided of Cr. This suggest that Ta has role in enhancing the stability of the precipitates. In order to ascertain the higher stability of precipitates due to Ta, Gibbs free energy of TiC formation as a function of Cr and Ta concentration was determined using

CALPHAD approach [140]. Results shown in Fig. 5.15, indicate that addition of Ta in TiC lowers the free energy of TiC phase whereas, addition of Cr results in increased free energy, suggesting that Ta promotes the stability of TiC precipitates in contrast to Cr.
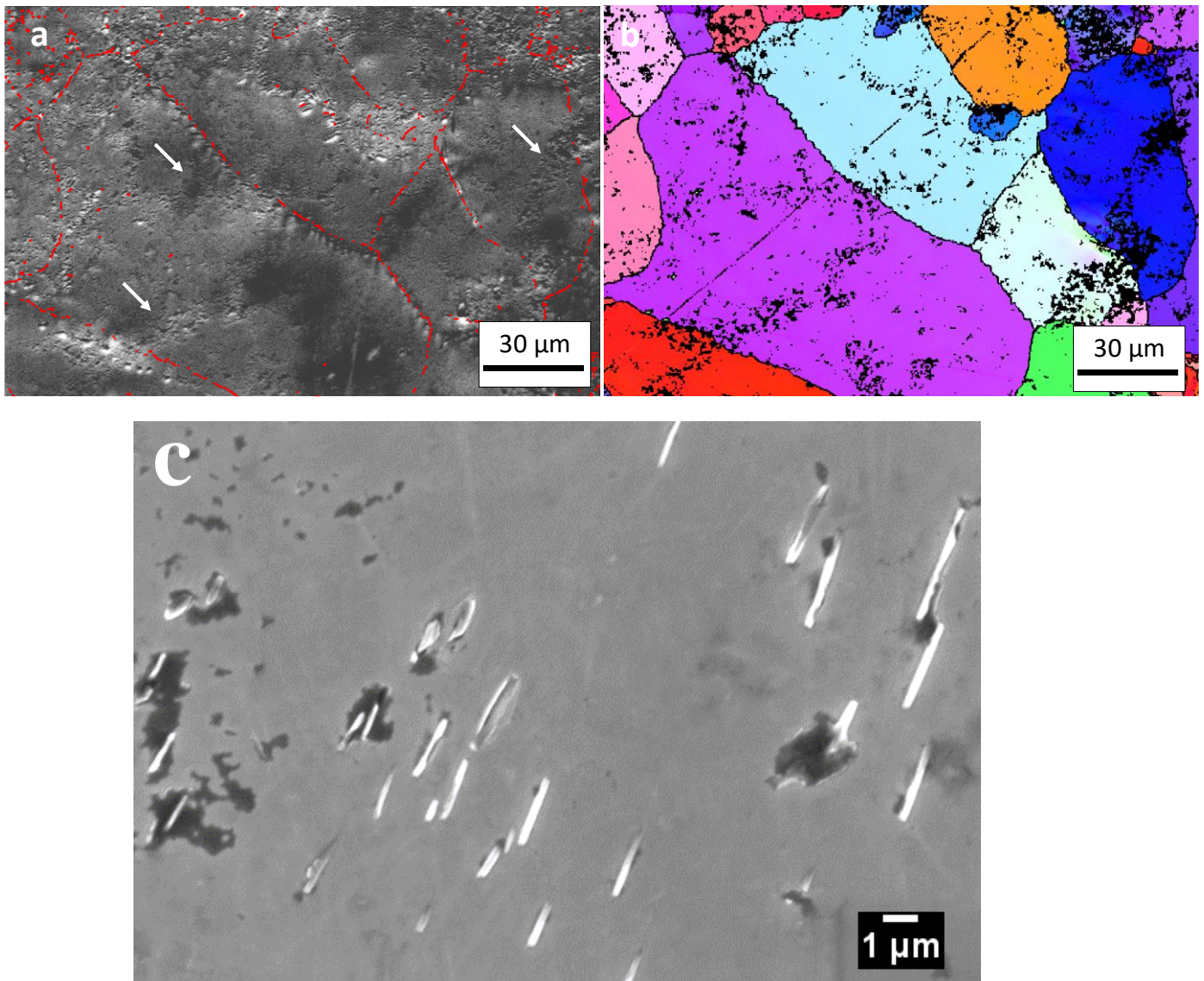
Figure 5.14 (a-c): (a) SEM micrograph obtained at 70° tilt angle (with superimposed grain boundaries in red) of V-7Ta-4Ti alloy after cold rolling, followed by heat treatment at 1300 °C and quenching. (b) The corresponding IPF colored obtained by EBSD technique. The white arrows highlight the presence of carbides along possible prior shear or deformation bands, which remained undissolved even after the abovementioned heat treatment (c) SEM micrograph obtained at 0° tilt angle showing the presence of precipitates.
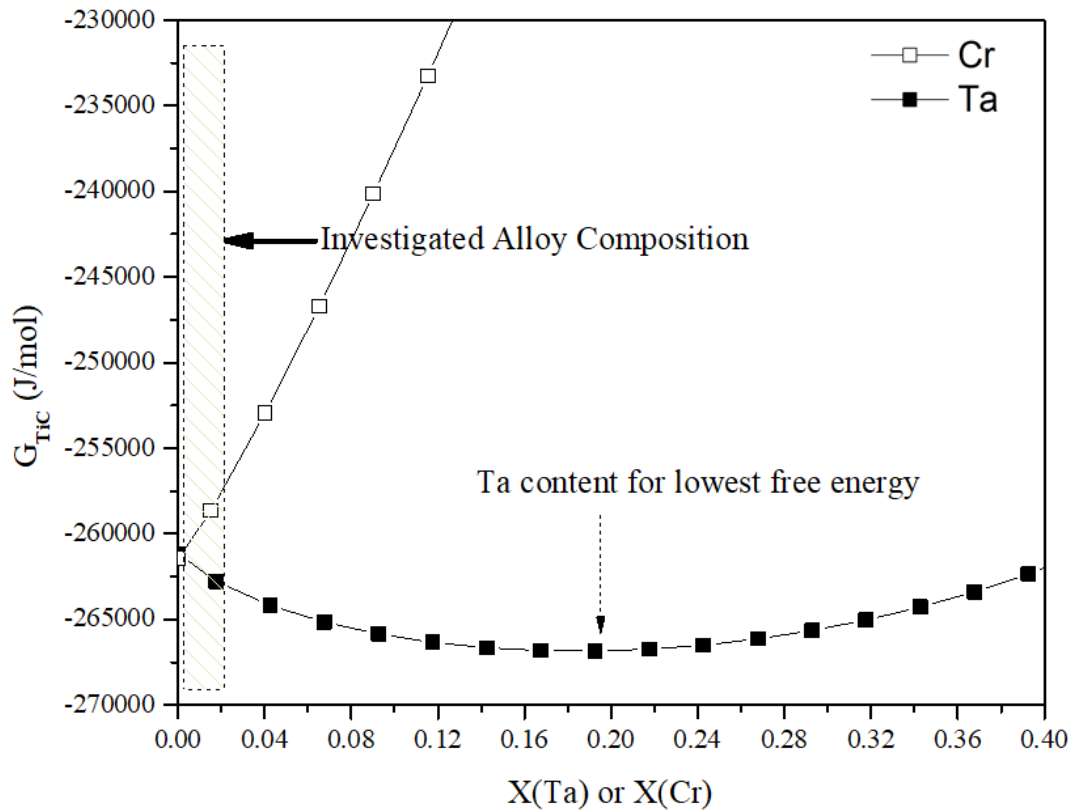
Figure 15: Free energy of TiC phase as a function of Ta and Cr composition showing the decrease in free energy due to presence of Ta and increase due to Cr.

These calculations thus indicate that Ta additions must result in increased stability of TiC precipitates or the dissolution of the precipitates becomes thermodynamically less favourable at any given processing temperature. In essence, stability of the precipitates increased due to the presence of Ta in the precipitates. This has an indirect beneficial effect on the applicability of the alloy at lower temperature. The applicability of the known reference alloy system (V-Ti-Cr) is restricted to above 400 °C. This is due to the radiation induced dissolution of the TiC precipitates [48-50], which results in increased interstitial content in the matrix leading to undesirable hardening and consequent upward shift in DBTT [48-50]. From this point of view, increased stability of the Ti(Ta)-C precipitates observed in the current system can push the low temperature limit to further lower side. Thus when combined with the advantage offered by solid solution strengthening of Ta and hence higher strength at higher temperature, can be an

effective means of increasing the operational temperature window for nuclear structural applications.

5.7 Summary

In the present study, role of Ta on the recrystallization parameters (time and temperature) of V-Ti-Ta alloys was studied. The study provided detailed evolution of microstructures in Vi-Ti-Ta alloys for different concentration of Ta during the process of recovery and recrystallization. In addition, detailed characterization of the precipitates presents in the as-solidified, deformed and annealed samples of V-Ti-Ta alloys was carried out. Mechanical properties, such as hardness and yield strength, were evaluated and correlations between microstructure and properties were brought out. The major findings could be summarized as follows:

1) Extended recovery was observed to be the major softening mechanism operative in cold working samples, which was observed to extend to 1150 °C in the V-4Ti-7Ta alloy.

2) Recrystallization temperatures in V-Ti-Ta alloys were estimated to be in the range of 1200-1300 °C, which is neraly 200 °C higher than the recrystallization temperature range observed in V-Ti-Cr alloys.

3) The rolled V-Ti-Ta alloy showed a rolling texture of θ-fibre which is generally not observed in the case of bcc alloys; except in Fe-Si alloy and based on this observation it was inferred that Ta imparts strong solid solution strengthening. On annealing in the temperature range 1000 °C -1300 °C, an apparent increase of the γ-fibre texture and a complimentary decrease in the strength of θ-fibre texture was observed. Based on the changes in the recrystallization texture it was proposed that oriented nucleation being the dominating mechanism for the recrystallization texture

4) V-Ti-Ta alloys exhibited superior strength characteristics and substitutional solid solution strengthening of Ta was found to be effective strengthening mechanism.

5) XRD and EDS analyses showed nearly equi-partitioning of Ta in the precipitates as well as matrix phases of V-Ti-Ta alloys, which is in contrast to the V-Ti-Cr alloys, where nearly all the precipitates are devoid of Cr.

6) Thermodynamic stability of the precipitates examined as a function of Ta concentration in the phase has clearly shown that the presence of Ta enhanced the stability of the (Ti,Ta)(CON) precipitates in V-Ti-Ta alloys.

High temperature oxidation behaviour of V-Ti-Ta alloys

6.1 Preamble

Recrystallization behaviour and microstructure-property correlation of V-Ti-Ta alloys has been described in previous chapter 5. It was shown that the presence of Ta increases the strength and stability of the TiC precipitates, which may have beneficial effect on widening the operation temperature window of the V-Ti-Ta alloys. It has also been shown in chapter 3 that activities of Ti and V decrease as Ta content increases in V-4Ti-xTa alloys, which shows higher thermodynamic phase stability of the V-Ti-Ta alloys. Therefore, combined effect of higher thermodynamic stability and improved thermo-mechanical properties of V-Ti-Ta alloys make them suitable for high temperature structural application in fusion reactor. However, in the case of any catastrophic events (leak) in a fusion reactor, the structural materials would likely to undergo abrupt oxidation and result in deterioration of the structural integrity of the reactor vessel [141, 142]. Hence, it is worth to investigate the high temperature oxidation behaviour of the developed V-Ti-Ta alloys. In view of this, isothermal and non-isothermal oxidation behaviour of V-Ti-Ta alloys in the expected operational temperature ranges between 250 -750 °C has been studied in the present chapter. Role of Ta in improving the oxidation behaviour of otherwise oxidation prone vanadium have also been discussed and a comparison of oxidation behaviour of V-Ti-Ta alloys have been made with pure vanadium and reference V-4Cr-4Ti alloy.

6.2   Experimental observation

6.2.1   Non isothermal oxidation studies (TG-DTA)

To conduct oxidation studies on V-Ti-Ta alloys, non-isothermal experiments were carried out in a thermo-analyser (TG-DTA). The details of the TG-DTA experiments are provided in Chapter 3. This study was carried out to know the initiation of oxidation and the oxidation behaviour of pure V, Ti and Ta. It is worth to mention here that these experiments were performed only for pure metals, not for the alloys. The results of the non-isothermal TG-DTA experiments on V, Ti and Ta pure metals heated up to 1000 °C are presented in Fig. 6.1 (a, b and c) respectively. The results are also summarized in Table 6.1.
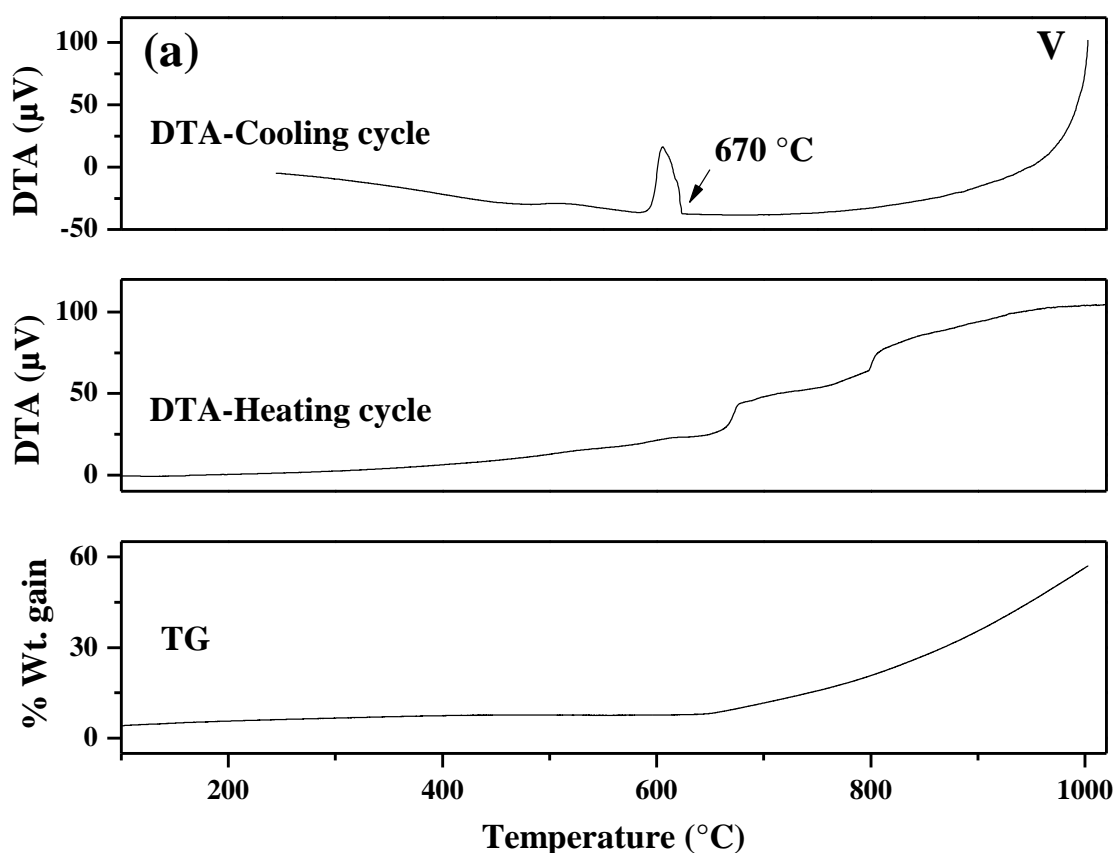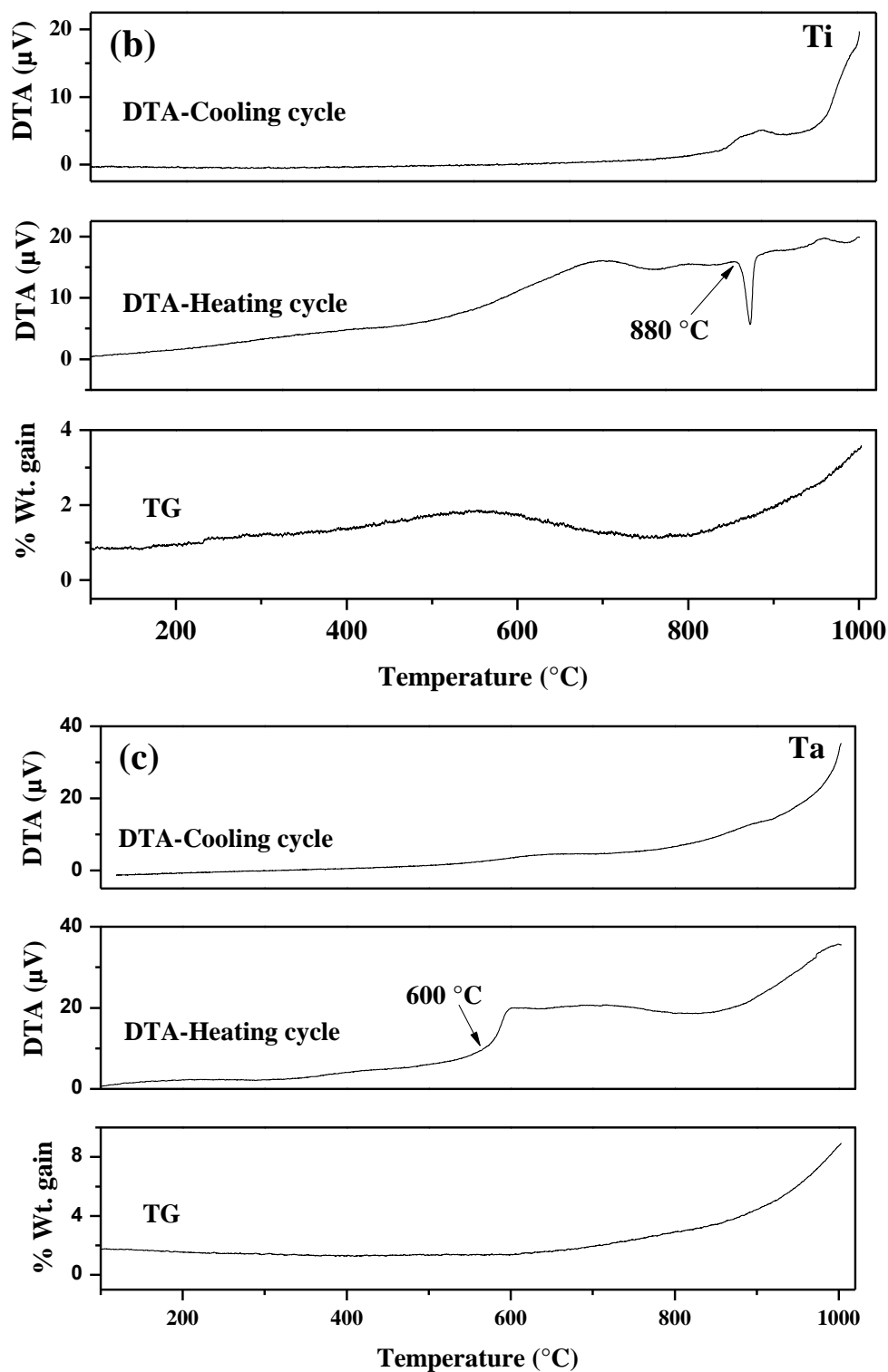
Figure 6.1(a-c): Non isothermal TG-DTA of V, Ti and Ta respectively in air upto 1000 °C showing the breakaway oxidation temperature of pure metals. In Fig 6.1(a) breakaway oxidation is due to melting of V_2O_5 (melting point 670 °C), Fig 6.1 (b) breakaway oxidation is due to peeling off the oxide layer resulting from α to β phase transition of Ti (Phase transformation temperature 880 °C) and in Fig 6.1 (c), breakaway oxidation is due to layered growth of oxide in Ta above 600 °C.

*Table 6.1: Result summary of Non isothermal oxidation studies of pure V, Ti and Ta metals (*RT- room temperature).*

Sample	Parabolic region		Linear region	
	Temperature	Weight gain (%)	Temperature	Weight gain (%)
V	RT to 670 °C	8	670 °C to 1000 °C	58
Ti	RT to 880 °C	2	880 °C to 1000 °C	3.6
Ta	RT to 600 °C	2	600 °C to 1000 °C	8.9

It can be observed from Fig. 6.1(a) that pure vanadium shows marginal weight gain from room temperature to about 670 °C. In this temperature range, weight gain follows the parabolic curve and the total weight gain was observed to be 8 %, however, for temperatures beyond 670 °C, weight gain increases abruptly and reaches to 58 % till 1000 °C. In contrast, Ti shows moderate weight gain till 880 °C (Figure 6.1 (b)) and the weight gain remained below 2 %, but above 880 °C, Ti showed substantial increase in weight gain with total weight gain as 3.6 % till 1000 °C. Ta also shows a similar behaviour of very slow initial weight gain (Fig. 6.1(c)) which remained below 2 % till 600 °C and then increased abruptly above 600 °C and final weight gain was 8.9 % upto 1000 °C. Table 6.1 summarises these results. From these results it could be inferred that among the three elements (V, Ti and Ta), V showed the poorest oxidation resistance, but all the elements show break away oxidation temperature, which is either due to oxide melting or peeling off oxide layer.

6.2.2   Isothermal oxidation studies

To study the oxidation behaviour of newly developed V-Ti-Ta alloys, isothermal oxidation experiments were performed in the furnace for different time periods ranging from 1 hr to 64

hrs. For the purpose of comparison, pure metals (V, Ti and Ta) were also subjected to similar oxidation conditions.
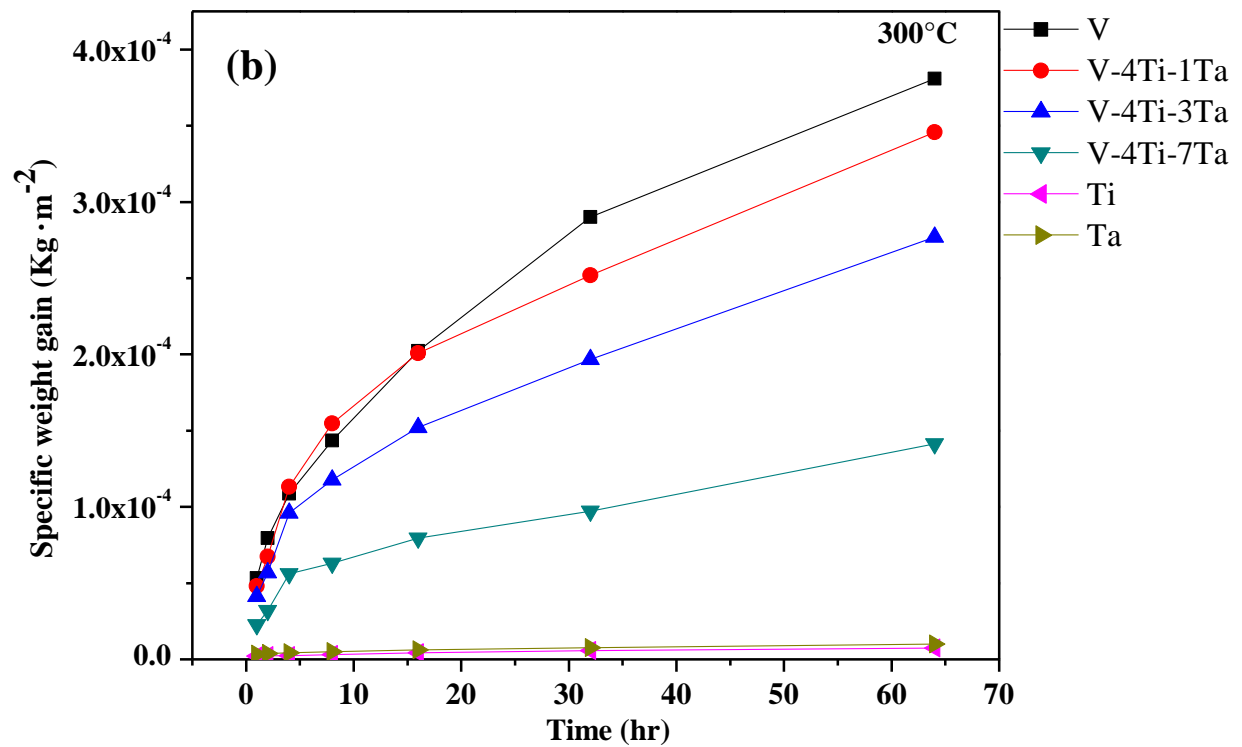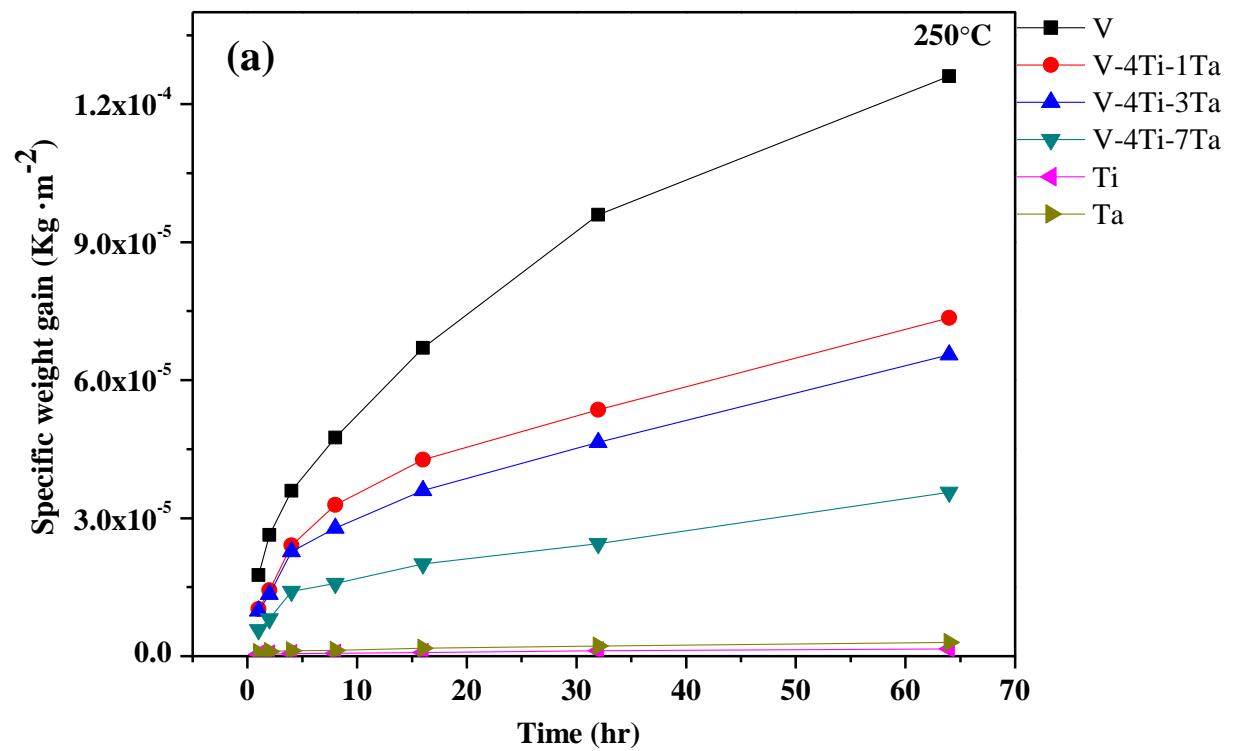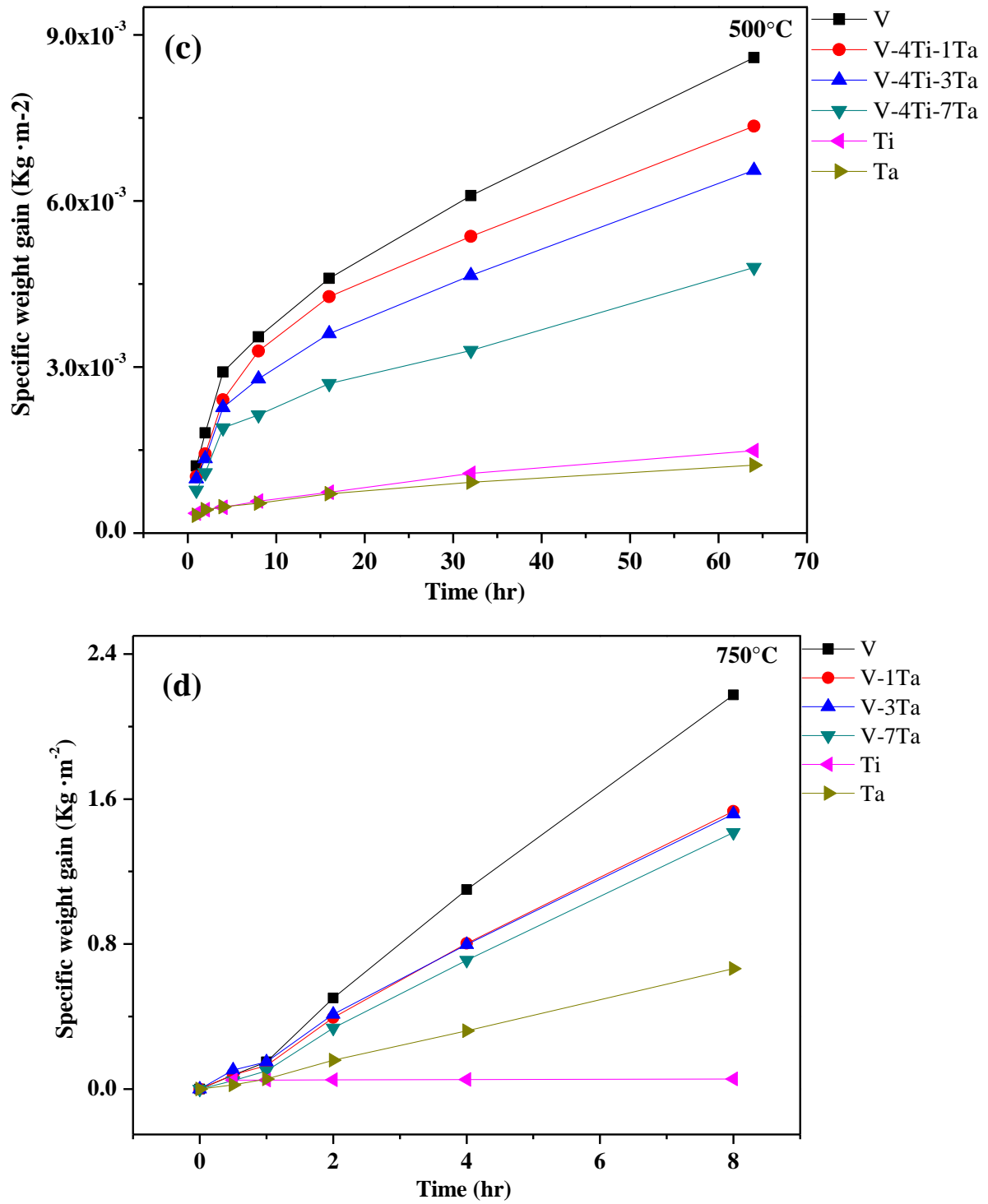
Figure 6.2 (a-d): Specific weight gain data with respect to holding time (Isothermal oxidation) of the studied samples after exposure in air at (a) 250 °C (b) 300 °C (c) 500 °C and (d) 750 °C. In the temperature range 250-500 °C, parabolic oxidation was observed in all samples, whereas, at 750 °C, all other samples showed linear oxidation rate except Ti which showed parabolic oxidation rate.

Table 6.2: Result summary of isothermal oxidation studies showing specific weight gain at particular temperature and time.

Temperature (°C)	Specific weight gain (Kg m^{-2})					
	V	Ti	Ta	V-4Ti-1Ta	V-4Ti-3Ta	V-4Ti-7Ta
250 (64 hrs)	1.26×10^{-4}	1.59×10^{-6}	2.95×10^{-6}	7.35×10^{-5}	6.55×10^{-5}	3.55×10^{-5}
300 (64 hrs)	3.80×10^{-4}	7.47×10^{-6}	1.00×10^{-5}	3.11×10^{-4}	2.77×10^{-4}	1.41×10^{-4}
500 (64 hrs)	8.59×10^{-3}	1.49×10^{-3}	1.23×10^{-3}	7.35×10^{-3}	6.55×10^{-3}	4.8×10^{-3}
750 (8 hrs)	2.17	0.055	0.66	1.53	1.52	1.41

Figs. 6.2 (a-d) show the isothermal oxidation behaviours of the pure V, Ti and Ta samples in addition to the alloys studied at 250, 300, 500 and 750 °C. Specific weight gain i.e., weight gain per unit area ($\Delta W/A$), data is plotted with respect to time and temperatures. Specific weight of all samples increased as time progressed at each temperature. These results are summarized in Table 6.2. At 250 °C, weight of vanadium sample increased with time and showed specific weight gain of 1.26 x 10^{-4} kgm^{-2} after 64 hrs (Fig. 6.2 (a)). The specific weight gains of Ti and Ta after 64 hrs of exposure were 1.59 x 10^{-6} kgm^{-2} and 2.95 x 10^{-6} kgm^{-2} respectively; which are two orders lower as compared to pure vanadium. Similar observation was noticed for pure V samples heated at 300 °C and 500 °C (Fig. 6.2 (b-c)), for vanadium similar trends have been reported by several authors [106, 109-111, 113]. Ti and Ta samples also exhibited parabolic oxidation at 300 and 500 °C. However, the nature of specific weight gain changed its pattern at 750 °C. At 750 °C, specific weight of pure vanadium increased rapidly with time and showed significantly higher (2.17 kgm^{-2}) specific weight gain after 8 hrs exposure (Fig. 6.2 (d)). Upon cooling the sample, yellowish solidified mass was noticed over the crucible along with the specimen. Similar to vanadium, oxidation of Ta sample was also

rapid and showed specific weight gain of 0.66 kgm^{-2} after 8 hrs exposure. However, the specific weight gain of Ti was only 5.5 x 10^{-2} kgm^{-2} (2 order lesser as compare to V and Ta) after 8 hrs of exposure at 750 °C and specific weight gain curve was still parabolic.

The V-4Ti-1Ta alloy showed lower specific weight gain (7.35 x 10^{-5} kgm^{-2}) as compared to pure V after 64 hrs of exposure at 250 °C. With further addition of Ta into V, i.e. V-4Ti-3Ta and V-4Ti-7Ta alloys, the specific weight gain was further lowered to 6.55 x 10^{-5} kgm^{-2} and 3.56 x 10^{-5} kgm^{-2} respectively. Similar behaviour could be observed for the samples heated at 300 °C and 500 °C. This implies that the addition of Ti and Ta into vanadium enhanced the oxidation resistance of the V alloys. On comparison with commercial V-4Cr-4Ti (V44 alloy), it can be seen that the commercial alloy [107] has a higher weight gain of 6.0 x10^{-3} kgm^{-2} as compared to V-4Ti-7Ta alloy (4.8 x 10^{-3} kgm^{-2}) under similar conditions (500 °C, 64 hrs). Both the alloy systems, V-Ti-Ta specimens in our study (Fig. 6.2(a-c)) and V-Cr-Ti alloys reported in literature [107, 109-111], show parabolic behaviour in the temperature range of 250-500 °C.

V-4Ti-xTa (x = 0,1,3, 7) alloys also exhibited linear oxidation characteristics at 750 °C similar to that of pure vanadium. From Fig. 6.2(d), it could be seen that at 750 °C, V-4Ti-1Ta alloy showed rapid oxidation and the specific weight gain was 1.53 kgm^{-2} after 8 hrs. The alloys having higher Ta, i.e. V-4Ti-3Ta and V-4Ti-7Ta alloys showed marginally improved oxidation resistance with specific weight gain of 1.51 and 1.41 kgm^{-2} respectively.

6.2.3   Oxidation kinetics and thermodynamic properties

In order to determine oxidation kinetics, the weight change data obtained by isothermal oxidation experiments were correlated with time by fitting the weight gain data into the following equation [143-148].

$$\left(\frac{\Delta W}{A}\right)^n = kt \dots\dots\dots\dots\dots\dots\dots\dots\dots\dots\dots . (6.1)$$

Where, $\frac{\Delta W}{A}$ is the weight gain per unit surface area, k is oxidation rate constant, n is reaction index, and t is time. Regression analysis of the weight gain data would yield the k value through calculation of the slope of the best fit line of $\frac{\Delta W}{A}$ vs. t plot. The temperature dependence of k can be quantified by an Arrhenius type equation.

$$k = k_0 e^{\frac{-Q}{RT}} \dots\dots\dots\dots\dots\dots\dots\dots\dots\dots . (6.2)$$

Where k_0 is the frequency factor (constant for a given material), Q the activation energy for oxidation, R the gas constant (8.314 J.mol^{-1}.K), and T is absolute temperature. The value of Q can be calculated by plotting ln K against 1/T, in which the slope of the best fit line is equal to Q/R.

Since all the studied samples (V and V-4Ti-xTa alloy) were showing parabolic nature of specific weight gain with time in the temperature range of 250-500 °C, the square of specific weight gains $(\Delta W/A)^2$ in the above temperature range (250, 300 and 500 °C) were plotted against time (t), as shown in Fig. 6.3(a-c) respectively. Using relationship given in equation 6.1, parabolic oxidation rate constant k_p was determined from the slope of $(\frac{\Delta W}{A})^2$ versus t plot. The values of the constant parabolic oxidation rate were determined by means of a linear regression method. The obtained values of oxidation rate constant k_p values for each temperature are presented in Table 6.3. It can be seen from Table 6.3 that oxidation rate constant k_p increases with increasing temperature. Rate constant of vanadium at 250 °C was found to be 2.50×10^{-10} Kg^{2}m^{-4}h^{-1}, which increased to 1.13×10^{-6} Kg^{2}m^{-4}h^{-1} at 500 °C. In the temperature range of 250-500 °C, the oxidation rate was maximum at 500 °C and minimum at

250 °C for all the samples. Rate constant exhibited by V-4Ti-xTa alloys was significantly lower as compared to vanadium in the studied temperature range. V-4Ti-7Ta alloy exhibited one order lower rate constant (3.43×10^{-7} $Kg^2m^{-4}h^{-1}$) as compared to V (1.13×10^{-6} $Kg^2m^{-4}h^{-1}$) at 500 °C

The activation energy for air oxidation was determined using equation 6.2. The Arrhenius plots for the all samples (plot of $\ln k_p$ vs 1/T) are shown in Fig. 6.4. The slope of the best fit line obtained from the "$\ln(k_p)$ vs. 1/T" plot yielded the activation energy for air oxidation (Qox). Activation energies for air oxidation obtained from slope of Fig. 6.4 are summarized in Table 6.3.
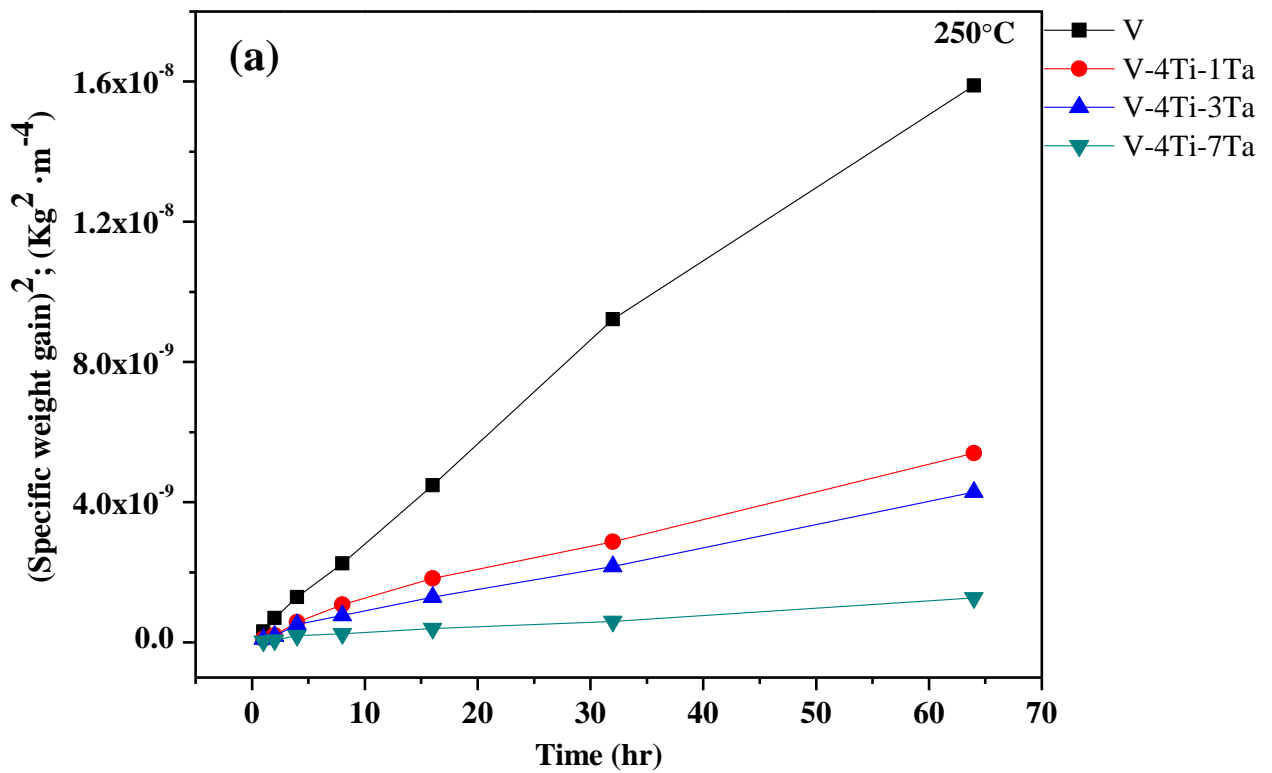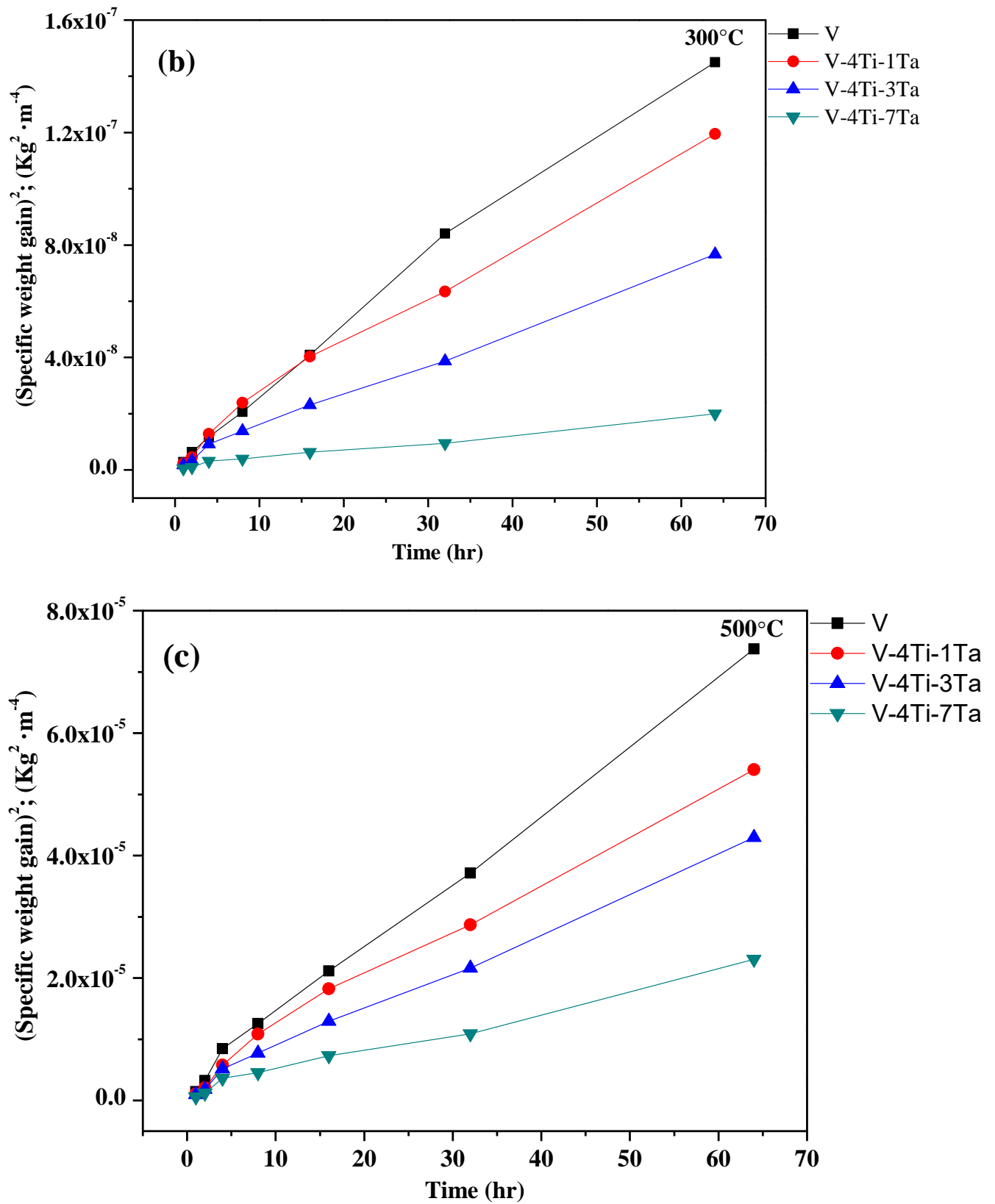
Figure 6.3(a-c): A plot of (ΔW/A)² vs. time for obtaining the parabolic oxidation rate (kₚ) constant at different temperatures (a) 250 °C (b) 300 °C and (c) 500 °C respectively. V-Ti-Ta alloys showed substantially less weight gain compared to vanadium.
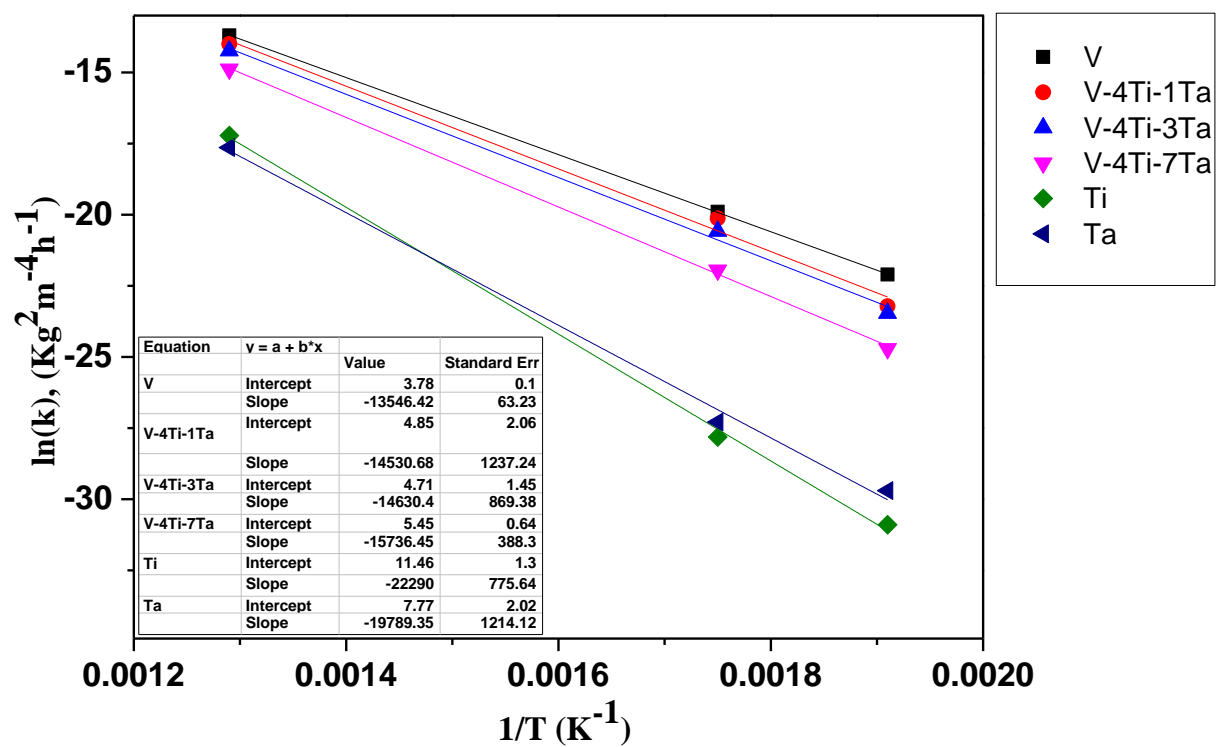
Figure 6.4: Parabolic rate constant in air environment as a function of the reciprocal absolute temperature.

Table 6.3: Oxidation parameters at various temperatures for V and V-4Ti-xTa alloys.

Metal or Alloy	Temp (°C)	Rate constant ($Kg^2 m^{-4} h^{-1}$)	Activation energy for air oxidation ($kJ mol^{-1}$) (Q_{ox})	Diffusion coefficient of oxygen ($m^2 h^{-1}$) (D_O)	Activation energy for diffusion of O in oxide ($kJ mol^{-1)}$) (Q_D)
V	250	2.50×10^{-10}		5.73×10^{-17}	149
	300	2.28×10^{-9}	112	5.23×10^{-16}	154
	500	1.13×10^{-6}		2.58×10^{-13}	176
V-4Ti-1Ta	250	8.22×10^{-11}		1.88×10^{-17}	155
	300	1.82×10^{-9}	120	4.16×10^{-16}	156
	500	8.32×10^{-7}		1.90×10^{-13}	179
V-4Ti-3Ta	250	6.48×10^{-11}		1.48×10^{-17}	157
	300	1.16×10^{-9}	121	2.65×10^{-16}	159
	500	6.55×10^{-7}		1.50×10^{-13}	182
V-4Ti-7Ta	250	1.85×10^{-11}		4.25×10^{-18}	164
	300	2.92×10^{-10}	130	6.70×10^{-17}	167
	500	3.43×10^{-7}		7.86×10^{-14}	189

Based on the phase analysis of oxide, using Grazing incidence X-ray diffraction (GIXRD) technique, described later, diffusion coefficient (D_{oxygen}) was calculated using the relation proposed by Wach et al. [109, 113, 149], from the parabolic rate constant (k_p) as

$$k_p = 2D_{oxygen}W_{MO_x}^2\rho_{MO_x}^2 \dots\dots\dots\dots\dots\dots\dots\dots\dots (6.3)$$

Where D_{oxygen} is diffusion coefficient of the oxygen, is W_{MO_x} mass fraction of oxygen in the oxide MO$_x$ that forms, and ρ_{MO_x} is the density of the metal oxide (MO$_x$). For V$_2$O$_5$, $W_{V_2O_5} = 0.4398$ and $\rho_{V_2O_5} = 3.357 \times 10^3 \, kg.m^{-3}$. The activation energy for diffusion(Q$_D$) was estimated by using diffusion coefficient (D_{oxygen}) at a temperature T as follows which has been already described [109, 113, 150, 151]:

$$D = D_\theta exp(\frac{Q_D}{R\theta} - \frac{Q_D}{RT}) \,................................. (6.4)$$

Where D_θ, and θ are constants characteristic of the diffusant oxygen.

$$D_\theta = \frac{h}{4\pi m} \text{ and } \theta = \frac{h\nu}{k_B} \,...........................(6.5)$$

where h and k$_B$ are the Planck's and Boltzmann's constants, respectively; m the mass per atom of the diffusing species and ν its vibrational frequency. For oxygen the expression becomes

$$D_{oxygen} = 1.99 \times 10^{-9} exp[\frac{Q_D}{R}(\frac{1}{2050} - \frac{1}{T})] \,..................... (6.6)$$

Diffusivity of oxygen and activation energy for diffusion of oxygen calculated from these equations are summarized in Table 6.3.

6.2.4 Phase analysis of surface layer

The GIXRD patterns obtained from the oxide scales on the samples for the V and V-4Ti-7Ta samples obtained after 64 hrs exposure at 500 °C are shown in Fig. 6.5. It can be seen that in the case of V and V-4Ti-7Ta samples most dominant peaks were pertaining to the V$_2$O$_5$ phase which indicates that the majority of the oxide layer on these samples were comprised of V$_2$O$_5$. The presence of some additional smaller peaks of VO$_2$ in the GIXRD pattern also indicated that a small amount of VO$_2$ is also present in the oxide layer. In the case of V-Ti-Ta alloys, any

separate peak of oxides of Ti and Ta was not noticed in any of the oxidized sample surfaces. Absence of the peaks of Ti and Ta or their oxides on the oxide layer indicates that either both the elements (Ti and Ta) remain in a solid solution with V_2O_5 oxide phase or their amount is below the detection limit of XRD. However, during SEM-EDS analysis of V-4Ti-7Ta samples, apart from the presence of O and V, presence of Ti and Ta were also detected in the oxide layer. Natesan et al. have reported that during the oxidation of V-4Cr-4Ti alloy at 1 atm oxygen pressure, formation of V_2O_5 is invariably associated with the formation of minor complex oxide $V_2Ti_3O_9$ [108]. In the present study, detailed investigation did not reveal the presence of $V_2Ti_3O_9$ and therefore we believe that addition of Ta has retarded the formation of the complex oxide. Two observations can be put forward to support this conjecture. First, XRD pattern did not reveal any additional peak pertaining to the complex oxide. Secondly, partial melting of surface oxide layer on a V-4Ti-7Ta sample exposed in air at 750 °C further supported the view that V_2O_5 which has melting point of 670 °C is the predominant oxide. Other complex oxides reported have higher melting temperatures; hence the possibility of complex oxides could be precluded. These results of predominance presence of V_2O_5 with minor VO_2 in the present study are in agreement with those reported in literature for V and V-Cr-Ti alloys [109, 113, 150]. Formation of the single VO_2 phase at lower oxygen pressure (36 Torr and below) has also been reported [109, 113, 150]. XRD patterns of pure Ti and Ta showed the presence of single rutile phase of TiO_2 and β-Ta_2O_5 respectively.
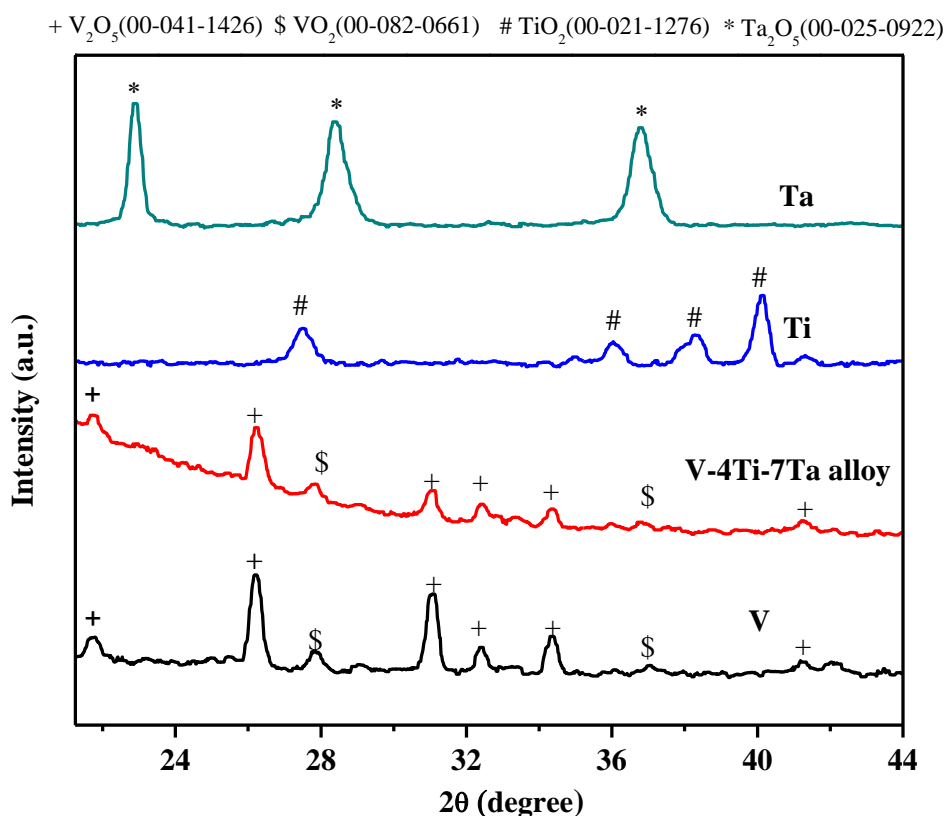
Fig. 6.5 XRD patterns of V, V-4Ti-7Ta, Ti and Ta samples treated at 500 °C in air for 64 hrs duration. V and V-4Ti-7Ta alloy showed presence of V_2O_5 phase while Ti and Ta samples showed the presence of TiO_2 and Ta_2O_5 phases respectively.
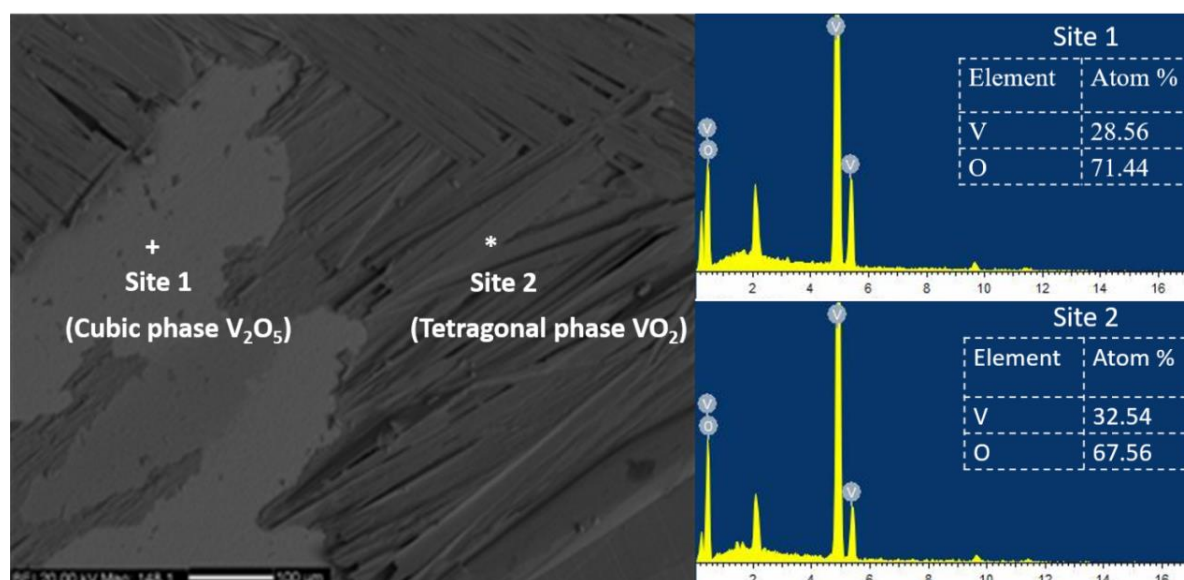
Figure 6.6: Microstructure of vanadium sample exposed at 750 °C in air for 8 hrs showing continuous (site 1) and needle shaped morphologies (site 2). Site 1 corresponds to cubic V_2O_5 phase and site 2 is tetragonal VO_2 phase.

138
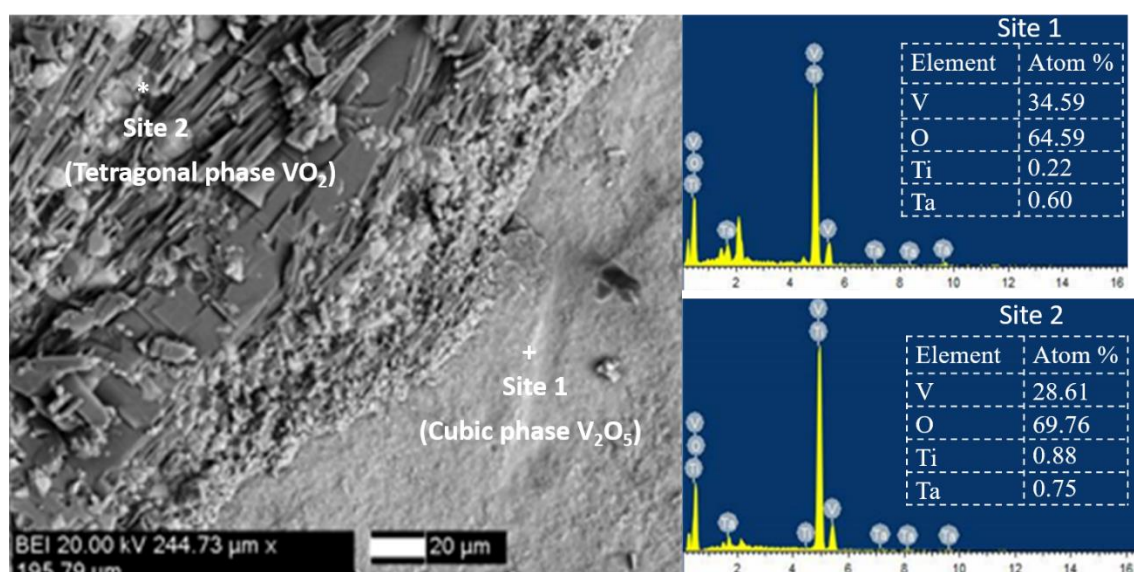
Figure 6.7: Microstructure of V-4Ti-7Ta alloy sample exposed at 750 °C in air for 8 hrs showing needle shape morphologies with reduced aspect ratio. Site 1 corresponds to cubic V_2O_5 phase and site 2 is tetragonal VO_2 phase.

6.2.5 Surface morphology of the oxide layer

Typical back scattered electron micrograph from the surface of the pure V sample is shown in Fig. 6.6. Two distinct regions, white continuous and needle shaped regions, could be observed in the microstructures of oxidised samples. White continuous region shown in Fig. 6.6 is nearly monolithic and devoid of any feature. It could, therefore, be due to the molten V_2O_5 spreading across the surface and later forming a solidified layer. EDS results have shown that the peaks of V and O and the composition of the oxide phase was V_2O_5. These results indicated that the molten V_2O_5 wetted the surface to cover whole area but it could not form a protective layer. Apart from V_2O_5, the needle shaped phase on EDS analysis was found to be containing VO_2. In addition, preferential growth of the VO_2 phase along specific direction was observed. The preferential growth along specific crystallographic direction shown by VO_2 phase may be attributed to its tetragonal crystal structure. Presence of similar needle shape VO_2 phase was also observed on the oxidised surface of V-4Ti-7Ta (Fig. 6.7). However, one major difference in the form of the length of needle was observed. Lower aspect ratio of the needle phase in the

case of the V-4Ti-7Ta alloy as compared to pure V was obvious. It seems that length of the needle is governed by the presence of Ti and Ta.
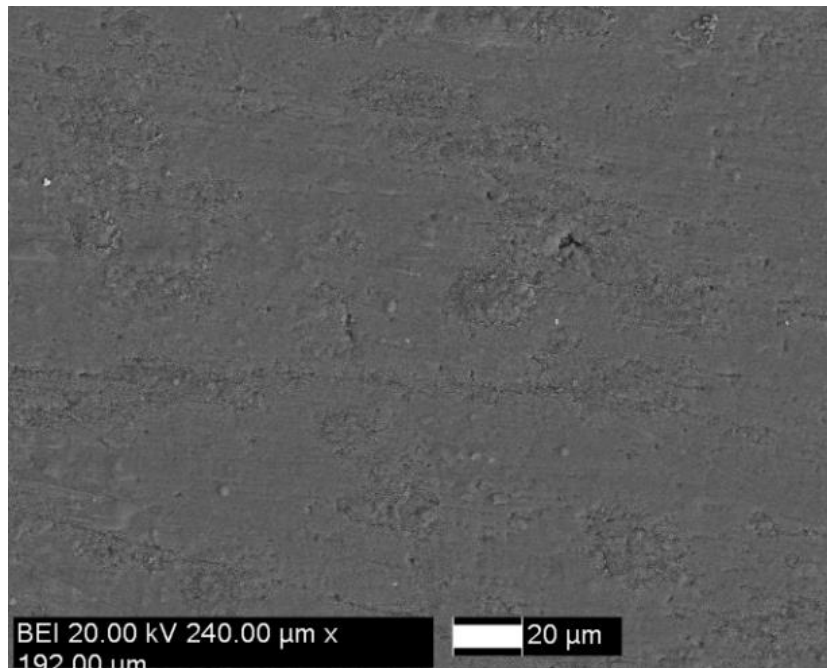
Figure 6.8: Microstructure of Ti sample exposed at 750 °C in air for 8 h showing continuous oxide layer.
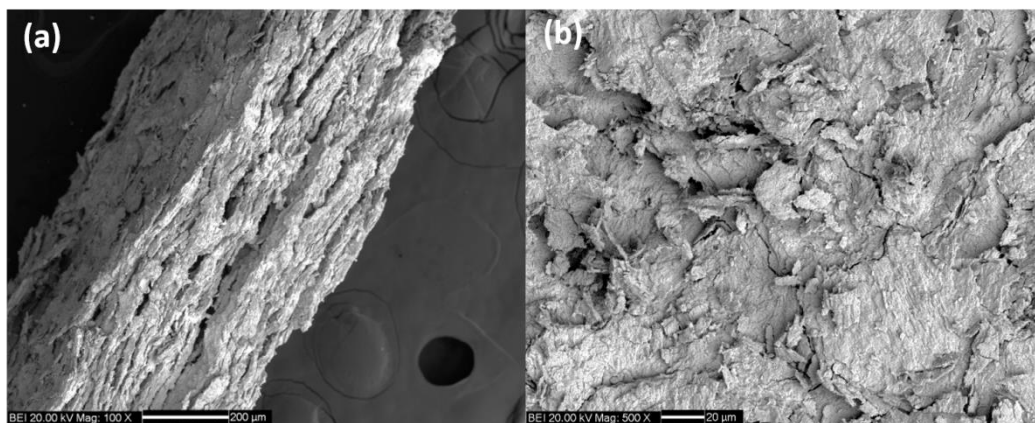
Figure 6.9 (a-b): Microstructure of Ta sample exposed at 750 °C in air for 8 hrs showing layered morphology.

Surface morphology of Ti sample is shown in Fig. 6.8. Ti forms an adherent oxide layer (TiO_2). Adherent oxide layer on Ti surface provides good oxidation resistance which manifests in form of lower weight gains during isothermal oxidation experiments. In Ta sample it was found that at 750 °C, the oxide layer was non adherent to base metal and it was peeling off.

The SEM micrographs of the cross section of the oxide layer is shown in Fig. 6.9 (a-b). It can be seen that oxide layer was found to be a layered structure. The oxide scales were identified to contain predominant of micro cracks which could expose the base material upon further oxidation.

In the aforementioned temperature range, among the metals or alloys selected in the present study, Ti was found to be the most oxidation resistant material followed by Ta and V was the least resistant to oxidation.

6.3   Discussion

In the present study, it was observed that all samples (V, Ti, Ta and V-Ti-Ta alloys) showed parabolic oxidation behaviour in the temperature range of 250-500 °C. The parabolic oxidation indicates protective nature of the oxide layer. However, at 750 °C, all samples, except Ti, exhibited linear oxidation behaviour which indicates that oxide layer became non-protective. Ti continued to show parabolic oxidation behaviour even utpo 750 °C. In the aforementioned temperature range, among the metals or alloys selected in the present study, Ti was found to be the most oxidation resistant material followed by Ta and V was the least resistant to oxidation. This study has also shown that the addition of Ti and Ta into vanadium has enhanced its oxidation resistance.

6.3.1   Oxidation behaviour of pure metals (parabolic to linear)

Parabolic oxidation behaviour up to 500 °C exhibited by vanadium is due to the protective oxide layer (V_2O_5). Results based on decreasing oxidation rate with increasing time (parabolic oxidation behaviour) clearly show that oxidation mechanism of V in air must involve the diffusion of oxygen ions through oxygen deficient V_2O_5 lattice. It has been reported that V_2O_5 is an 'n-type' oxide having oxygen ion vacancies [110], which contributes for the diffusion of oxygen ions. However, at elevated temperature (750 °C), results show that

vanadium exhibits linear oxidation which is non protective in nature. Presence of yellowish solidified mass over the crucible along with the specimen during isothermal oxidation of vanadium at 750 °C strongly indicated that the occurrence of melting and solidification of the oxide phase during the experiment and subsequent cooling respectively. The signature of solidification of oxide was also confirmed by the presence of a sharp exothermic peak in the cooling cycle of DSC. Melting of V_2O_5 near 670 °C has already been reported in literature [107, 152]. This melting of oxide layer exposes fresh surface which enhances the rate of weight gain. Events of melting and consequently acceleration in oxidation during the heating of vanadium have also been reported [109, 152-155]. Price et al., for example, have reported that liquid oxide drips from the specimen surface and consequently the metal surface get covered with a freshly formed thin layer of liquid, thickness of which depends on the rate of formation and rate of drip off of the liquid phase [154]. The rate of drip off is a function of viscosity of liquid oxide. Lower oxidation rate of V-Ti-Ta alloys at 750 °C could be attributed either to lower rate of formation of V_2O_5 or lower drip off rate from surface due to higher viscosity of liquid V_2O_5 containing Ti and Ta also. These aspects will be dealt with in the later part of the discussion.

During TG-DTA experiment, Ti showed abrupt increase in the weight gain above 880 °C suggesting oxidation layer is no more protective above this temperature. By comparing the corresponding DTA plot of Ti a sharp endothermic peak at 880 °C was recorded which pertains to the allotropic transformation from closed packed HCP α-Ti to BCC structure β-Ti [156]. This α to β transformation leads to changes in the specific volume (0.17 ± 0.1 %) [156]. This induced cracking in the oxide layer and thus exposing fresh surface for oxidation and eventually enhancing the rate of weight gain. This event was missing during isothermal experiments as maximum temperature was limited to 750 °C. In addition, bcc-Ti is a relatively open structure which provides faster diffusion of oxygen to form oxide.

From TG-DTA experimental results, as shown in Fig 6.1 (c), it can be seen that Ta shows very small weight gain till 600 °C and weight gain increases abruptly above 600 °C. Sharp oxidation exothermic peak corresponding to the rapid weight gain could be seen in the DTA peak (Fig 6.1(c)). Isothermal experiments at 750 °C showed formation of non-adherent white colour oxide layer which was peeling off. This peeling-off nature of the oxide layer could be attributed to the change in the behaviour from parabolic to linear. Voitovich et al. [157] have also reported linear oxidation kinetics in Ta between 600 °C-800 °C. Kofstad et al. [158] have proposed the following series of steps during the oxidation of Ta:

(i)   Ta+O_2→Ta-O solid solution

(ii)   Ta-O solid solution → TaO_x

(iii) TaO_x→Ta_2O_5.

They observed that between 500 °C to 800 °C, wedge wise growth of TaOx sub-oxide platelets from the over saturated oxygen solid solution causes rapid failure of the samples. Similar behaviour was observed in the present study for Ta samples treated at 750 °C.

6.3.2   Oxidation behaviour of the alloy and role of activation energy

During oxidation in most of the metals and alloys, in the very first step, oxygen molecules gets adsorbed on the clean metal surface. Subsequently, oxygen molecule dissociates into oxygen atoms which bond chemically with the atoms of metal surface. This leads to formation of a layer of oxygen atoms over the whole surface of the metal, which is called as chemisorption. After chemisorption, oxide is nucleated at favourable sites on the surface viz. ends of dislocations, impurity atoms etc. This nucleation occurs slowly at low temperatures and surface get covered with a thin film of oxide. The oxide gradually become thicker as the temperature and time increases. The whole process is shown in equation 6.7.

$$\frac{1}{2}O_{2(g)} \rightarrow \frac{1}{2}O_{2(ad)} \rightarrow O_{(ad)} \rightarrow O^-_{chem} \rightarrow O^{-2}_{Lattice} \ldots\ldots\ldots\ldots\ldots\ldots\ldots\ldots.. (6.7)$$
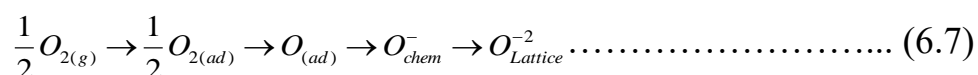
The initial oxidation represents direct-chemical reaction between the metal and the oxygen. After forming oxide layer, further oxidation can take place by two ways:

(i) Diffusion through the oxide layer: When the initial oxide film formed on the exposed metallic surface is protective in nature, then further oxidation is electro-chemical in nature. The oxidation proceeds through ionic conduction of oxygen and metal ions, as described in chapter 2. So diffusion coefficient of oxygen / metal ion though oxide lattice and defects in oxide layer will decide the rate of further oxidation.

(ii) Penetrating through the pores or cracks in the oxide layer: When the oxide layer is non protective and initial oxide layer having pores on the surface, then the molecular oxygen diffuses through the pores and reacts with the metal to form more oxide at the metal-oxide interface.

In the present study, as described earlier, it was observed that vanadium alloys exhibited parabolic oxidation upto 500 °C (Fig. 6.2), which indicates protective nature of the oxide layer. Hence mechanism (i), in which diffusion of ions takes place would be a major contributor for the oxidation of vanadium alloys. XRD results revealed that V_2O_5 is the major oxidation product. V_2O_5 being a 'n-type' oxide having oxygen ion vacancies [110], hence oxidation takes place by diffusion of oxygen ions thought V_2O_5 oxide layer. Hence, in case of vanadium alloys, improved oxidation behaviour could be explained due to combination of two factors:

(1) By controlling chemisorption and making nucleation of oxide more difficult (Activation energy for initiation (onset) of oxidation)

(2) By controlling the diffusion of oxygen ions though oxide layer (Activation energy for diffusion of oxygen ions through oxide layer)

The schematic of oxidation process of vanadium is shown in Fig 6.10. Fig. 6.10 (a) shows the onset of oxidation of vanadium according to equation 6.7. As described above, after forming

thin oxide layer of V_2O_5, further oxidation takes place by the diffusion of oxygen ion through the V_2O_5 oxide layer, which is shown in Fig. 6.10 (b).

From Fig. 6.10 (a), initially oxidation rate is governed by its activation energy for onset of oxidation. The activation energy for oxidation (Qox) of V in the present study (Table 6.3) was estimated as 112 kJ mol^{-1} which with addition of Ti and Ta into V increases to 120 kJ mol^{-1} (i.e. V-4Ti-1Ta alloy). On increasing Ta content, it was seen that Qox increases further to 130 kJ mol^{-1} for V-4Ti-7Ta alloy. It is evident that the addition of Ti and Ta in vanadium increases activation energy of oxidation of the alloy which, in turn, improves the oxidation resistance of the alloys.
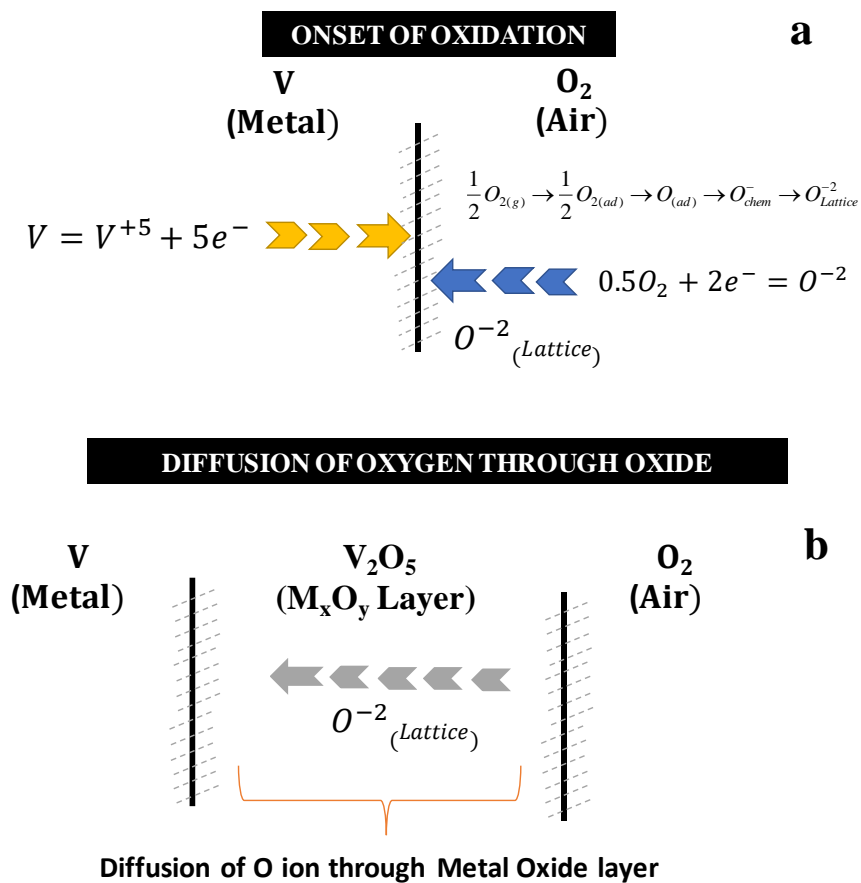
Figure 6.10(a-b): Schematic of oxidation of vanadium showing the process of (a) initiation of oxidation and (b) diffusion of oxygen through oxide layer.

In addition to increase in activation energy for the onset of oxidation, it could also be noted from Table 6.3, addition of Ti and Ta significantly affects the diffusion of oxygen ions

though the oxide layer. Diffusion coefficients of oxygen (Do) values are significantly lower for V-4Ti-7Ta alloy (7.86×10^{-14} m^2/h) in comparison to vanadium (2.58×10^{-13} m^2/h) at 500 °C. This may be attributed to increasing Ti and Ta content, which slows the diffusion of oxygen into the V- oxide lattice and thus reduces the rate of oxide (V_2O_5) formation. The activation energy for the diffusion of oxygen in oxide is also significantly lower in the case of V (176 kJ/mol) as compared to V-4Ti-7Ta alloy (189 kJ/mol). It was observed that activation energy for diffusion of oxygen in oxide increases as Ta content increases in V–Ti–Ta alloys.

These results also correlate well with the thermodynamic investigation on the change in activity of vanadium on account of Ta addition in V-Ti-Ta alloys. It has been shown in chapter 3, that addition of Ta to V-4Ti alloy decreases the activity of its constituents which decreases the partial free energy and its excess value [159]. This provides higher thermodynamic stability to V-4Ti-xTa alloys as compared to V. As V is one of the most prone element for oxidation in V-Ti-Ta alloys, reducing activity of vanadium also results in the reduction of oxidation which could be observed in increasing activation energy for oxidation of the V-Ti-Ta alloys (Fig. 6.11).

Hence it can be concluded that due to synergetic effect of increase in activation energy for onset of oxidation and reduction in diffusivity of oxygen ions through oxide layer enhances the oxidation resistance of V-Ti-Ta alloys.
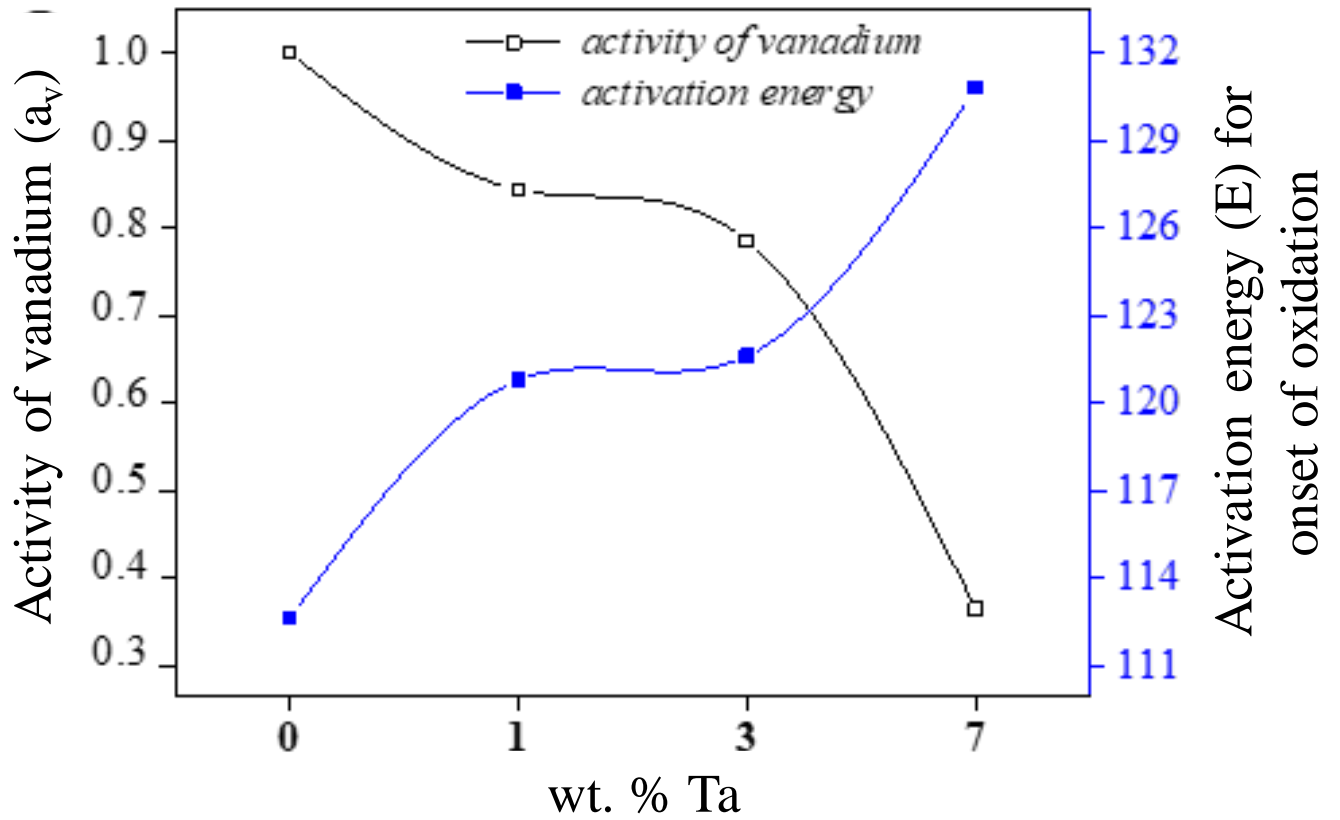
Figure 6.11: Activity of vanadium and activation energy for onset of oxidation in V-4Ti-xTa alloys showing decrease in activity of vanadium with a corresponding increase in activation energy for onset of oxidation with increase Ta content of the alloy.

Table 6.4: Comparison of oxidation properties at 500 °C in air for 64 hrs duration.

Properties at 500 °C	V	V-4Cr-4Ti (Distenfeno et al. [107])	V-4Ti-7Ta
Specific weight gain (Kg m^{-2}) after exposure in air for 64 hrs	8.60×10^{-3}	6.00×10^{-3}	4.80×10^{-3}
Diffusion coefficient of oxygen (m^2 h^{-1}) (D_O)	2.58×10^{-13}	1.61×10^{-13}	7.86×10^{-14}
Activation energy for diffusion of O in oxide (kJ mol^{-1}) (Q_D)	176	181	189

It is now worthwhile to compare the oxidation performance of the newly developed V-Ti-Ta alloys with existing V-4Cr-4Ti alloys. It can be seen from Table 6.4 that V-4Ti-7Ta exhibited 4.8×10^{-3} Kg.m^{-2} specific weight gain which is 20 % lower compared to V-4Cr-4Ti alloy (6×10^{-3} Kgm^{-2}), after exposure in air for 64 hrs at 500 °C [107, 113]. It was also found that V-4Ti-7Ta alloy exhibited lower diffusion coefficient of oxygen (7.86×10^{-14} m^{2}h^{-1}) as compared to V-4Cr-4Ti alloys (1.61×10^{-13} m^{2}h^{-1}) [107, 113]. The improved oxidation behaviour of V-Ti-Ta alloy as compared to V-4Cr-4Ti alloy could be attributed to lower activity of vanadium which increases the activation energy for diffusion of oxygen to 189 kJ mol^{-1} (V-4Ti-7Ta) from 176 kJ mol^{-1} (V-4Cr-4Ti). In view of the superior oxidation properties, from the view point of accidental exposure of the structural material to atmosphere at elevated temperature V-Ti-Ta alloys provides a better alternative to the existing V-4Cr-4Ti alloys for structural application in fusion and fast reactor applications.

6.4 Summary

In the case of any catastrophic events (leak) in a fusion reactor, the structural materials would undergo abrupt oxidation and result in deterioration of the structural integrity of the reactor vessel. In view of this, isothermal and non-isothermal oxidation behaviour of V-Ti-Ta alloys in the expected operational temperature ranges between 250-750 °C has been studied in the present study. The highlights of the work can be summarized in the following points:

1. The specific weight gain versus time follows a parabolic law in the temperature range of 250–500 °C and linear behaviour was observed at 750 °C.

2. The oxidation studies of V and V-Ti-Ta alloys showed that alloys undergo severe oxidation at and above 670 °C. However, The V-Ti-Ta alloy exhibited higher oxidation resistance than pure V. It was attributed to the presence of Ta in the V matrix.

3. V_2O_5 was the predominant oxide phase in specimens of V and V-Ti-Ta alloy.

4. Addition of Ta in V increases the activation energy for oxidation of vanadium by reducing the activity, which was found to be one of the effective reason in improving the oxidation performance of V-Ti-Ta alloys.

5. Presence of Ti and Ta significantly affects the diffusivity of oxygen in V-oxide lattice (3 times lower diffusivity) and reduces the rate of oxide formation.

6. The study has shown that the presence of alloying elements governs the morphology of oxide grown (mean aspect ratio of oxide scale reduced to half) inferring the superior protection to oxidation.

Wear behaviour of V-Ti-Ta alloys under reciprocating sliding conditions

7.1 Preamble

Detailed investigation of the high temperature oxidation behaviour of the V-Ti-Ta alloys, which is presented in Chapter 6, has shown that the V-4Ti-7Ta alloy exhibits superior oxidation resistance as compared to the reference V-4Ti-4Cr alloy. In fusion reactor, it is also known that structural materials undergo wear during their service conditions, as the flowing molten metal coolant is expected to induce the wear due to flow induced vibrations. In fast neutron reactor also, the structural materials, such as, fuel rod and control rod cladding assemblies, are reported to undergo "wear" during the service conditions majorly due to the relative motion of the sub-assemblies by the flow induced vibrations in reactor pool [114, 115]. Thus, tribological properties of the proposed material to be used as structural component are important for its application. Thus, in order to get comprehensive picture about the utility of the V-Ti-Ta alloy, wear aspects of the alloys have been explored in the present chapter. In the present work, wear characteristics of V-Ti-Ta alloys using ball-on-flat reciprocative sliding experiments have been studied. For the purpose of comparison pure V metal has also been subjected to the similar wear conditions. These materials have been tested at different sliding conditions (load and frequency) against hardened steel (AFBMS Grade-10) ball as counter-body. Based on the vibration load experienced by subassemblies in the reactor, in the present study the load was selected in the range of 5-15 N. Coefficient of friction, wear volume and specific wear rate were measured and evaluated. Identification of wear mechanism, effect of alloying additions on wear behavior and the comparison of wear performance of vanadium alloys with respect to commercially established Ti and Al alloys has also been made.

7.2 Experimental observations

7.2.1 Coefficient of friction (COF)

COFs of un-alloyed vanadium and V-4Ti-xTa alloys were recorded at different loads (5 N-15 N) and frequencies (5 Hz-15 Hz) conditions for a fixed duration of 100 minutes. COF of unalloyed vanadium as a function of time is shown in Fig. 7.1 (a-c). The mean coefficient of friction obtained as a function of different loads (5, 10 and 15 N) for constant sliding frequency of 5 Hz and 15 Hz for un-alloyed vanadium and its alloys is given in Fig. 7.2 (a-c).
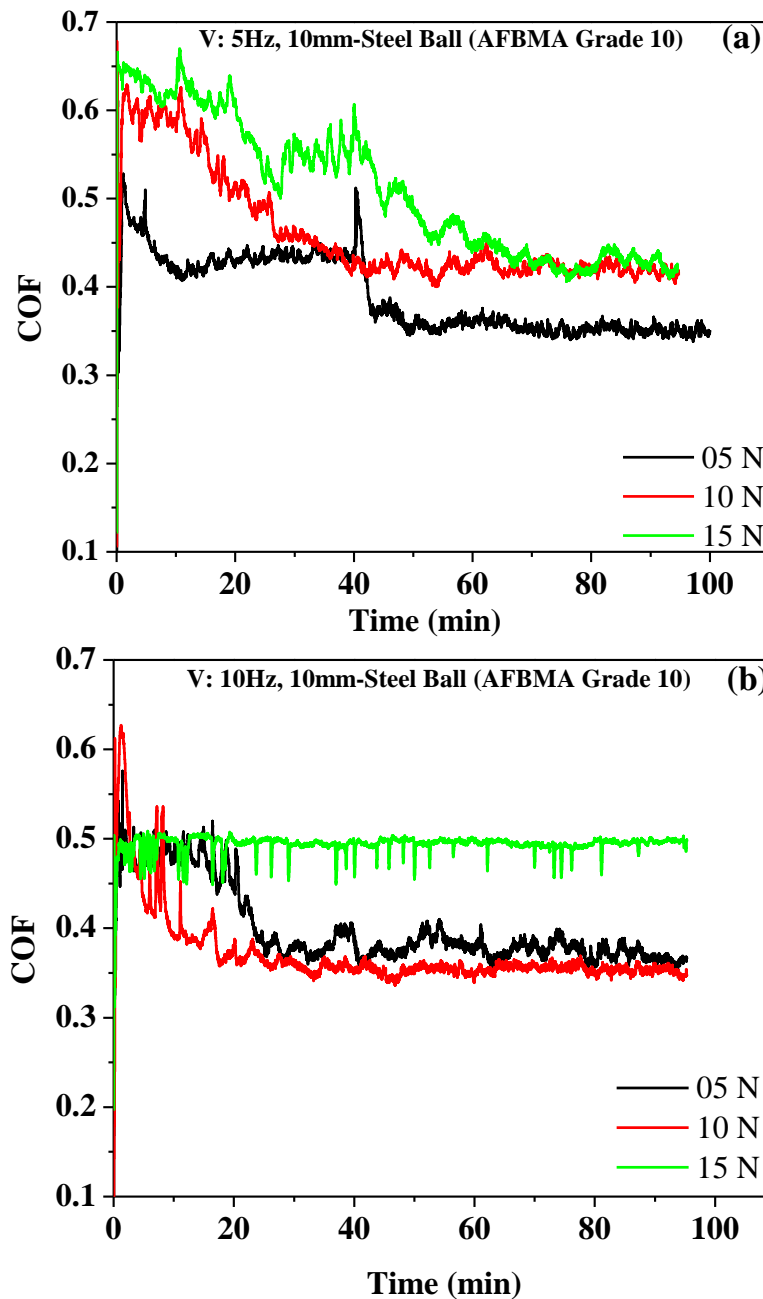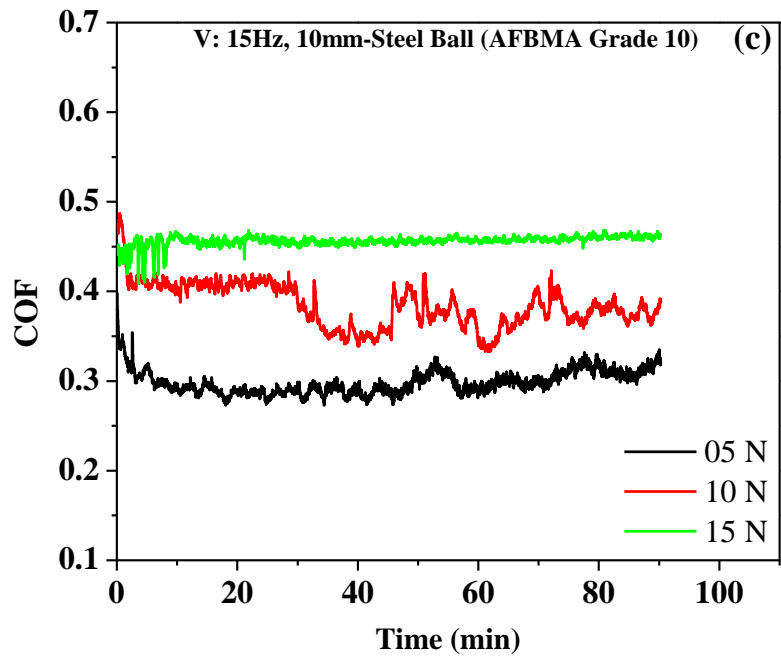
Figure 7.1(a-c): Typical coeffient of friction plots obtained as a function of time for pure-vanadium samples tested at different loads (5,10 and 15 N) for a fixed frequencies of (a) 5 Hz (b) 10 Hz and (c) 15 Hz respectively.
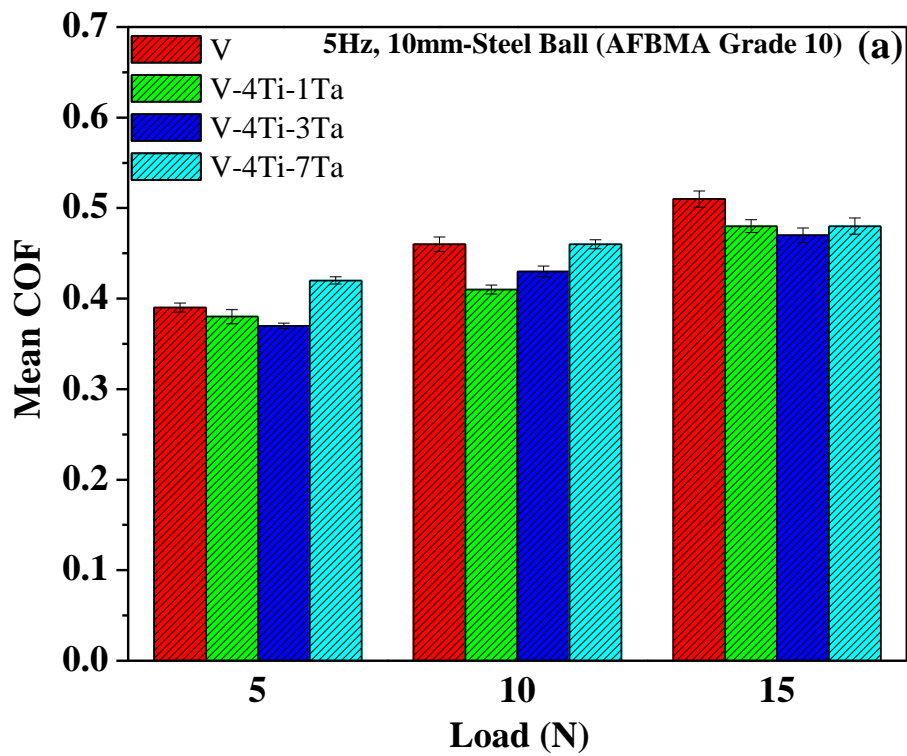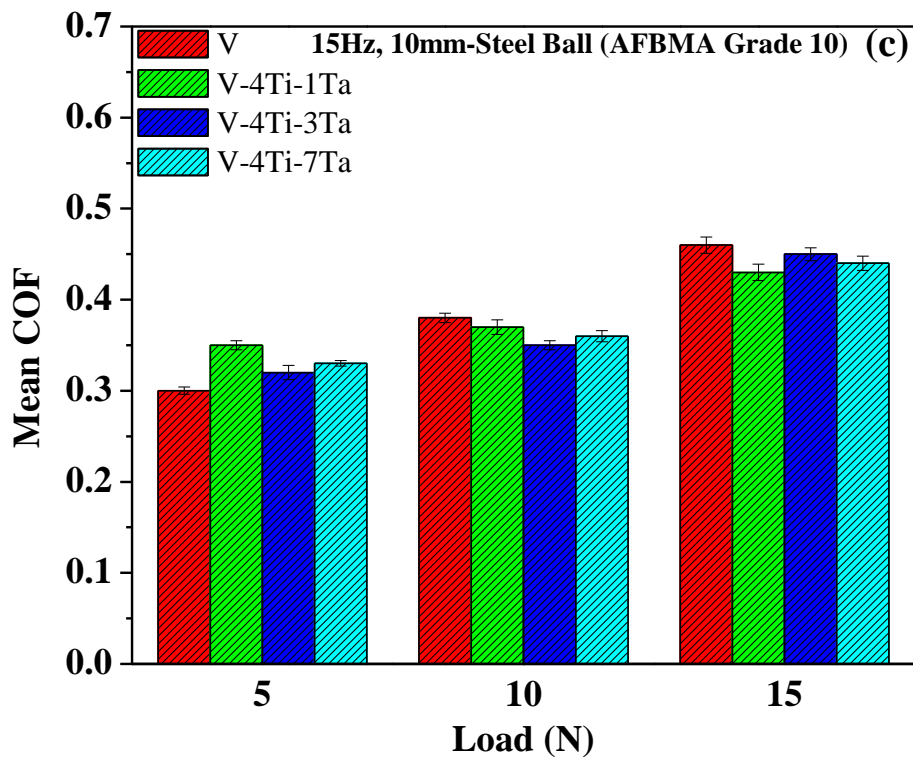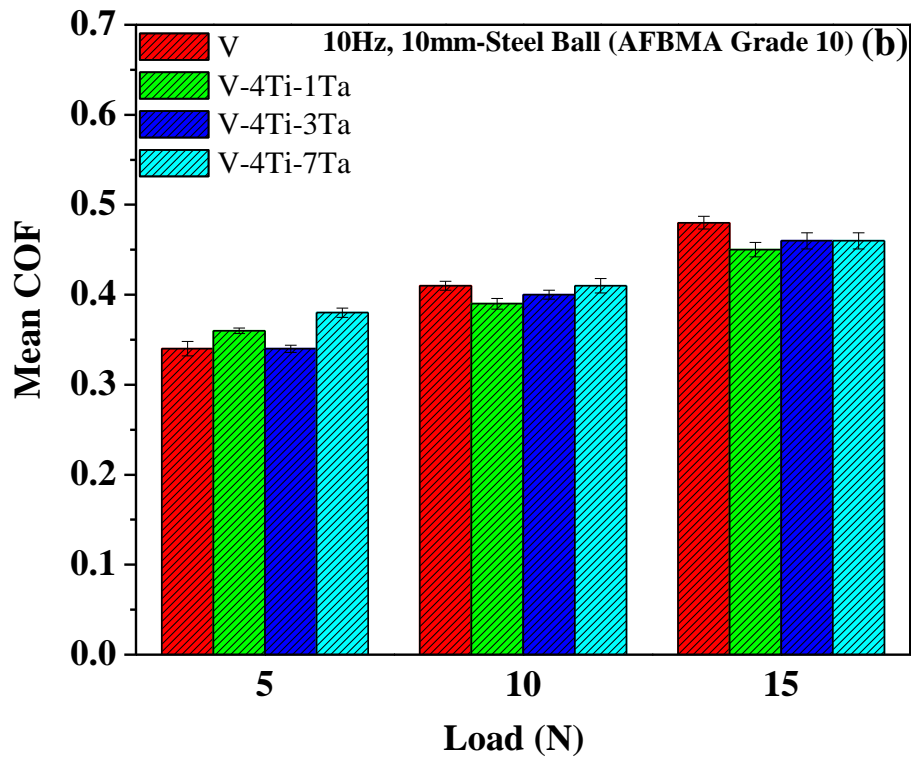
Figure 7.2(a-c): Comparison of mean COF obtained as a function of load at (a) 5 Hz, (b) 10 Hz and (c) 15 Hz frequencies for un-alloyed V and V-Ti-Ta alloys.

It was observed that at 5 Hz and 5 N condition, the mean COF recorded for un-alloyed vanadium sample was 0.39. At 5 Hz, upon increasing the normal load from 5 N to 15 N, the

COF of vanadium was found to increase from 0.39 to 0.51. At 15 N normal load, variation of sliding frequency from 5 Hz to 15 Hz resulted in marginal decrease in COF from 0.51 to 0.46 in un-alloyed vanadium sample. The V-Ti-Ta alloys exhibited similar trend in COF with respect to the applied normal load (Fig. 7.2(a-c)). On comparing vanadium and its alloys, it could be noticed that the alloying addition to V results only in marginal variation in COF values. It could also be inferred that variation in the normal load brings much larger changes in the mean COF values as compared to the changes in the sliding frequency conditions. The strong dependence of COF on the applied load could be rationalized in terms of higher the normal load inducing higher stresses which, in turn, results in severe fracturing and fragmentation of the investigated material and contribute to increase in COF values.

7.2.2   3D Profilometry

Figs. 7.3(a-b) show the results of 3D optical profilometry obtained for an un-alloyed sample tested at (a) 5 N and 15 Hz and (b) 15 N and 15 Hz loading conditions respectively. Surface profiles of worn regions consist of abraded abrasive regions with continuous grooves parallel to the sliding directions. The derived cross-sectional depth profiles show the presence of shallower (42 µm) and deeper (65 µm) grooves, when tested at 5 N and 15 N conditions respectively, for a constant frequency of 15 Hz. The wear volume obtained using optical profilometry for un-alloyed vanadium was measured to vary from 2.9×10^{-3} mm^3 to 2.5×10^{-2} mm^3 corresponding 5 N and 15 N conditions respectively. The V-Ti-Ta alloys also exhibited similar trend in the measured wear volume with respect to the changes in loading conditions.

The profilometric results corroborate the dominance of applied load on the wear behaviour of the material. Fig. 7.4(a-c) show wear scar regions of (a) un-alloyed vanadium, (b) V-4Ti-3Ta and (c) V-4Ti-7Ta obtained under identical wear testing conditions (5 N and 15 Hz). It was observed that the extent of the damage (based on the depth profile) was maximum

in un-alloyed vanadium sample. However, on increasing the Ta content, damage intensity decreases, which indicates enhanced wear performance of the V-Ti-Ta alloys as compared to un-alloyed vanadium. The wear volume measured for V-4Ti-7Ta was 60-70 % lower as compared to unalloyed vanadium metal under similar conditions.
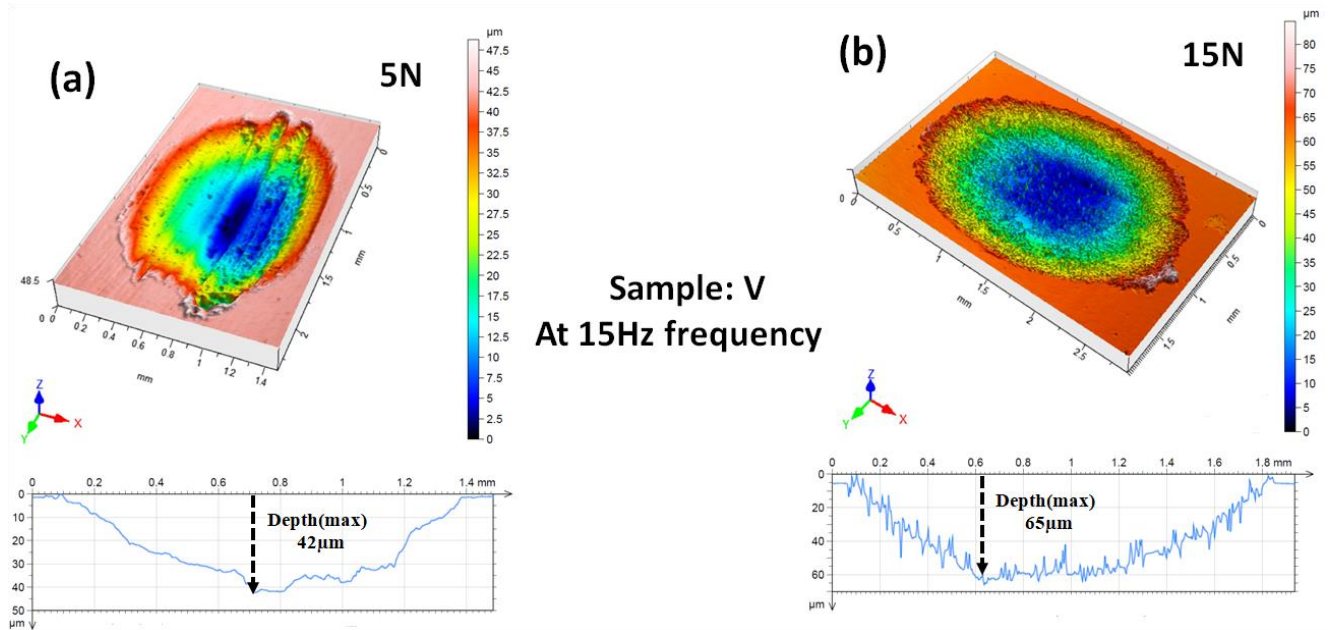
Figure 7.3(a-b): 3D optical profilometry obtained for un-alloyed vanadium tested at (a) 5 N and 15 Hz and (b) 15 N and 15 Hz loading conditions showing the presence of shallower (42 μm) and deeper (65 μm) grooves, respectively.
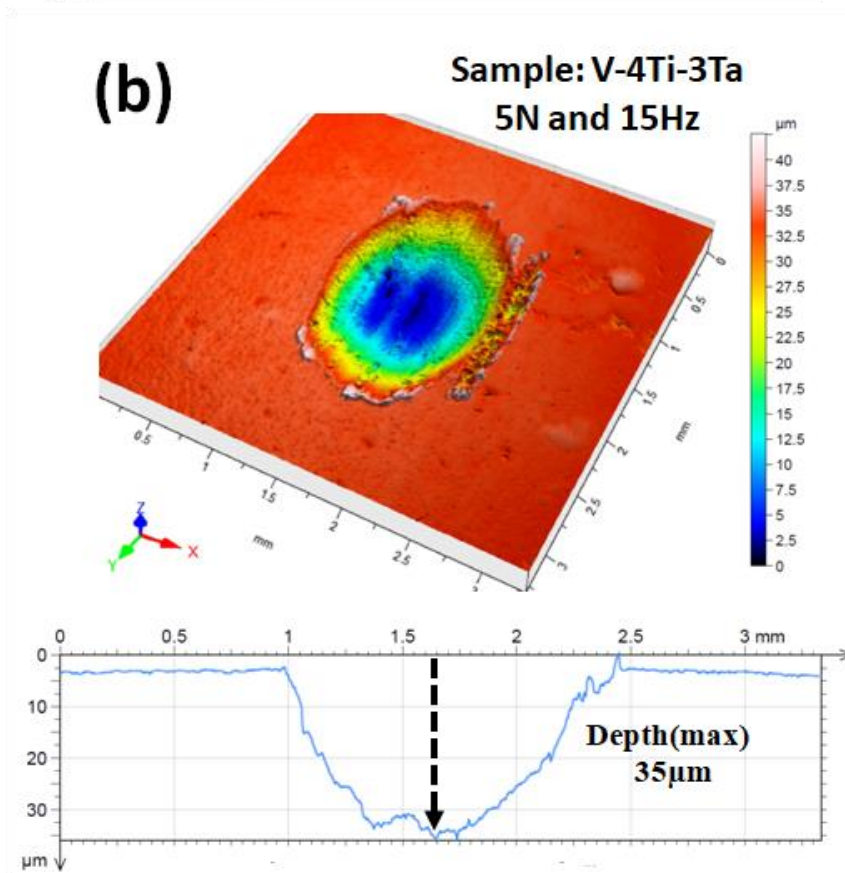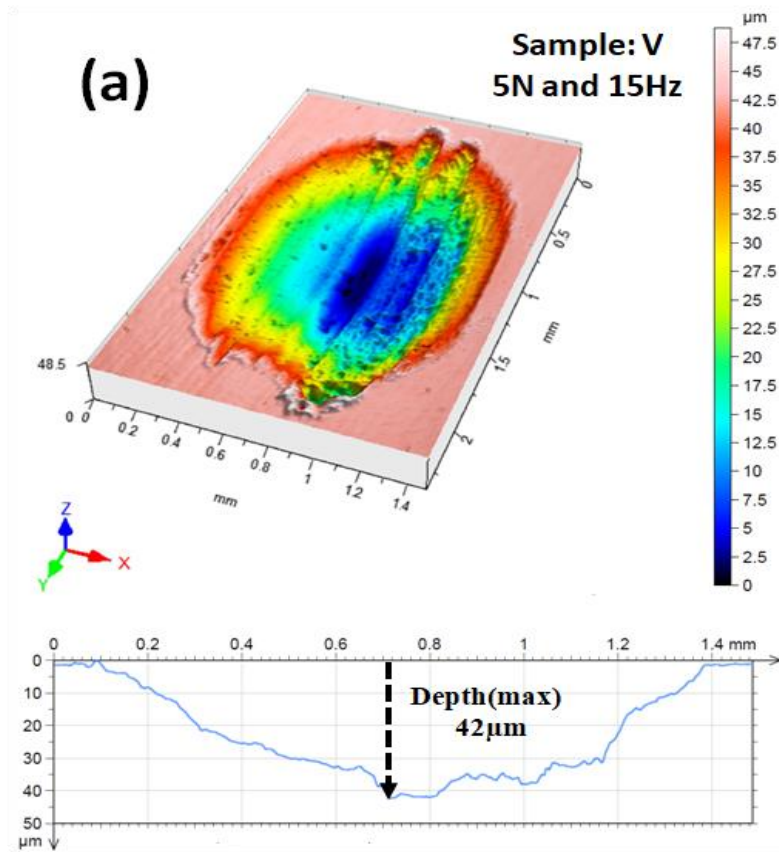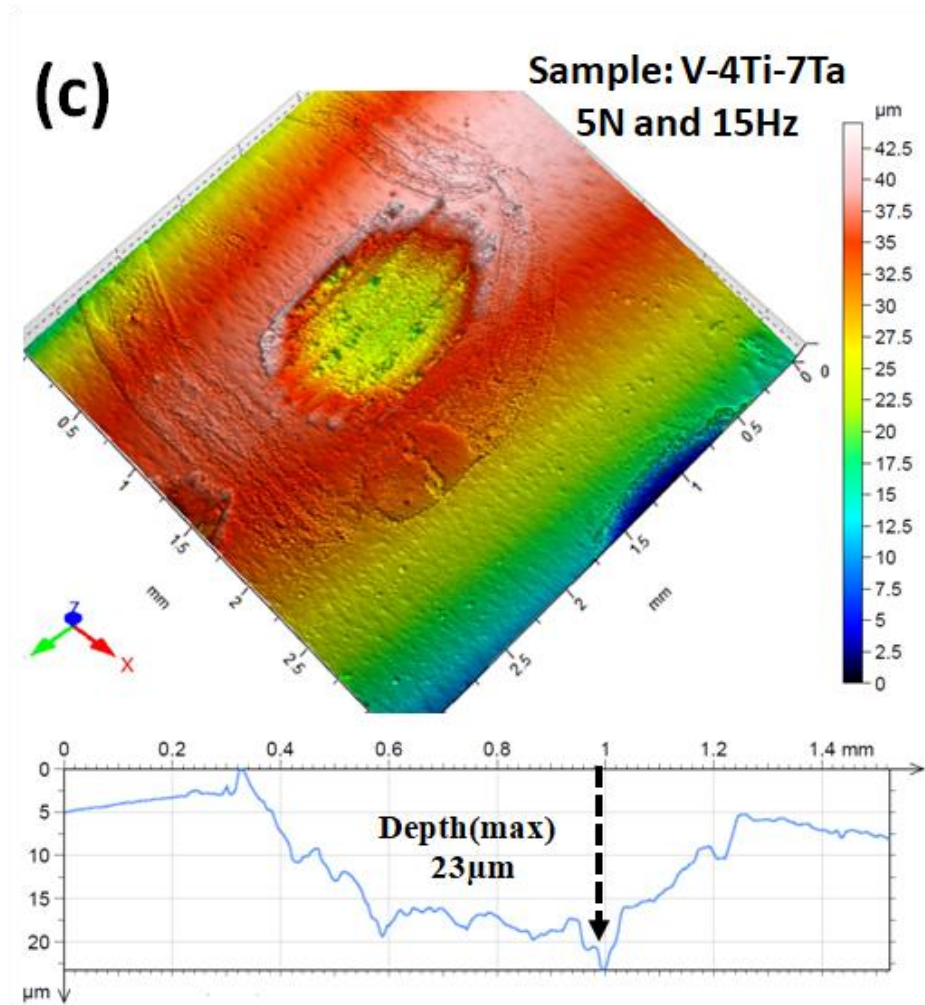
Figure 7.4(a-c): 3D optical profilometric images obtained for 5 N and 15 Hz condition, showing the extent of damage profile (wear scar regions) with respect to alloying contents ((a) an un-alloyed vanadium (b) V-4Ti-3Ta alloy and (c) V-4Ti-7Ta alloy).

7.2.3 Specific wear rate

Effect of wear testing parameters on the wear rate is shown in Fig. 7.5(a-c). It could be observed from Fig. 7.5(a) that at a constant frequency of 5 Hz, the wear rate of un-alloyed vanadium increased from 9.78×10^{-6} to 2.79×10^{-5} mm^3 N^{-1} m^{-1}, upon increasing the load from 5 N to 15 N respectively. This increase in the wear rate in un-alloyed vanadium is almost 3 times with respect to increase of normal load. In contrast, At 5 N normal load, increase of sliding frequency from 5 to 15 Hz results only in marginal rise in the wear rate of un-alloyed vanadium (Fig. 7.5).
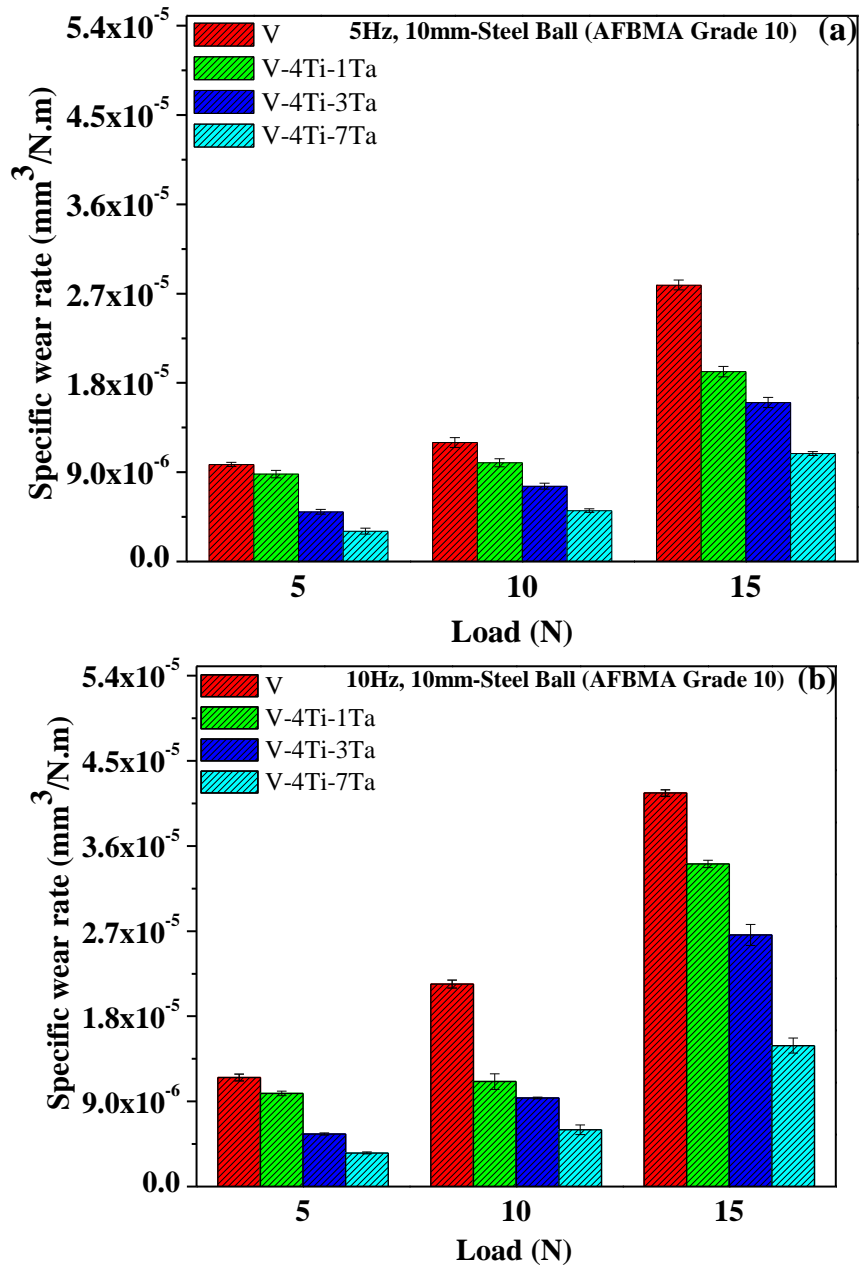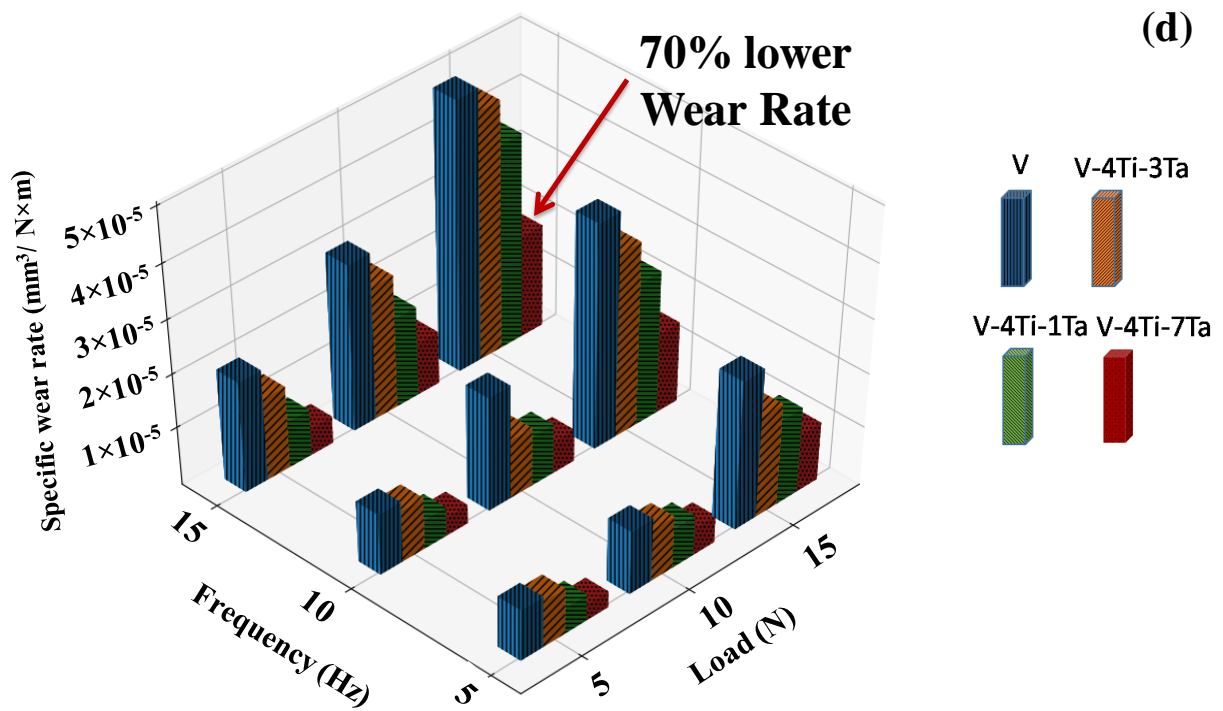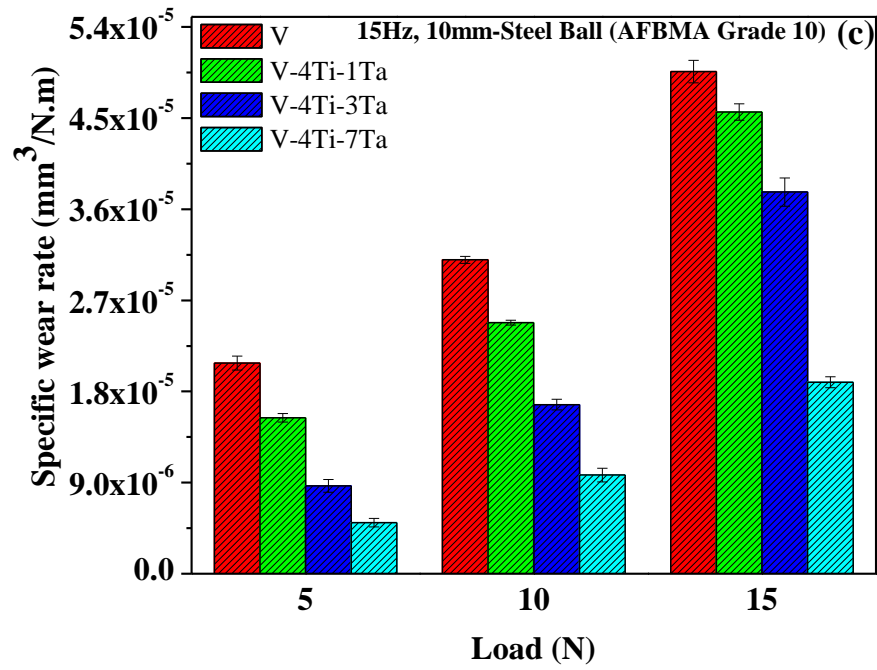
Figure 7.5(a-d): Specific wear rate of un-alloyed V and V-Ti-Ta alloys obtained using steel ball as counter body material. Illustrating improved wear resist characteristics with respect to alloying additions (Ti and Ta) to V.

Samples of V-Ti-Ta alloys also exhibited similar behaviour in wear rates upon increasing normal load; irrespective of the sliding frequencies. It is reported that the other established non-ferrous alloy systems, like Ti [160] and Al [161-164], also exhibit similar trend of increased wear rates with increasing applied load. This increase in the wear rate could be attributed to the generation of deeper and severe sub-surface defects at higher loading conditions. Figs. 7.6 (a-b) show the severity of cracks that formed when sample was tested at 15 N load and the cracking was minimal in the case of 5 N condition. Insets on the micrographs showing the two-dimensional depth profiles of the wear scar regions tested at 5 N and 15 Hz (Fig. 7.6 (a)); 15 N and 15 Hz (Fig. 7.6 (b)) conditions.
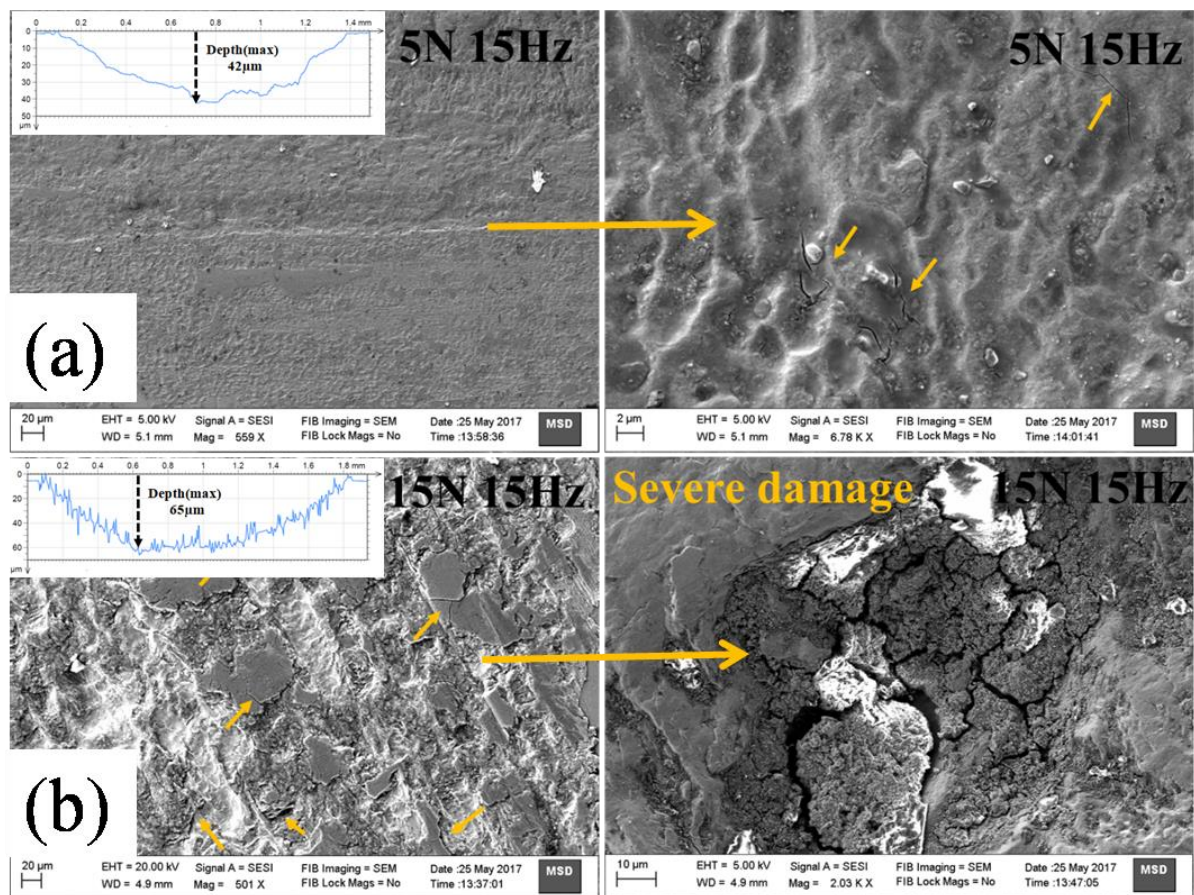
Figure 7.6 (a-b): SEM micrograph of un-alloyed vanadium sample depicting the severity of the cracks that are formed when the load was increased from (a) 5 N to (b) 15 N; (Smaller arrow mark indicates the cracks and inserts in the micrograph shows the corresponding depth profile of the wear scar region obtained using profilometry).

Wear rate estimated for V-4Ti-1Ta alloy sample at 5 N and 5 Hz condition is 8.82×10^{-6} mm^3 N^{-1} m^{-1} which is about 10 % lower than the wear rate of un-alloyed vanadium sample. At 5 N and 5 Hz, upon increasing the Ta content to 3 wt.%, the wear rate reduced to 5.01×10^{-6} mm^3 N^{-1} m^{-1} which is about ~ 48 % lower in comparison with un-alloyed vanadium. V-4Ti-7Ta alloy exhibited the least wear rate of 3.06×10^{-6} mm^3 N^{-1} m^{-1} at 5 N and 5 Hz condition in comparison to all the investigated samples in this study. It is evident that wear rate decreases upon alloying Ti and Ta in V and exhibited superior wear performance in comparison to un-alloyed vanadium sample. This superior wear performance of V-4Ti-7Ta alloy sample shall be attributed to increased yield strength of the V-Ti-Ta alloys. Addition of Ti and Ta strengthens the vanadium matrix by solid solution strengthening and contributes in enhancing the yield strength of the material in the present study. This strengthened matrix offers enhanced resistance to the sliding motion of hardened steel ball when compared to un-alloyed vanadium. The higher hardness of V-4Ti-7Ta alloy in comparison to un-alloyed vanadium contributes towards the lowering the wear rate. Similar observations have been reported on the role of yield strength and hardness in improving wear resist behaviours of Al and Ti alloys [121, 165-167].

It is worth to compare the evaluated wear rates of the developed vanadium alloys with respect to the established non-ferrous alloys, such as Al and Ti, which have been commercially exploited for the tribological/engineering applications. On comparing wear rate data taken from literature under closely matching experimental conditions (refer Table 7.1), it was found that the developed vanadium alloys exhibit two order lower wear rate with respect to Al and Ti alloys. The wear rate of Al-Si alloys and Ti-6Al-4V alloys were reported to be of the order of 10^{-4} mm^3 N^{-1} m^{-1} [119, 120, 167-170]; whereas, the wear rate of the vanadium alloys examined in the present study is in the range of 10^{-6} mm^3 N^{-1} m^{-1}. In view of superior wear characteristics exhibited by the developed vanadium alloys, it warrants to explore the applicability of developed alloys for different tribological applications in addition to nuclear structural material.

Table 7.1: Comparison of wear properties of some established non-ferrous alloys and the developed alloys of this present study.

Material	Counter body	Test configuration	Sliding Speed (m/s)	Load (N)	Relative humidity	Coefficient of friction (COF)	Specific wear rate mm^3 N^{-1} m^{-1}	Reference
Al-2Si	High carbon chromium steel	Pin on disk	0.25	5	60%	-	9×10^{-4}	H. Torabian et al. [123]
Al-20Si	High carbon stainless steel	Ball on disk	0.10	5 and 8	-	0.42 and 0.62	9.4×10^{-4} and 6.9×10^{-4}	Gang Liu et al. [169]
Ti-6Al-4V	Maraging steel	Pin on flat	0.025	75 and 250	-	0.41 and 0.37	8×10^{-4}	Marc Long et al. [170]
Ti-6Al-4V	6 mm diameter steel ball	Ball-on-disk	0.10	5	35–45 %.	0.52	5×10^{-4}	Farokhzadeh et al. [120]
V-4Ti-1Ta	10 mm diameter hardened steel ball	Ball-on-disk	0.01	5	60 %	0.38	8.8×10^{-6}	Present study
V-4Ti-3Ta	10 mm diameter hardened steel ball	Ball-on-disk	0.01	5	60 %	0.37	5×10^{-6}	Present study
V-4Ti-7Ta	10 mm diameter hardened steel ball	Ball-on-disk	0.01	5	60 %	0.42	3×10^{-6}	Present study

7.2.4 Phase identification and microstructural investigation

Wear debris gathered from un-alloyed V and V-Ti-Ta alloys were characterized for their phases and compositions. Analyses of XRD patterns obtained from the wear debris of both un-alloyed V and V-4Ti-7Ta alloy samples indicated the possible presence of either V_2O_5 / $Fe_{0.11}V_2O_{5.15}$ phases (Fig. 7.7).
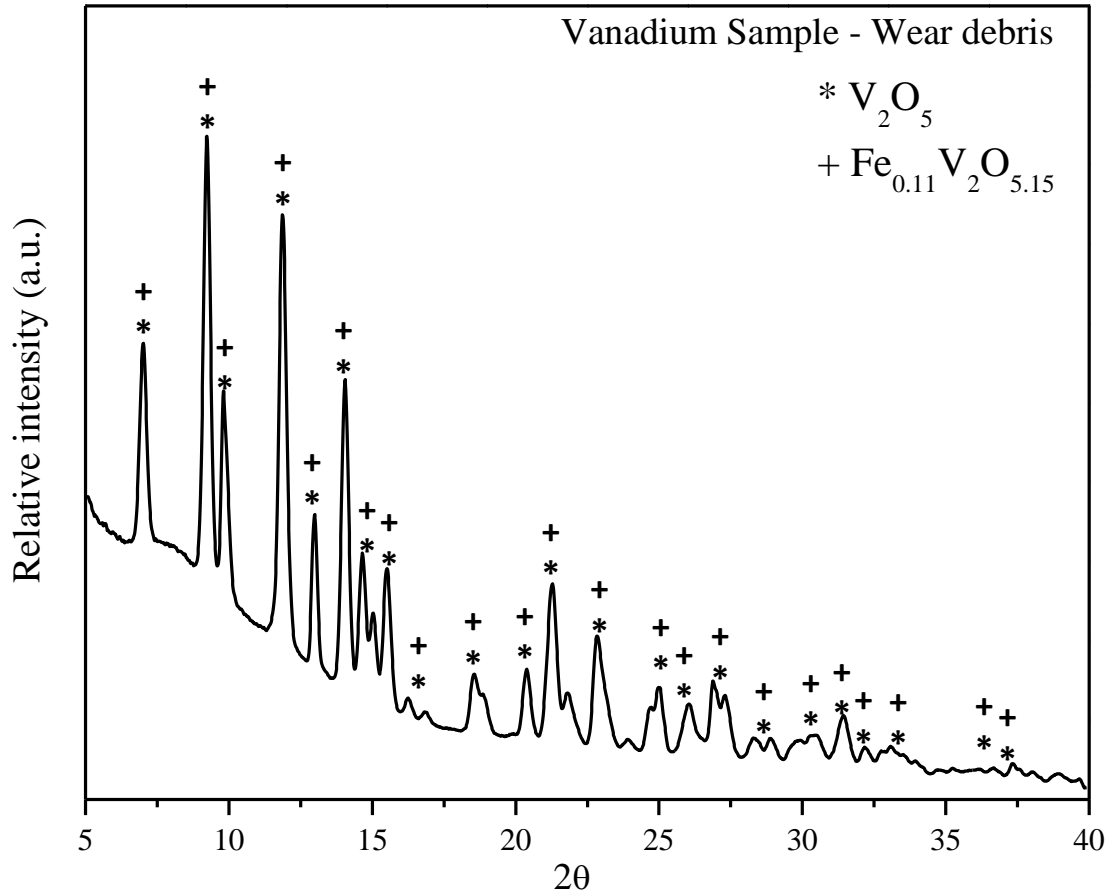
Figure 7.7: XRD pattern of wear debris generated from vanadium sample indicates the possible presence of V_2O_5 / $Fe_{0.11}V_2O_{5.15}$ crystalline phase.
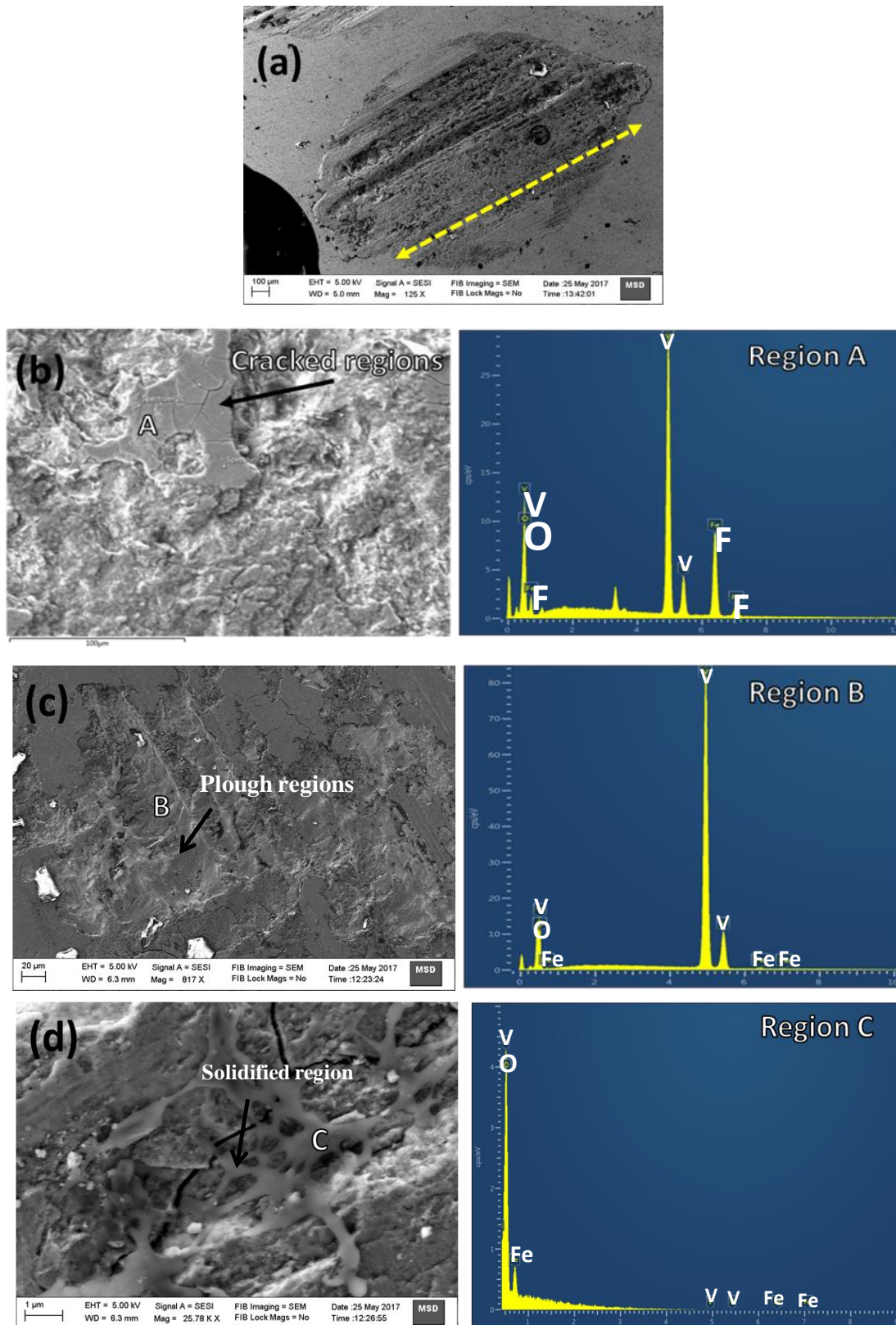
Figure 7.8(a-d): Scanning secondary electron micrograph of worn out surface vanadium after wear experiment (15 N, 15 Hz) illustrating (a) Typical worn scars formed on samples consisting of abraded abrasive regions with continuous grooves parallel to the sliding direction (b) cracked regions, (c) plough regions and (d) solidified regions.

As these two mentioned oxides phases maintain close inter-planar spacing's, it was difficult to decipher the nature of oxide present in the debris. In order to establish the identity of the oxide phase, detailed EDS analysis of the debris was carried out (Fig. 7.8). EDS spot pattern analysis indicates the invariable co-existence of regions that are composed of elements like (a) V, Fe and O, (b) V and O, and (c) V, Fe, Ti, Ta and O (observed in case of vanadium alloys only). Based on the information obtained from XRD and EDS analyses, the wear scar regions were identified to contain both V_2O_5 and mixed (V-Fe-O) oxide phases. The composition of mixed oxide region was identified to be $Fe_{0.11}V_2O_{5.15}$. The source of iron in oxide phase could be attributed to the hardened steel ball (counter body) majorly by adhesive wear mechanism. No sign of individual oxides was found in XRD patterns of V-Ti-Ta alloy debris which signifies that elements like Ti and Ta would remain in the vanadium oxide phase in solid solution form. Electron micrographs of wear scar showed the presence of three distinct regions which were identified as (A) cracked regions, (B) plough regions and (c) solidified regions (Fig. 7.8(a-d)). The chemical compositions of these regions (A, B and C) are summarized in Table 7.2.

Table 7.2: Chemical characterization of wear scar regions of vanadium sample.

Name of region		Composition in atom%		
		V	Fe	O
Region A	Cracked region	30.7	7	62.3
Region B	Plough region	95.6	0.6	3.8
Region C	Solidified region (Solidified V_2O_5)	29.3	0.4	70.3

7.3 Discussion

The major findings of the present study could be summarized as:

(i)   The COF of the V-Ti-Ta alloys was found to be in the range of 0.29 to 0.61.

(ii) V and V-Ti-Ta alloys show wear rate in the range of 10^{-6} mm^3/Nm

(iii) Microstructural characterization revealed that wear surface consists three distinct regions and XRD patterns of the wear debris showed the presence of V_2O_5 and/or $Fe_{0.11}V_2O_{5.15}$ phases

Based on promising results, it appears that vanadium alloys have good wear resistance properties. In order to realize full real time application, wear properties of V-Ti-Ta must be comparable or superior to other wear application materials. Among the established nonferrous systems which have been commercially exploited for the tribological /engineering applications, aluminium, titanium and their alloys are most preferred candidates [171, 172]. Excellent combination of thermo-physical properties, low density and high specific strength make them suitable for tribological applications. However, due to the poor protection provided by the debris (majorly oxides), generated as a consequence wear process, restricts their usage to the fullest potential. In the case of Ti, wear properties can be greatly improved by means of surface treatments and alloying additions [167], which alters the chemistry of the wear debris formed. The specific wear rate of 'work-horse' material Ti-6Al-4V alloys is reported to be in the range of 2-5 x 10^{-4} mm^3/N-m against the steel ball [120]; whereas typical specific wear rates observed in the case of pure Ti are in the range of 10^{-3} mm^3/Nm.

Al and Al-Si alloys are widely used in the automobile industry due to their superior wear characteristics. Al-Si alloys are reported to have specific wear rate of the order of 10^{-4} mm^3/Nm, which is similar to the specific wear rate of Ti alloys. Though, Al-2%Si and Ti-6Al-4V alloys show similar wear characteristic, the strength/density ratio of the Ti-6Al-4V alloy (205) are far superior to Al-2%Si alloys (~20) which is nearly one order higher than that of

aluminium alloys [123, 170]. In this regard, it may be noted here that vanadium alloys offer 3 times higher strength/density ratio (~70) in comparison to Al-Si alloys (~20). Despite having superior strength/density ratio, in comparison to Al alloys, the tribological behaviour of vanadium-based alloys has not been given due consideration. The present study, therefore, is an attempt to bring out the wear behaviour of vanadium and its alloys under reciprocating sliding dry conditions and SS-ball counter body vis-à-vis to Al and Ti based alloys.

As vanadium and its alloys exhibit two order lower wear rate in comparison to the established systems like Al and Ti (refer Table 7.3), it requires detailed investigations to probe the underlying reasons behind. Analyses of XRD patterns obtained from the wear debris indicated the possible presence of either V_2O_5 / $Fe_{0.11}V_2O_{5.15}$ phases (Fig. 7.7). As these two mentioned oxides phases maintain close inter-planar spacings (refer Table 7.4), it was difficult to decipher the nature of oxide present in the debris. In order to establish the identity of the oxide phase, detailed EDS analysis of the debris was carried out (Fig. 7.8). EDS spot pattern analysis indicates the invariable co-existence of regions that are composed of (i) V, Fe and O and (ii) V and O only. By combining the information obtained from XRD and EDS analyses, it was inferred that the wear scar regions contain both V_2O_5 and mixed (V-Fe-O) oxide phases. The composition of mixed oxide region was identified to be $Fe_{0.11}V_2O_{5.15}$. The source of iron in oxide phase could be attributed to the steel ball (counter body). No sign of individual oxides was found in XRD patterns of V-Ti-Ta alloy debris which signifies that elements like Ti and Ta would be associated with vanadium oxide phase in solid solution form.

Table 7.3: Comparision of properties of Al-Si, Ti-6Al-4V and V-4Ti-7Ta alloys.

Properties	Al-Si alloys	Ti-6Al-4V alloy	V-4Ti-7Ta alloy
Specific wear rate (mm^3/Nm)	9.4×10^{-4} (5 N)	5.0×10^{-4} (5 N)	3.0×10^{-6} (5 N)
Maximum allowable operating Temeparture (°C)	350	< 400	750
Density, ρ (g/cm^3)	2.6	4.4	5.8
Strength, σ (MPa)	50-80	900	370
Strength/Density ($\frac{\sigma}{\rho}$)	~ 20	~205	~70
Hardness (VHN)	40-70	350	250
$\frac{B}{C_{44}}$	1.5	1.76	3.42

Table 7.4: X-ray diffraction peak positions of crystalline V_2O_5 and $Fe_{0.11}V_2O_{5.15}$ phases.

Plane index hkl	2θ	
	V_2O_5 JCPDS No. (00-041-1426)	$Fe_{0.11}V_2O_{5.15}$ JCPDS No. (00-082-1871)
200	7.0263	7.023
001	9.2593	9.3006
101	9.9152	9.9435
201	11.652	11.6637
110	11.9059	11.9146
300	14.089	14.0763
011	14.6938	14.7185
111	15.1066	15.1357
310	15.5445	15.5385
211	16.3126	16.3249
401	16.9064	16.8942
002	18.6064	18.6632
102	18.9359	18.9963
202	19.9134	19.9631
411	20.4211	20.4175
600	21.2228	21.1761
302	21.4443	21.4816
012	21.866	21.9136
020	22.8753	22.879
212	22.9941	23.0311
601	23.2119	23.1719
402	23.4226	23.4503
021	24.731	24.7449
121	24.9832	25.0003
412	26.1138	26.1378
701	26.5421	26.4986
710	27.3714	27.3244
003	28.0668	28.1536
421	28.5773	28.5775
022	29.6454	29.6871
303	30.0682	30.1395
013	30.3742	30.4561
702	31.1937	31.1842
313	32.2508	32.3137
621	32.8068	32.7904
422	32.9693	32.9939
712	33.3077	33.2966
413	33.6333	33.6946

Detailed microstructural analysis and compositional analysis ((Fig. 7.8 (a-d)), and Table 7.2) of the three regions (cracked regions, plough regions and solidified regions) showed predominant presence of adhesive wear regions in the microstructure of the sample subjected to wear testing at 15 N and 15 Hz condition (Fig. 7.8). This kind of morphology was made through squashing and ploughing actions of the counter-body material. Metal-to-metal contact would result in severe adhesive wear in the initial stages of dry sliding generating metallic wear debris comprising majorly V and Fe, as its elements. As sliding continues, the relative motions between base metal (vanadium) and counter body (hardened steel) would generate very high temperatures at the contact points that induces diffusion bonding at the interface. These localized bonds would resist further movement of the counter body material. Once the load applied exceeds the yield strength of the material, the interface regions undergo plastic deformation and further results in cracking (severity of cracking was realized in higher load 15 N condition Fig. 7.6 (b)). Upon further erosion, particle smearing and re-densification occurs, contributing to the formation of tribo-chemical layer (third body debris), an oxidation of third body as well. Evidences of such third body oxides have been found during EDS analysis, which confirmed formation of mixed oxide.

The enhanced wear performance noticed in the case of V-Ti-Ta alloy samples shall be correlated to the nature of debris (oxides) formed during wear experiments, as these debris govern the further erosion of the base material. As mentioned in the preceding paragraph, these debris were identified to be the V_2O_5 phase containing Ti and Ta (in case of V-Ti-Ta sample). The presence of elements, like Ti, Ta, Fe, in solid solution with V-oxides (in tribo-layer) enhanced the hardness of the oxide layer which offered increased resistance to the base material erosion and contributed to superior wear performance over unalloyed V-sample. The synergistic effect of both strengthened matrix (by Ta alloying) and by the formation of mixed oxide tribo-layer contributed to superior wear performance over unalloyed V-samples.

170

Superior wear performance of vanadium and its alloys over Al and Ti alloys (refer Table 7.3) could also be attributed to the nature of debris (oxides) formed during wear experiments. In this regard, attention may be drawn towards the river flow patterns in the microstructure of wear scars (Fig. 7.8(d)), which on EDS analysis identified to mainly contain V and O as its elements. These river flow patterns signify partially melted microstructural regions and based on the relative concentration of V and O, the composition of the vanadium oxide was identified to be V_2O_5 (Table 7.2). It may be noted that among oxides of vanadium, V_2O_5 has the lowest melting temperature (660 °C) and therefore, not surprising to observe its presence in the wear scar regions. River flow patterns were particularly noticed under high frequency (15 Hz) conditions. At higher frequency, the time available for heat dissipation would be less. Hence, the oxide (V_2O_5) experiencing high temperatures for a longer period got melted locally. In the case of V-Ti-Ta alloys, no sign of solidified regions in the wear track regions were observed. This could be due to the presence of Ti, Ta and Fe elements along with V_2O_5, which would elevate the melting point of vanadium oxide. Even in the case when V_2O_5 has not undergone melting, it would still provide a lubrication action to retard further erosion of material and contribute in lowering wear rates of the material. This aspect is dealt in the later part of the chapter.

In contrast to the debris generated during the wear testing of vanadium, which was identified to contain vanadium oxides in the form of V_2O_5 majorly, the debris of Al and Ti systems were reported to contain Al_2O_3 and TiO_2 respectively [123, 168]. Al_2O_3 and TiO_2 do not undergo any liquefaction due to higher melting point and therefore do not provide effective lubrication. Based on the nature and properties of debris formed during wear experiments the enhanced wear performance of the vanadium system when compared with other nonferrous members (Al and Ti) shall now be discussed.

V$_2$O$_5$ formed during wear experiment is reported to exhibit orthorhombic crystal structure, which is its most stable configuration. It is composed of distorted square pyramids which share corners and edges resulting in the formation of layer like structures parallel to the (001) plane [173]. Bonds within the layers are strong while the interlayer bonding is weaker and for this reason it is easy to cleave V$_2$O$_5$ along the plane perpendicular to c axis [173]. Easy cleaving of the layered structure configuration in V-O contributes for lowering of friction coefficients at elevated temperatures even when the phase has not transformed into the liquid phase [174]. This phenomenon is absent in the case of Al and Ti alloy systems.

Bulk modulus (B) and shear modulus (C44) of the oxide crystals have been also reported to influence the tribological behaviour of the material [175]. Crystals having higher B/C44 ratio show ease of plasticity which provides the lubricious behaviour. V$_2$O$_5$, Al$_2$O$_3$ and TiO$_2$ are reported to exhibit B/C44 values as 3.42, 1.50 and 1.76 respectively [175-178]. Due to large B/C44 ratios for V$_2$O$_5$, it is expected to possess better lubricating properties compared with Al$_2$O$_3$ and TiO$_2$.

Ionic potential of a crystal is also reported to influence the friction behaviour of the oxides. It has been reported that higher is the ionic potential, greater is the extent of screening of a cation of an oxide by surrounding anions [179]. This gives rise to a soft and easy to shear (low friction coefficient) tribo-films. The reported value of ionic potential of V$_2$O$_5$ is 7.35, whereas oxides of Ti and Al systems, i.e., TiO$_2$ and Al$_2$O$_3$, exhibit 5.36 and 4.40 as their ionic potential respectively [179]. This observation is also in line with the experimental results where vanadium containing V$_2$O$_5$ layer exhibited least wear rate because of its lubricating nature.

In addition to these attractive wear and mechanical properties (Table 7.3), V alloys, unlike Ti alloys, do not undergo any phase transformation before its melting and therefore offer a scope to go beyond the temperature ranges offered by Ti and Al alloys. In short, it can be stated that, though, V based alloys have been developed and studied for structural application

in fusion technology, their wear properties can be exploited to a much wider application, which is still an unexplored area.

7.4   Summary

Vanadium and the newly developed V-Ti-Ta alloys have been tested for wear characteristics using ball-on-flat reciprocative sliding wear experiment. In general, the structural materials encounter series of wear events in service conditions and those components are expected to move with greater reliability and with least contact stresses with respect to other critical structural members. The developed alloy (V-4Ti-7Ta) has demonstrated superior wear resist behaviour (68 % lower wear rate compared to unalloyed vanadium) without significantly affecting the friction coefficient values, which is of prime importance considering nuclear reactor applications. The salient features of the study have been summarized below:

1. Coefficient of friction of vanadium and its alloys was measured to be in the range of 0.30 to 0.51 when tested for a normal load of 5 N and 15 N.

2. Increase of normal load increases COF values both for vanadium and its alloys. Application of normal load was found to play a significant role in COF values as compared to sliding frequency. The presence of alloying elements, such as Ti and Ta, were not found to influence COF as compared with un-alloyed vanadium.

3. Almost 3 times higher wear rate was noticed in the case of vanadium when the applied load was increased from 5 N to 15 N. The increase of normal load increases the severity of surface cracking which, in turn, causes increase in the wear rate of the investigated material.

4. Microstructural investigation of wear track showed three distinct regions (a) cracked regions (b) plough region and (c) partially melted regions.

5. V-4Ti-7Ta alloy exhibited superior wear performance (~ 68 % lower wear rate) in comparison to un-alloyed vanadium. The presence of alloying elements such as Ti and Ta

increase the yield strength of the material by solid solution strengthening and thereby offer increased wear resistance.

6. The presence of elements like Ti, Ta, Fe in solid solution with vanadium oxides (in tribo-layer) enhances the hardness of the oxide phase which offers enhanced resistance to the base material erosion and contributes to superior wear performance over un-alloyed vanadium sample.

7. One of the main contributing factor for the lower wear rate of vanadium based alloys was the formation of V_2O_5 which provides lubricious behaviour in the high frequency region by melting and in low frequency region when it is in solid state by easy cleaving due to its layered structure having high B/C44 ratio.

Conclusions

The present work is focused on the development of vanadium based alloys that can widen the working temperature window for a structural material proposed for fusion reactors. For a material to qualify for structural material applications, it should have adequate strength upto 800 °C, adequate ductility upto room temperature, good oxidation resistance at elevated temperature and good wear resistance against moving liquid metal front, apart from favourable nuclear properties. After carrying out detail literature survey it was found that the properties of V-Ti-Cr, currently proposed structural material for fusion reactor, can be improved by replacing Cr with a refractory metal. For this purpose, in the present study a series of V-4Ti-xTa (x = 0,1,3,7) alloys were investigated for the evolution of microstructure during deformation, recrystallization, phase stability, oxidation and wear resistance. In this study, Ta content in the alloy was systematically varied and the synthesized alloys were investigated to identify the optimal alloy compositions exhibiting superior high temperature thermodynamic stability and properties. Recrystallization parameters of these V-Ti-Ta alloys were optimized as a function of Ta content by annealing at various temperatures for different time duration. The microstructural evolution in Vi-Ti-Ta alloys revealed formation of precipitates in the as-solidified, deformed and annealed samples. Crystallographic details and orientation relationship of the precipitates with the matrix were established. The role of Ta on the stability of the precipitates was evaluated using thermodynamic estimations and correlated with the experimentally observed high temperature stability of the precipitates. Thermo-mechanical processed and recrystallized samples were subjected for mechanical properties evaluation such as hardness, yield strength and subsequently microstructural features were correlated with the obtained mechanical properties in V-Ti-Ta alloys. Keeping in view of the fact that V-Ti-Ta

alloys are developed for high temperature structural application in fusion reactor, the microstructurally optimized alloys were tested for their high temperature oxidation performance, as in the case of any catastrophic events (leak) in a fusion reactor, the structural materials would undergo abrupt oxidation which would result in deterioration of the structural integrity of the reactor vessel. Further, wear behaviour of these alloys were investigated to test the wear rate of samples, as flowing molten metal coolant is expected to induce the wear of structural materials due to flow induced vibrations in the reactor. The important conclusions that have been drawn from the present investigations are chapter wise listed below:

8.1 Effect of Ta addition on thermodynamic properties of V-Ti-Ta alloys

1. Thermodynamic properties of V-Ti-Ta alloys were experimentally measured using Knudsen effusion vapor pressure measurements in the temperature range of 1900-2100 K. Vapor pressures of both V and Ti were found to decreases on the addition of Ta in the V-4Ti-xTa alloys.

2. Activities of V and Ti showed negative deviation from the ideal behaviour. Partial free energies of Ti and V and their excess values became increasingly negative with the addition of Ta, which is indicative of increasing thermodynamic stability of V-4Ti-xTa alloys.

3. Concentration dependence of thermodynamic activities of V-Ti-Ta alloys investigated in this study have shown that the energetics in the ternary alloys are influenced by the strong Ti-Ta and V-Ta bond energy leading to negative deviations from the ideal behavior.

4. Based on the partial pressure measurements, V-4Ti-7Ta composition was identified as the composition exhibiting superior thermodynamic stability among the investigated compositions.

8.2 Recrystallization and structure-property correlation in V-Ti-Ta alloys

1. Heat treatments of deformed samples at different temperatures and time showed lower Ta content alloy (V-4Ti-1Ta) undergo full recrystallization at temperature as low as 1150 °C, on the other hand, higher Ta containing alloy (V-4Ti-7Ta) requires an annealing treatment of 3 hrs at 1300 °C to achieve nearly fully recrystallized microstructure. Slower recrystallization kinetics in V-4Ti-7Ta alloys were attributed to the presence of Ta, which retarded diffusion kinetics resulting in slower recovery, nucleation and growth processes of newer recrystallized grains.

2. SEM investigation revealed the presence of needle shaped precipitates in all the samples (80-150 nm (width)). Using a combination of phase analysis (synchrotron XRD) and microscopic investigations, the precipitate phase was identified as (Ti,Ta)CON. Unique orientation relationship between the precipitates and matrix was determined as: (020)m ||(200)p, [001]m || [011]p (Baker Nutting OR). XRD and EDS analyses showed nearly equi-partitioning of Ta in the precipitates as well as in the matrix of V-Ti-Ta alloys. This behavior is in contrast to the V-Ti-Cr alloys, where nearly all the precipitates are devoid of Cr.

3. In V-Ti-Ta alloys, the presence of precipitates was noticed even in those samples which were annealed at temperature as high as 1300 °C. In V-4Ti-4Cr alloy, TiC precipitates were reported to get dissolved at temperatures above 1100 °C. It could, therefore, be inferred that the precipitates formed in V-Ti-Ta alloys exhibit superior stability over TiC precipitates observed in V-Ti-Cr alloys.

4. Thermodynamic estimations using CalPhad calculations have shown that addition of Ta increases the stability of the precipitate phase, whereas, Cr destabilizes the phase. This was attributed to be the reason for the presence of Ta in the precipitate phase (Ti,

Ta) (CON). Based on this study, it is expected that precipitates with superior phase stability resist dissolution, which would reduce the chance of redistribution of interstitials in the matrix phase and thereby it would lower the low-temperature working limit below 400 °C.

5. Yield strength of V-4Ti-7Ta was found to be 20 % higher in comparison to the V-4Ti-4Cr alloy. Substitutional solid strengthening was found to be the major governing factor for the higher strength in V-Ti-Ta alloys. Hence, the synergistic effect of Ta addition on strengthening of V-Ti-Ta alloy and as well as on enhancing high temperature precipitate phase stability, would increase the limit of high temperature window beyond 700 °C. In short, for fusion reactor structural material applications, a wider operational temperature window could be expected in the case of V-Ti-Ta alloys.

8.3   High temperature oxidation behaviour of V-Ti-Ta alloys

1. Non-isothermal oxidation in thermo-analyser showed that V alloys undergo severe oxidation above 670 °C. Isothermal oxidation studies revealed parabolic oxidation behaviour of the V-Ti-Ta alloys in the temperature range of 250–500 °C and linear behaviour was observed at and above 750 °C.

2. During isothermal oxidation upto 500 °C, V-4Ti-7Ta alloy exhibited almost 50 % lower specific weight gain in comparison to unalloyed V. This implied that the addition of Ti and Ta into V has enhanced oxidation resistance of the alloys. SEM-EDS and XRD investigations revealed the presence of V_2O_5 as the major phase in the oxidized surface of V-Ti-Ta alloys with co-presence of Ti and Ta in the solid solution.

3. Based on the oxidation mechanism, enhanced oxidation performance of V-Ti-Ta alloys were attributed to the combination of two factors:

   a. Increased activation energy for the initiation (onset) of oxidation from 112 kJ/mol to 130 kJ/mol, due to decrease in the activity of vanadium in V-Ti-Ta alloys.

   b. Decrease in diffusivity of oxygen ions (70 %) through V-oxide layer on account of

the presence of Ti and Ta in the oxide layer, which reduces the rate of oxide formation.

8.4 Wear behaviour of V-Ti-Ta alloys under reciprocating sliding conditions

1. Coefficients of friction of vanadium and its alloys measured in the present study were found to be in the range of 0.30 to 0.51 when tested for a normal load of 5 N and 15 N. Increase of normal load increases COF values both for vanadium and its alloys. Application of normal load was found to play a significant role in COF values as compared to sliding frequency. The presence of alloying elements, such as Ti and Ta, did not found to influence COF as compared to un-alloyed vanadium.

2. Wear rates were measured using the optical profilometry of wear track surfaces. Like COF, Wear rates of V-Ti-Ta alloy also depend on the applied load, as almost three times higher wear rate was noticed when the applied load was increased from 5 N to 15 N. The increase of normal load increases the severity of surface cracking which, in turn, increases the wear rate of the investigated material.

3. V-4Ti-7Ta alloy exhibited superior wear performance (~68 % lower wear rate) in comparison to un-alloyed vanadium. This enhanced wear performance of V-Ti-Ta alloys were explained with the help of microstructural characterization of wear track regions and phase characterization of wear debris. SEM-EDS of wear track showed three distinct regions (a) cracked regions (b) plough region and (c) partially melted regions. Based on this extensive investigations, wear mechanisms were proposed. Wear mechanism of V-Ti-Ta alloys mainly involves adhesive wear and oxidative wear which resulted in the formation of a mixed oxide tribo-chemical layer.

4. Based on the wear mechanism, superior wear performance of V-Ti-Ta alloys were attributed to three major factors:

a. Presence of alloying elements, such as Ti and Ta in V matrix, increase the yield strength of the material by solid solution strengthening and thereby offer increased wear resistance.

b. The presence of elements, like Ti, Ta, Fe, in solid solution with vanadium oxides (in tribo-layer) enhances the hardness of the oxide phase which offers enhanced resistance to the base material erosion and contributes to superior wear performance over un-alloyed vanadium sample.

c. Formation of V_2O_5 which provides lubricious behaviour in the high frequency region by melting and in low frequency region when it is in solid state by easy cleaving due to its layered structure having high B/C44 ratio.

8.5   Summary

Major finding of this study can be summarized in Fig. 8.1, which illustrates the effect of Ta addition in V-Ti-Ta alloys with respect to (a) thermodynamic properties, (b) mechanical properties, (c) oxidation properties and (d) wear properties, by keeping in mind about its possible structural applications in the proposed fusion reactor. These alloys have shown that the addition of Ta increased high temperature phase stability, induced high strength, better stabilities of precipitate phase, higher oxidation resistance at elevated temperature and reduced wear rate in the V-Ti-Ta alloy system. Among all the investigated compositions, V-4at%Ti-2at%Ta alloy exhibited the most optimum combination of properties. Comparison of the newly developed V-4at.%Ti-2at.%Ta alloy with the already established V-4at.%Cr-4 at.% Ti alloys is shown in Fig. 8.2. It can be seen that in contrast to the vanadium alloys containing Cr, Ta containing vanadium alloys exhibited negative deviation from ideal behaviour, which ensures better high temperature phase stability of the alloys. It could also be seen that V-4Ti-2Ta alloy exhibit higher precipitate stability and increased yield strength (20 % higher) compared to V-4Ti-4Cr alloy. So the developed V-4Ti-2Ta alloy even having lesser alloying content, exhibited

improved properties, which will be useful in increasing operation temperate window of fusion reactor. It can also be seen from Fig. 8.2 that V-4Ti-2Ta alloy exhibited 20 % lower specific weight gain, 70 % lower diffusion coefficient of oxygen and higher activation energy for oxidation compared to V-4Ti-4Cr alloy. The improved oxidation behaviour of V-4Ti-2Ta alloy would enhance safety and reliability of the reactor operation. On the basis of the above summarization, it can be concluded from this study that V-Ti-Ta alloys offer better properties in comparison to V-Ti-Cr alloys as potential structural material for fusion reactor.
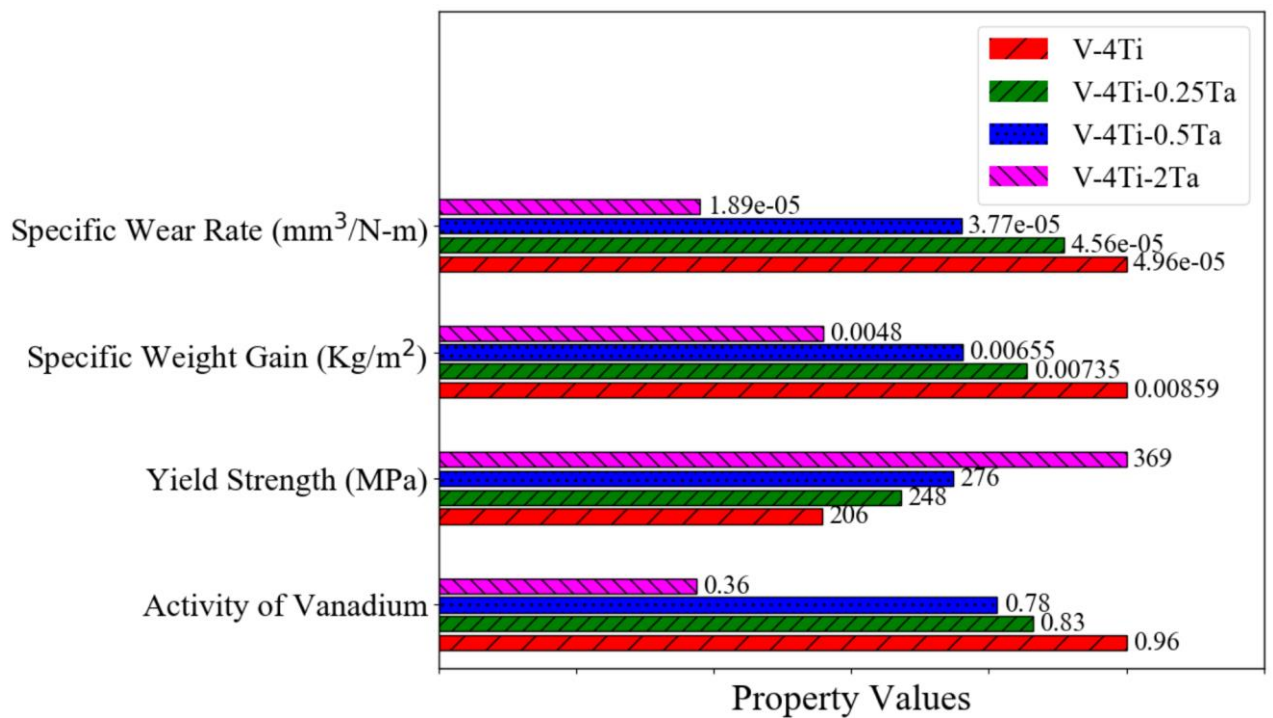
Fig. 8.1 Effect of Ta addition in V-Ti-Ta alloys on (a) thermodynamic activity of V, (b) yield strength, (c) oxidation properties measured as specific weight gain, and (d) wear properties measured as specific wear rate.
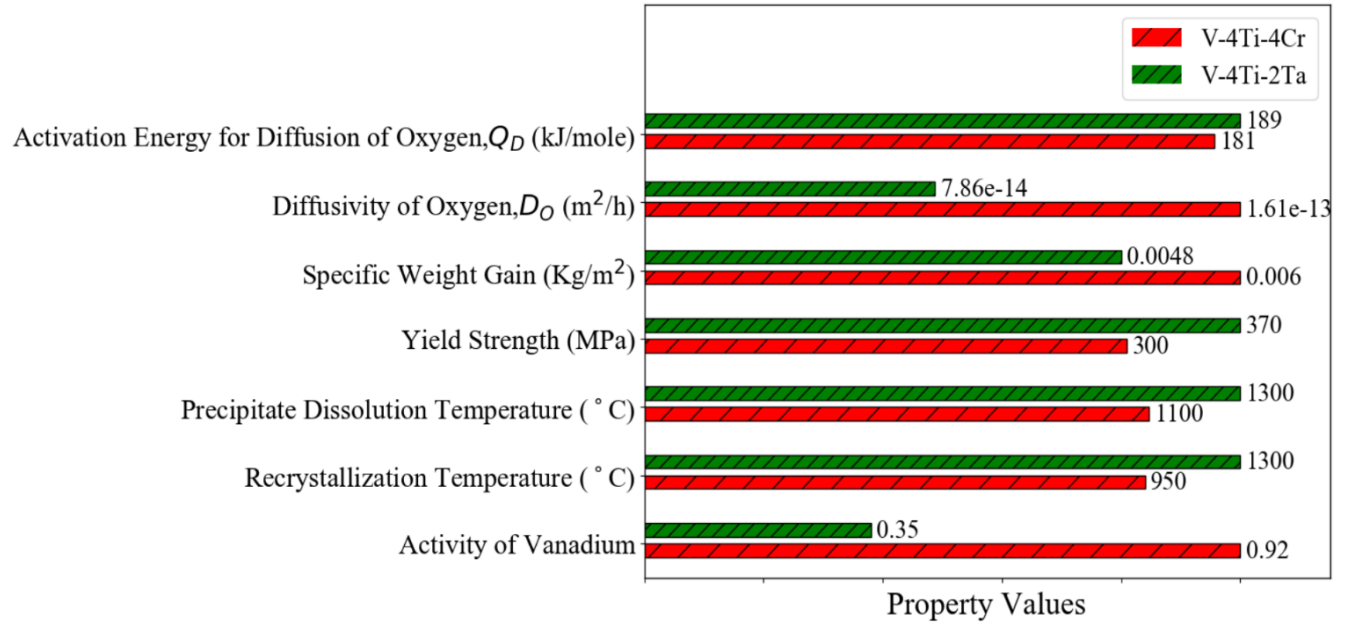
Figure 8.2: Comparison of properties of newly developed V-4Ti-2Ta alloy with already proposed V-4Ti-4Cr alloy [80,94,50,81,107,108].

Scope for Further Research

On the basis of the work carried out in this dissertation, the following are a few suggestions for further work:

1. The developed V-Ti-Ta alloys would be evaluated for high temperature properties for its use as plasma facing structural material in fusion reactor. The alloys would be investigated for mechanical properties in the expected operational temperature of a fusion reactor (between 500-800 °C).

2. The precipitates likely to undergo irradiation assisted dissolution and result in shifting the ductile to brittle transformation temperature to above room temperature. The resultant DBTT transition would severely affect the impact properties of the material. Hence, it is important to establish the irradiation stability of precipitates and its impact on mechanical properties. Examination of irradiation response of the alloy at high temperature to test the He embrittlement and void swelling behaviour of the alloys.

3. Exploration of Vanadium containing high entropy alloys as an alternate candidate for high temperature structural applications in fusion reactor.

Bibliography

[1] "Nuclear Reactor Materials", C.K. Gupta, K.H.J. Buschow, R.W. Cahn, M.C. Flemings, B. Ilschner, E.J. Kramer, S. Mahajan, P. Veyssière (Eds.), Encyclopedia of Materials: Science and Technology, Elsevier, Oxford, **2001**, 6339-6349.

[2] "Nuclear Energy Systems: Advanced Alloys and Cladding", K.H.J. Buschow, M. Samaras, R.W. Cahn, M.C. Flemings, B. Ilschner, E.J. Kramer, S. Mahajan, P. Veyssière (Eds.), Encyclopedia of Materials: Science and Technology, Elsevier, Oxford, **2011**, 1-7.

[3] "Structural materials issues for the next generation fission reactors", I. Chant, K.L. Murty, JOM, **2010**, *62 (9)*, 67-74.

[4] "Nuclear Reactors: Generation to Generation", S.M.G.a.R. Rosner, American Academy of Arts and Sciences, **2011**.

[5] "Research Reactors for the Development of Materials and Fuels for Innovative Nuclear Energy Systems", International atomic energy agency, Vienna, **2017**.

[6] "Comparison of Displacement and Gas Production Rates in Current Fission and Future Fusion Reactors", G.L. Kulcinski, D.G. Doran, M.A. Abdou, in: C.J. Baroch (Ed.), ASTM International, West Conshohocken, PA, **1975**, 329-351.

[7] "Structural materials for fission & fusion energy", S.J. Zinkle, J.T. Busby, Materials Today **2009**, *12*, 12-19.

[8] "Modelling materials for fusion power", D. Duffy, International Materials Reviews, **2011**, *56(5-6)*, 324-340.

[9] "Materials issues in fusion reactors", A.K. Suri, N. Krishnamurthy, I.S. Batra, Journal of Physics: Conference Series, **2010**, *208*, 012001.

[10] Operating temperature windows for fusion reactor structural materials, S.J. Zinkle, N.M. Ghoniem, Fusion Engineering and Design, **2000**, *51-52,* 55-71.

[11] "Vanadium Alloys for Fusion Blanket Applications", T. Muroga, Materials transactions **2005**, *46(3),* 6.

[12] "International strategy for fusion materials development", K. Ehrlich, E.E. Bloom, T. Kondo, Journal of Nuclear Materials, **2000**, *283-287*, 79-88.

[13] "Low activation structural materials for fusion", G.J. Butterworth, Fusion Engineering and Design, **1989,** *11(1-2)*, 231-244.

[14] "Nuclear data needs for low-activation fusion materials development", S. Cierjacks, Fusion Engineering and Design, **1990**, *13(2)*, 229-238.

[15] "Reduced Activation Materials for Fusion Reactors", R.L. Klueh, ASTM Committee E-10 on Nuclear Technology and Applications; ASTM International, **1990**.

[16] "Experimental investigation of radioactivities induced in fusion reactor structural materials by 14-MeV neutrons", D.V. Markovskij, R.A. Forrest, H. Freiesleben, V.D. Kovalchuk, D. Richter, K. Seidel, V.I. Tereshkin, S. Unholzer, Fusion Engineering and Design **2000**, *51-52*, 695-700.

[17] "The Acta of Hugh of Wells", D.M. Smith, Bishop of Lincoln, **2000**, 1209-1235

[18] "Atomically resolved chemical ordering at the nm-thick TiO precipitate/matrix interface in V-4Ti-4Cr alloy", A. Impagnatiello, D. Hernandez-Maldonado, G. Bertali, E. Prestat, D. Kepaptsoglou, Q. Ramasse, S.J. Haigh, E. Jimenez-Melero, Scripta Materialia, **2017**, *126*, 50-54.

[19] "Development and testing of vanadium alloys for fusion applications", H.M. Chung, B.A. Loomis, D.L. Smith, Journal of Nuclear Materials, **1996**, *239(1-3)*, 139-156.

[20] K. Fukumoto, T. Morimura, T. Tanaka, A. Kimura, Abe, H. Takahashi, H. Matsui, Mechanical properties of vanadium based alloys for fusion reactor, Journal of Nuclear Materials, **1996**, *239(1-3)*, 170-175.

[21] "Research and development on vanadium alloys for fusion applications", S.J. Zinkle, H. Matsui, D.L. Smith, A.F. Rowcliffe, E. van Osch, K. Abe, V.A. Kazakov, Journal of Nuclear Materials, **1998**, *258-263*, 205-214.

[22] "Overview of the vanadium alloy researches for fusion reactors", J.M. Chen, V.M. Chernov, R.J. Kurtz, T. Muroga, Journal of Nuclear Materials, **2011**, *417(1)*, 289-294.

[23] "Void swelling behavior in ion-irradiated vanadium alloys", T. lwai, N. Sekimura, F.A. Garner, Journal of Nuclear Materials, **1996**, *239*, 157-161.

[24] "Irradiation hardening of V–4Cr–4Ti", E.V. van osch, M.I. de Vries, Journal of Nuclear Materials, **1999**, *271-272*, 162-166.

[25] "Swelling of pure vanadium and V-5Cr at ∼430 °C in response to variations in neutron flux-spectra in FFTF", F.A. Garner, T. Okita, N. Sekimura, Journal of Nuclear Materials, **2011**, *417(1)*, 314-318.

[26] "Investigation of vanadium-based alloys corrosion resistance in liquid lithium", I.V. Borovitskaya, I.E. Lyublinski, V.V. Paramonova, S.N. Korshunov, A.N. Mansurova, M.M. Lyakhovitskiy, Inorg. Mat. Appl. Res. **2015**, **6**, 133-138.

[27] "Liquid metal compatibility issues for test blanket modules", B.A. Pint, J.L. Moser, P.F. Tortorelli, Fusion Engineering and Design, **2006**, *81(8),* 901-908.

[28] Fusion Reactor Materials Part AVanadium alloys for structural applications in fusion systems: a review of vanadium alloy mechanical and physical properties, R.K. Klueh, R.E. Stoller, D.S. Gelles, B.A. Loomis, D.L. Smith, Journal of Nuclear Materials, **1992**, *191*, 84-91.

[29] "Vanadium alloys as structural materials for fusion reactor blanket", S. N. VOTINOV, Plasma Devices and operations, **1996**, 9.

[30] Prospects and problems using vanadium alloys as a structural material of the first wall and blanket of fusion reactors, S.N. Votinov, M.I. Solonin, Y.I. Kazennov, V.P. Kondratjev, A.D. Nikulin, V.N. Tebus, E.O. Adamov, S.E. Bougaenko, Y.S. Strebkov, A.V. Sidorenkov, V.B. Ivanov, V.A. Kazakov, V.A. Evtikhin, I.E. Lyublinski, V.M. Trojanov, A.E. Rusanov, V.M. Chernov, G.A. Birgevoj, Journal of Nuclear Materials, **1996**, *233-237*, 370-375.

[31] R.J. Kurtz, K. Abe, V.M. Chernov, D.T. Hoelzer, H. Matsui, T. Muroga, G.R. Odette, Recent progress on development of vanadium alloys for fusion, Journal of Nuclear Materials, **2004**, *329-333*, 47-55.

[32] "Current Status of Fusion Reactor Structural Materials R&D", A. Kohyama, Materials Transactions, **2005**, *46(3)*, 10.

[33] "Present status of vanadium alloys for fusion applications",T. Muroga, J.M. Chen, V.M. Chernov, R.J. Kurtz, M. Le Flem, Journal of Nuclear Materials, **2014**, *455(1–3)*, 263-268.

[34] "Towards V-based high-entropy alloys for nuclear fusion applications", P.J. Barron, A.W. Carruthers, J.W. Fellowes, N.G. Jones, H. Dawson, E.J. Pickering, Scripta Materialia, **2020**, *176*, 12-16.

[35] "Materials to deliver the promise of fusion power – progress and challenges", E.E. Bloom, S.J. Zinkle, F.W. Wiffen, Journal of Nuclear Materials, **2004**, *329-333* 12-19.

[36] "Vanadium-base alloys for fusion first-wall/blanket applications", D.L. Smith, M.C. Billone, K. Natesan, International Journal of Refractory Metals and Hard Materials, **2000,** *18(4),* 213-224.

[37] "Fusion power: a challenge for materials science", D.M. Duffy, Philosophical Transactions of Royal Society A, **2010**, *368,* 3315–3328.

[38] "Reduction of impurity levels of vanadium and its alloys for fusion application", T. Muroga, T. Nagasaka, International Journal of Refractory Metals and Hard Materials, **2000,** *18(4),* 225-230.

[39] "Vanadium alloys – overview and recent results", T. Muroga, T. Nagasaka, K. Abe, V.M. Chernov, H. Matsui, D.L. Smith, Z.Y. Xu, S.J. Zinkle, Journal of Nuclear Materials, **2002**, *307-311*, 547-554.

[40] "Mechanical properties of vanadium and vanadium-base alloys", D.L. Harrod, R.E. Gold, International Metals Reviews, **1980,** *25(1),* 163-222.

[41] "Vanadium-base alloys for fusion reactor applications — a review", D.L. Smith, B.A. Loomis, D.R. Diercks, Journal of Nuclear Materials, **1985**, *135(2)*, 125-139.

[42] "Alloying and impurity effects in vanadium-base alloys", D.R. Diercks, B.A. Loomis, Journal of Nuclear Materials, **1986**, *141-143*, 1117-1124.

[43] "Effect of Ti addition on microstructural evolution of V–Cr–Ti alloys to balance irradiation hardening with swelling suppression", K. Fukumoto, K. Tone, T. Onitsuka, T. Ishigami, Nuclear Materials and Energy, **2018**, *15*, 122-127.

[44] "Monolayer-thick TiO precipitation in V-4Cr-4Ti alloy induced by proton irradiation", A. Impagnatiello, S.M. Shubeita, P.T. Wady, I. Ipatova, H. Dawson, C. Barcellini, E. Jimenez-Melero, Scripta Materialia, 2017, 130, 174-177.

[45] "The recovery and recrystallization of cold rolled V–W–Ti alloys", J. Chen, T. Muroga, T. Nagasaka, Y. Xu, S. Qiu, Journal of Nuclear Materials, **2003**, *322(1)*, 73-79.

[46] "Precipitation behavior in V–6W–4Ti, V–4Ti and V–4Cr–4Ti alloys", J.M. Chen, T. Muroga, T. Nagasaka, Y. Xu, C. Li, S.Y. Qiu, Y. Chen, Journal of Nuclear Materials, **2004**, *334(2–3)*, 159-165.

[47] "The development of advanced vanadium alloys for fusion applications", J.M. Chen, T. Muroga, S.Y. Qiu, T. Nagasaka, W.G. Huang, M.J. Tu, Y. Chen, Y. Xu, Z.Y. Xu, Journal of Nuclear Materials, **2004**, *329–333*, 401-405.

[48] "Effect of precipitates on high-temperature strength and irradiation behavior of vanadium-based alloys", S.n. Jiang, L.q. Xu, F.r. Wan, Journal of Iron and Steel Research International, **2018**, *25(12)*, 1270-1277.

[49] "Stability of oxide particles under electron irradiation in a 9-Cr ODS steel at 400 °C", F. Li, H. Abe, T. Ishizaki, Y. Li, T. Nagasaka, T. Muroga, T. Nagase, H. Yasuda, Journal of Nuclear Materials, **2014,** *455(1)*, 724-727.

[50] The effect of final heat treatment temperature on radiation response of V–4Cr–4Ti, T. Muroga, T. Nagasaka, H. Watanabe, M. Yamazaki, Journal of Nuclear Materials, **2011**, *417(1)*, 310-313.

[51] "Oxidation studies of Indian reduced activation ferritic martensitic steel", A. Mukherjee, U. Jain, G.K. Dey, Journal of Thermal Analysis and Calorimetry, **2017**, *128(2)*, 819-824.

[52] "Oxidation of beryllium—a scanning Auger investigation, C. Tomastik", W. Werner, H. Stori, Nuclear Fusion, **2005**, *45(9)*, 1061-1065.

[53] Exploration of vanadium base alloys, R.W. Yamamoto A. S., Mcpherson D. J. , Hansen M;, WADC Technical report Part (1-3), **1952-1955**, 52-145.

[54] The development of improved vanadium-base alloys for use at temperatures up to 1800 °F, B.R. Rajala, R.J. Van Thyne, Journal of the Less Common Metals, **1961**, 3(6), 489-500.

[55] "Consolidation and fabrication techniques for Vanadium-20 wt.% Titanium (TV-20)", J. Burt, W. R. Kramer, W. C. McGowan, R. D. Karasek, F. J. Mayfield, R. M. , Argonne National laboratory, **1965**, 6928, 1-85.

[56] Vanadium Alloy Screening Studies and Fabrication of V-15 w/oTi-7.5 w/o Cr Tubing for Nuclear Fuel Cladding, B.J.W. Kramer , Karasek FJ, Flinn JE, Mayfield R. M., Argonne National Laboratory report, **1966**, *ANL-7206*, 1-64.

[57] "Vanadium alloy cladding development". M.P.A.R.D. Westinghouse Electric Corp, Quarterly progress report for the period ending December 31, 1969, United States, **1970**, p. 24.

[58] "Vanadium Alloys vs Stainless Steel for Sodium-Cooled Fast Reactor Cladding", Nuclear applications and technology, **1969**, *7(5)*, 443-455.

[59] "Report on the Elevated-Temperature Properties of Stainless Steels", W.S.H. Cross, ASTM International, West Conshohocken, PA, **1952**.

[60] "Technical assessment of vanadium-base alloys for fusion reactor applications", R.E. Gold, D.L. Harrod, R.L. Ammon, R.W. Buckman, Jr., R.C. Svedberg, **1978,** *1*, 57.

[61] "Corrosion and oxidation of vanadium-base alloys", B.A. Loomis, G. Wiggins, Journal of Nuclear Materials, **1984**, *122(1)*, 693-697.

[62] "Status of vanadium alloys for fusion reactors", H. Matsui, K. Fukumoto, D.L. Smith, H.M. Chung, W. van Witzenburg, S.N. Votinov, Journal of Nuclear Materials, **1996**, *233-237*, 92-99.

[63] "Mechanical properties and microstructures of high-chromium V–Cr–Ti type alloys", K. Sakai, M. Satou, M. Fujiwara, K. Takanashi, A. Hasegawa, K. Abe, Journal of Nuclear Materials, **2004,** *329-333*, 457-461.

[64] "Effects of neutron irradiation and hydrogen on ductile-brittle transition temperatures of V-Cr-Ti alloys", B.A. Loomis, H.M. Chung, L.J. Nowicki, D.L. Smith, Journal of Nuclear Materials, **1994,** *212-215*, 799-803.

[65] "Lattice Parameter and Coefficient of Thermal Expansion of Vanadium", J.J. William, M.E. Straumanis, Zeitschrift für Physikalische Chemie, **1961,** *29(1-2)*, 134-142.

[66] "Phase equilibrium of the Ti–Cr–V ternary system in the non-burning β-Ti alloy region", J.Y. Lee, J.H. Kim, S.I. Park, H.M. Lee, Journal of Alloys and Compounds, **1999,** *291(1)*, 229-238.

[67] "The mo-v system (molybdenum-vanadium)", J.F. Smith, Journal of Phase Equilibria, **1992,** *13(1)*, 50-53.

[68] "The Nb−V (Niobium-Vanadium) system", J.F. Smith, O.N. Carlson, Bulletin of Alloy Phase Diagrams, **1983,** *4(1)*, 46-49.

[69] "The Ta-V (Tantalum-Vanadium) system", J.F. Smith, O.N. Carlson, Bulletin of Alloy Phase Diagrams, **1983,** *4(3)*, 284-289.

[70] "Thermodynamic and kinetic modeling of the Cr-Ti-V system", G. Ghosh, Journal of Phase Equilibria, **2002**, *23(4),* (2002) 310.

[71] "The Ta-Ti-V system (tantalum-titanium-vanadium)", M. Enomoto, Journal of Phase Equilibria, **1992,** 13(1), 91-94.

[72] "The Ta−Ti (Tantalum-Titanium) system", J. L. Murray, Bulletin of alloy Phase Diagrams, **1981**, *2(1)*, 62-66.

[73] "Effect of nitrogen and carbon on the low-temperature embrittlement of vanadium", Journal of the Less Common Metals, **1965**, *9(5)*, 354-361.

[74] "Fabrication of a 1200 kg ingot of V–4Cr–4Ti alloy for the DIII–D radiative divertor program", W.R. Johnson, J.P. Smith, Journal of Nuclear Materials, **1998**, *258-263*, 1425-1430.

[75] "French investigation of a new V–4Cr–4Ti grade: CEA-J57 – Fabrication and microstructure", V. Duquesnes, T. Guilbert, M. Le Flem, Journal of Nuclear Materials, **2012,** *426(1),* 96-101.

[76] "Low activation vanadium alloys for fusion power reactors – the RF results", V. Chernov, V. Drobyshev, M. Potapenko, D. Blokhin, N. Budylkin, N. Degtyarev, I. Izmalkov, E. Mironova, I. Kudryavtseva, A. Tyumentsev, I.A. Ditenberg, K. Grinyaev, B. Kardashev, R. Blokhin, N. Loginov, V. Romanov, A. Sivak, P. Sivak, S. Psakhie, K. Zolnikov, 24th IAEA Fusion Energy Conference, US, **2012**.

[77] "Peculiarities of helium bubble formation and helium behavior in vanadium alloys of different chemical composition", M.S. Staltsov, I.I. Chernov, B.A. Kalin, K.Z. Oo, A.A. Polyansky, O.S. Staltsova, K.Z. Aung, V.M. Chernov, M.M. Potapenko, Journal of Nuclear Materials, **2015,** *461*, 56-60.

[78] "Influence of thermal treatment on helium trapping at fine-size precipitates in V–4Cr–4Ti", Journal of Nuclear Materials, **1998**, *258-263*, 1400-1403.

[79] "Examination of fabrication process parameters for improvement of low-activation vanadium alloys", T. Nagasaka, N.J. Heo, T. Muroga, M. Imamura, Fusion Engineering and Design, **2002,** *61-62*, 757-762.

[80] "Recrystallization and precipitation behavior of low-activation V–Cr–Ti alloys after cold rolling", N.J. Heo, T. Nagasaka, T. Muroga, Journal of Nuclear Materials, **2004**, *325(1),* 53-60.

[81] "Improvement of Vanadium Alloys by Precipitate Control for Structural Components of Fusion Reactors", T. Muroga, T. Nagasaka, A. Nishimura, J.M. Chen, Materials Science Forum, **2005,** *475-479*, 1449-1454.

[82] "The formation of precipitates and its effect on grain structure in V-4Cr-4Ti alloys with yttrium addition", L. Peng, C. Jiang, X. Li, P. Zhou, Y. Li, X. Lai, Journal of Alloys and Compounds, **2017**, *694*, 1165-1174.

[83] "A quasi-in-situ EBSD observation of the transformation from rolling texture to recrystallization texture in V-4Cr-4Ti alloy", L. Peng, X. Li, Z. Fan, C. Jiang, P. Zhou, X. Lai, Materials Characterization, **2017,** *126*, 35-41.

[84] "Formation and evolution of platelet-like Ti-rich precipitates in the V–4Cr–4Ti alloy", B. Zhu, S. Yang, M. Zhang, J. Ding, Y. Long, F. Wan, Materials Characterization, **2016**, *111,* 60-66.

[85] "Effect of precipitation and solution behavior of impurities on mechanical properties of low activation vanadium alloy", A. Nishimura, A. Iwahori, N.J. Heo, T. Nagasaka, T. Muroga, S.I. Tanaka, Journal of Nuclear Materials, **2004,** *329-333*, 438-441.

[86] "Effect of the modes of thermomechanical treatment on the formation of the multiphase and grain structure of V–4Ti–4Cr alloys", A.N. Tyumentsev, A.D. Korotaev, Y.P. Pinzhin, I.A. Ditenberg, S.V. Litovchenko, Y.V. Shuba, N.V. Shevchenko, V.A. Drobishev, M.M. Potapenko, V.M. Chernov, Journal of Nuclear Materials, **2004,** *329-333s*, 429-433.

[87] "High-resolution electron microscopy studies of the structure of Cu precipitates in α-Fe", P.J. Othen, M.L. Jenkins, G.D.W. Smith, Philosophical Magazine A, **1994,** *70(1)*, 1-24.

[88] "A survey of vanadium binary systems", W. Rostoker, A. Yamamoto, Trans. ASM, **1954,** *46,* 1136-1167.

[89] "Preparation and Properties of Iodide Vanadium", J.W. Nash, H.R. Ogden, R.E. Durtschi, I.E. Campbell, Journal of The Electrochemical Society, **1953**, *100(6)*, 272.

[90] "Properties of vanadium consolidated by extrusion", C. Lacy, C. Beck, Trans.Asm, **1956**, *48*, 579-594

[91] "The Role of Dilute Binary Transition Element Additions on the Recrystallization of Vanadium", E.P. Abrahsomson, Transactions of AIME, **1961,** *221*, 1193-1196.

[92] "U.S. Bureau of Mines", E. Loria, W. Ludemann, E. Rowe, Rept. of Invest., **1964**, *6547* 38.

[93] "Mechanical properties of vanadium-base binary alloys", N. Iwao, T. Kainuma, T. Suzuki, R. Watanabe, Journal of the Less Common Metals, **1982,** *83(2),* 205-217.

[94] "Recovery and recrystallization of vanadium alloys", A.N. Gubbi, A.F. Rowcliffe, Journal of Nuclear Materials, **1996,** *233-237*, 497-501.

[95] "Making vanadium-based radiation-resistant alloys for fast-neutron reactor pin sheaths", S.N. Votinov, V.P. Kolotushkin, S.A. Nikulin, V.Y. Turilina, Metal Science and Heat Treatment, **2009**, *51(5)* 238.

[96] "The hydrogen-induced ductility loss and strengthening of V-base alloys", J.M. Chen, S.Y. Qiu, T. Muroga, Y. Xu, T. Nagasaka, Y. Chen, Y. Deng, Z.Y. Xu, Journal of Nuclear Materials, **2004,** *334(2–3)*, 143-148.

[97] "Properties of V-4Cr-4Ti for application as fusion reactor structural components", H.M. Chung, B.A. Loomis, D.L. Smith, Fusion Engineering and Design, **1995,** *29*, 455-464.

[98] "Fracture toughness and micromechanics in a V-4Cr-4Ti alloy", G.R. Odette, G.E. Lucas, E. Donahue, J.W. Sheckherd, Journal of Nuclear Materials, **1996**, *233-237*, 502-506.

[99] "Fracture properties of high-purity V–4Cr–4Ti alloy (NIFS-HEAT-2) at room temperature", Journal of Nuclear Materials, **2002**, *307-311*, 571-575.

[100] "Influence of flux-spectra differences on transmutation, dimensional changes and fracture of vanadium alloys", F.A. Garner, L.R. Greenwood, B.A. Loomis, S. Ohnuki, N. Sekimura, Journal of Nuclear Materials, **1996,** *233-237,* 406-410.

[101] "High temperature creep of vanadium", A. Juhász, I. Kovács, I. Vitányi, Journal of the Less Common Metals, **1978,** *61(2),* 309-320.

[102] "Effects of purity on high temperature mechanical properties of vanadium alloys", M. Koyama, K. Fukumoto, H. Matsui, Journal of Nuclear Materials, **2004**, *329-333*, 442-446.

[103] "High-temperature creep properties of NIFS-HEAT-2 high-purity low-activation vanadium alloy", T. Nagasaka, T. Muroga, T. Tanaka, A. Sagara, K. Fukumoto, P.F. Zheng, R.J. Kurtz, Nuclear Fusion, **2019**, *59(9)*, 096046.

[104] "Introduction to the High Temperature Oxidation of Metals", N. Birks, G.H. Meier, F.S. Pettit, 2 ed., Cambridge University Press, Cambridge, **2006**.

[105] "Corrosion behavior of vanadium-base alloys in pressurized water at 288 °C", D.R. Diercks, D.L. Smith, Journal of Nuclear Materials, **1986**, *141-143* (1986) 617-621.

[106] "Oxidation of vanadium and vanadium alloys in gaseous helium coolants containing water vapor impurities", G. Busch, A. Tobin, Journal of Nuclear Materials, **1986,** *141-143*, 599-603.

[107] "Reactions of oxygen with V-Cr-Ti alloys", J.R. DiStefano, J.H. DeVan, Journal of Nuclear Materials, **1997**, *249(2),* 150-158.

[108] "Oxidation performance of V-Cr-Ti alloys", K. Natesan, M. Uz, Fusion Engineering and Design, **2000,** *51-52,* 145-152.

[109] "Kinetics of the oxidation of vanadium in the temperature range 350–950 °C", A. Mukherjee, S.P. Wach, Journal of the Less Common Metals, **1983,** *92(2)*, 289-300.

[110] "Oxidation of Vanadium in Dry and Moist Oxygen–Argon Mixtures", J.R. Wilson, M.E. Lewis, Nature, **1965,** *206,* 1350.

[111] "The Kinetics of the Reactions of Vanadium with Oxygen and Nitrogen", K.F. Anderson, E.A. Gulbransen, J. Electrochem. Soc., **1950**, *97(11),* 396-404.

[112] "Oxygen diffusion in vanadium-based alloys", R.R. de Avillez, PhD thesis, University of Illinois, United States, **1981**.

[113] "Oxidation kinetics and microstructure of V-(4–5) wt.% Cr-(4–5) wt.% Ti alloys exposed to air at 300–650°C", M. Uz, K. Natesan, V.B. Hang, Journal of Nuclear Materials, **1997,** *245(2),* 191-200.

[114] "Experimental qualification of subassembly design for Prototype Fast Breeder Reactor", V. Prakash, M. Thirumalai, M. Anandaraj, P.A. Kumar, D. Ramdasu, G.K. Pandey, G. Padmakumar, C. Anandbabu, P. Kalyanasundaram, Nuclear Engineering and Design, **2011**, *241(8)*, 3325-3332.

[115] "Materials and Manufacturing Technologies for Sodium Cooled Fast Reactors and Associated Fuel Cycle: Innovations and Maturity", Energy Procedia, **2011**, *7,* 186-198.

[116] "Effect of Normal Stiffness in Loading System on Wear of Carbon Steel—Part 1: Severe-Mild Wear Transition", Y.C. Chiou, K. Kato, T. Kayaba, Journal of Tribology, **1985,** *107(4)*, 491-495.

[117] "Grain-Size and R-Curve Effects in the Abrasive Wear of Alumina", S.J. Cho, B.J. Hockey, B.R. Lawn, S.J. Bennison, Journal of the American Ceramic Society, **1989,** *72(7)*, 1249-1252.

[118] "Investigation on wear characteristics of a titanium alloy/steel tribo-pair", K.M. Chen, Y. Zhou, X.X. Li, Q.Y. Zhang, L. Wang, S.Q. Wang, Materials & Design, **2015,** *65,* 65-73.

[119] "A parametric study of the relationship between microstructure and wear resistance of Al–Si alloys", M. Elmadagli, T. Perry, A.T. Alpas, Wear, **2007,** *262(1)*, 79-92.

[120] Transition between mild and severe wear in titanium alloys, K. Farokhzadeh, A. Edrisy, Tribology International, **2016,** *94*, 98-111.

[121] "Studies on the dry sliding wear behaviour of hypoeutectic and eutectic Al–Si alloys", S.A. Kori, T.M. Chandrashekharaiah, Wear, **2007,** *263(1)*, 745-755.

[122] "Effects of silicon content on the mechanical and tribological properties of monotectoid-based zinc–aluminium–silicon alloys", T. Savaşkan, A. Aydıner, Wear, **2004,** *257(3)*, 377-388.

[123] "Wear characteristics of Al-Si alloys", H. Torabian, J.P. Pathak, S.N. Tiwari, Wear, **1994,** *172(1)*, 49-58.

[124] "Tribological study of nitrogen implanted niobium", T.M. Wang, X.J. Wang, W.J. Wang, J. Shi, Wear, **1996,** *196(1)*, 197-201.

[125] "Surface Modification of Titanium, Titanium Alloys, and Related Materials for Biomedical Applications", L. Xuanyong, K. Chu Paul, D. Chuanxian, Materials Science and Engineering R, **2004,** *47,* 49-121.

[126] "Tribological study of vanadium-based alloys ion implanted at low energy and high temperature", J.A. García, R. Rodríguez, R. Sánchez, R. Martínez, M. Varela, D. Cáceres, A. Muñoz, I. Vergara, C. Ballesteros,Vacuum, **2002,** *67(3),* 543-550.

[127] "The Design, Construction, and Testing of a Knudsen Effusion Mass Spectrometric System Suitable for Studies of Nuclear Fuel Materials", D.D.A. Raj, R. Viswanathan, P. Manikandan, ECS Transactions, **2013,** *46(1)*, 77-97.

[128] "Analysis of flow behaviour of iron and steel using power law models", C. Gupta, B. Kumawat, Materials Science and Technology, **2017,** *33(8)*, 971-983.

[129] "Thermochemical data of pure substances", VCH Verlagsgesellschaft mbH and VCH Publishers, Weinheim and New York, **1995.**

[130] "JANAF THERMOCHEMICAL TABLES" Third Edition, Analytical Chemistry, **1990,** *62(10)*, 588A-588A.

[131] "Electron Impact Ionization of Atoms", A.B. Tsipinyuk, E. Kolodney,eprint arXiv:physics/0407030 (**2004**).

[132] "Determination of thermodynamic interaction parameters in solid V-Ti alloys using the mass spectrometer", E.J. Rolinski, M. Hoch, C.J. Oblinger, Metallurgical Transactions, **1971,** *2(9),* 2613-2618.

[133] "Current issues in recrystallization: a review", R.D. Doherty, D.A. Hughes, F.J. Humphreys, J.J. Jonas, D.J. Jensen, M.E. Kassner, W.E. King, T.R. McNelley, H.J. McQueen, A.D. Rollett, Materials Science and Engineering: A, **1997,** *238(2)*, 219-274.

[134] "Room temperature compression properties of two heats of unirridiated V-4Cr-4Ti". M. Toloczko, R. Kurtz, In Fusion Materials: Semiannual Progress Report for Period Ending June 30, **2004.**

[135] "Texture formation in metal alloys with cubic crystal structures", Materials Science and Technology, **2016,** *32(13)*, 1303-1315.

[136] "Rolling and Annealing Textures of BCC Metals", D. Raabe, K. Lücke, Materials Science Forum, **1994,** *157-162,* 597-610.

[137] "Effect of skin pass rolling reduction rate on the texture evolution of a non-oriented electrical steel after inclined cold rolling", M. Mehdi, Y. He, E.J. Hilinski, A. Edrisy, Journal of Magnetism and Magnetic Materials, **2017,** *429,* 148-160.

[138] "Influence of the angle between cold rolling direction and hot rolling direction on the texture evolution of non-oriented electrical steels", Y. He, E. Hilinski, M. Attard, D. Bibby, R. Santos, R. Zavadil, IOP Conference Series: Materials Science and Engineering, **2015,** *82,* 012091.

[139] "Microstructure and room temperature properties of a high-entropy TaNbHfZrTi alloy", O.N. Senkov, J.M. Scott, S.V. Senkova, D.B. Miracle, C.F. Woodward, Journal of Alloys and Compounds, **2011,** *509(20)*, 6043-6048.

[140] "Thermo-Calc & DICTRA, computational tools for materials science", J.O. Andersson, T. Helander, L. Höglund, P. Shi, B. Sundman, Calphad, **2002,** *26(2)*, 273-312.

[141] "Oxidation studies of Indian reduced activation ferritic martensitic steel", A. Mukherjee, U. Jain, G. Dey, Journal of Thermal Analysis and Calorimetry, **2017,** *128*, 819–824.

[142] "Oxidation of beryllium—a scanning Auger investigation", Nuclear Fusion, **2005,** *45(9),* 1061.

[143] "Oxidation behavior of titanium alloy under diffusion bonding", H.-S. Lee, J.-H. Yoon, Y.-M. Yi, Thermochimica Acta, **2007,** *455(1),* 105-108.

[144] "Oxidation of Ti–6Al–4V alloy", H. Guleryuz, H. Cimenoglu, Journal of Alloys and Compounds, **2009,** *472(1),* 241-246.

[145] "Isothermal oxidation of Ti–6Al–7Nb alloy", K. Aniołek, M. Kupka, M. Łuczuk, A. Barylski, Vacuum, **2015,** *114(Supplement C)*, 114-118.

[146] "Isothermal oxidation mechanism of Nb–Ti–V–Al–Zr alloy at 700–1200°C: Diffusion and interface reaction", J. Zheng, X. Hou, X. Wang, Y. Meng, X. Zheng, L. Zheng, Corrosion Science, **2015,** *96(Supplement C),* 186-195.

[147] Isothermal oxidation mechanism of a newly developed Nb–Ti–V–Cr–Al–W–Mo–Hf alloy at 800–1200°C, J. Zheng, X. Hou, X. Wang, Y. Meng, X. Zheng, L. Zheng, International Journal of Refractory Metals and Hard Materials, **2016,** *54(Supplement C)*, 322-329.

[148] "Experimental study and modeling of high temperature oxidation of Nb-base in situ composites", D. Yao, R. Cai, C. Zhou, J. Sha, H. Jiang, Corrosion Science, **2009,** *51(2),* 364-370.

[149] S. Wach, Proc. Spring Residential Conf. on Degradation of High Temperature Materials, **1980,** *2,* 1-1,

[150] S. Wach, Proc 2nd Int. Conf. on Hydrogen in Metals, Pergamon,Oxford, 1978 **(JUNE 1977,** *1A1*

[151] S. Wach, Proc. 3rd Int. Conf. on Hydrogen in Materials, Paris, Pergamon, Oxford, **1982,** *1*, D2.

[152] T. Takahashi, Y. Minamino, H. Hirasawa, T. Ouchi, High-Temperature Oxidation and Its Kinetics Study of Ti-6Al-4V, Ti-Al and Ti-V alloys in air, **2014,** *55*, 290-297.

[153] "Effect of temperature on wear behavior in a Ti-V-Cr base fireproof titanium alloy", G.-B. Mi, K. Yao, X.-H. Min, International Journal of Precision Engineering and Manufacturing, **2017,** *18(11)*, 1553-1559.

[154] "The oxidation of vanadium in the temperature range 700°–1000°C", W.R. Price, S.J. Kennett, J. Stringer, The non-linear rate law, Journal of the Less Common Metals, **1967,** *12(4),* 318-325.

[155] "The oxidation of vanadium at high temperatures", Journal of the Less Common Metals, W.R. Price, J. Stringer, **1965,** 8(3) (1965) 165-185.

[156] "Analysis of volume effects of phase transformation in titanium alloys", W. Szkliniarz, G. Smołka, Journal of Materials Processing Technology, **1995,** *53(1),* 413-422.

[157] "High-temperature oxidation of tantalum of different purity", V.B.V. Golovko, Oxidation of Metals, **1995,** *43(5-6),* 509-526.

[158] "The Oxidation Behavior of Tantalum at 700 °C–1000 °C", P. Kofstad, Journal of the Electrochemical Society, **1963,** *110,* 491-501.

[159] "Thermodynamic properties of Ti in V-Ti-Ta alloys: Effect of Ta addition", U. Jain, A. Mukherjee, G.K. Dey, Journal of Alloys and Compounds, **2016,** *686 (c),* 946-950.

[160] "Dry Sliding Wear Behaviour of Titanium (Grade 5) Alloy by Using Response Surface Methodology", S.R. Chauhan, K. Dass, Advances in Tribology, **2013,** 9.

[161] "Effect of Load and Sliding Speed on Wear and Friction of Aluminum– Silicon Casting Alloy", R. A. Al-Samaraid, Haftirman, K. Ahmad, Y. Al-Douri, International Journal of Scientific and Research Publications, **2012,** *2,* 1-4.

[162] "Effects of Load and Speed on Wear Rate of Abrasive Wear for 2014 Al Alloy", D. Odabas, IOP Conference Series: Materials Science and Engineering, **2018,** *295,* 012008.

[163] "Comparison of Wear and Friction Behavior of Aluminum Matrix Alloy (Al 7075) and Silicon Carbide based Aluminum Metal Matrix Composite under Dry Condition at Different Sliding Distance", K. Singh, S. Singh, A. Shrivastava, Materials Today: Proceedings, **2017,** *4(8),* 8960-8970.

[164] "The effect of sliding speed and normal load on friction and wear property of aluminum", M. Chowdhury, M.K. Khalil, D.M. Nuruzzaman, M. Rahaman, **2011**.

[165] "Wear behaviour of cast hypereutectic aluminium silicon alloys", D.K. Dwivedi, Materials & Design, **2006,** *27(7),* 610-616.

[166] "Effect of copper on the tribological properties of Al-Si base alloys", R. Dasgupta, S.K. Bose, Journal of Materials Science Letters, **1995,** *14(23),* 1661-1663.

[167] "Wear resistance enhancement of titanium alloy (Ti–6Al–4V) by ball burnishing process", G.D. Revankar, R. Shetty, S.S. Rao, V.N. Gaitonde, Journal of Materials Research and Technology, **2017,** *6(1)*, 13-32.

[168] "Friction and wear of titanium alloys sliding against metal, polymer, and ceramic counterfaces", J. Qu, P.J. Blau, T.R. Watkins, O.B. Cavin, N.S. Kulkarni, Wear, **2005,** *258(9)*, 1348-1356.

[169] "The influence of Strontium addition on wear properties of Al–20wt.% Si alloys under dry reciprocating sliding condition", G. Liu, G. Li, A. Cai, Z. Chen, Materials & Design, **2011,** *32(1)*, 121-126.

[170] "Friction and surface behavior of selected titanium alloys during reciprocating-sliding motion", M. Long, H.J. Rack, Wear, **2001,** *249(1),* 157-167.

[171] "Dry sliding wear behavior of Al-4Si-4Mg alloys by addition of cerium", A. S Anasyida, A.R. Daud, M. Ghazali, International Journal of Mechanical and Materials Engineering, **2009**, *4(2).*

[172] "Microstructure and mechanical properties of hypo/hyper-eutectic Al–Si alloys synthesized using a near-net shape forming technique", M. Gupta, S. Ling, Journal of Alloys and Compounds, **1999,** *287(1)*, 284-294.

[173] "Single crystal V2O5 and lower oxides. A survey of their electronic, optical, structural, and surface properties, L. Fiermans, P. Clauws, W. Lambrecht, L. Vandenbroucke, J. Vennik, physica status solidi (a), **1980,** *59(2)*, 485-504.

[174] "A review of the growth of V2O5 films from 1885 to 2010", S. Beke, Thin Solid Films, **2011,** *519(6)*, 1761-1771.

[175] "Coulomb-potential-dependent decohesion of Magnéli phases", T. Reeswinkel, D. Music, J.M. Schneider,Journal of Physics: Condensed Matter, **2010,** *22(29),* 292203.

[176] "Ab initio calculations of the structure and mechanical properties of vanadium oxides", R. Thomas, M. Denis, M.S. Jochen, Journal of Physics: Condensed Matter, **2009,** *21(14)* 145404.

[177] "Calculation of Elastic Moduli of Polycrystalline Alumina and Zirconia from Monocrystal Data", W. Pabst, G. Tichá, E. Gregorová, Effective Elastic Properties of Alumina-Zirconia Composite Ceramics, **2004**, *part 3.*

[178] "Ab initio study of the elastic properties of single and polycrystal TiO 2 , ZrO 2 and HfO 2 in the cotunnite structure", M.A. Caravaca, J.C. Miño, V.J. Pérez, R.A. Casali, C.A. Ponce, Journal of Physics: Condensed Matter, **2009,** *21(1)*, 015501.

[179] "A crystal chemical approach to the formulation of self-lubricating nanocomposite coatings", A. Erdemir, Surface and Coatings Technology, **2005,** *200(5),* 1792-1796.

Nuclear fusion reactor and expected operating conditions

A.1.1 Fusion Energy

In fusion energy, two light nuclei fuse together to produce a heavier nucleus, nucleons (neutron or proton) and the loss of mass in that reaction is manifested as energy according to Einstein energy mass equivalence formula:

$$E = \Delta mc^2 \dots\dots\dots\dots\dots\dots\dots\dots\dots\dots\dots (A1.1)$$

where Δm is the difference in the mass of the reactants and products (Δm) and c is the velocity of light . The released energy is manifested as an increase in temperature of the system where the reaction takes place. In contrast to fission, fusion is practically feasible with light nuclei only, for which binding energy per nucleon forms the basis of the reaction. Fig. A.1.1 shows the binding energy per nucleon as a function of mass number.
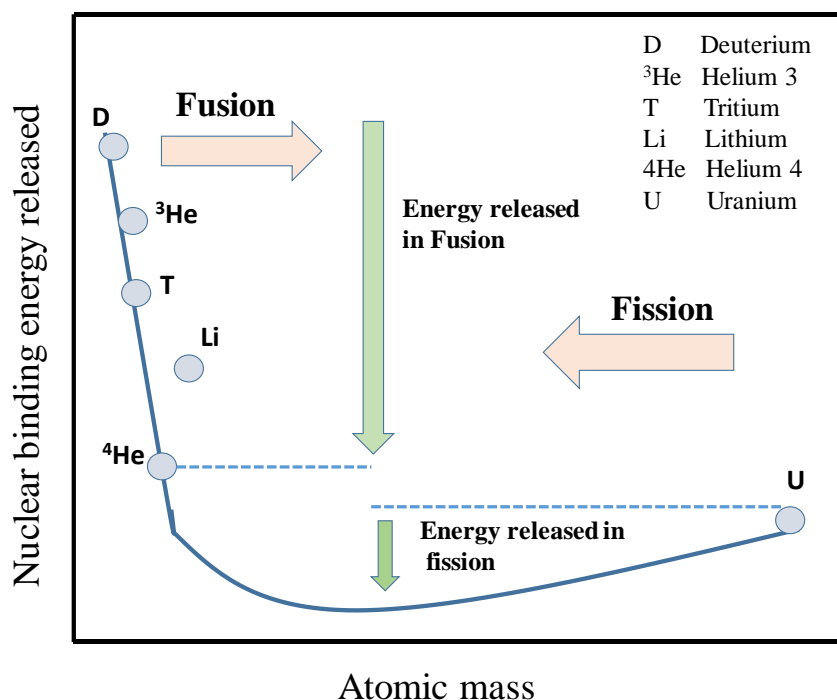
Figure A.1.1: Binding energy per nucleon released as a function of the atomic mass number.

It can be seen from the figure that the amount of energy released by the fusion of light nuclei is much higher in comparison to the amount of energy released by the fission of heavy nuclei. However, to initiate the nuclear fusion of light elements, nuclei need to overcome the columbic barrier to come closer for the fusion to start. Columbic barrier can be surpassed by increasing the kinetic energy of nuclei by heating them to very high temperatures which are in the order of 150 million °C. At such high temperatures atoms convert into ionised gases which are also called as plasma. In theory, any two light nuclei can undergo fusion reaction provided sufficient energy is supplied to them, but in practice, these three fusion reaction are widely considered due to their energetics and practical feasibility.

Table A.1.1: Widely considered fusion reactions showing the energetics of the reactions and the products.

Sl No.	Reaction	Ignition energy (keV)	Output energy (MeV)
1.	$D + D \rightarrow He^3 + n$	35.0	4.0
2.	$D + D \rightarrow T + p$	35.0	4.0
3.	$D + T \rightarrow He^4 + n$	4.0	17.6

Out of these fusion reactions, the most promising and energetically favoured fusion reaction is listed at no 3 in the Table A.1.1, which is the fusion of deuterium (D) and tritium (T) which led to the formation of an α particle (He4) and a neutron. In this fusion process 17.6 MeV energy is released due to energy and momentum conservation, out of which neutrons carry 14.1 MeV energy and the remaining energy is carried away by the α-particles. From energetic point, fusion generates four time more energy in comparison to fission reaction for normalized mass. It can be seen that D and T are the fuel for the fusion reaction, out of which deuterium is available in plenty, which can be obtained from sea water, but the availability of tritium is not

in abundance in the nature. Therefore, tritium need to be produce to sustain the chain of reaction which can be produced in-situ by the following nuclear reaction:

$$n + Li^6 \rightarrow T + He + Energy \text{...........................} (A1.2)$$

$$n + Li^7 \rightarrow T + He + n - Energy \text{.......................} (A1.3)$$
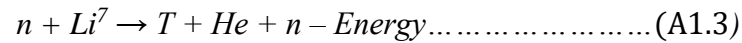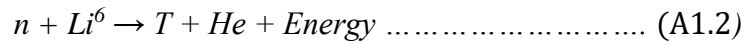
Lithium is abundant in oceans and earth's crust. It must be noted that lithium has two isotopes in nature, out of which Li^6 gives exothermic reaction while Li^7 requires net energy to be supplied to generate tritium.

A1.2 Brief description of nuclear fusion reactors

Fusion of light nuclei generates huge amount of concentrated energy, but the construction of a fusion power plant that can withstand this huge energy load released by the fusion reaction is very challenging from the materials point of view. The magnitude of the challenge can be understood from the point that even after 70 years of the discovery of fusion reaction, whole world is struggling to make the first fusion test reactor which can generate net positive energy. Scientific feasibility of controlled fusion of the light elements like deuterium and tritium in plasma under magnetic confinement has already been proven since long. However, tests for technological feasibility is still under question. Most important challenge in the development of a fusion reactor is the confinement of plasma in such a way that it is not in contact with the structural components of the reactor. There are two general ways to confine the plasma: (1) by inertial confinement or (2) by magnetic confinement. In inertial confinement, chain reaction is initiated by heating and compressing a fuel target using lasers inside a chamber. Magnetic confinement, a more popular, confines the plasma in a device called as 'Tokamak'. International fusion community are presently making coordinated effort to build a Tokamak or test reactor called as ITER (International Thermonuclear Experimental Reactor), to show the world for the feasibility of net fusion energy production. ITER will

contain Test blanket modules (TBM) to test various structural and functional materials. Six half ports have been provided to each country to test their TBM in the reactor. TBM will consist of different combination of functional as well as structural materials, which will be tested in ITER reactor. For example, India has selected RAFMS as structural material, Pb-Li eutectic alloy as tritium cum breeder material, and Li_2TiO_3 as solid breeder material. So basically ITER will deliver two fold objectives (i) breed tritium with Tritium Breeding Ratio (TBR) >1, and to (ii) extract the high grade heat from the tokamak with acceptable thermal efficiency. The results from the study of the behaviour of ITER will be used in the final DEMO and fusion power plant design. The operating conditions and parameters will be almost similar for ITER and DEMO reactors. A cross sectional view of ITER is shown in Fig. A.1.2.
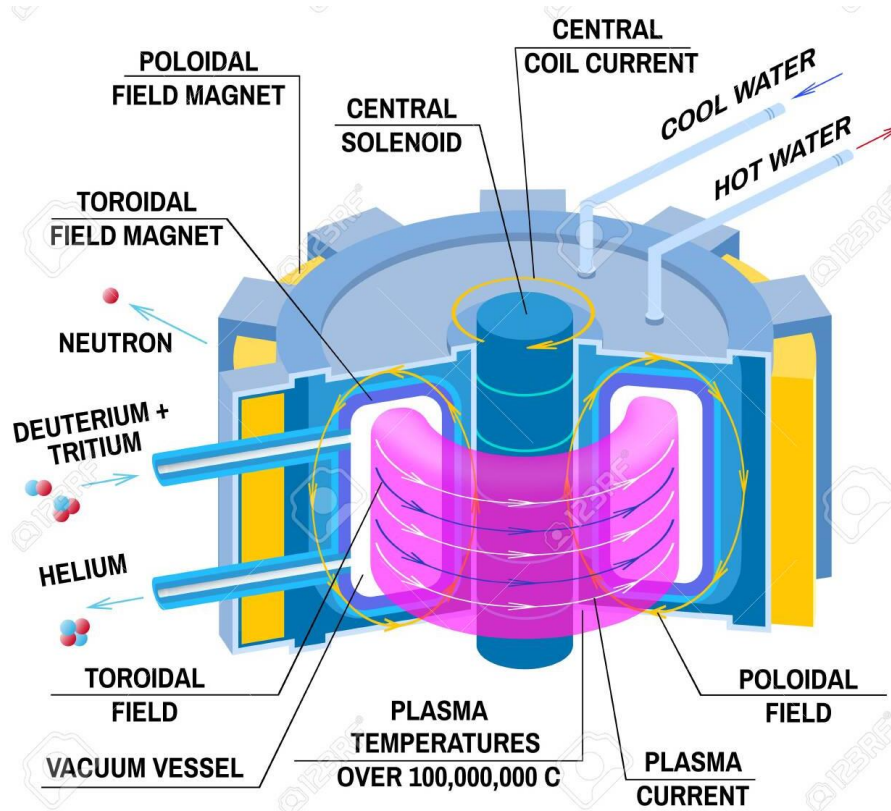
Figure A.1.2: Schematic of a magnetically-confined fusion reactor showing the key components.
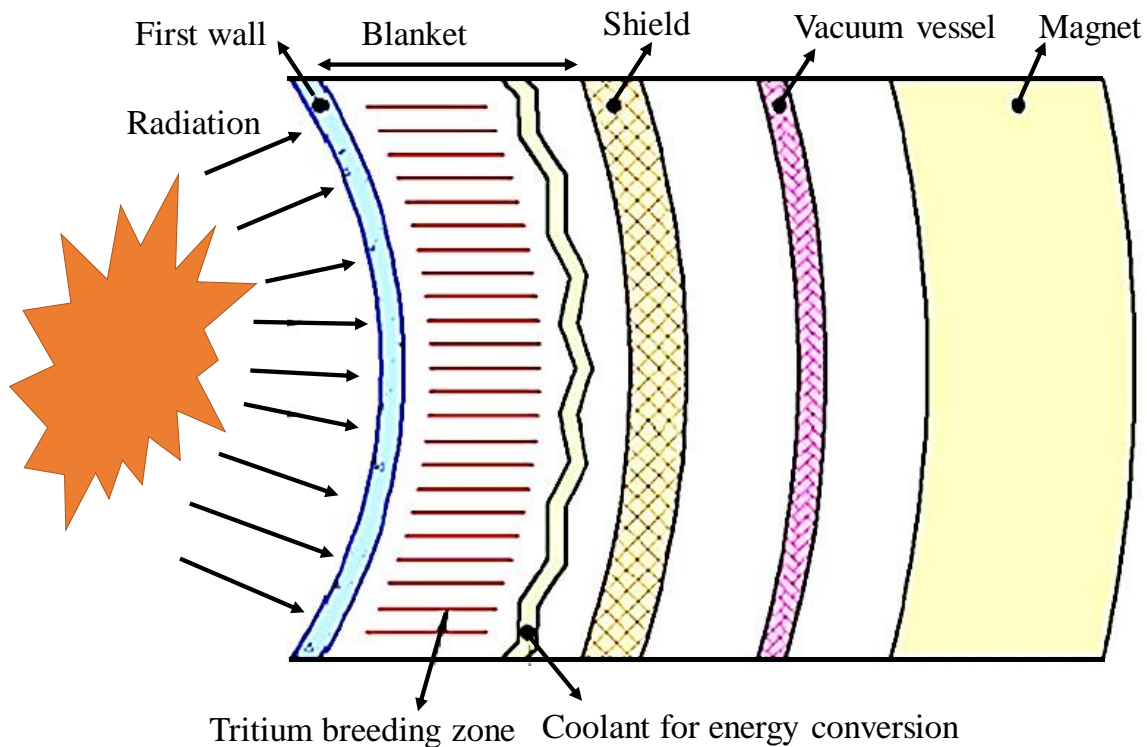
Figure A.1.3: Cross sectional view of core components of ITER.

It can be seen that heart of the reactor is toroidal shape chamber in which deuterium and tritium are filled in the gaseous state and subsequently heated by various heating methods, like induction and electromagnetic waves. These ignition condition leads to the plasma formation in the chamber. In order to confine the plasma and to avoid any harmful contact with the chamber wall, three different magnetic fields, named as (i) toroidal magnet (ii) poloidal magnet and (iii) central solenoid are used. The resultant magnetic field of these magnetic coils results in torus shape plasma formation, which prevents it from hitting to the chamber wall. It can be seen from Fig. A.1.3 that apart from plasma, ITER have several other allied components, which are as described in brief here:

1. First wall : This consists of the three basic components namely plasma facing material, heat sink material and the first wall structural material. (i) Plasma facing material could either be a low atomic no. (Z) carbon based material which will have low quenching effect on plasma but suffers from high supttering rate, or high Z tungsten bsed alloys

which will have low sputtering rate but quenching effect on plasma will be high. (ii) First wall heat sink will be of Cu-Cr-Zr alloy, which will disspiate heat from plasma facing materials. (iii) First wall structural materials, which will bear the mechancial load, have 3 potential choices (a) Reduced activation ferritic martensitic steel (b) Vanadium based alloys and (c) Silicon carbide.

2. Vacuum vessel and breeding blanket: The vacuum vessel is kept at a vacuum level of $\sim 10^{-6}$ Pa, which is used to hold the plasma. As mentioned before, fusion reaction lead to the formation of neutron and He. The heat is transported to the coolant through the walls of the TBMs both by radiative heat transfer from the plasma and by the electrically neutral 14.1 MeV neutrons that escape from the plasma into their walls and the functional materials. It may be noted here that various concepts of TBM have been proposed by different partnering nations of ITER. The heat from the fusion is extracted by an appropriate liquid (Pb-Li eutectic or Li) or gaseous coolant (He gas) flowing in the test blanket modules in the vacuum vessel close to plasma. Also, since the blanket consists of Li^6 containing compound either in the form of a ceramic compound (lithium titanate or lithium silicate) or liquid metal (pure lithium or lead-lithium eutectic alloy), it transmutes to tritium by (n, α) reaction. Tritium breeding is required to produce tritium at a rate higher than that of its consumption in the plasma, in order to make the whole process self-sufficient. The heat generated in tritium breeding is also removed by coolant.

3. Superconducting Magnets : These magnets are used to confine the plasma in a tokamak. Two choices Nb_3Sn and NbTi superconducting magnets have been selected to generate required magnetic field.

A.1.3 Operating condition and radiaition damage in fusion reactor
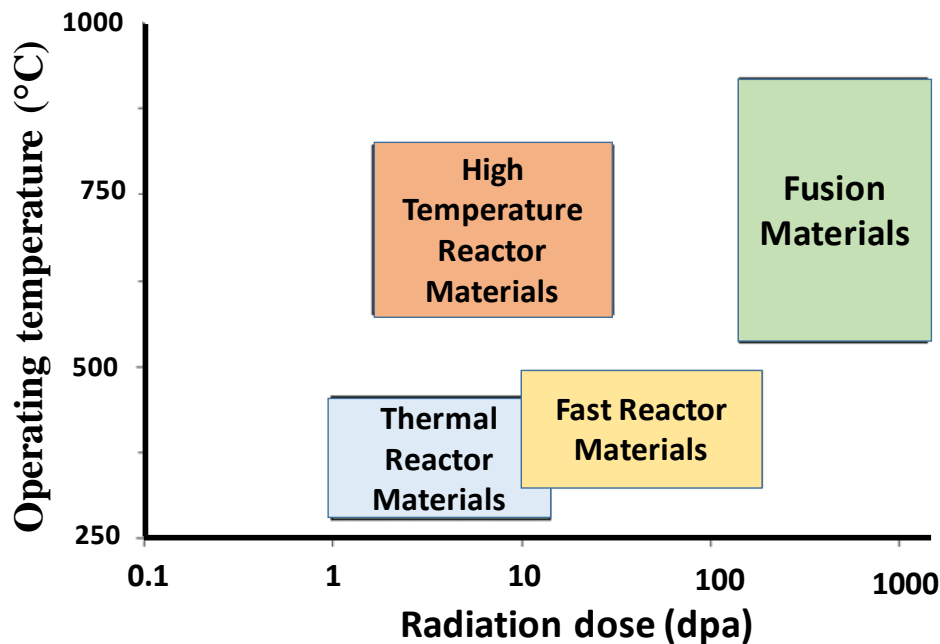
Figure A.1.4: Overview of operating temperature and expected radiation damage level (dpa)
for nuclear structural materials in fission and fusion reactors.

Fig. A.1.4 shows the typical operating temperature and radiation damage experienced by nuclear structural materials in different nuclear reactor. It can be seen that structural materials of a fusion reactor experiences typical temperature of 500- 1000 °C and 100-1000 dpa damage in its life time, which is much higher than the fission based reactors. Further, when high energy 14.1 MeV neutrons after escaping from the plasma strike to the walls of the structural materials, complications arise due to the intense radiation damage (both in terms of displacements and transmutations) of lattice atoms caused by them. Displacement of atoms results in structural vacancies formation which causes void swelling in the materials. The high energy neutrons also undergo transmutation reactions with structural materials to cause the (n, α) and the (n, p) reactions with almost all elements constituting the walls of the TBMs undergo these reactions leading to the formation of both helium and hydrogen in them at high rates. These particles

cause additional embrittlement related issues in the structural material. These irradiation effects

on materials phenomena are summarized in Table A.1.2.

Table A.1.2: Type of radiation damage and consequential degradation of structural materials

in a fusion reactor.

Effect	Consequence in material	Kind of degradation in component	Temperature range	Displacement damage (dpa)
Displacement damage	Point defect and dislocation loop formation	Hardening and Embrittlement	< 0.4 Tm	0.1
Irradiation induced segregation and precipitation	Diffusion of selective elements to grain boundaries, Formations of phases not expected according to phase diagram,	Embrittlement, Grain boundary cracking	0.3 to 0.6 Tm	> 10
Swelling	Increase in volume due to defect cluster and voids	Localized deformation which eventually led to residual stresses	0.3 to 0.6 Tm	> 10
Irradiation creep	Permanent deformation	Creep life is reduced	< 0.45 Tm	> 10
He formation and diffusion	Void formation	Embrittlement	> 0.5 Tm	> 10

Radiation damage of structural materials can be broadly categorized in five different effects which are emerging at different operating temperatures and damage levels. These damages can significantly affect the operation of structural materials. These phenomena are summarized in Table A.1.2. At low temperatures (below 0.3-0.4 Tm, where Tm is the absolute melting temperature), radiation-induced point defects and dislocation loops are formed which serve as strong hindrance to dislocation motion. This result in hardening of the structural material accompanied by substantial reductions in ductility. This causes embrittlement related issues in the materials viz. loss of fracture toughness in BCC metals and alloys. This radiation induced hardening and embrittlement occurring at relatively low doses (0.001 to 0.1 dpa), defines the lower operating temperature limit for structural materials in nuclear reactors; particularly more severe in fusion reactors.

At intermediate temperatures (0.3-0.6 Tm), three distinct radiation effects phenomena are of potential significance for doses above ~1 to 10 dpa: (i) radiation induced segregation (RIS) and precipitation, that can lead to localized grain boundary corrosion or grain boundary embrittlement, (ii) void swelling due to vacancy accumulation causing volumetric expansion, and (iii) radiation induced creep and/or radiation induced anisotropic growth that can produce dimensional changes along directions of high stress and / or specific crystallographic directions.

At very high temperatures (> 0.5 Tm), helium produced by neutron transmutation reactions (n, α) in the structural material migrates towards grain boundaries and dislocation due to its insolubility in the matrix. This results in the bubble formation, which also stabilises vacancy clusters formed by displacement damage, and the resulting bubbles inhibit dislocation motion which causes embrittlement. Embrittlement effects due to helium are more prominent at high temperatures (> 0.5 Tm) due to the nucleation and growth of He bubbles at grain boundaries. This high temperature helium embrittlement of grain boundaries typically emerges

for helium concentrations above 10 to 100 appm (~1 to100 dpa, depending on material and neutron energy spectrum and becomes increasingly severe with increasing temperature, applied stress. He bubbles also cause swelling in the material, resulting in dimensional changes and residual stress.   Along with chemical compatibility and thermal creep strength, high temperature helium embrittlement defines the maximum allowable operating temperature for a structural material in nuclear fusion reactor.

These extreme reactor operating conditions pose greater challenge in the selection of material for structural application. In addition, structural materials selection in fusion reactor have an additional constraints of low activation criteria. Fusion reactors prime objective is towards minimal environmental impact, which is achieved by selecting low half-life daughter product materials. This puts a great challenge for material scientists for the development of materials which can extend the operating temperature window with selection of low activation elements as alloying agents.

References:

[1] "Materials issues in fusion reactors", A.K. Suri, N. Krishnamurthy, I.S. Batra, Journal of Physics: Conference Series, **2010,** *208*, 012001.

[2] "Operating temperature windows for fusion reactor structural materials", S.J. Zinkle, N.M. Ghoniem, Fusion Engineering and Design, **2000,** *51-52*, 55-71.

Thermodynamic properties determination using Knudsen effusion mass spectrometer (KEMS)

A.2.1 Preamble

Accurate measurements of thermodynamic properties are important parts for the development and optimization of compositions in alloy systems. These measurements are vital for understanding the solid solution behaviour of multiple component alloys, as these thermodynamic properties provide useful data to predict stability of a given system under a range of environments very accurately. One fundamental way to obtain thermodynamic properties is to measure the vapor pressure of gas species which are in thermodynamic equilibrium with the condensed phases. Since a material for high temperature applications should have very low vapor pressure, information on vapor pressure and the vapor composition as a function of temperature are obviously of great importance. Vapor pressure data provide many useful information. Some of the salient points are listed below:

1. Vapor pressure data as a function of temperature are useful in determining the enthalpy of sublimation (ΔH_{sub}) of a reaction, which is the amount of heat evolved in the reaction and is a key input for many thermodynamic databases.

2. The chemical potentials of the vapor phase and condensed phase will be equal under the equilibrium conditions. Under such equilibrium conditions in vapor and condensed phases, different thermodynamic properties of various reactions can be calculated by employing simple thermodynamic relations. For example, Gibbs free energy change can be determined by measuring the equilibrium constant of a vaporization reaction, which forms the basis for obtaining other thermodynamic quantities such as partial free energy, excess free energy.

These thermodynamic data form the basis for the optimization of the composition of an alloy and high temperature stability.

Hence the accurate measurements of vapor pressures are very crucial in determining the thermodynamic properties. Vapor pressure of the materials have been measured by various common methods like static, boiling point, transpiration, isopiestic method and Knudsen effusion based methods. Out of these methods, Knudsen effusion technique is the most versatile, which will be described in detail. Other methods are not in the scope of present thesis, hence not described henceforth.

A.2.2 Vapor pressure measurement using Knudsen effusion mass spectrometer

In Knudsen effusion technique, a small cell having knife edged effusion orifices of 0.2-0.5 mm diameter (Knudsen cell), which contains a sample for which vapor pressure is to be measured, is heated under vacuum. The whole system consists of two chambers, one containing the Knudsen cell furnace assembly and the other compartment having a quadruple mass spectrometer (QMS) chamber. KEMS apparatus used in present study is shown in Fig A.2.1. Design of the equipment used in the present study is based on the KEMS described by Darwin et al. [1]. The detailed description of the machine along with the figures can be found in the reference [1]. The Knudsen cells made of alumina (with dimensions – inner diameter: 7.5 mm, outer diameter: 10.0 mm, height: 10.0 mm) was used to hold the samples. The cell was provided with a lid having knife edged effusion orifices of 0.3 mm diameter. The alumina cell with the sample was kept inside a tantalum cup with a tight-fitting lid made of tantalum and having a 2 mm diameter circular hole collinear with the Knudsen cell orifice. The tantalum cup (Knudsen cell) was heated by radiation and electron bombardment (EB) by two independent tungsten filaments that encircled it. Three concentric radiation shields, made of tantalum, were placed all around the filaments which aided the temperature stability of the Knudsen cell. The top and

bottom were also shielded with tantalum sheets. The Knudsen cell furnace showing Ta rods and Knudsen cell is shown in Fig. A.2.2. Through careful consideration of the inner shape of the cell, effusion orifice, and surface area of the sample, near equilibrium conditions are attained between the condensed phases and the vapor phase while the orifice continuously samples the vapor by effusion. The molecular flux in the effusing molecular beam from the Knudsen cell is fed into the ion source of a mass spectrometer where it is mass analyzed to find out quantitatively the different kinds of species present in it. This is the basis of the Knudsen Effusion Mass Spectrometric (KEMS) method. The schematic of effusion path is shown in Fig. A.2.3. This method has distinct advantages of high sensitivity and its ability to obtain partial pressures and molar mass of the different species present in the effusing molecular beam. Mass spectrometric analysis can be categorized in to 3 different stages, which are:

     i.   Production of ions from effusing vapor beam by electron ionization

    ii.   Mass analysis of the ions produced (Mass analyzers).

   iii.   Collection of the mass separated ions and its quantification.

The output obtained from the mass spectrometer is the ion intensity (ion current) produced by a particular species. Various stages are involved in calculating the vapor pressure from this ion intensity of the selected species. The main considerations in this regard are:

   i. Background/residual ionization: Detected ions form a species that is present inside the Knudsen cell or from the residual gases/species present in mass spectrometer chamber.

  ii. Fragmentation process: Ions which are detected in mass-spectrometer, whether the ion is produced as a result of ionization of a species effusing out of the Knudsen cell or produced due to fragmentation in the ion source

 iii. Calculation of the vapor pressure from the measured ion intensity: After differentiating and eliminating all the possible interferences and by selecting the species that has its origin from the Knudsen cell, it is possible to relate its intensity to the vapor pressure.

Additional discussion on the calculation of vapor pressure from the ion intensity is given in the next section.
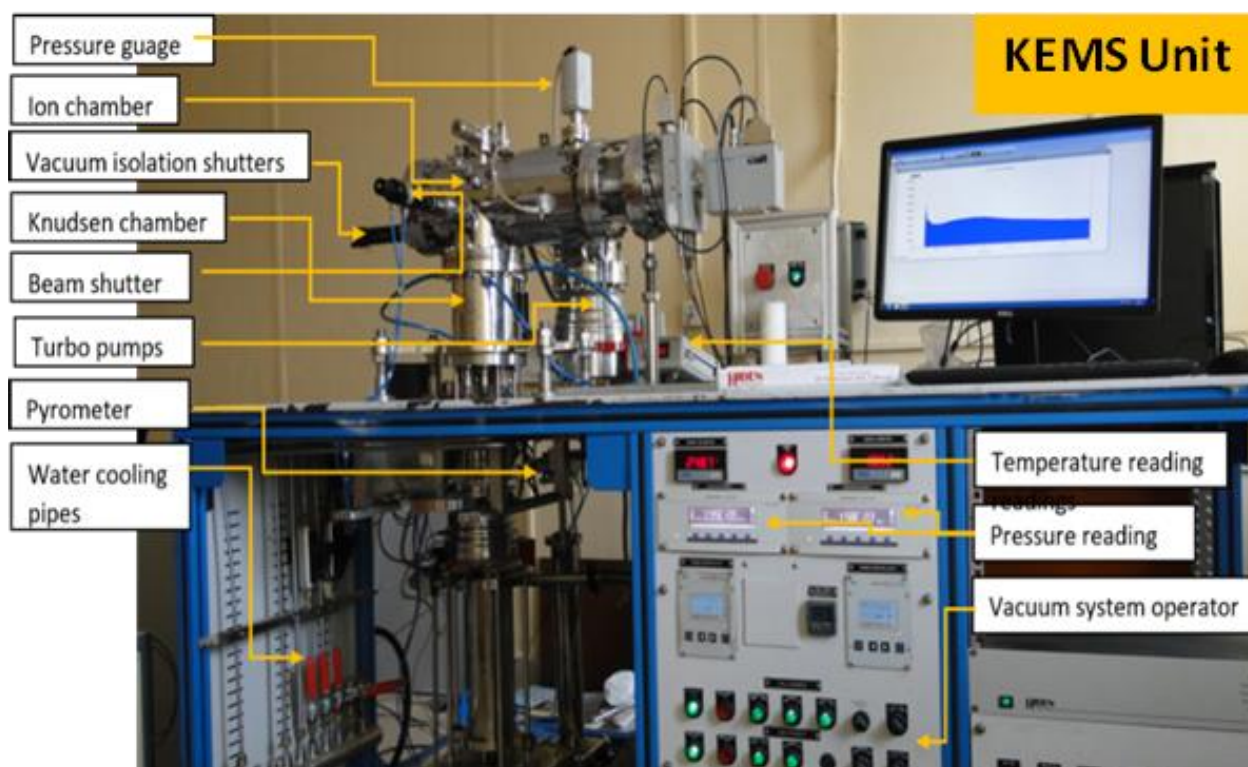
Figure A.2.1: KEMS system used in present study showing different parts.
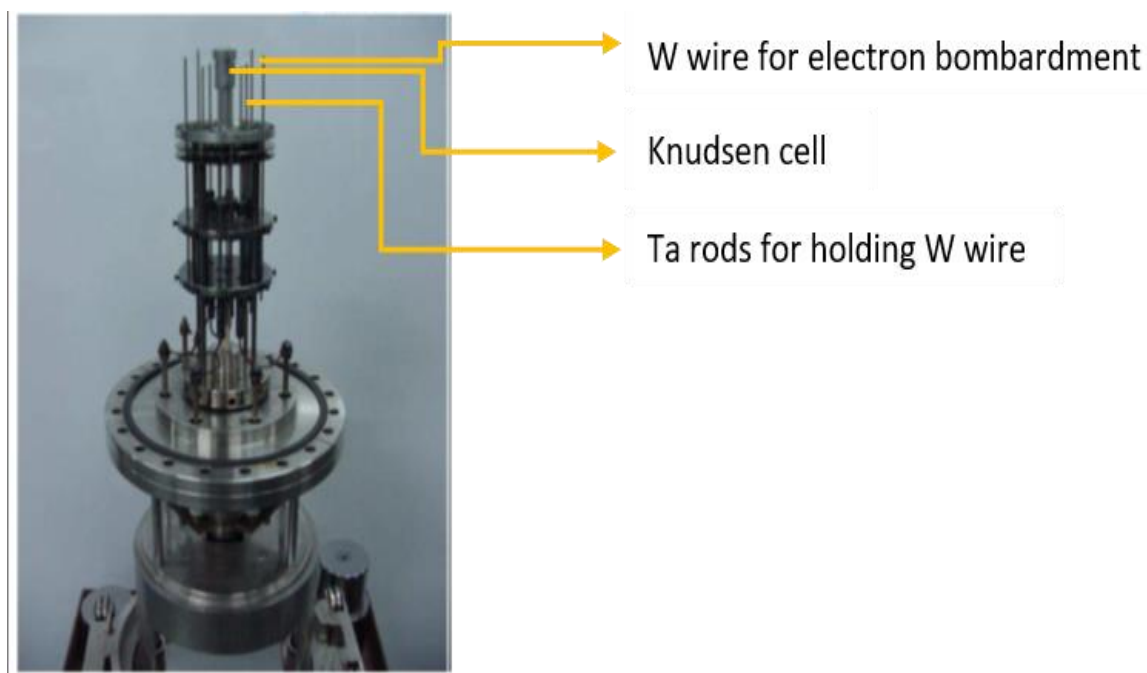
Figure A.2.2: Knudsen cell furnace used in present study.
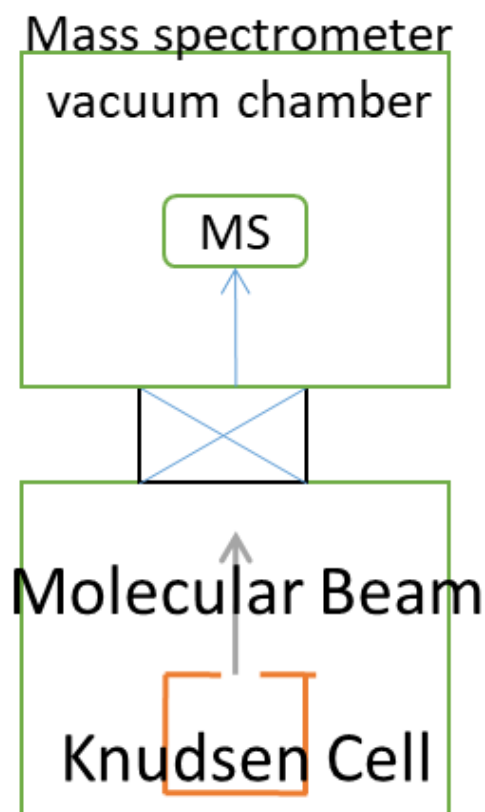
Figure A.2.3: Schematic of Knudsen effusion mass spectrometer.

A.2.3 Relationship between ion intensity and vapor pressure

Ion intensity I^+ of any particular mass number obtained in a mass spectrometric measurement

is directly proportional to the number of ions at the collector n_{col}^+ . Therefore

$$n_{col}^+ \; \alpha \; I^+ \; .... \; (A2.1)$$

In order to improve sensitivity, multiplying type detectors are used with γ as the multiplication

efficiency of such a detector, then

$$n_{col}^+ \; \alpha \; \frac{I^+}{\gamma} \; .... \; (A2.2)$$

If a particular isotope has relative isotopic abundance as A_b, then number of ions that arrive at

the detector from the selected species will be

$$n^+_{col} \; \alpha \; \frac{I^+}{\gamma A_b} \quad .... \quad (A2.3)$$

Only a fraction of the total number of ions produced in the ion source, will enter the analyzer region. This fraction is known as the transmission coefficient η of the ion source. Therefore, the number of ions inside the ion source n^+_{source} can be given as

$$n^+_{source} \; \alpha \; \frac{I^+}{\eta \gamma A_b} \quad .... \quad (A2.4)$$

Ion source ionizes a fraction of total vapor particles, which give rise of Ionization efficiency (IE) factor of the ion source. Therefore, the number of neutral particles present inside the ion source will be given by

$$n_{source} \; \alpha \; \frac{I^+}{(IE)\eta \gamma A_b} \quad .... \quad (A2.5)$$

By applying the cosine distribution law, a relationship between the number density of atoms/molecules arriving at a target (ion source) n_{source} at a distance L from a Knudsen cell having an orifice area a_0 and a number density n_{cell} inside it as

$$n_{source} = n_{cell} \cdot \frac{a_0}{4\pi L^2} \quad .... \quad (A2.6)$$

Substituting for n_{source} from equation (A2.5) in equation (A2.6) and rearranging,

$$n_{cell} \; \alpha \; \frac{I^+ . 4\pi L^2}{(I.E.).\eta . \gamma . A_b . a_0} \quad .... \quad (A2.7)$$

Equation (A2.7) gives a relationship between the number of atoms of a species inside the Knudsen cell and the ion intensity produced by that species effusing out of it. From fundamental principles we know that

$$p = n_{cell}kT \quad \text{.. } (A2.8)$$

Substituting for n_{cell} from equation (A2.7) in equation (A2.8) and removing proportionality constant,

$$p = \frac{4\pi L^2 . k . I^+ . T}{(I.E.).\eta.\gamma.A_b.a_0} \quad \text{.................... } (A2.9)$$

Equation (A2.9) gives the relationship between the measured ion intensity of a species at temperature T and the partial pressure of that species inside the Knudsen cell.

A.2.4 Determination of pressure calibration constant

The relationship between the measured ion intensity of a species and its pressure inside the Knudsen cell -represented by equation (A2.9) can be used for the estimation of vapor pressure if all the factors in the equation are known. In principle, it is not difficult to know these parameters and therefore it should be possible to find out the vapor pressure. However, the uncertainties connected with some of the terms (for example the path length of the ionizing electrons, the transmission factor of the ion source etc.) and the varying nature of some others (for example the multiplication efficiency) will render this procedure more difficult and less reliable. A more practical way to use this equation is explained below.

Equation (A2.9) can be rearranged and written as

$$p = \left[\frac{4\pi L^2 . k}{I_{eV}^- . \ell . \eta . \gamma . A_b . a_0} \right] . \frac{I^+ . T}{\sigma_i} \quad \text{................ } (A2.10)$$

Where ℓ is path length of the ionizing electron beam and σ_i is ionization cross section of the species. All factors inside the bracket can be taken as a single constant k and the equation can be rewritten as

$$p = k \cdot \frac{I_i^+ \cdot T}{\sigma_i} \quad \text{...} \quad (A2.11)$$

in which k is known as the pressure calibration constant. If k is experimentally determined,

p can be calculated since I_i^+ and T can be measured and σ_i can be determined or obtained from

literature.

The pressure calibration constant k can be determined experimentally by many

methods. The most direct method is applicable to cases where the species 'i' present over a

calibration substance (for which p – T relationship is known) and over the substance of study.

Measurement over the calibration substance at different temperatures will yield which then can

be employed to determine p_i from measured over the substance of study.

Very often, it will not be possible to find a species common for pressure calibration and

the sample material of interest. Equation (A2.11) can still be used in such cases, with a slightly

modified approach. In this method, which is referred to as the 'Indirect Calibration Method', a

calibration substance, (for which vapor pressure – temperature relationship is well established

and the ionization cross section of the vapor species for the electron energy used is well known)

is taken in the Knudsen cell and the intensity of the species is measured at some known

temperatures. Using the values of I^+, T and σ_i, k can be calculated. The pressure of the unknown

species j can be deduced, using the value of k calculated as above and by using the ionization

cross section of the species j along with the measured ion intensity and temperature. Obviously,

this method requires the knowledge of the ionization cross section of the species i and j.

A.2.5 Evaluation of thermodynamic quantities from partial pressure

A number of thermodynamic parameters can be obtained from the measured ion

intensities or the partial pressures

1. Activities of components in an alloy:

$$a = \left(\frac{p_i}{p_i^\circ}\right) \dots \dots \dots \dots \dots \dots \dots \dots \dots (A2.12)$$

where p_i is the partial pressure of the component over the alloy and p_i^0 is the pressure of the pure component at the same temperature.

2. Enthalpy of sublimation:

$$\frac{d \ln p}{d \left(\frac{1}{T}\right)} = \frac{d \ln(IT)}{d \left(\frac{1}{T}\right)} = \frac{-\Delta H_{sub}}{R} \dots \dots \dots \dots \dots \dots (A2.13)$$

where R is the universal gas constant and ΔH_{sub} is enthalpy of sublimation.

3. Partial free energy of component i

$$\Delta \bar{G}_i = RT \ln a_i \dots \dots \dots \dots \dots \dots \dots \dots \dots \dots \dots (A2.14)$$

4. Excess partial free energy of component i

$$\Delta \bar{G}_i^{XS} = \Delta \bar{G}_i - RT \ln x_i \dots \dots \dots \dots \dots \dots \dots \dots \dots (A2.15)$$

5. Enthalpy and entropy of mixing

$$\ln a_i = \frac{\Delta H_i^{mix}}{RT} - \frac{\Delta S_i^{mix}}{R} \dots \dots \dots \dots \dots \dots \dots \dots (A2.16)$$

The mass spectrometric method in conjunction with Knudsen effusion, which has the distinct advantage of giving information on vapor composition and partial pressure data, enables identification as well as measurement of vapor pressures of gaseous species in a wide dynamic range of ~ 10 Pa to ~ 10^{-7} Pa [2]. It is interesting to note that most of the well-established vapor pressure data in JANAF tables have been recorded using this technique [3].

References:

[1] "The Design, Construction, and Testing of a Knudsen Effusion Mass Spectrometric System Suitable for Studies of Nuclear Fuel Materials", D.D.A. Raj, R. Viswanathan, P. Manikandan, ECS Transactions, **2013,** *46(1)*, 77-97.

[2] "Twenty Years of Knudsen Effusion Mass Spectrometry: Studies Performed in the Period 1990-2010", M. Miller, K. Armatys, Open Thermodynamics Journal, **2013,** *7(1)*, 2-9.

[3] "Thermodynamic activity measurements with Knudsen cell mass spectrometry", E.H. Copland, N.S. Jacobson, Interface-Electrochemical Society, **2001,** *10(2),* 28-33.